Numéro d'ordre : 2005-004

**Université Claude Bernard Lyon 1**
**et**
**Institut National des Sciences Appliquées de Lyon**

# HABILITATION A DIRIGER DES RECHERCHES

**Patrick Clarysse**

**Docteur de l'Université des Sciences et Technologies de Lille**

# ANALYSE D'IMAGES CARDIAQUES ASSISTEE PAR LES MODELES

27 Mai 2005

**Rapporteurs**

| | | |
|---|---|---|
| Leon | AXEL | M.D., Ph.D., Professor of Radiology, NY University |
| Nicholas | AYACHE | Directeur de Recherche INRIA, INRIA Sophia-Antipolis |
| Alain | HERMENT | Directeur de Recherche INSERM, INSERM U494, Paris |

**Examinateurs**

| | | |
|---|---|---|
| Jacques | BITTOUN | Professeur de Biophysique et Médecine Nucléaire, Paris-Sud |
| Isabelle | MAGNIN | Directeur de Recherche INSERM, Creatis, Lyon |
| Jérome | POUSIN | Professeur, INSA de Lyon |
| Didier | REVEL | PUPH, Université Claude Bernard-Lyon1 |

**Creatis, unité de recherche CNRS UMR 5515, INSERM U630, Lyon, France**

# SOMMAIRE

# CURRICULUM VITAE

**Patrick CLARYSSE**

Né le 3 décembre 1963, à Lille (59), Nationalité française

Adresse professionnelle : CREATIS CNRS UMR 5515, INSERM U630
INSA – Bât. Blaise Pascal,
69621 Villeurbanne cedex, France
Tél : 04 72 43 81 48, Fax : 04 72 43 85 26
e-mail : patrick.clarysse@creatis.insa-lyon.fr
web : http://www.creatis.insa-lyon.fr/~clarysse/

**Statut Actuel :** Chargé de Recherche CNRS, Classe 1, Section 30, Dépt SDV-STIC

## Responsabilités actuelles :

- Responsable du thème STIC « imagerie dynamique » à CREATIS
- Co-responsable du sous-thème SDV « Imagerie fonctionnelle de l'ischémie myocardique » à CREATIS avec P. Croisille.

## Domaines de compétences :

*Analyse d'images médicales* : traitement numérique d'images multi-dimensionnelles et multi-modalités : segmentation, estimation de mouvement, recalage d'images. Applications à l'imagerie cardiaque

## Diplômes

1991 Thèse: Automatique et Informatique Industrielle, Mention Très Honorable, USTL
1987 DEA de Productique: Automatique Robotique et Informatique Industrielle, USTL, mention AB
1986 Maîtrise EEA, filière Automatique, USTL, Mention AB
1983 DUT de Génie Electrique, Université des Sciences et Technologies de Lille (USTL)

## Déroulement de carrière

Octobre 1996- Chargé de Recherche CNRS 1ère classe, section 22 puis 30, CREATIS, Villeurbanne

1992-1996 Chargé de Recherche CNRS 2ième classe, Section 22, dept SDV-SPI, LTSU (Laboratoire de Traitement du Signal et Ultrasons), Villeurbanne

1991-1992 Attaché Temporaire d'Enseignement et de Recherche (1991-1992), Université des Sciences et Technologies de Lille

1988-1991 Chercheur doctorant au CAL (Centre d'Automatique de Lille), Université des Sciences et Technologies de Lille et au Laboratoire de Biophysique du CHU de Lille. Titulaire d'une allocation du MESR.

## Publications

- 17 publications dans des revues spécialisées avec comité de lecture
- 34 communications dans des colloques avec actes
- 2 actes de congrès co-édités (FIMH'01, FIMH'03)

## Encadrement de jeunes chercheurs (voir détail en page suivante)

- **Thèses soutenues: 5, en cours: 3, Post-doctorants: 2**
- **DEA : >10, Stages : >10**

## Relations internationales

- Laboratory of Biomedical engineering, Helsinki University of Technology (depuis 1998)
- Cardiac Research Institute Maastricht, Maastricht University, Pays-Bas (depuis 2003)

## Animation et administration de la recherche

- Co-responsable avec L. Desbat (UJF, Grenoble) du projet "ADéMo : Modélisation et suivi spatio-temporel pour le diagnostic et le traitement", thématiques de Recherche de la Région RA, 2000-2003.
- Co-responsable avec F. Frouin (INSERM-U494) de l'Action Spécifique du CNRS ICoMIM, 2002-2003
- Responsable Français d'un PICS du CNRS avec le Laboratory of Biomedical Engineering, Helsinki University of Technology, Finlande, 2003-2005
- Membre de la commission de spécialistes de la 61ème section CNU de l'INSA de Lyon jusqu'en 1997, de l'UCB Lyon (depuis 1995), université Lyon 2 (depuis 2001), USTL (1998-2001)
- Membre de la commission d'Emergence N°5, «Chirurgie micro-invasive et robotisée » de l'INSERM depuis 2003
- **Référé de Journaux :** IEEE Trans. Med. Imaging, IEEE Trans. Image Processing, IEEE Trans. Biomed. Eng, IEEE Trans. ITB, MEDIA, J. of Mathematical Imaging and Vision, Pattern Recognition Letter, Investigative Radiology, Journal of Electronic Imaging, J. Computing and Information Technology (CIT), Innov. Techn. Biol. Med.
- **Référé de Conférences**: ICPR'02, ISBI, ICIP, FIMH, IISPA, ISPA, RFIA, GRETSI, Forum des Jeunes Chercheurs en GBM.
- **Comités de programme :** Participation à la création de la conférence internationale FIMH (3$^{ième}$ édition en 2005), Membre du comité scientifique de ISPA, FIMH.
- **Jurys de thèses externes**: 2

## Sociétés savantes :

Membre de la Société française de Génie Biologique et Médical

## Encadrement de jeunes chercheurs

- ***Thèses soutenues : 5***

**PAUNA** Nicoletta, 'Evaluation des méthodes de mise en correspondance en imagerie multimodale IRM/TEP thoracique et cardiaque'. Numéro d'Ordre : UCBL66-2004, Université Claude Bernard LYON 1 en co-tutelle avec l'Université de Cluj, Roumanie, **2004**. Jury : I. Magnin (Pdt), B. Gibaud (R), R. Ciupa (R), M. Janier (Dir.), O. Cozar (Dir.), P. Clarysse (Co-Dir), A. Georgescu. Co-encadrement à 40% avec M. Janier et O. Cozar.

Actuellement en Post-Doc à l'IPNL, Lyon.

**MÄKELÄ** Timo, double thèse et co-tutelle

- 'Data registration and fusion for cardiac applications', Helsinki University of Technology, Mai **2003.** Oponent : N. Ayache (INRIA).
- 'Mise en correspondance en imagerie cardiaque multimodale : vers un modèle anatomo-fonctionnel individualisé du cœur'. Numéro d'Ordre : ISAL106, INSA LYON, **2004.** Jury : P. Cinquin (R, Pdt), N. Ayache (R), T. Katila (Dir.), I. E. Magnin (Dir.), P. Clarysse (Co-Dir.), U. Ruotsalainen. Co-encadrement à 50% en collaboration avec les partenaires Finlandais.

Actuellement hospitalo-universitaire à l'hôpital de Oulu, Finlande.

**PHAM** Quoc-Cuong, Segmentation en imagerie cardiaque multimodale conduite par un modèle réaliste du cœur, INPG, **2002.** Jury : J-M. Chassery (Pdt), F. Heitz (R), H. Delingette (R), I. E. Magnin (Dir.), P. Clarysse (Co-Dir.), J. Pousin, P. Croisille, T. Katila. INPG, 2002. Co-encadrement à 80% avec I. Magnin.

Actuellement chercheur au CEA, Saclay.

**VINCENT** Fabrice, Gabarits déformables élastiques pour la segmentation et le suivi de mouvement du cœur en Imagerie par Résonance Magnétique. Numéro d'ordre : 01ISAL0079, INSA LYON, **2001.** Jury : J. Pousin (Pdt), N. Ayache (R), Ph. Cinquin (R), I. Magnin (Dir), P. Clarysse (Co-Dir), P. Croisille. Co-encadrement à 80% avec I. Magnin.

Actuellement ingénieur société Théralys.

**HAN** Meimei, Analyse exploratoire de la déformation spatio-temporelle du myocarde à partir de l'Imagerie par Résonance Magnétique de Marquage tissulaire. Numéro d'Ordre : ISALY004, INSA LYON, **1999.** Jury : I. Magnin (Pdt), M. Lamure (R), J-G. Postaire (R), P. Clarysse (Dir.), P. Croisille, D. Revel, J. Rousseau. Co-encadrement à 80% avec I. Magnin.

Actuellement ingénieur entreprise Bombardier, Montréal, Canada

- ***Thèses en cours :3***

**HADDAD** Rana, 3ème année thèse Images & Systèmes, 'Modèle anthropomorphique de cœur battant'. Co-encadrement à 80% avec I. Magnin.

**DELHAY** Bertrand, 2ème année thèse Images & Systèmes, 'Estimation conjointe forme et mouvement en 3D – Application au mouvement du thorax et du cœur'. Co-encadrement à 80% avec I. Magnin.

**SCHAERER** Joël, 1ère année thèse Instrumentation, Système, Signal & Image, 'Modèle spatio-temporel pour la segmentation de structures en mouvement – application à l'imagerie du cœur'. Co-encadrement à 80% avec I. Magnin.

- ***Post-doctorants : 2***

**MILLES** Julien, nationalité Française, Univ. Post-doc à Maastricht, Pays-Bas, 12 mois. Co-encadrement à 50% avec T. Arts, **2003-2004.**

**QIU** Bo, nationalité Chinoise, Creatis. Co-encadrement à 50% avec D. Vray, **2003-2004.**

# 1. INTRODUCTION GENERALE

Ce document présente mes activités de recherche dans le domaine de l'analyse d'images médicales débutées au cours de ma thèse effectuée au Laboratoire de Biophysique du CHU de Lille et au Centre d'automatique de l'Université des Sciences et Technologies de Lille (1988-1992) et poursuivies en temps que Chargé de Recherche au CNRS, au laboratoire CREATIS à Lyon depuis Octobre 1992. Ces deux périodes m'ont conduit à approfondir plusieurs domaines du traitement d'images, à savoir la segmentation, l'estimation de mouvement et la mise en correspondance d'images, pour deux applications médicales principales que sont l'imagerie cérébrale et l'imagerie cardiaque. Mes travaux de thèse ont porté sur le développement d'un système de repérage tridimensionnel et multi-modalités en stéréotaxie cérébrale. Ce système a été opérationnel au bloc opératoire du service de neurochirurgie du CHR de Lille et utilisé pendant plusieurs années pour la préparation et l'accomplissement des procédures stéréotaxiques du cerveau. L'imagerie cardiaque constitue mon second et actuel domaine d'application. Certains diront que de l'une à l'autre les techniques de référence sont les mêmes. Ceci est vrai en partie seulement, car si les fondements des techniques d'analyse d'images subsistent, les spécialités médicales sont quant à elles divisées en organes. Une des raisons en est sans doute que le fonctionnement, la physiologie, sont très spécifiques de chaque organe. Les déterminants d'un diagnostic ou d'un traitement peuvent être également très différents selon l'organe et la pathologie auxquels on s'intéresse même s'il existe certains fondements communs. On trouve ainsi des processus physiopathologiques similaires impliqués dans l'ischémie cérébrale et cardiaque. Sans prolonger ce débat, qui a été souvent abordé à CREATIS, on peut dire que quelle que soit l'application médicale visée une approche pluridisciplinaire s'impose. C'est ce que nous avons tenté d'adopter durant ces années de recherche. D'une formation initiale universitaire d'automaticien, je me suis efforcé d'élargir mon champ de connaissances dans plusieurs directions : en imagerie médicale, en médecine (bases) en particulier du système cardio-vasculaire; en modélisation mathématique au sens large, en mécanique des milieux continus, biomécanique et statistiques; et en informatique qui reste l'outil de base. Ceci a bien entendu été possible grâce à un environnement local très favorable, lié à la composante médicale de l'Unité et à d'autres compétences scientifiques externes.

Aujourd'hui, je perçois mon rôle à l'interface entre des communautés de spécialités; la communauté médicale (radiologie, cardiologie, physiologie) et la communauté des sciences « dures » (traitement du signal et des images, informatique, mathématiques appliquées, mécanique, optimisation…). C'est en tout cas ce que j'essaye d'appliquer au quotidien en particulier au sein du thème STIC « Imagerie dynamique » et du thème médical « Ischémie myocardique » à CREATIS. La principale difficulté étant de conserver un équilibre entre des activités de recherche totalement orientées vers les applications et, à l'inverse, des recherches exclusivement fondamentales.

Ce document est constitué de deux parties. La première partie présente mes contributions de recherche en analyse d'images cardiaques. J'ai cherché à mettre en évidence les verrous scientifiques et les solutions innovantes que j'ai apporté. Ces travaux ont été menés pour leur plus grande part en collaboration étroite avec des doctorants. La seconde partie résume l'ensemble de mes activités de recherche, d'enseignement et d'animation de la recherche ainsi que mes responsabilités collectives à l'intérieur et l'extérieur de CREATIS.

# PARTIE A :
# ACTIVITES DE RECHERCHE
# PERIODE 1992-2005

# 1. INTRODUCTION

L'imagerie médicale a vécu un essor considérable ces trente dernières années. L'Imagerie par Résonance Magnétique (IRM) en est peut-être un des exemples les plus marquant. De la découverte de la Résonance Magnétique Nucléaire par Bloch et Purcell en 1946 (prix Nobel de physique en 1952), il a fallu attendre le début des années soixante dix pour qu'apparaissent les premières applications en imagerie médicale sous l'impulsion de Paul C. Lauterbur, Sir Peter Mansfield et Raymond Damadian. Depuis les années quatre vingt, cette modalité n'a cessé de se diversifier et a diffusé très largement dans le milieu médical et clinique. Le prix Nobel 2003 de Médecine a été attribué conjointement à Paul C. Lauterbur et Sir Peter Mansfield, reconnaissant ainsi l'impact majeur de leur découverte dans la pratique médicale [1]. L'imagerie des organes en mouvement introduit un nouveau 'challenge' car en dépit de développements technologiques sans précédent, peu de modalités sont aujourd'hui capables d'acquisition en (quasi-) temps réel. L'imagerie ultrasonore (échographie) permet de réaliser des acquisitions à très hautes cadences (25 images/seconde de façon courante et jusqu'à 300 images/secondes et plus). Elle présente de plus l'avantage d'un coût nettement moins élevé que des tomographes à rayons X ou IRM mais la qualité de l'information image reste encore nettement en deçà et limitée en pratique clinique au 2D[1]. La tomographie à rayons X opère un retour sur le devant de la scène de l'imagerie cardiaque avec les scanneurs multi-barrettes. Cependant, comme en IRM, des techniques de synchronisation avec l'Electrocardiogramme (ECG) et la respiration sont requises pour reconstruire une information dans le temps. L'acquisition rapide d'images constitue actuellement un enjeu majeur comme le montre par exemple les sessions du prochain congrès de la Société Internationale de Résonance Magnétique en Médecine en Mai 2005 (ISMRM, Tutoriel de Jürgen Hennig « Fast imaging horizons in rapid MR Imaging »).

Cette évolution remarquable s'accompagne d'un accroissement massif des données acquises dans les centres hospitaliers. Ainsi, la production annuelle d'un département de radiologie, toutes spécialités confondues, dépasse les 10 TéraOctets ($10^{12}$) et l'on parle maintenant de PetaOctets ($10^{15}$) au niveau des pays. Ceci implique une première difficulté qui est de pouvoir gérer, stocker et accéder à cette masse de données. C'est l'objet des systèmes d'archivage et de communication d'images (PACS, '*Picture Archiving and Communication Systems*') de plus en plus présents dans les centres hospitaliers. La seconde difficulté concerne l'exploitation intelligente des images. Par intelligente, on entend qu'il s'agit d'extraire de manière efficace une information pertinente destinée à aider le praticien à établir un diagnostic ou à réaliser un geste chirurgical. Les travaux rapportés dans ce document sont une *contribution au développement de systèmes d'analyse d'images médicales*. Ils proposent des *solutions pour l'extraction d'information et de paramètres quantitatifs en imagerie cardiaque*. Ce contexte est très exceptionnel du fait de la complexité du système physiologique cardio-vasculaire et de la grande diversité des processus fonctionnels impliqués. On rappelle également l'enjeu de santé publique des maladies cardio-vasculaires qui représentent la première cause de décès dans les pays dits industrialisés. L'appréhension, la compréhension et la modélisation du système cardiaque nécessitent une approche pluridisciplinaire intégrant des connaissances de la physique et des spécificités des systèmes d'acquisition de données, de la physiologie et de la physio-pathologie du cœur et du système cardio-vasculaire, des techniques de traitement de signal et de l'image. Le dénominateur commun des méthodes développées est précisément constitué par la démarche pluri-disciplinaire et le recours systématique à des techniques de modélisation que se soit de formes ou de fonctions. Dans le cadre de l'action spécifique (AS) du CNRS intitulée « Intégration de connaissances et

[1] Des sondes ultrasonores multiplans 3D existent depuis bientôt 10 ans.

modélisation en imagerie médicale » (ICoMIM), qui a réunit de nombreux acteurs français impliqués dans l'analyse d'images en Génie Biologique et Médical, nous avons tenté de formaliser la démarche de conception des systèmes de production et d'analyse d'images médicales, de l'idée originale du système à son utilisation dans un contexte médical en passant par son élaboration et son implantation. Les développements décrits dans ce mémoire suivent cette démarche et la particularisent à l'analyse d'images fonctionnelles du cœur.

## 2. CONTEXTE MEDICAL

Les maladies cardiovasculaires représentent une pathologie majeure dans les pays industrialisés. On peut prendre la mesure d'un tel état de fait en notant qu'aux Etats-Unis une personne sur cinq souffre d'une forme de maladies cardiovasculaires et 2600 personnes en décèdent chaque jour[2]. Enfin, le coût direct et indirect de ces pathologies est estimé à près de 400 milliards de dollars par an. En Europe, 40% des décès avant l'age de 74 ans sont dus à une maladie cardiovasculaire, même si on observe des disparités selon les pays[3].

Depuis sa création, le Laboratoire de Traitement du Signal et Ultrasons devenu CREATIS, né de la réunion de chercheurs en Sciences et Technologies de l'Information et de chercheurs en médecine, a fait des maladies cardiovasculaires un de ses domaines médicaux d'investigation privilégié. La pathologie à laquelle nous nous intéressons plus particulièrement est *l'ischémie myocardique* qui provient d'un déficit de l'irrigation du muscle cardiaque (myocarde) du à l'obstruction plus ou moins prononcée d'un ou plusieurs vaisseaux (les artères coronaires). La forme critique de la maladie engendre l'infarctus du myocarde. L'altération des tissus myocardiques qui en résulte est un phénomène évolutif complexe. La séquence des évènements consécutifs à un épisode ischémique est connue sous le nom de *cascade ischémique* (Figure 1).

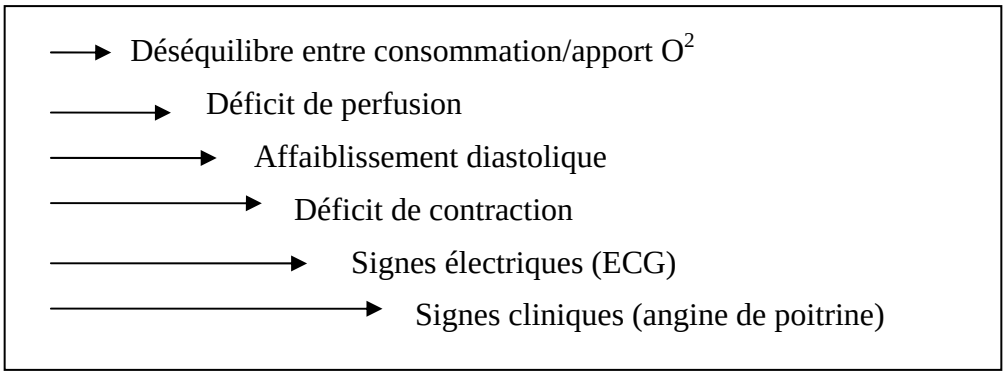


*Figure 1. La cascade ischémique illustre les conséquences de l'obstruction d'une artère coronaire*

Le clinicien doit tout d'abord identifier la ou les artères obstruées et les territoires du cœur menacés. Puis il lui faut déterminer la procédure thérapeutique la mieux adaptée : traitement médicamenteux, angioplastie ou revascularisation chirurgicale. La revascularisation est cependant un geste invasif et risqué dont il est important de déterminer les bénéfices a priori. On conçoit intuitivement que le déficit d'apport en nutriments aux cellules myocardiques engendre un dérèglement de leur fonction qui peut aboutir à la mort cellulaire. Le concept de *viabilité tissulaire* a été introduit afin de traduire l'état fonctionnel des tissus et leur potentiel à recouvrer une fonction normale. En clinique, l'analyse *in vivo* à l'échelle cellulaire n'étant pas possible, on doit se contenter d'observations à l'échelle macroscopique grâce aux techniques d'imagerie médicale. Les études de la physiopathologie cardiaque d'origine ischémique ont porté sur la *perfusion*, le *métabolisme*, la *contractilité cardiaque* et leurs interrelations. De manière schématique, un équilibre existe entre perfusion, métabolisme et fonction contractile dans le myocarde normal. L'équilibre est rompu lors d'un épisode ischémique. Selon sa durée et ses caractéristiques, l'évolution peut-être très diverse et de nombreux mécanismes et phénomènes ont été identifiés, comme la sidération,

[2] Source: American Heart Association, 2005, http://www.americanheart.org/
[3] Source: Eurostat, 2002

l'hibernation, etc. Ainsi, des régions où la captation relative du glucose est supérieure à la perfusion relative (régions dîtes de « *mismatch* ») sont considérées comme indicatrice de l'hibernation myocardique. Elles sont censées être dysfonctionnelles au repos et améliorer leur fonction contractile après revascularisation. Alejandro Mazzadi montre dans sa thèse sur l'étude des couplages entre perfusion, métabolisme glucidique et fonction contractile en imagerie fonctionnelle cardiaque chez l'homme [2], que la réalité semble plus complexe. Il a ainsi mis en évidence des discordances entre viabilité fonctionnelle (fonction contractile) et viabilité métabolique et conclut à une faible valeur prédictive des paramètres issus des imageries pour l'estimation de la récupération fonctionnelle à l'issu d'une revascularisation. Cependant, l'étude des couplages semble intéressante pour l'évaluation de nouvelles molécules pharmacologiques ou les nouvelles thérapies géniques.

Ce très court résumé des enjeux actuels en cardiologie montre les besoins en termes de mesure de paramètres caractéristiques des différentes fonctions considérées que sont la *perfusion*, le *métabolisme* et la *fonction contractile* myocardique. La *perfusion* peut être évaluée en tomographie d'émission monophotonique (TEMP) grâce à l'utilisation d'un radiotraceur émetteur de photons $\gamma$, en échocardiographie de contraste, en IRM et en Tomographie par Emission de Positons (TEP) qui est considérée comme la technique de référence. La TEP et la spectrométrie RMN permettent une mesure du *métabolisme*. Seule la TEP, en particulier avec injection de déoxyglucose marqué au fluor (18F-FDG) est utilisée en clinique. Enfin, la *fonction contractile* peut être évaluée de manière très partielle en angiocardiographie à rayons X. En médecine nucléaire, la fonction contractile est habituellement évaluée de manière globale par gamma-angiographie à l'aide d'un traceur radioactif. L'échocardiographie permet également d'apprécier la fonction de manière plus locale et bénéficie d'une très bonne résolution temporelle. Les scanners à rayons X récents à acquisition hélicoïdale ou multi-barettes permettent l'étude de la fonction avec une très bonne résolution spatiale et une résolution temporelle en augmentation. L'IRM avec en particulier l'IRM de marquage tissulaire apparaît comme la modalité non invasive de référence pour l'estimation globale et locale de la fonction contractile. Les séquences de réhaussement tardif donnent, par ailleurs, une information assez précise sur l'étendue des zones de nécrose. Notons que les techniques tomographiques qui permettent une étude en 3D requièrent une synchronisation à l'ECG et à la respiration pour l'acquisition des informations au cours du cycle cardiaque. D'autres fonctions cardiaques, comme l'activité électrique et magnétique, peuvent être étudiées grâce à l'électrocardiographie (ECG) et la magnétocardiographie (MCG). Les arythmies sont des anomalies du rythme cardiaque qui peuvent être détectées par de telles techniques. Certaines études ont montré que des cartographies de champ magnétique issues de la MCG lors d'épreuves d'effort pouvaient permettre la détection d'une ischémie [3, 4]. Le Tableau 1 synthétise les différentes modalités utilisées pour les études fonctionnelles du cœur avec leurs principales caractéristiques.

La plupart de ces techniques ne délivre pas une information directement utilisable et quantitative. Un post-traitement des données s'avère généralement nécessaire pour extraire les paramètres structurels et fonctionnels pertinents. Nous présentons dans la section suivante les principaux verrous que l'on peut identifier dans le domaine de l'analyse d'images cardiaques.

| Modalités | Fonction mesurable | Traceurs / Agent de contraste | Résolution spatiale | Résolution temporelle | Invasivité | Limitations | Disponibilité | Coût |
|---|---|---|---|---|---|---|---|---|
| **TEP** | Métabolisme<br>- glucidique<br>- oxydatif<br>Récepteurs innervation cardiaque<br>Perfusion | $^{18}$F-FDG<br>$^{11}$C-Acétate<br>$^{11}$C-MHED<br>$^{11}$C-MQNB<br>$^{11}$C-CGP<br>$^{11}$C-NH3,<br>$^{15}$O-H2O | 3D, ~isotrope,<br>= 4 mm typique, 2.1mm pour les meilleures caméra<br>~mm pour la µTEP | ~40ms (20 phases), Synchro ECG | + | • Equipement conséquent, Nécessité d'un cyclotron<br>• Résolution spatiale | -- | +++ |
| **TEMP** | Perfusion<br>Fonction G | Thallium 201, 99Tc-Sestamibi, 99Tc-tétrofosmine | ~ 8 mm, courant<br>~<mm pour la µTEMP | Synchro ECG | +++ | • Résolution spatiale,<br>• Injection d'un produit contraste | ++ | + |
| **Angiocardiographie** | Fonction G | Agent de contraste iodé | 2D, multi-plans,<br>Projections,<br><1mm | 20ms | +++ | • Injection d'un produit contraste<br>• Imagerie en projection | + | + |
| **Tomodensitométrie à Rayons X**<br>Spiralée | Anatomie (cœur-vaisseaux)<br>Fonction<br>Perfusion | Agent de contraste iodé | 3D, 600µm | ~100ms, Synchro ECG | + | • Résolution temporelle encore limitée,<br>• Injection d'un produit contraste | ++ | ++ |
| **IRM**<br>Anatomique<br>Ciné, tagging<br>Seq. Perfusion | Formes, volumes<br>Fonction G/L<br>Perfusion | Gadolinium,… | 3D, ~1mm<br>2D+, ~1/7mm<br>2D+, 2-3 mm<br>500 µm pour la µIRM | ~15ms,<br>Synchro ECG<br>Apnée ou respiration libre | - | Contre-indications : pacemakers… | + | +++ |

| | | | | | | | | |
|---|---|---|---|---|---|---|---|---|
| **Echocardiographie** | Perfusion (animal) | µParticules gazeuses | 2D | <5ms | ++ | • Qualité image,<br>• Reproductibilité,<br>• Images en éventail | +++ | +/++ |
| Mode B | Anatomie | | 2D | | -- | | | |
| | | | 3D, 0.3mm en profondeur, | | | | | |
| Doppler | Flux | | 1D+ | | -- | | | |
| Doppler tissulaire | Fonction G/L | | 1D+, ~1µm/2mm | | -- | | | |
| **ECG** | | | | | | | | |
| Standard | Activité élect. G | | - | | -- | Information globale | ++ | -- |
| Mapping de potentiels de surface | Activité élect. L | | | | +++ | Peu pratiqué | --- | ++ |
| **MCG** | Activité magn. L | | ~6mm$^3$ | 1ms | -- | • Résolution spatiale,<br>• Problème inverse | --- | +++ |

Tableau 1. Les différentes modalités et leurs principales caractéristiques (G=globale, L= Locale)

# 3. HISTORIQUE ET VERROUS

L'exposé du contexte montre que l'étude des pathologies cardiaques repose sur une imagerie fonctionnelle multi-modalités. A partir de cette imagerie, les besoins du médecin sont de:

- bénéficier d'une information pertinente et utile
- disposer de paramètres quantitatifs précis et discriminants
- corroborer des informations d'origines diverses (multi-modalités)

Il s'agit donc de développer de nouvelles méthodes de traitement numérique d'images afin de:

- Améliorer la qualité des images (bruit, contraste…)
- Extraire des structures et des paramètres anatomiques et fonctionnels
- Mettre en correspondance des données multi-modalités
- Analyser les données d'un même patient ou de patients différents.

Dans l'objectif de l'évaluation des fonctions cardiaques principales (perfusion, contraction, métabolisme, activité électro-magnétique) et pour chaque modalité (voir Tableau 1), on peut identifier des difficultés associées à chacune de ces opérations de traitement d'images. Nous nous limiterons ici à l'analyse des problèmes posés en termes de traitement d'images par l'évaluation de la perfusion et, surtout, de la fonction contractile et d'aide à la quantification et à l'interprétation. Nous parlerons peu du développement d'agents de contraste ou de nouvelles techniques d'acquisition qui sont pourtant à la base de nos travaux mais qui ne sont pas notre spécialité. L'efficacité des méthodes d'analyse d'images est en effet directement conditionnée par la qualité des données à traiter. Nous avons pu constater au cours de ces années de recherche combien les difficultés rencontrées à l'origine d'un développement se sont trouvées grandement diminuées ou, au contraire, compliquées avec l'évolution des techniques d'acquisition. Il existe de fait une dépendance directe naturelle entre la qualité des données acquises, les résultats escomptés et les résultats obtenus.

## 3.1. EVALUATION DE LA PERFUSION

La perfusion myocardique est étudiée de longue date au laboratoire. Il s'agit d'études qualitatives et quantitatives qui ont débouchées sur une meilleure connaissance des agents de contraste en IRM, sur la mise au point de méthodes de correction d'artefacts et sur le développement de méthodes d'analyse quantitative de la perfusion conduisant à la génération de cartes paramétriques régularisées de la perfusion [5]. Les séquences IRM disponibles sur les imageurs récents fournissent aujourd'hui des images de très bonne qualité qui permettent une analyse correcte de la perfusion myocardique [6]. De nombreuses études cliniques ont démontré que l'IRM est une technique opérationnelle d'estimation de la perfusion myocardique au repos et sous stimulation [7]. Les évolutions futures envisageables de l'imagerie de premier passage en IRM concernent le développement d'agents intravasculaires plus performants, l'optimisation des séquences d'excitation RF et l'imagerie à plus au champ (3T) pour augmenter le rapport signal sur bruit (RSB) [8]. Jerosh-Herold remarque cependant que la qualité des résultats dépend beaucoup des approches choisies pour l'analyse de la perfusion [9]. La diffusion des logiciels et des méthodes d'analyse d'une part et des études cliniques d'autre part devrait déboucher sur une standardisation des procédures. Le calcul des cartes de perfusion repose aussi sur le développement de techniques de compensation du mouvement cardiaque, indispensables pour la reconstruction locale correcte des courbes de

premier passage à partir des séries dynamiques d'images acquises. Les artefacts engendrés par les inhomogénéités de champ ne semblent en revanche pas avoir d'impact direct sur l'estimation des paramètres quantitatifs de la perfusion comme le débit et le volume régional sanguins [6].

### 3.2. EVALUATION DE LA FONCTION CONTRACTILE

L'effet des occlusions coronaires sur la contraction myocardique a été mis en évidence par Tennant et Wiggers dans les années trente [10]. La dynamique cardiaque est aussi une des premières fonctions à avoir pu être observée d'abord de manière directe et expérimentale chez l'animal puis grâce aux techniques d'imagerie chez l'homme. Comme le souligne D. Friboulet [11], l'estimation du mouvement cardiaque en terme d'analyse d'images est un problème difficile au moins pour deux raisons principales :

- le mouvement cardiaque est un phénomène 4D (3D + temps) de nature complexe [12] piloté par la propagation d'une onde de dépolarisation à la surface du cœur et les régimes de pression dans les différentes structures cardiaques et vasculaires. La phase d'éjection du sang, par exemple, débute lorsque, la pression intraventriculaire dépassant la pression aortique, la valve aortique s'ouvre. Le ventricule gauche se contracte ce qui se traduit par un raccourcissement circonférentiel et un épaississement radiaire des fibres musculaires du myocarde (fibres myocardiques).
- la "vision" de ce phénomène que nous donnent actuellement les modalités d'imagerie disponibles est encore parcellaire. Tout d'abord, on mesure essentiellement les effets c'est-à-dire les formes et leur évolution au cours du cycle cardiaque. D'un point de vue mécaniste, seules les déformations sont accessibles, pas les contraintes. Du point de vue de la mesure des déformations, les données "idéales" devraient non seulement présenter une très bonne résolution dans les 3 dimensions spatiales et dans la dimension temporelle (on notera que la vitesse de la paroi cardiaque peut atteindre des valeurs de l'ordre de 15 cm/s) mais de plus fournir des informations sur la vitesse ou le déplacement des structures cardiaques. Malgré les évolutions récentes sur ce dernier aspect (IRM de marquage tissulaire et de contraste de phase, imagerie Doppler myocardique en échographie ultrasonore), aucune des modalités concernées n'est à l'heure actuelle capable de fournir de telles données. Elles obligent donc à un compromis entre résolution temporelle, résolution spatiale et obtention des informations de déplacement.

Une somme considérable de travaux en imagerie et en traitement d'images a été consacrée à l'estimation et à la caractérisation du mouvement tridimensionnel du cœur à partir de séquences d'images [13]. Dans la mesure où il représente la cavité principale du cœur, la plupart de ces études se sont particulièrement intéressées au ventricule gauche (VG).

#### 3.2.1. Approches initiales

La quantification du mouvement cardiaque a d'abord reposé sur l'analyse de la balistique de marqueurs radio-opaques implantés chirurgicalement sur des animaux et observés en angiocardiographie. Une telle approche est manifestement traumatisante et ne permet l'étude que d'un nombre restreint de sites. Des approches moins invasives se sont intéressées à l'analyse de la cinétique de la paroi cardiaque et l'identification de cas de figure particuliers (Figure 2). Pour l'aide au diagnostic, les centres cliniques se sont mis à développer chacun leur propre technique de quantification de la cinétique pariétale (méthodes de la ligne centrale, des rectangles, radiale, surface, etc.). En 1982, à l'occasion du symposium international 'Ventricular wall motion', les organisateurs U. Sigwart et P. H. Heintzen concluent à la grande variabilité individuelle et inter-individuelle des paramètres de

mouvement [14]. Ils déplorent le manque de mise en commun et de standardisation des procédures et incitent à la réunion de cardiologues et d'ingénieurs pour faire émerger de nouvelles solutions.

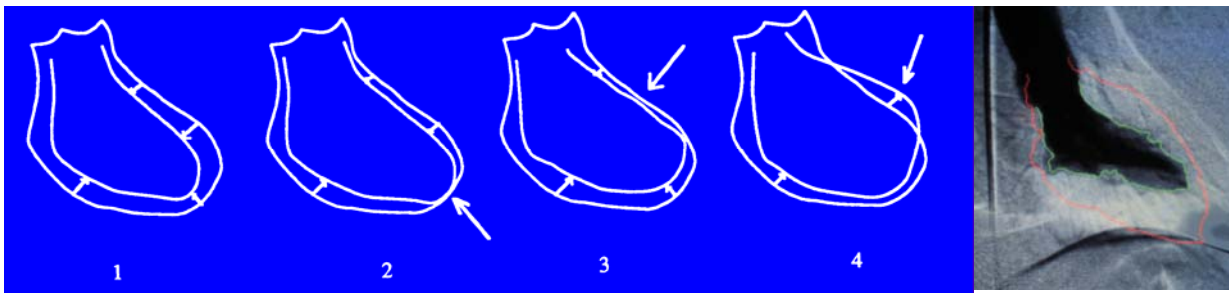


*Figure 2. La dynamique pariétale. 1- Normal. 2- Akinésie. 3- Hypokinésie. 4- Dyskinésie (extension systolique paradoxale). Ventriculographie à droite.*

Mancini est un des premiers à proposer la courbure pour caractériser localement les variations de forme du VG entre la télédiastole et la télésystole et également comme une alternative de mesure de la cinétique pariétale [15]. Duncan et *al.* ont proposé peu après de caractériser la forme locale du contour télé-diastolique par une énergie de flexion nécessaire à la déformation de ce contour vers un contour moyen représentant la normalité [16]. Ces travaux ont constitué le point départ d'une série de développements sur la segmentation et la mise en correspondance de surfaces cardiaques (voir par exemple [17-19]) grâce aux données délivrées par le prototype de reconstructeur spatial et temporel à rayons X, DSR (Dynamic spatial Reconstructor), développé à la Mayo Clinic, Rochester, USA [20]. Equipé de 14 sources, ce système pouvait acquérir 120 coupes adjacentes d'épaisseur 0.9mm en 1/60$^{ème}$ de seconde [21]. De nombreuses études expérimentales et méthodologiques ont ainsi pu être réalisées grâce à ce système.

### 3.2.2. IRM

Les séquences anatomiques en IRM (ciné IRM) ont suscité des développements en termes d'analyse d'images en particulier pour l'estimation de paramètres globaux du cœur comme les volumes cavitaires, la fraction d'éjection et des paramètres régionaux comme l'épaississement segmentaire pariétal. De plus, l'IRM est reconnue comme étant reproductible et non-invasive [22]. Des logiciels, destinés à faciliter l'analyse, ont été développés dont le plus connu est sans doute MRI-MASS[4]. Bien que de plus en plus de fonctionnalités (semi-) automatiques soient intégrées dans ces logiciels, l'analyse de la fonction cardiaque en 3D+temps reste une opération qui demande un contrôle continu de la part de l'utilisateur et beaucoup de temps. En effet, un protocole d'acquisition standard comporte plusieurs niveaux de coupes (5 à 10, typiquement) et de 10 à trente phases. Il s'agit d'extraire les contours endocardiques et épicardiques de l'ensemble de ces images avant d'accéder à une reconstruction surfacique 3D des parois. Les outils destinés à faciliter ce type d'opération sont toujours au stade d'étude. Les approches 3D+temps que l'on voit apparaître actuellement reposent généralement sur des modèles anatomiques a priori.

Pour une estimation locale du mouvement, des méthodes d'estimation de champs denses de mouvement ont été proposées [23] (voir [24, 25] pour des applications en tomodensitométrie X). Mais l'IRM standard, comme les autres imageries tomographiques anatomiques, se heurte au manque de correspondances explicites entre les images des séquences dynamiques. La technique de marquage tissulaire en IRM [26, 27] tente de pallier

[4] http://www.medis.nl/MainFrameProducts/Products/MriMass/

ce problème. Initialement réservée à quelques centres spécialisés dans le développement de séquences IRM, cette technique est aujourd'hui disponible dans certains sites de recherche mais rarement en routine clinique. De nombreuses études méthodologiques ont été menées par les groupes disposant non seulement des séquences IRM adéquates mais aussi des programmes de post-traitement indispensables pour l'exploitation quantitative des images. Il s'agit essentiellement de groupes nord-américains (Johns Hopkins Hospital and University - E. Zherouni, E. MCVeigh, J. Prince, University of Pennsylvania - L. Axel, D. Metaxas, University of Auckland - A. A. Young) et du groupe de Zurich (University and ETH-Zurich - P. Boesiger). A Lyon, ce type de séquence est arrivé vers 1993-1994. C'est à cette époque que nous avons débuté nos travaux de recherche sur ce type d'images, travaux qui ont été renforcés à l'issu du séjour de Pierre Croisille au Johns Hopkins Hospital. Une dizaine d'années de développement dans ce domaine est consignée dans l'ouvrage collectif récents « Measurement of cardiac deformations from MRI : physical and mathematical models » [28]. Les évolutions actuelles tendent par la combinaison de différentes techniques à augmenter la résolution temporelle, la densité spatiale et la persistance du marquage. Ainsi dans [29], la combinaison d'une séquence de marquage tissulaire de type CSPAMM (Complementary SPAMM) et d'une séquence d'imagerie spiralée a permis d'acquérir des séquences d'images avec un espacement de marquage de 4 mm en une apnée (16 phases de résolution temporelle 35 ms). Alternativement, une séquence avec une résolution temporelle de 13 ms a été acquise avec un espacement de marquage de 8 mm. On observe une excellente persistance du marquage et une stabilité du contraste dans les images sur tout le cycle cardiaque. L'utilisation en clinique de l'IRM de marquage tissulaire est toujours limitée du fait de l'absence d'outils de traitement d'images adaptés pour accéder aux propriétés contractiles locales intra pariétales. Les premières méthodes de traitement développées essentiellement dans le cadre de l'évaluation de la technique d'imagerie elle-même étaient majoritairement basées sur l'extraction du motif de marquage et l'analyse de sa déformation. Ce type d'approche est difficilement envisageable en clinique même si des techniques de traitement d'images peuvent y aider. L'utilisateur doit en effet contrôler chaque ligne de marquage extraite et vérifier sa cohérence spatiale et temporelle. La technique d'images par RM harmoniques de phase (IRM-HARP, Harmonic Phase MRI (HARP-MRI) en anglais) est la première à pouvoir revendiquer un temps de traitement compatible avec la pratique clinique même si elle est 2D jusqu'à présent. Introduite par Osman et Prince [30-32], elle a été validée chez l'homme et l'animal [33]. Un de ses avantages principal est la limitation de l'intervention de l'utilisateur et sa rapidité. Les inventeurs, conscients de l'intérêt stratégique de la quantification en IRM de marquage tissulaire, ont créé la Société Diagnosoft[5]. L'avancée majeure à venir concerne l'extension en 3D+temps de cette technique (ou d'une technique équivalente) pour une utilisation en routine clinique.

La technique d'IRM de contraste de phase repose sur la mesure de décalages de phase induits par le mouvement [34]. Cette technique souffre cependant d'une grande sensibilité au bruit et d'un temps d'acquisition long en 3D (d'où des artefacts dus à la respiration, entre autres). L'équipe de Stanford a récemment proposé une approche 4D, validée par rapport à l'approche 2D classique, qui semble prometteuse [35] mais pas encore utilisable en clinique.

### 3.2.3. Tomodensitométrie à rayons X

Outre le cas assez exceptionnel du Dynamic Spatial Reconstructor, l'utilisation de la tomodensitométrie pour l'imagerie cardiaque a pendant longtemps été limitée par la nécessité de disposer d'un équipement particulier : l'Electron Beam CT (EBCT) dont la résolution

[5] http://www.diagnosoft.com/

temporelle est de 33ms. L'arrivée de la technologie multi-barettes change cet état de fait et l'imagerie 3D rapide synchronisée sur l'ECG du cœur devient accessible [36]. Il est ainsi possible de reconstruire rétrospectivement une série de phases du cycle cardiaque (8 phases et plus) en une apnée comme en Ciné-IRM [37]. Cette technique peut être utilisée dans des cas contre indiqués en IRM pour les patients possédant un pacemaker implanté ou une prothèse en matériau magnétique. Par contre, le patient est soumis à des radiations ionisantes avec injection d'un produit de contraste iodé. Les performances sont comparables voire supérieures à l'IRM en particulier pour la détection d'anomalies des coronaires [36]. La tomodensitométrie multi-détecteurs avec injection de produit de contraste peut également fournir des indications sur la perfusion myocardique [38].

### 3.2.4. Echocardiographie

Les évolutions en échocardiographie sont surtout marquées par l'augmentation significative des cadences d'acquisition ce qui a pour principal effet de diminuer la décorrélation entre les images successives de la séquence. L'imagerie doppler des tissus est une technique récente permettant la mesure des vitesses intra-myocardiques avec une bonne résolution temporelle [39],[40]. Mais l'exploration spatiale reste limitée au 1D ou 2D pour l'instant. L'extension en 3D des techniques ultrasonores (modeB, doppler de flux et tissulaire) est sans doute un enjeu majeur. On peut distinguer 3 catégories de systèmes tridimensionnels ultrasonores [41]. Avec les *systèmes mains libres*, des plans images sont acquis à des positions et dans des orientations arbitraires. Un dispositif de localisation 3D enregistre la position du transducteur 2D dans l'espace et au cours du temps. La reconstruction d'un volume repose sur l'intégration en 3D des plans acquis. Les principales limitations de cette méthode reposent sur la précision du système de localisation et sur l'habileté du clinicien à positionner la sonde pour acquérir suffisamment de données afin de réaliser une reconstruction 3D correcte. Il existe par ailleurs des *systèmes à balayage mécanique* linéaires, coniques ou en rotation [42] qui conduisent généralement à des reconstruction 3D de l'anatomie plus précise que les systèmes mains libres au prix d'une cadence d'acquisition plus lente et d'un champ de vue plus réduit. Une synchronisation à l'ECG est requise pour le tri des données. Les *systèmes électroniques à matrices 2D de transducteurs* sont les seuls dispositifs conduisant à une réelle imagerie 3D ultrasonore en temps réel. Cette technologie a été explorée par Olaf von Ram et Stephen Smith à la Duke University [43]. Elle souffre cependant d'une résolution spatiale limitée et d'un fort niveau de bruit. La géométrie d'acquisition est pyramidale couvrant un espace de 63° x 63° en azimut et en élévation. Un transducteur matriciel standard peut acquérir une matrice 64x64x512 tous les 1/22ème de seconde sans nécessiter de synchronisation à l'ECG ou la respiration, permettant ainsi l'étude de la dynamique cardiaque [41]. Côté constructeurs, le système Live 3D Echo de Philips[6] est annoncé comme devant révolutionner la pratique de l'échocardiographie. Equipé d'un transducteur matriciel de 3000 µéléments, il est capable de produire des séquences de volumes du cœur battant, et de permettre une évaluation et une quantification directement en 3D. Nous n'avons pas vu fonctionner ce système mais il est certain qu'il ouvre de grandes perspectives pour de nombreuses applications cliniques. Selon [44] et [41], le déploiement des systèmes d'échographie 3D temps réel en routine clinique repose sur l'amélioration de la qualité des transducteurs matriciels (résolutions spatiales, speckle, artefacts d'atténuation), le développement d'outils interactifs et simples de manipulation des images 3D acquises selon des plans de coupes quelconques, la mise au point de nouvelles méthodes, adaptées à la modalité, de débruitage, de segmentation et de quantification (formes, mouvement) spatio-temporelles. Nous partageons ces conclusions.

[6] http://www.medical.philips.com/main/products/ultrasound/cardiology/

L'analyse du mouvement en échocardiographie est une tâche difficile. Les techniques de flux optique, bien que peu adaptées en principe compte tenu de la décorrélation du speckle dans la séquence ont été utilisées pour extraire le mouvement en échocardiographie 2D [45, 46]. Plus récemment, des méthodes basées sur les modèles déformables avec intégration de connaissances de la forme (active shape models) et de la dynamique cardiaque (filtrage de Kalman) ont été introduites [47-49] et donnent des résultats prometteurs. L'analyse factorielle est une alternative originale à la quantification de la cinétique pariétale [50]. Elle est en court d'évaluation dans le cadre d'un projet national. Des techniques plus spécifiques à la modalité reposant sur l'analyse du signal RF sont prometteuses pour l'estimation des vitesses, avec une bonne précision dans la direction axiale [40]. En échocardiographie 3D+temps, une analyse spatio-temporelle 4D des données constituée d'un filtre de débruitage espace-fréquence suivi d'une segmentation par modèle déformable conduit à des résultats intéressants [51].

### 3.3. COMBINAISON D'INFORMATIONS MULTI-MODALITES

Dans la section précédente, nous avons mis en évidence l'intérêt d'étudier conjointement différents aspects de la fonction cardiaque dans le cadre de l'évaluation de la viabilité myocardique. La perfusion, le métabolisme et la fonction contractile peuvent être estimées par différentes modalités d'imagerie en vue de l'étude de la viabilité myocardique (Figure 3). La viabilité myocardique pourrait, selon certains auteurs, être estimée uniquement en IRM en combinant IRM dynamique, de test d'effort et de rehaussement tardif, cette dernière donnant l'étendue transpariétale des zones infarcies [52].

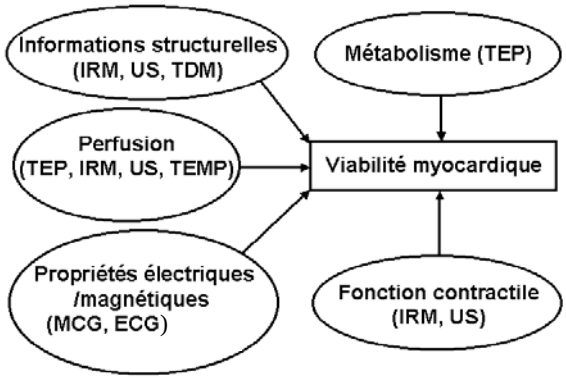


*Figure 3: Recalage et fusion de données cardiaques pour l'étude de viabilité myocardique*

L'analyse conjointe requiert la mise en correspondance d'images aux caractéristiques très différentes que se soit en termes de géométrie d'acquisition, de résolutions spatiale et temporelle et de niveaux de gris. Le recalage d'images a fait l'objet de très nombreux travaux, particulièrement en imagerie cérébrale. Le recalage en imagerie cardiaque est plus ardu compte tenu des mouvements permanents respiratoire et cardiaque. Le cœur présente également peu de repères anatomiques sur lesquels appuyer la mise en correspondance. Enfin, les images cardiaques sont acquises avec des résolutions spatiales plus faibles comparativement à l'imagerie cérébrale. Nous avons réalisé un état de l'art des méthodes de recalage en imagerie thoracique et cardiaque [53] qui ont été divisées en 2 catégories principales: les méthodes basées sur des structures géométriques préalablement extraites des images et les méthodes basées sur les mesures de similarité de niveaux de gris (méthodes aussi appelées iconiques). Il ressort de cette étude que la grande majorité des méthodes (tout au moins jusqu'à fin 2002) implique des transformations rigides. Comte tenu des mouvements, des transformations non-rigides ou progressivement non-rigides semblent plus

appropriées. Les méthodes sont très spécialisées à des modalités et un contexte clinique donnés. Il est encore difficile d'envisager une approche générique capable de traiter tous les cas de figure. Dans un contexte particulier, il est aussi difficile de faire un choix du fait du manque d'éléments objectifs permettant de comparer les méthodes. Des bases de données de référence pourraient contribuer à l'évaluation objective des méthodes en termes de précision de recalage, de robustesse à l'initialisation et au bruit, et de temps de calcul.

### 3.4. MODELISATION FONCTIONNELLE DU CŒUR

Parallèlement, des progrès considérables ont été réalisés en ingénierie biomédicale pour la description et la modélisation des grandes fonctions du vivant de la molécule à l'organe [54], [55]. Selon Bassingthwaighte, l'ampleur et la variété des avancées des connaissances dans ce domaine sont dissimulées par leur dispersion [56]. Des informations élémentaires comme la composition des tissus, les propriétés matérielles et le comportement mécanique des cellules et des tissus ne sont pas largement accessibles. C'est ce qui a motivé le projet multicentriques Physiome aux Etats-Unis (http://www.physiome.org/), le Physiome étant défini comme la *description quantitative et intégrative de la physiologie des organismes en fonctionnement normal et pathologique*. L'objectif premier était de centraliser et mettre à disposition à travers les réseaux informatiques l'ensemble des données expérimentales des différents systèmes décomposés en modules. A la suite de nombreux travaux antérieurs [57, 58], le système cardio-vasculaire est une cible de choix pour expérimenter l'intégration des résultats expérimentaux et des modèles. Dans le projet Cardiome, les différentes tâches ont été ainsi définies [56]:

1. Electrophysiologie
2. Mécanique
3. Couplage excitation-contraction
4. Flux, transport et échanges
5. Métabolisme des substrats énergétiques
6. Régulation du métabolisme, de la force contractile, réponse à des anomalies
7. Régulation de l'expression des gènes en réponse à l'activité global et locale

Ceci montre la complexité du projet de cette étude à travers les échelles, reposant au niveau le plus bas sur la chimie des ions Calcium dans la myosite. La performance mécanique du cœur gauche résulte de l'action contractile de l'ensemble des cellules myocardique constituant la paroi du ventricule gauche [59]. Sa description repose généralement sur les contraintes et déformations pariétales locales qui déterminent la consommation d'oxygène dans les tissus myocardiques, elle-même dépendante de la perfusion tissulaire. L'efficacité de la perfusion est fonction de l'état fonctionnel, en particulier mécanique, du tissu myocardique. Nous avons tenté de résumer en Figure 4 les relations entre les déterminants anatomiques et fonctionnels de la performance mécanique cardiaque. Chaque élément fait l'objet de recherches fondamentales qui se concrétisent par des modèles en perpétuelle évolution, de l'échelle moléculaire à celle des tissus et de l'organe. L'électrophysiologie de la cellule cardiaque et du couplage excitation/contraction est un exemple particulièrement éloquent. Sachse répertorie ainsi près d'une trentaine de modèles depuis 1962 d'une sophistication croissante [60]. Dans une approche ascendante de la complexité, les éléments doivent être assemblés pour donner une interprétation des fonctions physiologiques normales et pathologiques du coeur. Cette intégration de la cellule à l'organe pose précisément des

problèmes relatifs aux choix des modèles simplifiés (ensemble d'équations) et au calcul numérique de la solution. Des modèles intégrant la géométrie 3D des structures cardiaques, l'architecture des fibres myocardiques ainsi que des éléments de fonction cellulaire ont été développés pour décrire le comportement électrique et mécanique du cœur entier. Ces modèles reposent généralement sur la méthode des éléments finis [61-63]. Une approche basée sur un automate cellulaire a également été proposée récemment et semble être une alternative intéressante [60].

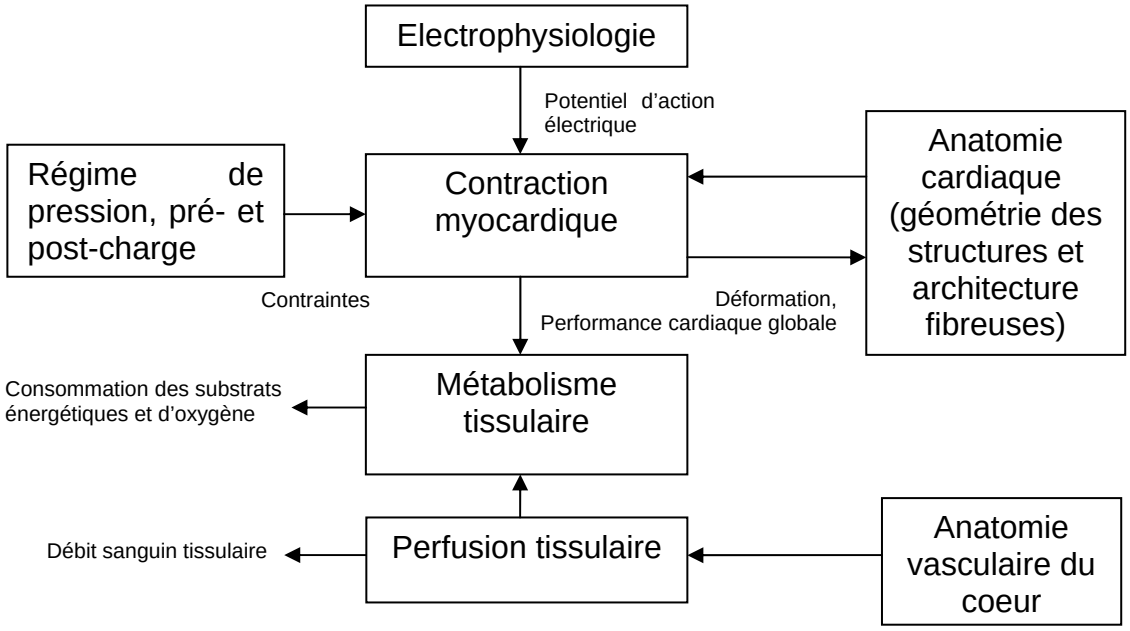


*Figure 4. Diagramme des relations entre anatomie et les différentes fonctions cardio-vasculaires, et paramètres mesurables associés.*

Les avancés en simulation peuvent être exploitées dans les problèmes inverses rencontrés en analyse d'images cardiaques comme l'estimation de mouvement. Ainsi, certains auteurs proposent d'exploiter ces modèles, en introduisant des simplifications, pour simultanément extraire les structures anatomiques et des paramètres fonctionnels relatifs au mouvement ou l'activité électrique [64-69]. L'objectif est d'obtenir par instanciation du modèle aux données des cartographies paramétriques directement exploitables par les médecins. C'est un projet ambitieux mais aussi extrêmement motivant.

En résumé, nous pouvons résumer les principaux enjeux actuels en imagerie cardiaque :

**Du point de vue médical :**

1. Imagerie haute résolution spatiale et temporelle, et estimation quantitative des principales fonctions du cœur, en particulier de la perfusion myocardique et de la fonction contractile segmentaire et locale en 3D et au cours du cycle cardiaque. Analyse de l'évolution de ces paramètres en espace (détermination de régions anormales) et en temps (étude des anomalies de synchronisme de la contraction, par exemple)
2. Confrontation des données issues de plusieurs modalités pour une analyse individualisée du patient. Etude de la viabilité myocardique à partir d'une imagerie multimodalités. Comparaison de cas.

**Du point de vue du traitement et de l'analyse d'images :**

1. Développement de méthodes de quantification des diverses fonctions cardiaques (mouvement, perfusion, métabolisme, activité électrique) précises, les plus automatiques possible, spatio-temporelles et utilisables en clinique
2. Développement de techniques de recalage d'images non rigides en 3D+temps. Construction de cartographies anatomo-fonctionnelles paramétriques spécifiques au patient destinées à faciliter l'interprétation par le médecin.

Les méthodes développées répondent à des problèmes inverses. Elles bénéficient de l'intégration d'informations a priori et des connaissances de la physiologie cardiaque et de ses modèles.

## 4. CONTRIBUTIONS

Nos contributions concernent de nouvelles méthodes d'analyse d'images cardiaques pour l'aide à l'interprétation et au diagnostic. Elles portent plus précisément sur les 3 thèmes suivants:

1. Extraction de l'anatomie cardiaque 3D en imagerie dynamique IRM du cœur
2. Estimation et analyse du mouvement du cœur
3. Mise en correspondance de données cardiaques multi-modalités

L'ensemble de nos contributions dans ce domaine est résumé dans la Figure 5. Un premier groupe concerne des développements en monomodalité (IRM) qui intègrent l'extraction de l'anatomie du cœur et l'analyse de son mouvement. Les travaux en multi-modalités concernent essentiellement le recalage d'images et la construction de cartographies multiparamétriques.

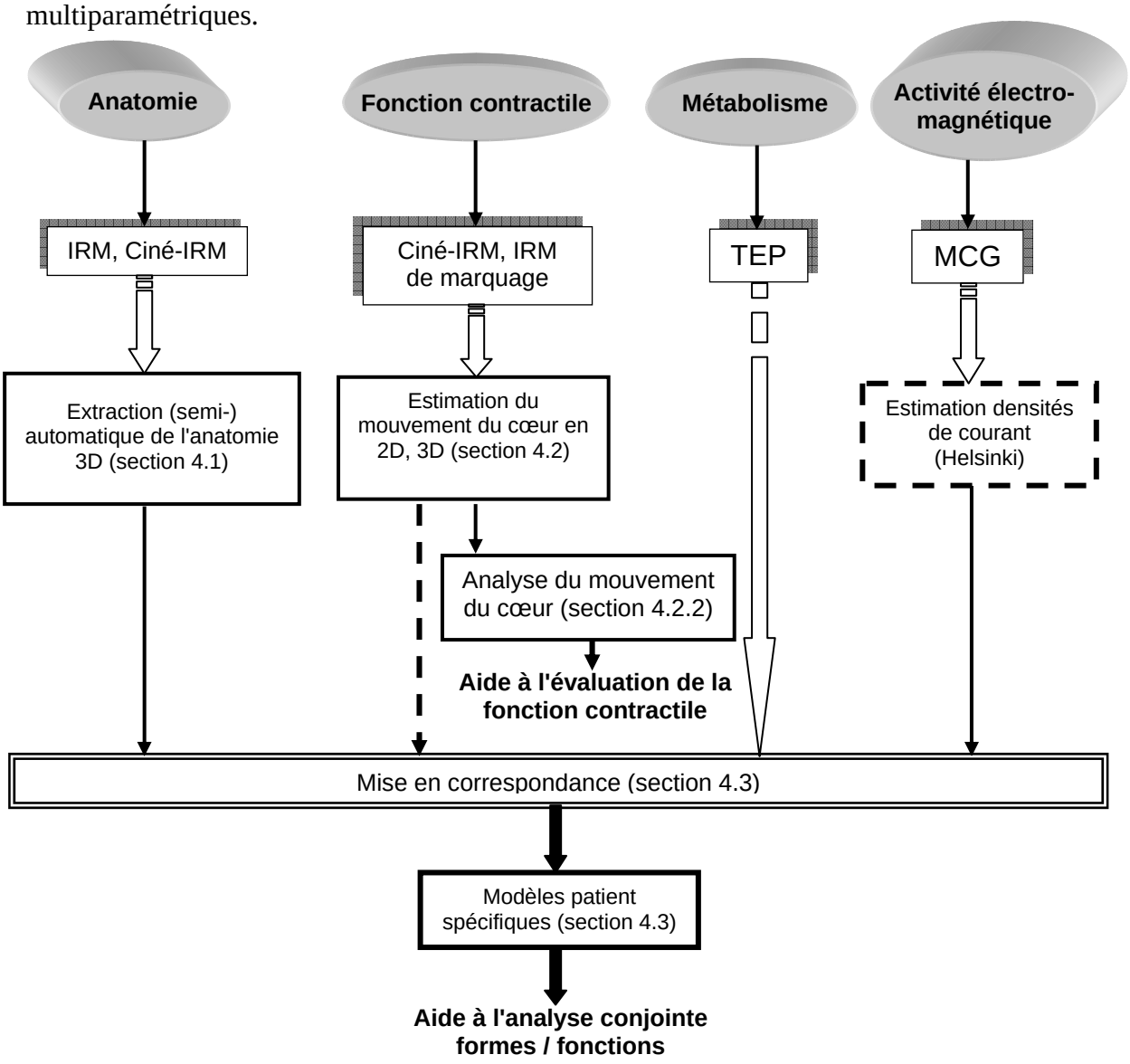


*Figure 5. Vue générale des travaux en analyse d'images cardiaques*

Il nous semble utile à ce niveau de resituer nos travaux dans un cadre général d'*intégration de connaissances* dans la conception des systèmes de production et d'analyse d'images médicales qui a fait l'objet de réflexions dans le cadre de l'Action

Spécifique ICoMIM du CNRS que nous avons pilotée en collaboration avec Frédérique Frouin (INSERM U494, Paris) [70]. En effet, la caractéristique commune des méthodes développées est qu'elles intègrent des connaissances à divers niveaux. Le terme de connaissance est ici très général et recouvre des faits avérés, des connaissances de spécialités, des compétences d'experts (Figure 6). L'intégration de connaissances est quasi-implicite lorsqu'on traite des images médicales ; le simple seuillage d'une image requiert de définir les structures que l'on cherche à mettre en évidence, leurs propriétés de luminance dans la modalité considérée (ex : les unités Hounsfield en tomodensitométrie à rayons X). La connaissance peut être aussi beaucoup plus élaborée.

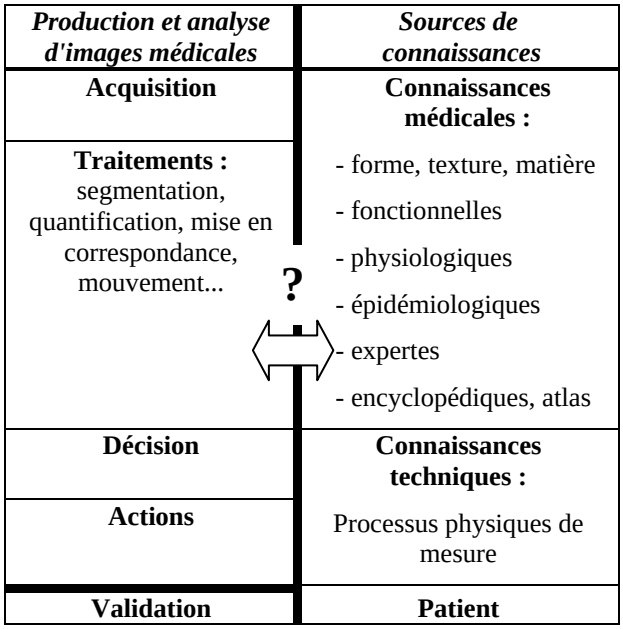


*Figure 6. Relation entre la chaîne de production et d'analyse d'images et les sources de connaissances (issu de [70])*

Dans cette étude, nous avons identifié 3 étapes clés pour lesquelles de nombreuses contributions nous semblent devoir être apportées :

1. *Acquisition et extraction des connaissances*. C'est le domaine de l'ingénierie des connaissances médicales. Certaines connaissances, comme celles relatives aux métiers, à des aptitudes, sont difficiles à extraire et formaliser. Des méthodes peuvent aider à cela.
2. *Intégration de connaissances*. Ceci concerne l'ensemble des techniques permettant d'intégrer dans les système de production et d'analyse d'images des connaissances généralement hétérogènes, c'est-à-dire dont le support de description peut être extrêmement divers (numérique, statistiques, textuel, graphique, sous forme de lois, de règles, etc.). Dans [70], nous avons distingué les approches basées sur un formalisme mathématique, les approches statistiques et les techniques d'aide à la décision introduites en Intelligence Artificielle.
3. *Evaluation des systèmes développés et de l'apport des connaissances*. Il s'agit d'un point souvent négligé dans les publications mais il est fondamental. Il permet de répondre aux questions : Qu'apporte ma méthode par rapport à l'existant ? Quel est son point de fonctionnement optimal ? Est-elle précise, robuste aux bruits et aux conditions initiales, sensible, spécifique… ? Mais aussi, dans le contexte médical, est-elle utilisable dans un contexte clinique ? Apporte t-elle un gain dans la prise en charge des patients, une réduction des coûts ?

Nos contributions portent principalement sur les points 2 et 3.

### 4.1. EXTRACTION DE L'ANATOMIE CARDIAQUE

**Mots clés:** segmentation spatio-temporelle, gabarit déformable élastique, éléments finis

L'extraction des structures cardiaques dans les images est une étape indispensable pour l'estimation de paramètres globaux standards en cardiologie comme la masse myocardique, les volumes ventriculaires ou la fraction d'éjection. La Figure 7 illustre une série dynamique de 9 images (9 phases) d'un même niveau de coupe en petit axe acquise en IRM en apnée en synchronisation avec l'ECG. On réalise couramment des séries dynamiques à plusieurs niveaux (5 à 10) du cœur de la base à l'apex. En routine clinique, le contourage des structures est encore réalisé manuellement sans doute du fait de l'inefficacité des logiciels disponibles sur les imageurs et de la durée de la procédure. En outre, la mesure des paramètres est plus précise si elle peut s'effectuer en 3D. La segmentation manuelle devient dans ce cas rédhibitoire et source d'erreurs. Le développement d'outils de segmentation (semi-) automatiques permet de gagner en robustesse vis-à-vis du bruit dans les images et des paramètres de l'algorithme, en répétabilité ainsi qu'en temps de traitement.

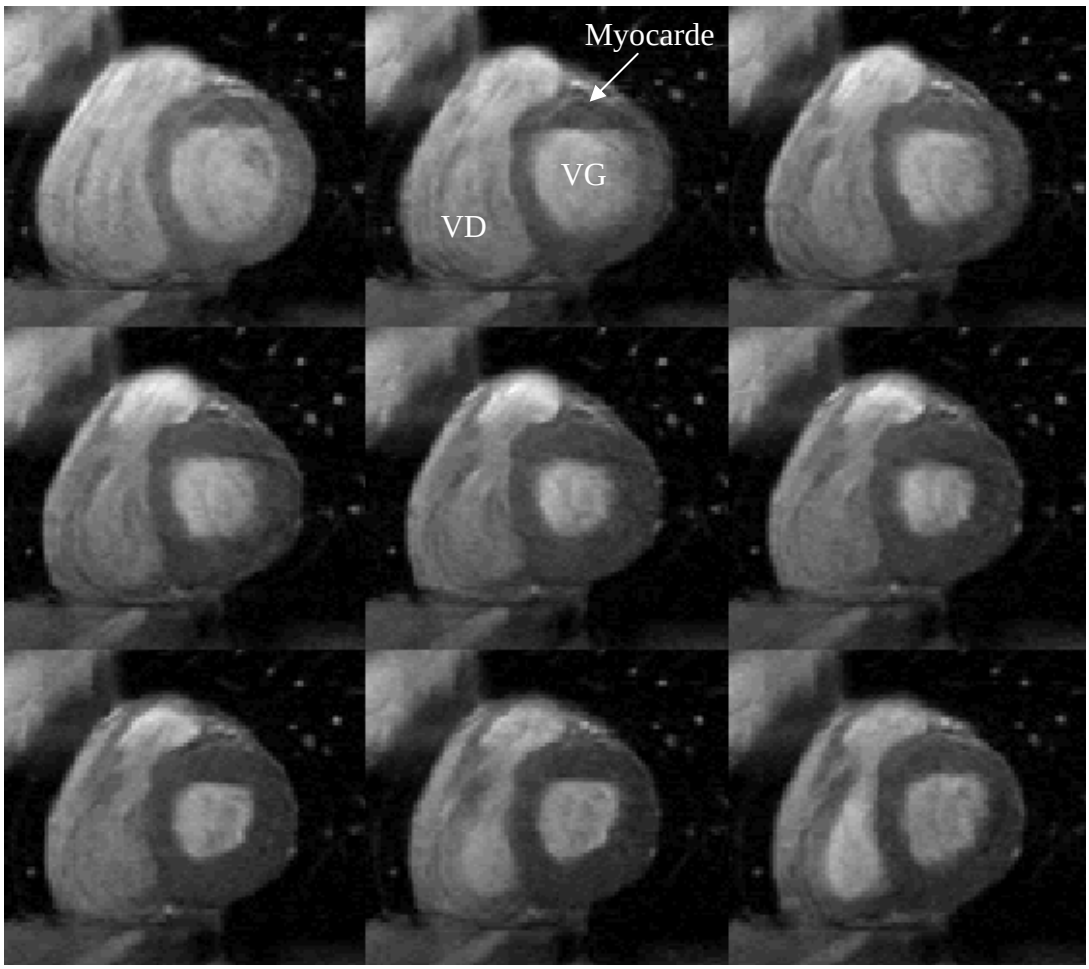


*Figure 7. Séquence dynamique en IRM : 9 phases du cœur au cours du cycle cardiaque pour un même niveau de coupe en petit axe (de gauche à droite et de haut en bas). Les cavités ventriculaires gauche (VG) et droite (VD) sont indiquées.*

L'approche que nous proposons repose sur l'exploitation de connaissances a priori sur la forme et la déformation du cœur. On fait de plus l'hypothèse raisonnable qu'en pratique

l'utilisateur médecin peut fournir au logiciel un nombre limité d'informations afin de faciliter la segmentation. Le concept général est celui des modèles déformables. Le cœur est considéré comme un objet déformable de géométrie plus ou moins complexe comportant plusieurs interfaces. Ce concept général, dénommé « Gabarit Déformable Elastique », a été initialement développé en 2D dans le cadre de la thèse de Fabrice Vincent puis étendu en 3D monocavité et 3D bicavités (thèse de Quoc Cuong Pham). Nous en rappelons ici le principe.

Un gabarit déformable élastique (GDE) est l'association d'une représentation géométrique réaliste et d'une loi de comportement. Il est soumis à des contraintes issues des images. On peut établir une analogie directe avec la mécanique des solides déformables [71] à la différence que les contraintes appliquées au gabarit pour le déformer proviennent de l'image. Dans le cas du cœur, par exemple, le muscle cardiaque du ventricule gauche est représenté en 2D par un anneau (Figure 8(a)) et par une coque ellipsoïdique en 3D (Figure 8(b)). Ce type de représentation permet d'intégrer dans une même représentation le myocarde comparativement aux modèles plus classiques de surfaces déformables qui se limitent aux interfaces [72].

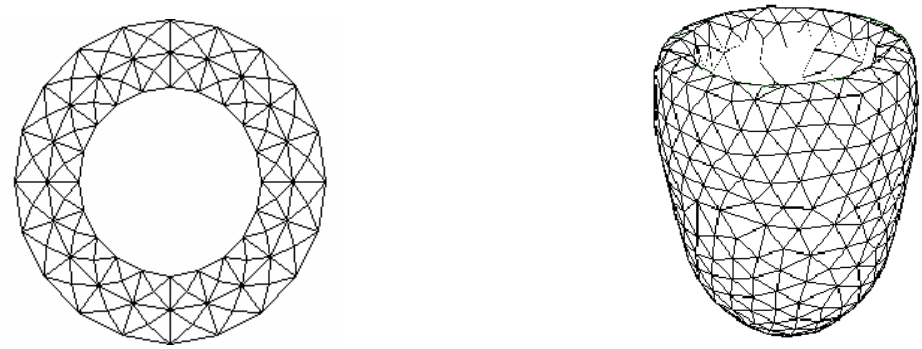

(a) (b)

Figure 8. Représentation du myocarde ventriculaire gauche. (a) en 2D. (b) en 3D

Le gabarit est doté des propriétés d'un matériau élastique linéaire isotrope. Le modèle est ensuite plongé dans les données d'imagerie qui vont agir sur lui par l'intermédiaire d'un champ de forces. Ce champ de force peut dériver d'un potentiel (Figure 9). Le comportement élastique du matériau régularise de manière naturelle et physique la déformation du modèle.

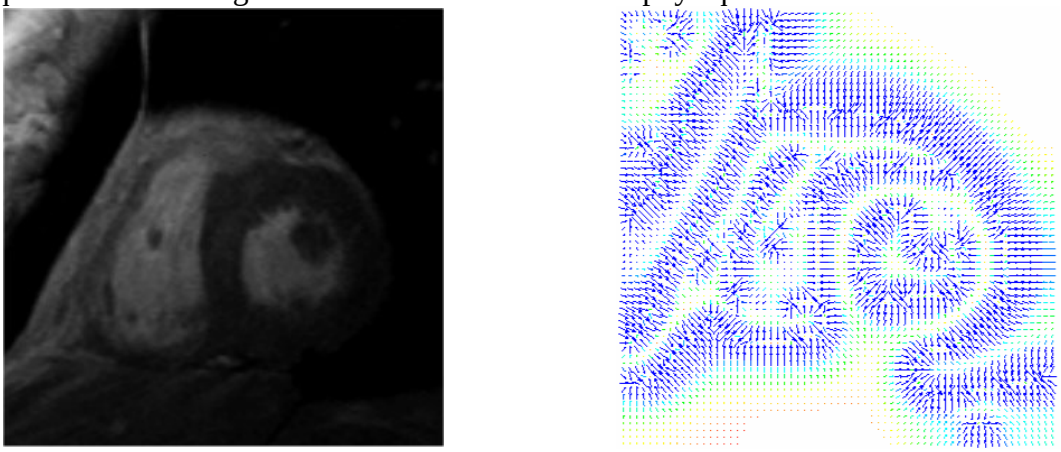

(a) (b)

Figure 9. (a) Image du cœur en petit axe (b). Champ de forces correspondant

La déformation du modèle sous l'action d'un champ de force est régie par les équations de l'élasticité tridimensionnelle [73]. Un milieu élastique occupe un domaine $\Omega_0$ de frontière

$\partial\Omega_0$ au repos. Soumis à des forces superficielles *t*, les points matériels **x** subissent un déplacement *u* à valeurs dans $\Re^3$ et la configuration à l'équilibre devient $\Omega$ de frontière $\partial\Omega$ (Figure 10). Le déplacement est lié à la déformation par la relation $\varphi(\mathbf{x}) = \mathbf{x} + u(\mathbf{x})$.

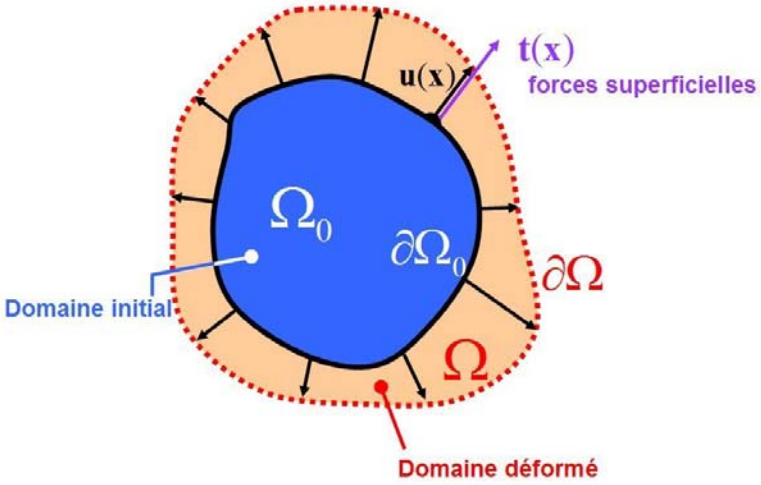


*Figure 10. Configurations de repos et déformée d'un milieu soumis à des forces superficielles*

Gradient de déformation et de déplacement sont liés par l'équation :

$$\nabla\varphi = I + \nabla u \tag{1}$$

Où *I* est la matrice identité. On définit le *tenseur des déformations de Cauchy* par

$$C = \nabla\varphi^T \nabla\varphi \tag{2}$$

et le *tenseur des déformations de Green-St Venant* :

$$E = \frac{1}{2}(C - I) = \frac{1}{2}\left(\nabla u^T + \nabla u + \nabla u^T \nabla u\right) \tag{3}$$

qui est une mesure de l'écart entre une déformation donnée et une transformation rigide. La théorie implique des forces de volume et des forces de surfaces. Les forces de surface *t* définissent un champ de vecteurs sur la frontière du domaine. En chaque point de la frontière, il existe un tenseur symétrique $\sigma$, appelé *tenseur des contraintes* défini à partir de *t*. En ignorant les forces de volume, les équations d'équilibre conduisent à :

$$\begin{cases} -div\,\sigma = 0 \text{ dans } \Omega_0 \\ \sigma.n = \sigma_n = t \text{ sur } \partial\Omega_0 \end{cases} \tag{4}$$

Où *n* désigne la normale extérieure unitaire. Les tenseurs sont des matrices 3x3. On définit la divergence d'un champ de tenseurs *T* (div *T*) comme le vecteur dont les composantes sont les divergences des vecteurs lignes de *T*.

Les équations d'équilibre sont indépendantes du matériau considéré. La spécialisation à un matériau est fournie par la loi de comportement qui s'écrit dans le cas d'un matériau élastique isotrope :

$$\sigma = \lambda(traceE)I + 2\mu E \tag{5}$$

Où $\lambda$ et $\mu$ sont les constantes de Lamé du matériau, reliées au module de Young *Y* et au coefficient de Poisson $\nu$ par :

$$\lambda = \frac{Y\nu}{(1-\nu)(1-2\nu)} \qquad \mu = \frac{Y}{2(1+\nu)} \tag{6}$$

Le problème aux limites (4) est équivalent à la formulation variationnelle :

$$\frac{1}{2}\int_{\Omega_0} \varsigma^T(w)\varepsilon(w)d\mathbf{x} = \int_{\partial\Omega_0} t.w\,ds \quad \forall w \in W \tag{7}$$

en introduisant les vecteurs des contraintes et des déformations, respectivement:

$$\varsigma = (\sigma_{11},\sigma_{22},\sigma_{33},\sigma_{12},\sigma_{23},\sigma_{31}) \quad \varepsilon = (E_{11},E_{22},E_{33},2E_{12},2E_{23},2E_{31}) \tag{8}$$

Le problème de segmentation revient à minimiser la fonctionnelle :

$$J(u) = \frac{1}{2}\int_{\Omega_0} \varsigma^T(u)\varepsilon(u)d\mathbf{x} - \int_{\partial\Omega_0} t.u\,ds \tag{9}$$

F. Vincent [74, 75] a d'abord proposé d'amener progressivement $\Omega_0$ vers $\Omega$ par une technique de charge incrémentale. La minimisation de la fonctionnelle $J$ est réalisée par la méthode des éléments finis (MEF). Le domaine est décomposé en éléments tétraédriques auxquels on associe des fonctions de base linéaires. La minimisation de (9) conduit à l'équation matricielle

$$KU = F(U) \tag{10}$$

Où $K$ est la matrice de raideur du milieu $\Omega_0$ (issue d'un assemblage sur l'ensemble des éléments) et $F$ le vecteur de force qui dépend du déplacement. L'estimation du déplacement repose sur l'équation d'évolution :

$$\frac{dU}{dt} + KU(t) = F(U(t)) \tag{11}$$

Qui se discrétise en :

$$(I + \Delta t\,K)U^{k+1} = U^k + \Delta t\,F(U^k) \tag{12}$$

Ce schéma (identifié M1) implique d'être déjà très proche de la solution. Q. C. Pham a proposé dans le cadre de sa thèse [66, 67] 2 autres schémas de résolution plus efficaces, en collaboration avec le Laboratoire de Mathématiques Appliquées de Lyon (Professeur J. Pousin, MAPLY, CNRS UMR 5585) et grâce au soutien d'un projet MATH-STIC du CNRS. Plus précisément, l'une des propositions concerne la mise à jour régulière du domaine du GDE (Algorithme M2). Ce qui revient à relâcher périodiquement l'énergie de déformation élastique. L'autre proposition ajoute la condition de contrainte nulle sur les bords, condition naturelle mais pas imposée dans les précédents schémas (Algorithme M3). L'algorithme M4 est une combinaison des deux précédents. Les différents schémas sont résumés en page suivante. Pour chaque algorithme, on donne la formulation algorithmique issue des équations différentielles et le schéma numérique de discrétisation du problème d'éléments finis ($k$ est l'indice d'itération). La Figure 11 donne l'organigramme de l'algorithme M2 avec mise à jour de la géométrie qui inclut également un contrôle de la qualité du maillage au cours de la déformation. L'algorithme M4 suit la même séquence avec la mise à jour du déplacement de l'algorithme M3.

- **Algorithme M1 de charge incrémentale :**

$$\mathbf{M1} \quad \begin{cases} \mathrm{u}^{k+1} - \Delta t \ \mathrm{div}\, \sigma(\mathrm{u}^{k+1}) = \mathrm{u}^{k} & \text{dans } \Omega_0 \\ \sigma_n(\mathrm{u}^{k+1}) = \mathrm{t}(\mathrm{I} + \mathrm{u}^{k}) & \text{sur } \partial\Omega_0 \end{cases}$$

$$(\mathrm{I} + \Delta t\, \mathrm{K})\mathrm{U}^{k+1} = \mathrm{U}^{k} + \Delta t\, \mathrm{F}(\mathrm{U}^{k})$$

- **Algorithme M2 de mise à jour de la géométrie :**

$$\mathbf{M2} \quad \begin{cases} \mathrm{u}^{k+1} - \Delta t \ \mathrm{div}\, \sigma(\mathrm{u}^{k+1}) = \mathrm{u}^{k} & \text{dans } \Omega_k \\ \sigma_n(\mathrm{u}^{k+1}) = \mathrm{t}(\mathrm{I} + \mathrm{u}^{k}) & \text{sur } \partial\Omega_k \\ \Omega_{k+1} = (\mathrm{I} + \mathrm{u}^{k})\Omega_k \end{cases}$$

$$(\mathrm{I} + \Delta t\, \mathrm{K}^{k})\mathrm{U}^{k+1} = \mathrm{U}^{k} + \Delta t\, \mathrm{F}(\mathrm{U}^{k})$$

- **Algorithme M3 de contrainte nulle à convergence :**

$$\mathbf{M3} \quad \begin{cases} \beta\mathrm{u}^{k+1} - \mathrm{div}\, \sigma(\mathrm{u}^{k+1}) = \beta\mathrm{u}^{k} & \text{dans } \Omega_0 \\ \sigma_n(\mathrm{u}^{k+1}) = \mathrm{t}(\mathrm{I} + \mathrm{u}^{k}) + \sigma_n(\mathrm{u}^{k}) & \text{sur } \partial\Omega_0 \end{cases}$$

$$\begin{cases} \mathrm{U}^{0} = 0 \\ \mathrm{U}^{1} = 0 \\ (\mathrm{I} + \Delta t\, \mathrm{K})\mathrm{U}^{k+2} = \mathrm{U}^{k+1} + \Delta t\, \mathrm{F}(\mathrm{U}^{k}) + \Delta t\, \mathrm{K}\mathrm{U}^{k+1} + (\mathrm{U}^{k} - \mathrm{U}^{k+1})_i \end{cases}$$

- **Algorithme M4 : Association de M2 et M3**

Les algorithmes M1 à M4 ont été évalués sur des objets tests (sphère vers cube, sphère vers ellipsoïde). Les résultats ont montré que la solution M4 était la plus satisfaisante en termes de rapidité de convergence et de sensibilité réduite à l'initialisation. D'un point de vue théorique cependant, la convergence et l'unicité de ces divers schémas n'ont pu être complètement démontrées. Dans le cadre de sa thèse au MAPLY, Youssef Rouchdy s'intéresse à un schéma d'élasticité non linéaire pour lequel ces propriétés ont pu être démontrées [76, 77].

Des résultats de segmentation sont donnés en Figure 12 à Figure 14. Le positionnement initial du modèle s'effectue par un recalage affine du modèle avec une région d'intérêt 3D interpolée. De plus, la configuration des fibres myocardiques a été prise en compte de manière simplifiée par passage à la limite en faisant tendre l'épaisseur des couches périphériques vers zéro ce qui permet de s'affranchir de la connaissance de leur orientation précise. La segmentation des différents instants d'une séquence dynamique s'effectue par report du modèle obtenu à l'instant précédent puis segmentation. Le GDE est actuellement en cours d'évaluation sur des séries d'images par RM acquises sur divers imageurs.

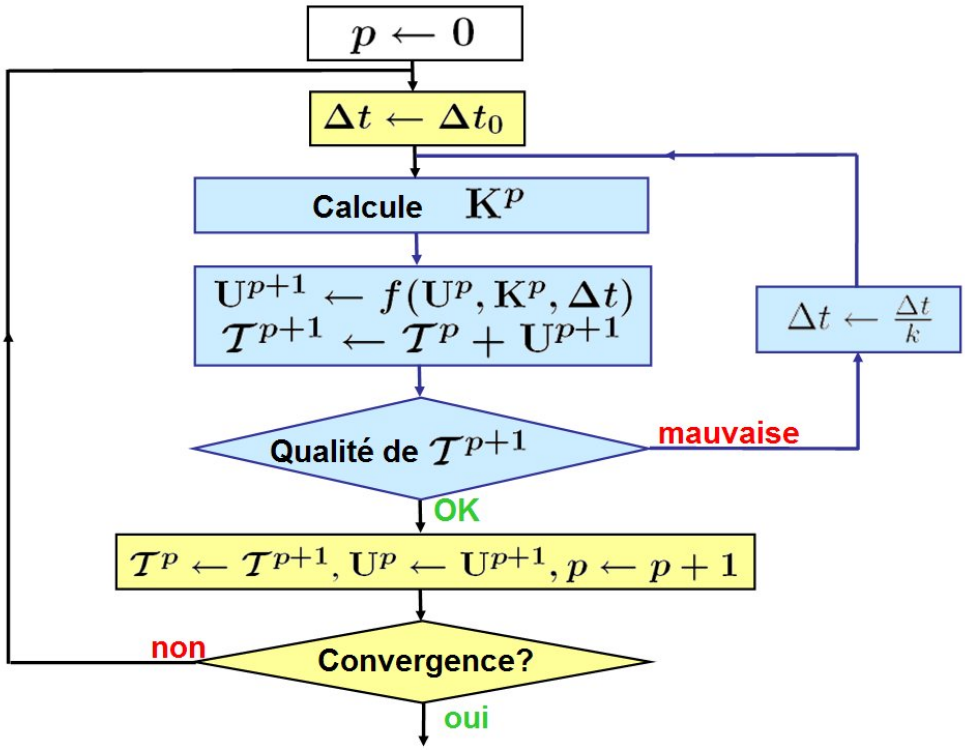


*Figure 11. Algorithme M2 avec mise à jour de la géométrie $\tau$ et test de sa qualité.*

Notons également que le concept de GDE étant général, il peut s'appliquer pour la segmentation d'autres structures pour lesquelles il est possible de disposer d'un modèle géométrique a priori. Il a en particulier été utilisé pour la segmentation d'images ultrasonores 3D d'embryons de souris [78, 79].

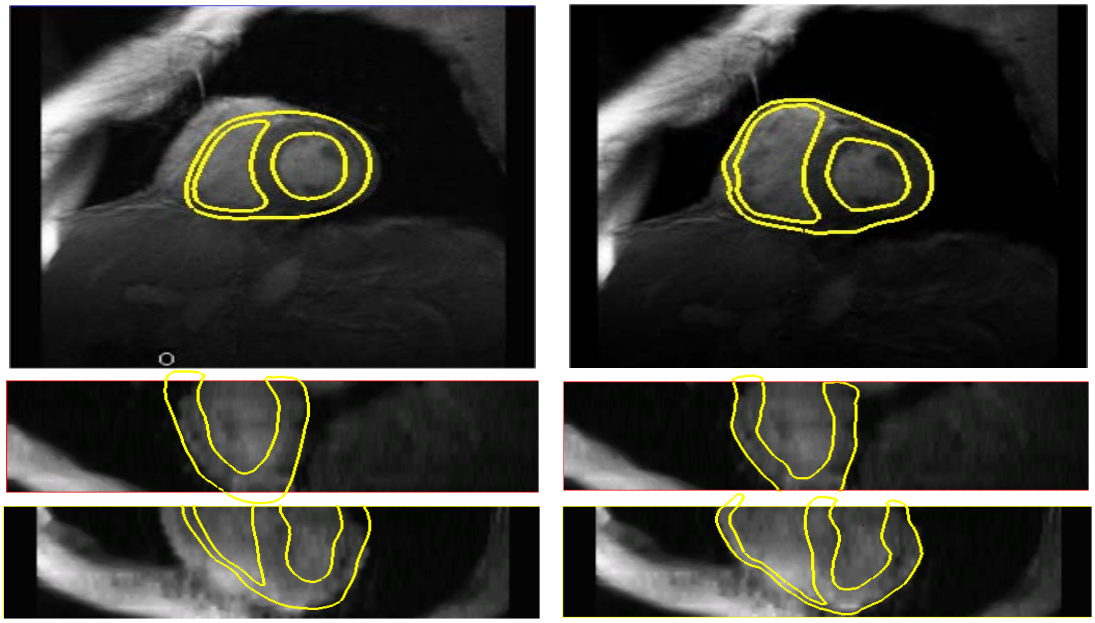

*(a)* *(b)*

*Figure 12. L'algorithme M4 est utilisé pour la segmentation 3D du cœur (Ventricules gauche et droit) en IRM à partir d'un modèle à 2 cavités (a) Positionnement initial du modèle bi-cavités du cœur. (b) Résultat de la segmentation*

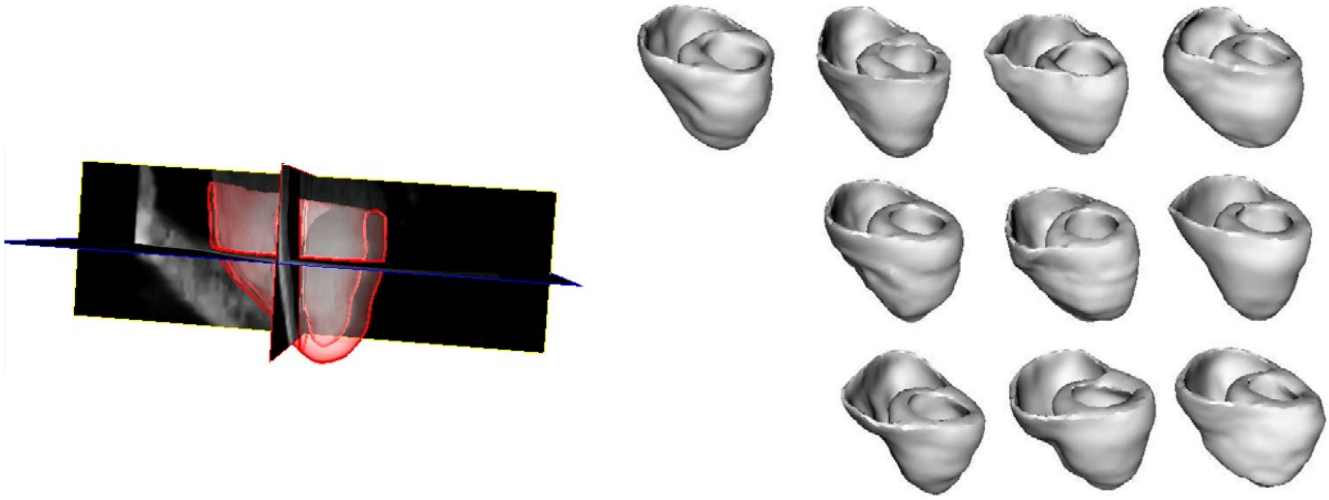

(a) (b)

*Figure 13. Segmentation 3D des ventricules du cœur. (a) Superposition du modèle à l'image. (b) Segmentations obtenues en télé-diastole pour 10 patients.*

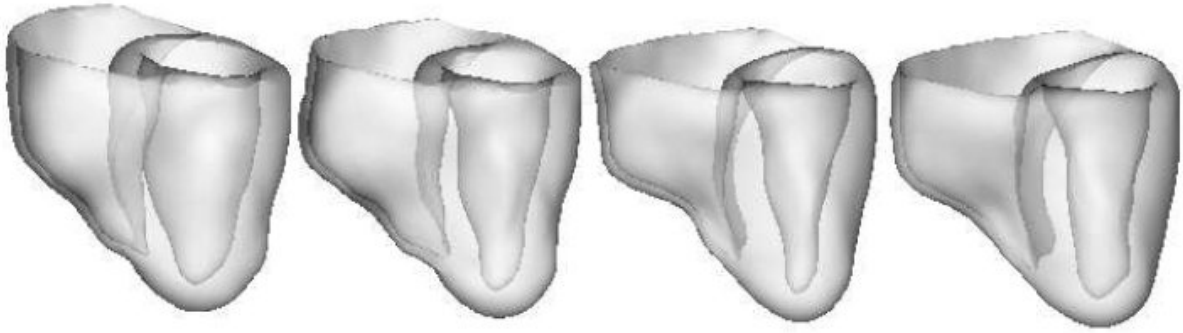

*Figure 14. Segmentation de 4 phases au cours du cycle cardiaque.*

Ce travail a fait l'objet de 2 thèses (F. Vincent et Q. C. Pham) et des articles dont la liste est donnée ci-dessous. Actuellement, une thèse STIC et une thèse de Mathématiques Appliquées sont en cours sur la suite du sujet à savoir l'extension au 3D+temps du GDE et la recherche de solutions mathématiquement bien posées pour le GDE non linéaire.

**Bibliographie :**

- Revues à comité de lecture

T. Mäkelä, Q. C. Pham, P. Clarysse, J. Nenonen, J. Lötjönen, O. Sipilä, H. Hänninen, K. Lauerma, J. Knutti, T. Katila, and I. E. Magnin, "A 3D model-based registration approach for the PET, MR and MCG cardiac data fusion, Medical Image Analysis," *Medical Image Analysis*, vol. 7, pp. 377-389, 2003.

- Articles longs de congrès

F. Vincent, P. Clarysse, P. Croisille, and I. E. Magnin, "Segmentation et suivi de mouvement d'objets déformables par région active," GRETSI'99, Vannes, France, pp. 163-166, 1999.

F. Vincent, P. Clarysse, P. Croisille, and I. E. Magnin, "An elasticity-based region model and its application to the estimation of the heart deformation in tagged MRI.," International Conference on Image Processing (ICIP), Vancouver, BC, Canada, 2000.

Q.-C. Pham, F. Vincent, P. Clarysse, P. Croisille, and I. E. Magnin, "A FEM-based deformable model for the 3D segmentation and tracking of the heart in cardiac MRI," 2nd International Symposium on Image and Signal Processing and Analysis (ISPA 2001), Pula, Croatia, pp. 250-254, 2001.

D. Vray, A. Discher, J. Lefloc'h, W. Mai, P. Clarysse, Q. C. Pham, J. Montagnat, and M. Janier, "3D quantification of ultrasound images : application to mouse embryo imaging in vivo," IEEE International Ultrasonics Symposium, Munich, Germany, pp. 1557-1560, 2002.
B. Qiu, P. Clarysse, J. Montagnat, M. Janier, and D. Vray, "Comparison of 3D deformable models for in vivo measurements of mouse embryo from 3D ultrasound images," IEEE International Ultrasonics Symposium, Montréal (Canada), 2004.

- Thèses

F. Vincent, "Gabarits déformables élastiques pour la segmentation et le suivi de mouvement du cœur en Imagerie par Résonance Magnétique", thèse de doctorat *CREATIS*. Institut National des Sciences Appliquée, Lyon, 120p, 2001.
Q.-C. Pham, "Segmentation en imagerie cardiaque multimodale conduite par un modèle réaliste du cœur", thèse de doctorat *CREATIS*. Institut National Polytechnique de Grenoble, 148p, 2002.

## 4.2. ESTIMATION ET ANALYSE DU MOUVEMENT DU COEUR

**Mots clés:** estimation de mouvement, analyse de mouvement, données fonctionnelles, fonction contractile, IRM de marquage tissulaire, aide à la décision

### 4.2.1. Estimation de mouvement

Nous présenterons les approches initiales de l'estimation du mouvement du cœur basée sur les surfaces puis les approches denses qui reposent sur l'IRM de marquage tissulaire.

#### *4.2.1.1. Dynamique des surfaces*

L'arrivée des techniques d'imagerie 3D, comme le DSR ou les systèmes tomographiques a permis d'envisager la reconstruction des surfaces cardiaques au cours du cycle. De nombreuses recherches ont été menées pour exploiter les formes anatomiques et leur évolution en vue de caractériser le mouvement du cœur. Dans la recherche de descripteurs capables de caractériser les formes et leur évolution, les caractéristiques différentielles de surface, comme la courbure et ses variantes, ont suscité beaucoup d'intérêt. Parmi les différentes mesures de courbure, le couple (courbure Gaussienne $K$, courbure moyenne $H$) a été introduit pour la reconnaissance d'objet 3D en analyse d'images de profondeur [80]. La courbure Gaussienne est une propriété intrinsèque d'une surface (indépendante de l'immersion de la surface dans l'espace 3D, invariant par isométrie), tandis que la courbure moyenne est une propriété extrinsèque. Ces deux mesures sont invariantes par transformation rigide et permettent de classer les points d'une surface en 8 catégories, ce qui les rend très attractives pour la reconnaissance de formes. Friboulet et al. ont réalisé des cartographies de courbure de Gauss des surfaces cardiaques issues d'une séquence de volumes 3D de données du DSR acquises sur un cœur de chien [81]. L'estimation de la courbure repose sur l'algorithme proposé par Sander et Zucker [82], qui intègre un raffinement itératif des estimées. Elle conduit à des représentations de $K$ cohérentes et stables au cours du temps et montre ainsi que son utilisation dans des procédures de mise en correspondance a un sens surtout pour la paroi libre, riche structurellement (ceci est moins vrai pour la paroi septale).

A la suite de ces travaux, nous avons proposé une représentation globale de la forme et de son évolution au travers du spectre dynamique de forme [19]. Une technique de suivi de région a également été présentée et expérimentée sur des surfaces simulées (Cas normal et pathologique) et réelles (DSR). Ces deux aspects reposent sur un nouveau couple de mesure de courbure introduit par Koenderink et van Doorn [83] : l'index de forme $s$ et l'intensité de courbure $c$, respectivement définis par :

$$s = \frac{2}{\pi} Arc\tan\frac{k_2 + k_1}{k_2 - k_1} = \frac{2}{\pi} Arc\tan\frac{-H}{\left(H^2 - K\right)^{\frac{1}{2}}},\ k_1 \geq k_2$$

$$c = \left(\frac{k_1^2 + k_2^2}{2}\right)^{\frac{1}{2}} = \left(2H^2 - K\right)^{\frac{1}{2}} \tag{13}$$

Où $k_1$ et $k_2$ sont les courbures principales. L'index de forme $s \in [-1,+1]$, invariant par homothétie, détermine une distribution continue de forme (Figure 15). L'intensité de courbure $c$ est inversement proportionnelle à la taille (analogue au rayon de courbure).

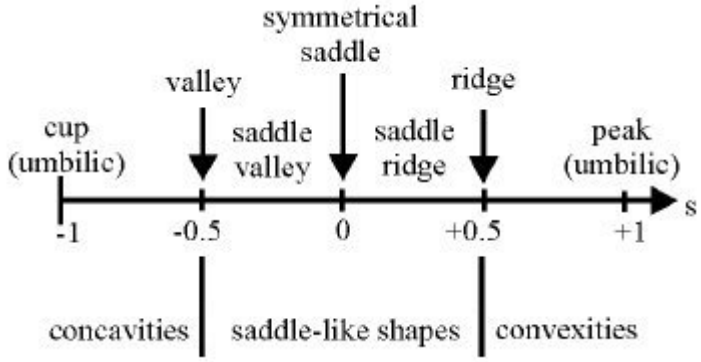


*Figure 15. Représentation des types de surface par l'index de forme s sur l'axe [-1, +1] (extrait de [19]).*

L'approche globale de caractérisation de forme en évolution repose sur le *spectre dynamique de forme* défini par :

$$\gamma(h,t) = \frac{1}{A}\iint_S \delta_1\left(s\left(p_t\right) - h\right) dS \tag{14}$$

Où $A = \iint_S dS$ est l'aire de la surface *S*, *dS* est un élément de surface autour d'un point $p_t$ de la surface, $\delta_1$ est la fonction Delta de Dirac 1D. L'argument *h* appartient à $[-1,+1]$ et *t* est la variable de temps discret à valeur dans $[0,1.....T]$. Cette équation réalise le cumul des aires de la surface pour chaque valeur de l'index de forme au temps *t*. La version discrète fait intervenir l'histogramme des index de forme. Une équation similaire donne le *spectre dynamique d'intensité de courbure*. La Figure 16 illustre ce mode de représentation pour des objets de synthèse simulant la déformation d'un VG au cours du cycle cardiaque. On observe que la forme évolue peu au cours du mouvement pour les deux premières séquences de synthèse, les points composants la surface restant majoritairement elliptiques. L'apparition de points concaves est en revanche clairement visible sur la 3$^{ième}$ séquence. L'évolution de l'intensité de courbure au cours du mouvement est également bien restituée par le spectre dynamique d'intensité de courbure. On observe le décalage vers le haut du spectre lors de la phase de contraction et le comportement inverse lors de la phase d'expansion. Une technique similaire est employée en version statique (pas de variable de temps) dans le système COSMOS de reconnaissance de formes en imagerie de profondeur [84, 85].

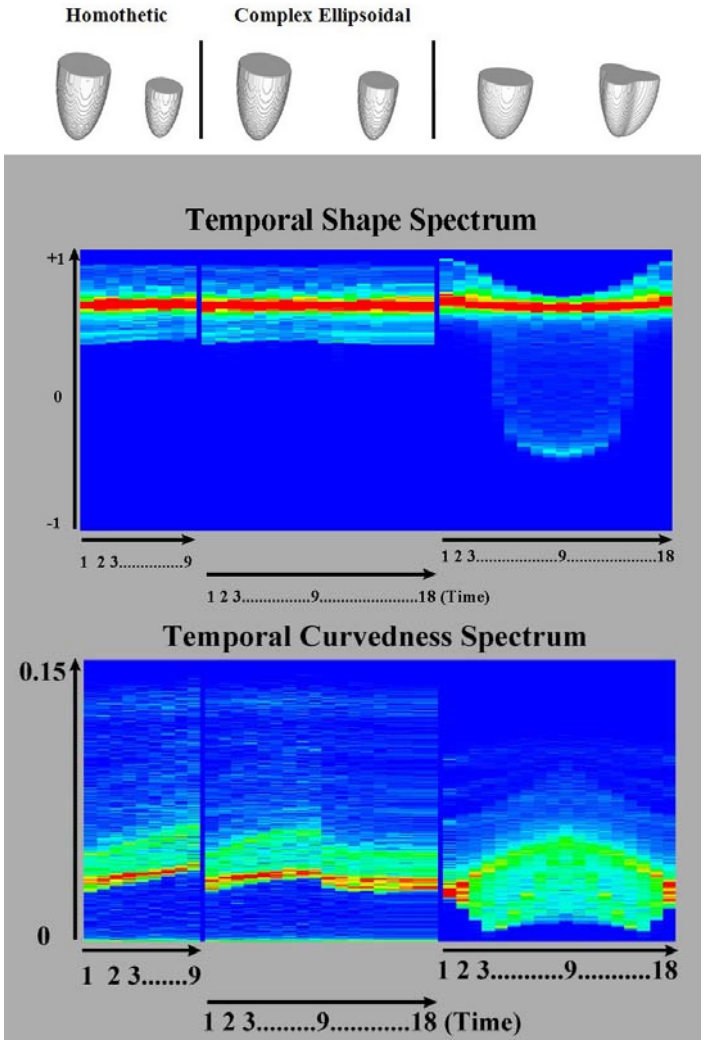


*Figure 16. Illustration de l'évolution des spectres dynamiques de forme et d'intensité de courbure pour un demi ellipsoïde de synthèse en déformation homothétique (à gauche), avec une déformation incluant des variations plus complexes des rayons avec une phase iso-volumique (au milieu), déformation avec apparition de concavités en télé-systole (à droite) (extrait de [19]).*

Le suivi de régions de la surface du VG s'appuie sur les mêmes indices de courbure et la capture de zones de forme similaire définies par un index de forme $s(p,t)$ au point $p$ à l'instant $t$, une variation de la forme $\Delta s$ autour d'un point $p$ et un nombre de points maximum. Sont également associés les valeurs moyennes et déviations standards de l'index de forme, de l'intensité de courbure, l'aire et le centre géodésique de la zone. La mise en correspondance de zone s'effectue d'abord par la compensation de la translation globale (moments d'inertie globaux) puis l'estimation d'un point de correspondance initial sur la surface suivante à $t+1$ selon la normale à la surface en $p$. Le centre géodésique de la zone de forme similaire définit le point de correspondance corrigé qui est le point départ d'un nouveau pas du suivi. Cette approche naïve fonctionne correctement sur des surfaces segmentées précisément. Elle a été illustrée sur des séquences de synthèse d'un VG en déformation au cours du cycle cardiaque obtenues par identification d'un modèle d'harmoniques sphériques [86] à partir de données réelles issues du DSR. Le suivi est illustré en Figure 17 pour 3 zones sur des séquences synthétiques d'un cœur normal et d'un cœur présentant une zone avec mouvement réduit (zone akinétique). Le suivi des paramètres d'index de forme et d'intensité de courbure dans ces régions met en évidence des différences d'évolution entre les cas normal et akinétique (voir publication jointe [19]).

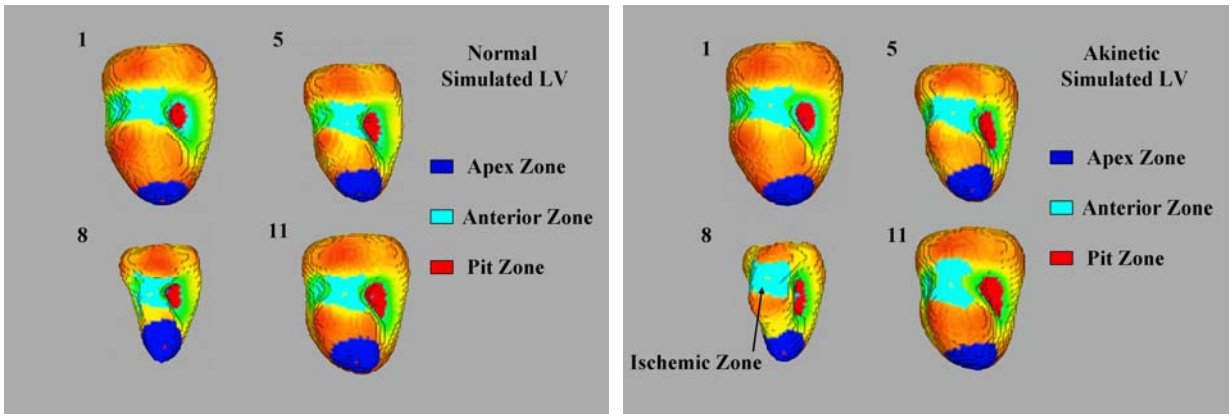


(a) (b)

*Figure 17. Suivi de 3 zones de forme similaire pour deux séquences simulées d'un cœur normal en (a) et d'un cœur présentant une zone akinétique (ischemic zone) en (b). Extrait de [19]*

Cette approche a donné lieu à une publication dans une revue internationale à comité de lecture et de nombreuses communications (liste ci-dessous). Elle n'a pas été poursuivie pour les raisons suivantes :

- Elle repose sur une segmentation très rigoureuse des contours des structures cardiaques au cours du cycle. Une telle segmentation est très délicate et souvent variable d'un expert à l'autre. La validation aurait nécessité au moins une dizaine de cas représentant des sujets sains et des patients dont la pathologie aurait été très précisément documentée en termes de localisation et de caractéristiques. Les données du DSR étaient à ce titre remarquables (pour une partie des données) du fait du fort contraste entre la cavité et le muscle. A l'époque, nous ne disposions que de 3 séquences de 16 volumes obtenues sur un coeur de chien anesthésié (courtoisie Dr. Erik. L. Ritman, Mayo Clinic, USA): une série contrôle, une série après occlusion, une série après revascularisation. Les deux dernières séries souffraient d'artefacts de reconstruction qui rendaient la segmentation beaucoup plus délicate. Des données équivalentes en IRM étaient encore rares.
- Une telle approche est réductrice puisque limitée à la zone sous-endocardique. Il subsiste aussi une indétermination au niveau des muscles papillaires. Le clinicien est davantage intéressé par ce qui se passe dans le myocarde.

Progressivement, les séquences IRM ont évoluées pour permettre la réalisation d'acquisitions anatomiques et dynamiques non invasives chez l'homme. L'étude des formes peut s'étendre à l'épicarde est donner accès à des paramètres plus robustes que la cinétique pariétale, comme l'épaississement pariétal. L'IRM de marquage tissulaire est également apparue comme l'outil le plus prometteur pour l'analyse de la dynamique cardiaque.

**Bibliographie :**

- Revues à comité de lecture

P. Clarysse, D. Friboulet, and I. Magnin, "Tracking geometrical descriptors on 3-D deformable surfaces: application to the left-ventricular surface of the heart," *IEEE Transactions on Medical Imaging*, vol. 16, pp. 392-404, 1997.

- Articles longs de congrès

P. Clarysse, D. Friboulet, and I. E. Magnin, "Curvature Assessment of the Heart Walls in 3D Dynamic Imaging," Computers in Cardiology, London, England, pp. 607-610, 1993.

P. Clarysse, D. Friboulet, and I. E. Magnin, "Time-evolution analysis of differential features on 3D surfaces of the heart walls," in *Proc. Nuclear Science Symposium and Medical Imaging Conf.* Norfolk, Virginia, USA, pp. 1807-1811, 1994.

P. Clarysse, O. Jaouen, I. E. Magnin, and J.-M. Morvan, "3D Representation and Deformation Analysis of the Heart Walls from X-ray and MR Images," Computers in Cardiology, Bethesda, Maryland, USA, pp. 657-660, 1994.

#### *4.2.1.2. Estimation de mouvement en IRM de marquage tissulaire*

L'IRM de marquage tissulaire est une technique d'imagerie spécialement développée pour l'analyse du mouvement du cœur. Son principe, très judicieux, exploite les concepts de l'IRM et des propriétés magnétiques des tissus pour créer un marquage virtuel dans les images qui se déforme suivant la déformation des tissus au cours du cycle cardiaque (Figure 18).

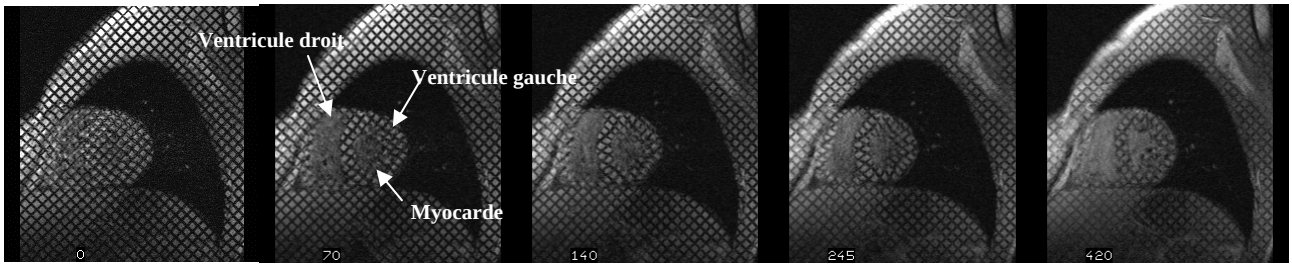


*Figure 18. Images par RM de marquage tissulaire avec marquage en grille. Le marquage régulier au départ se déforme en suivant la déformation du muscle cardiaque au cours de la systole (temps indiqué en millisecondes).*

Diverses géométries de marquage ont été proposées : marquage en bande selon 2 ou 3 directions orthogonales, marquage en grille, marquage radiaire. L'intérêt du marquage en grille est qu'il marque simultanément selon 2 directions au cours de la même acquisition, évitant ainsi les problèmes potentiels de recalage des images des séries. Une des difficultés est la persistance limitée du marquage au cours du cycle (tag fading), qui a pendant longtemps restreint l'analyse à une partie du cycle cardiaque (la systole).

Les principales étapes de l'analyse quantitative d'images par RM de marquage tissulaire sont indiquées en Figure 19. La seconde étape est encadrée en traits interrompus, signifiant que, selon les approches, la segmentation du motif de marquage est nécessaire. Historiquement, ce sont les premières à avoir été développées. Actuellement, des méthodes comme IRM-HARP ou celles basées sur des techniques de recalage non linéaires ne requièrent pas la segmentation du motif. Nos contributions à l'analyse d'images par RM de marquage tissulaire concernent l'estimation et la modélisation spatio-temporelle du champ de déplacement (étape 3) et le développement d'outils de segmentation du motif de marquage tissulaire et du cœur (étape 2). Chronologiquement, nous avons en réalité débuté nos travaux par l'analyse statistique des paramètres caractéristiques de déformation calculés en IRM de marquage tissulaire (étape 4, en section 4.2.2).

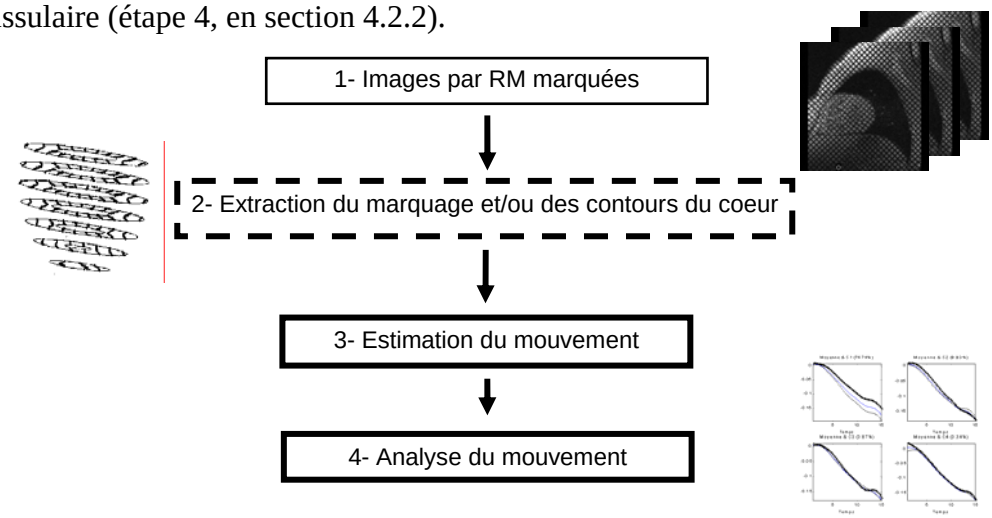


*Figure 19. Les étapes d'analyse d'images par RM de marquage tissulaire*

L’estimation du mouvement à partir des images par RM de marquage tissulaire n’échappe pas au problème d’ouverture, bien connu en vision par ordinateur. Cependant, la géométrie particulière du motif de marquage permet de considérer la déformation subit par rapport à la situation de référence au repos où le marquage est régulier et non déformé (comme en mécanique des milieux continus). La détermination des coordonnées du déplacement est ainsi découplée en fonction des orientations de marquage (Figure 20).

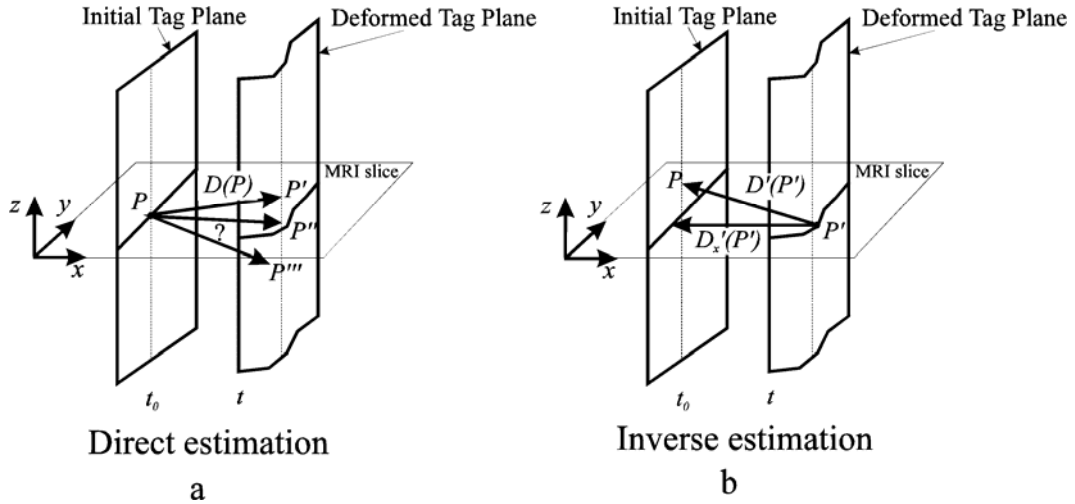


*Figure 20. (a) Dans le cas de l’estimation directe, l’ambiguïté de la détermination de l’image de P n’est pas résolue. (b) Dans le cas inverse, l’image de P’, situé dans le plan image permet la détermination univoque de la coordonnées x du déplacement par rapport à la position de repos (extrait de [87]).*

L’inconvénient principal des méthodes proposées initialement était d’estimer la déformation instant par instant sans intégrer de continuité temporelle. Dans [87], nous avons présenté un nouveau modèle d’interpolation de champ spatio-temporel en 2D du mouvement ventriculaire gauche. Les déplacements sont représentés par une série harmonique. En 2D, les coordonnées du déplacement inverse s’expriment par:

$$d_x'(x,y,t) = \sum_{k=0}^{K-1}\sum_{l=0}^{L-1}\sum_{m=0}^{M-1} A_{x,k,l,m}' \cos\left(\frac{\pi k x}{X}\right)\cos\left(\frac{\pi l y}{Y}\right)\cos\left(\frac{\pi m t}{T}\right)$$
$$d_y'(x,y,t) = \sum_{k=0}^{K-1}\sum_{l=0}^{L-1}\sum_{m=0}^{M-1} A_{y,k,l,m}' \cos\left(\frac{\pi k x}{X}\right)\cos\left(\frac{\pi l y}{Y}\right)\cos\left(\frac{\pi m t}{T}\right) \quad (15)$$

Où *K*, *L* sont les ordres spatiaux et *M* l’ordre temporel. Les paramètres *A’* du modèle sont estimés aux moindres carrés. Le déplacement direct est calculé à partir du déplacement inverse selon le même principe. Les ordres optimaux qui dépendent de la densité du marquage et du nombre de phases cardiaques sont estimés à partir d’une simulation réaliste d’une coupe de cœur en mouvement. Ce type de représentation permet de calculer directement les paramètres mécaniques associés à la déformation du myocarde comme la vitesse, l’accélération, les déformations principales ou les déformations selon les directions anatomiques. La Figure 21 illustre le champ de déplacement calculé avec cette méthode avec une représentation en texture de fourrure développée au laboratoire [88]. L’homogénéité de la contraction sur le pourtour myocardique est bien visible pour le sujet sain ainsi qu’un gradient transpariétal où le déplacement est plus élevé à l’endocarde qu’à l’épicarde. Chez un patient présentant une nécrose dans le territoire postéro-latéral, on observe une récupération fonctionnelle dans le territoire antérieur mais pas dans la zone nécrosée.

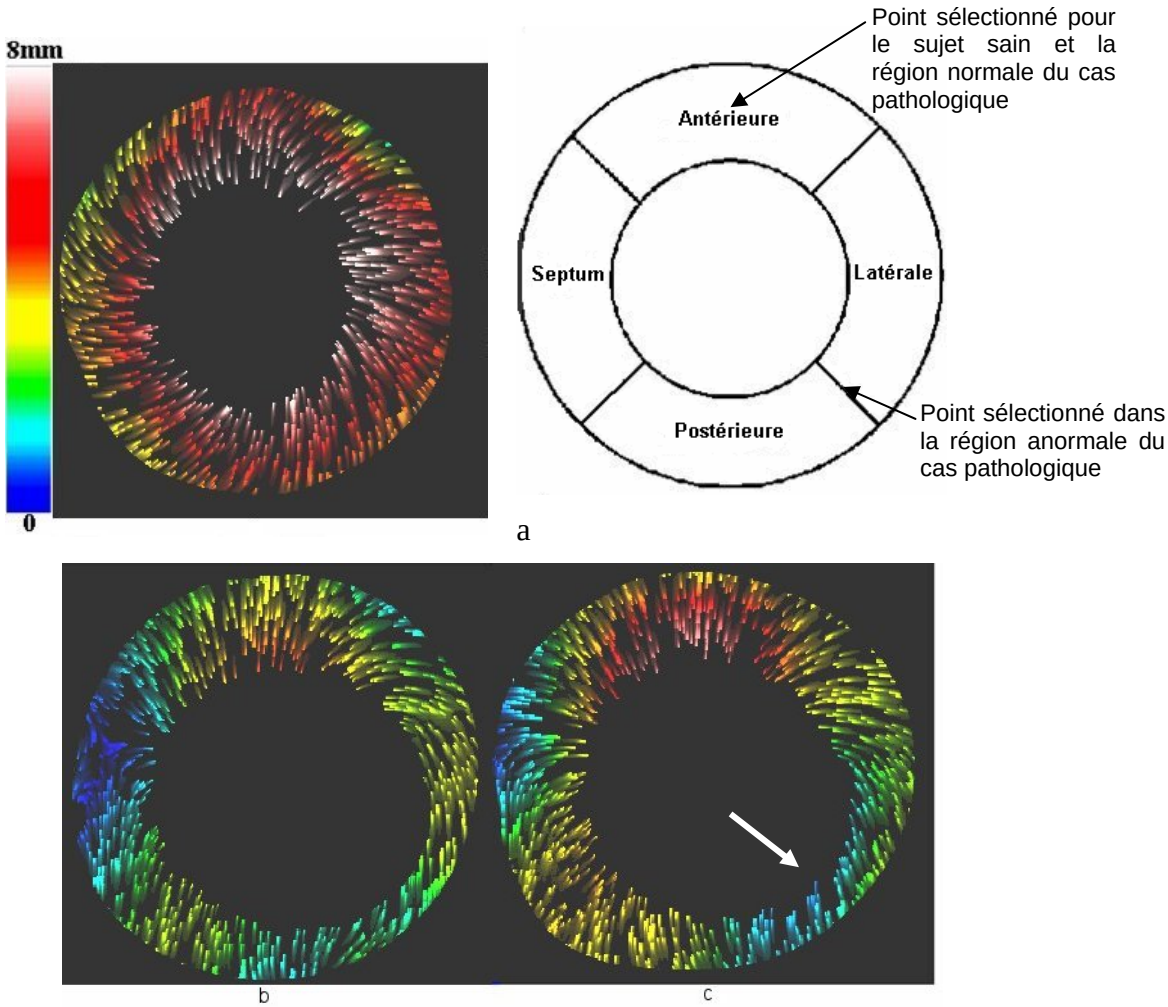


*Figure 21. Représentation du déplacement dans le myocarde ventriculaire gauche en coupe petit axe en fin de systole pour un sujet sain (a), un cas pathologique au repos (b) et sous stimulation pharmacologique (c).*

Il est également possible de suivre des points particuliers (trajectoires) et l'évolution des paramètres en ces points comme le montre la Figure 22. Ce qui permet une analyse fine spatio-temporelle des paramètres mécaniques de déformation. On observe une évolution similaire des déformations en un point matériel du myocarde sain et de la région 'normale' du cas pathologique. Ces évolutions sont très perturbées pour un point sélectionné dans le territoire nécrosé du cas pathologique.

Cette méthode est au cœur du logiciel *TagAnalyze* que nous avons développé pour l'aide à l'analyse d'images par RM de marquage tissulaire en 2D+temps [89]. Ce logiciel intègre également des fonctionnalités de segmentation assistée du motif de marquage basée sur une grille déformable (Figure 23). Les points des lignes de marquage extraites constituent les données d'entrée de l'algorithme d'estimation de mouvement précédemment décrit.

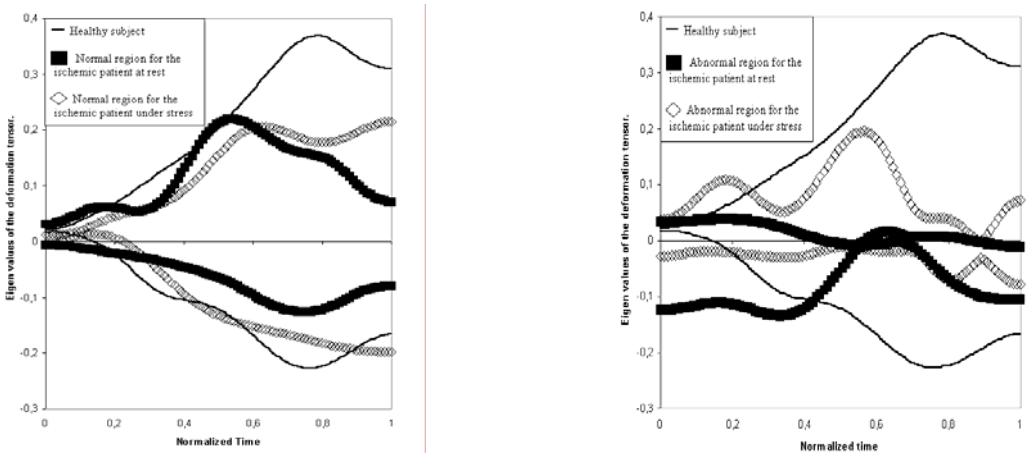


*Figure 22. Déformations principales pour des points myocardiques sélectionnés chez un sujet sain (à gauche) et un patient ischémique (à droite). Extrait de [87].*

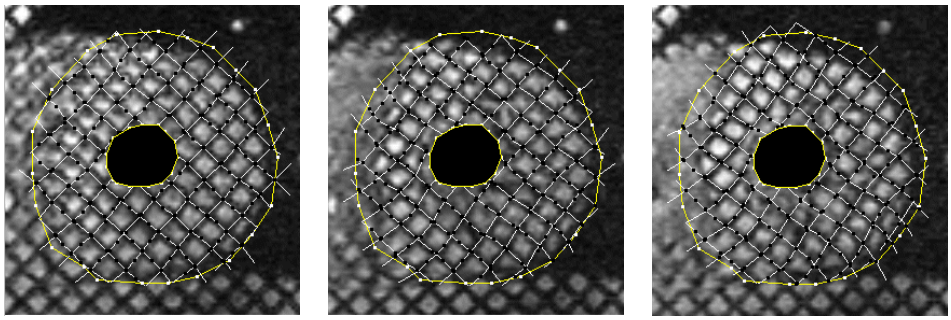

*Figure 23. Motif de marquage extrait dans les 3 premières images d'une séquence*

L'approche d'estimation et de modélisation du mouvement que nous avons proposée a été généralisée en 3D mais pas exploitée sur des données réelles principalement pour deux raisons :

- L'acquisition de séquences d'images par RM avec un motif de marquage 3D n'est en général pas réalisée en clinique pour des raisons de durée d'examen
- Le traitement des données 3D est particulièrement long et délicat. La cohérence spatiale et temporelle de chaque ligne de marquage extraite doit être contrôlée et éventuellement corrigée en 3D.

Le logiciel *TagAnalyze* constitue un prototype d'application d'analyse d'IRM de marquage tissulaire utilisé dans un cadre de recherche mais peu adapté à une exploitation clinique. En effet, l'extraction préalable du motif de marquage dans les images constitue un handicap du fait des corrections nécessaires de l'utilisateur. C'est pourquoi, nous nous intéressons maintenant à des techniques ne nécessitant pas cette étape rédhibitoire. Une alternative a été proposée dans la thèse de Fabrice Vincent pour le suivi du motif par mise en correspondance régularisée sur le concept de gabarit déformable élastique présenté en section 4.1 [75, 90]. La technique d'images par RM harmoniques de phase (IRM-HARP) est également une solution intéressante à ce problème.

Ce travail a été décrit dans deux publications dans des revues internationales à comité de lecture, dans la thèse de Fabrice Vincent et plusieurs communications (liste ci-dessous).

**Bibliographie :**


- Revues à comité de lecture

L. Khouas, P. Clarysse, D. Friboulet, and C. Odet, "Fast 2D vector field visualization using a 2D texture synthesis based on an autoregressive filter. Application to cardiac imaging," Machine Graphics and Vision, vol. 7, pp. 751-764, 1998.

P. Clarysse, C. Basset, L. Khouas, P. Croisille, D. Friboulet, C. Odet, and I. E. Magnin, "Two-dimensional spatial and temporal displacement and deformation field fitting from cardiac magnetic resonance tagging," *Medical Image Analysis*, vol. 4, pp. 253-268, 2000.

- Articles longs de congrès

F. Sottilini, P. Clarysse, D. Revel, and I. E. Magnin, "LV myocardial wall motion estimation with tagged cine MRI (SPAMM)," Computers In Cardiology, Vienna, Austria, pp. 529-532, 1995.

F. Vincent, P. Clarysse, P. Croisille, and I. E. Magnin, "An elasticity-based region model and its application to the estimation of the heart deformation in tagged MRI.," International Conference on Image Processing (ICIP), Vancouver, BC, Canada, pp. 629-632, 2000.

P. Clarysse, L. Bracoud, P. Croisille, and I. E. Magnin, "Integrated Quantitative Analysis of Tagged Magnetic Resonance Images," FIMH'01, Helsinky, Finland, pp. 69-75, 2001.

J. Milles, P. Clarysse, A. van Susteren, P. Croisille, I. E. Magnin, and T. Arts, "Automatic 2D segmentation of the left ventricle in tagged cardiac MRI using motion information," IEEE International Symposium on Biomedical Imaging (ISBI), Arlington, VA, USA, pp. 153-156, 2004.

- Thèses

F. Vincent, "Gabarits déformables élastiques pour la segmentation et le suivi de mouvement du cœur en Imagerie par Résonance Magnétique", thèse de doctorat *CREATIS*. Institut National des Sciences Appliquée, Lyon, 120p, 2001.


### 4.2.2. Analyse de paramètres de déformation

La possibilité de modéliser et de quantifier la déformation du muscle cardiaque ouvre la voie à des études de la fonction contractile normale et pathologique dans des populations. L'IRM de marquage tissulaire a révélé un mouvement du cœur normal plus complexe que ce qui avait été qualitativement décrit jusqu'alors. De manière encore un peu schématique et si l'on se place dans le repère anatomique circonférentiel-radial-longitudinal du VG, on observe un mouvement radiaire qui induit l'épaississement de la paroi myocardique au cours de la systole, un mouvement de torsion selon l'axe longitudinal du cœur qui implique que base et apex du cœur tournent en sens inverse dans un plan petit axe, un mouvement longitudinal qui fait que la base se rapproche significativement de l'apex (typiquement d'une dizaine de millimètres) qui, quant à lui, reste quasiment fixe. Le mouvement est d'amplitude plus importante dans la paroi libre que dans la région septale. On observe également un gradient du mouvement des couches endocardiques vers les couches épicardiques (voir Figure 21a). L'IRM de marquage tissulaire permet également de mieux décrire les implications sur le mouvement de certaines pathologies cardiaques comme les cardiomyopathies hypertrophiques et ischémiques en particulier. Mais d'autres indications sont envisageables [28, 91].

D'un point de vue plus quantitatif, une variabilité significative est observée dans les paramètres pour des sujets normaux ce qui pose le problème de l'estimation de cette variabilité. C'est dans ce but que nous avons développé dans le cadre de la thèse de Meimei Han une technique d'analyse des paramètres en espace et dans le temps [92]. Les motivations initiales de ces recherches sont des études menées sur des chiens et chez l'homme à la Johns Hopkins University à l'aide des logiciels TagStrainAnalysis (TEA) [93] et FindTags [94]

conduisant à une estimation de paramètres de déformation en 3D et au cours du cycle cardiaque (appelés dans la suite Paramètres Spatio-Temporels de Déformation ou PSTD). La Figure 24 illustre le modèle géométrique du VG considéré et les différents mode de représentation des PSTD. L'idée directrice était de proposer une méthode de caractérisation de l'évolution moyenne des paramètres et de leurs principales variations. On peut très directement faire l'analogie avec l'Analyse en Composantes Principales (ACP), classique en analyse exploratoire de données. La technique proposée s'appuie sur l'extension de l'ACP aux données évolutives introduite par Ramsay et Silverman [95] que nous appelons Analyse en Composantes Principales Fonctionnelles (ACPF). L'analyse de données fonctionnelles est un concept générique encore peu diffusé dont le champ d'applications potentielles est très étendu [96]. Pour en expliquer le principe, nous nous limiterons à l'analyse d'un paramètre évolutif *p(t)* dans une population de *N* individus. Pour chaque individu, nous disposons de la valeur du paramètre *p* en une succession d'instants, régulièrement espacés sur un intervalle de temps fixé *[a,b]*. Ces données peuvent être résumées dans un tableau où la variable *x(t)* est la version centrée par rapport à la moyenne des évolutions de *p(t)* sur les *N* individus:

$$X(t)=\begin{bmatrix} x_1(t) \\ ... \\ x_N(t) \end{bmatrix}, t \in [a,b] \qquad (16)$$

La variable *x* est à valeur dans un espace (hilbertien, rigoureusement). Mathématiquement, il s'agit de déterminer un sous-espace *H* de dimension *d* permettant d'obtenir une projection du nuage de fonctions $x_i$ dont l'inertie est maximale :

$\max_H \sum_{i=1}^{N} \left\| \overline{x_i^H} \right\|^2$, $\overline{x^H}$ désignant la projection orthogonale de *x* sur *H*

Le problème est alors décomposé en sous problèmes successifs :

**1-** Recherche d'une fonction $f_1(t)$ telle que :

$$\sum_{i=1}^{N} \|d_{i1}\|^2$$

où

$$d_{i1} = \langle x_i(t), f_1(t) \rangle = \int_a^b x_i(t) f_1(t) dt$$

soit maximale sous la contrainte $\|f_1\|^2 = \int_a^b f_1^2(t) dt = 1$

**2-** Recherche d'une fonction $f_2(t)$

.
.
.

**d-** Recherche d'une fonction $f_d(t)$ telle que :

$$\sum_{i=1}^{N} \| d_{id} \|^2 \text{ soit maximale, avec } d_{id} = \int_a^b x_i(t) f_d(t) dt$$

sous les contraintes :

$$\| f_d \| = 1 \text{ et } \forall j < d, \langle f_j, f_d \rangle = \int_a^b f_j(t) f_d(t) dt = 0$$

Où $\|.\|$ est la norme $L_2$ et <.> représente le produit scalaire.

Les $d$ fonctions orthogonales $\{f_\alpha(t), \alpha = 1...d\}$ sont les composantes principales fonctionnelles.

On montre que ce problème est équivalent à un problème de fonctions propres [95 , 97]. Le calcul pratique des fonctions propres repose sur une décomposition des $x_i$ et $f_\alpha$ dans une base de fonctions, splines par exemple.

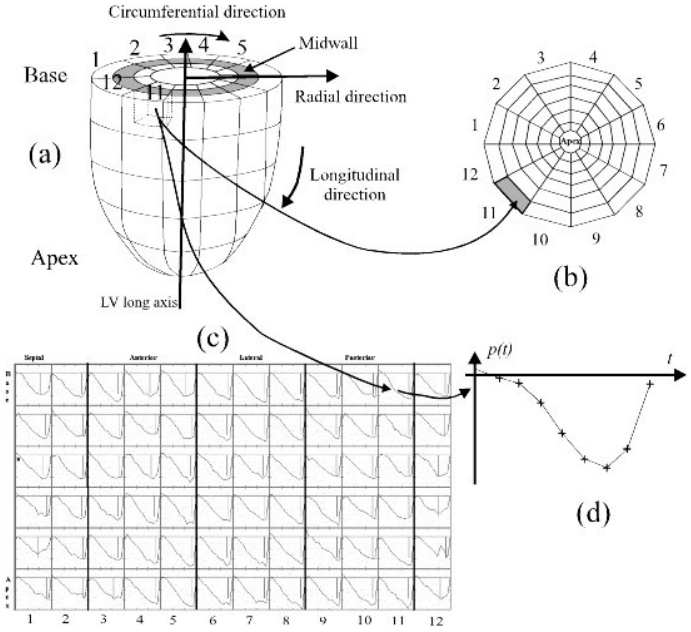


*Figure 24. (a) Le VG est décomposé en éléments de volume selon les directions anatomiques circonférentielle, radiale et longitudinale. Les paramètres spatio-temporels de déformation sont calculés en chaque élément. (b) la représentation polaire en œil de bœuf est couramment utilisée en cardiologie. Elle n'intègre pas le temps. (c) La représentation en tableau de courbes permet d'avoir une vision d'ensemble de l'évolution d'un paramètre sur l'ensemble du cœur, de la base à l'apex, à un niveau radiaire fixé comme pour la représentation polaire (Extrait de [97]).*

L'ACPF a été appliquée à l'exploration d'un ensemble de 9 examens sur sujets sains (acquisitions 3D+temps, Johns Hopkins Hospital, Baltimore, USA) et de 6 examens sur des patients (acquisitions 2D+temps, Hôpital Cardiologique de Lyon). L'analyse a porté sur le paramètre de déformation circonférentielle ($E_{cc}$ ) qui nous semblait le plus documenté dans la littérature et dont l'estimation est plus précise. La Figure 25 illustre les deux premières composantes principales fonctionnelles pour 8 des cas sains. On observe une remarquable homogénéité de comportement de cette population, les variations entre individus étant assez réduites. Cette décomposition constitue une modélisation du comportement du paramètre $E_{cc}$. Les cas pathologiques ont été comparés à cette référence selon la stratégie exposée en *Figure 26*. Celle-ci consiste à exprimer l'évolution de $E_{cc}$ pour le cas considéré à partir du modèle de

référence ‘sain’ et de calculer une distance sur les paramètres estimés. Si on se limite aux 2 premières composantes (ce qui est le cas en pratique), cette distance s’écrit :

$$DistF = \left[ \left( f_1 \cdot \frac{C1}{C1+C2} \right)^2 + \left( f_2 \cdot \frac{C2}{C1+C2} \right)^2 \right]^{1/2} \qquad (17)$$

Où $f_1$, $f_2$ sont les 2 premières composantes scalaires (appelées scores) qui représentent la position de la courbe candidate dans le système des composantes principales fonctionnelles et $C1$, $C2$ les contributions relatives respectives des 2 premières composantes exprimées en pourcents.

Il est ainsi possible de mettre en évidence les différences locales du cas pathologique considéré avec le modèle de référence d’un cœur normal. Ceci est illustré sur la Figure 27. D’après le nombre limité de cas étudiés, il semble que la comparaison des états au repos et sous stimulation pharmacologique soit davantage significative pour l’identification des anomalies de contraction.

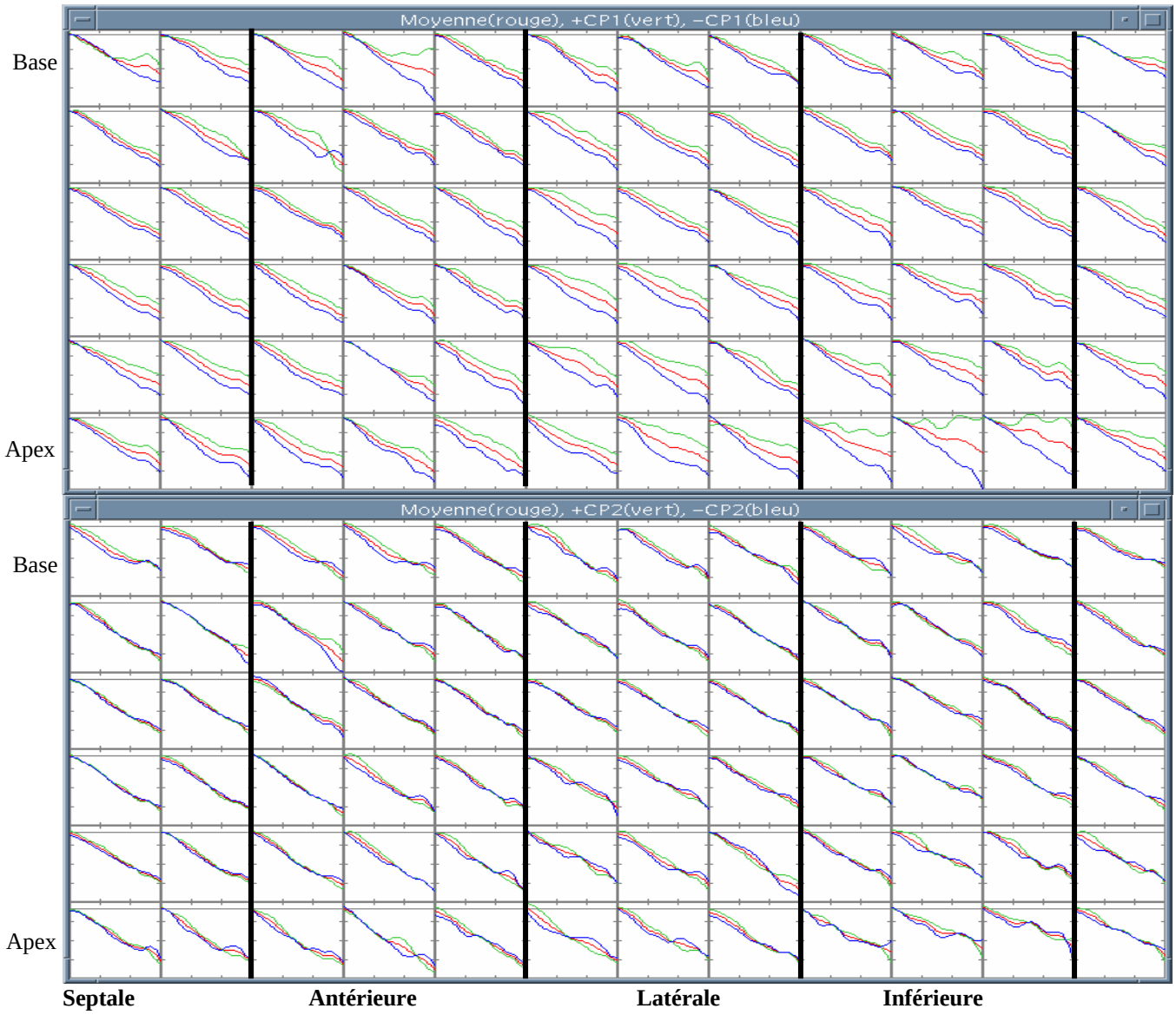


*Figure 25. Première et deuxième composantes principales fonctionnelles du paramètre $E_{cc}$ issues de l’analyse 3D des données de marquage de 8 sujets sains (mi-paroi). La moyenne du paramètre est en rouge, les composantes fonctionnelles en bleu et vert.*

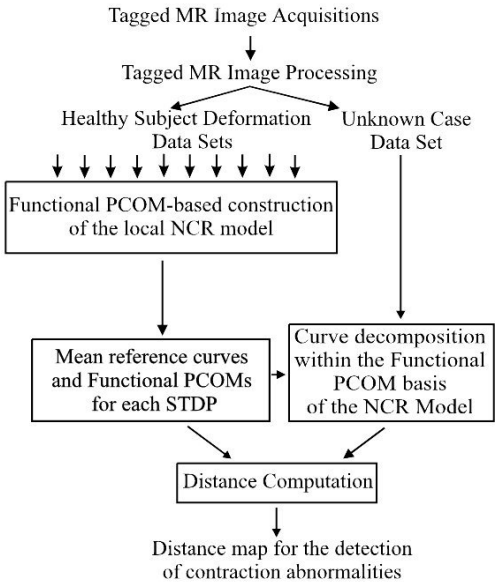


*Figure 26. Stratégie de comparaison d'un cas pathologique avec la référence issue de l'ACPF de l'ensemble des cas sains (Extrait de [97]).*

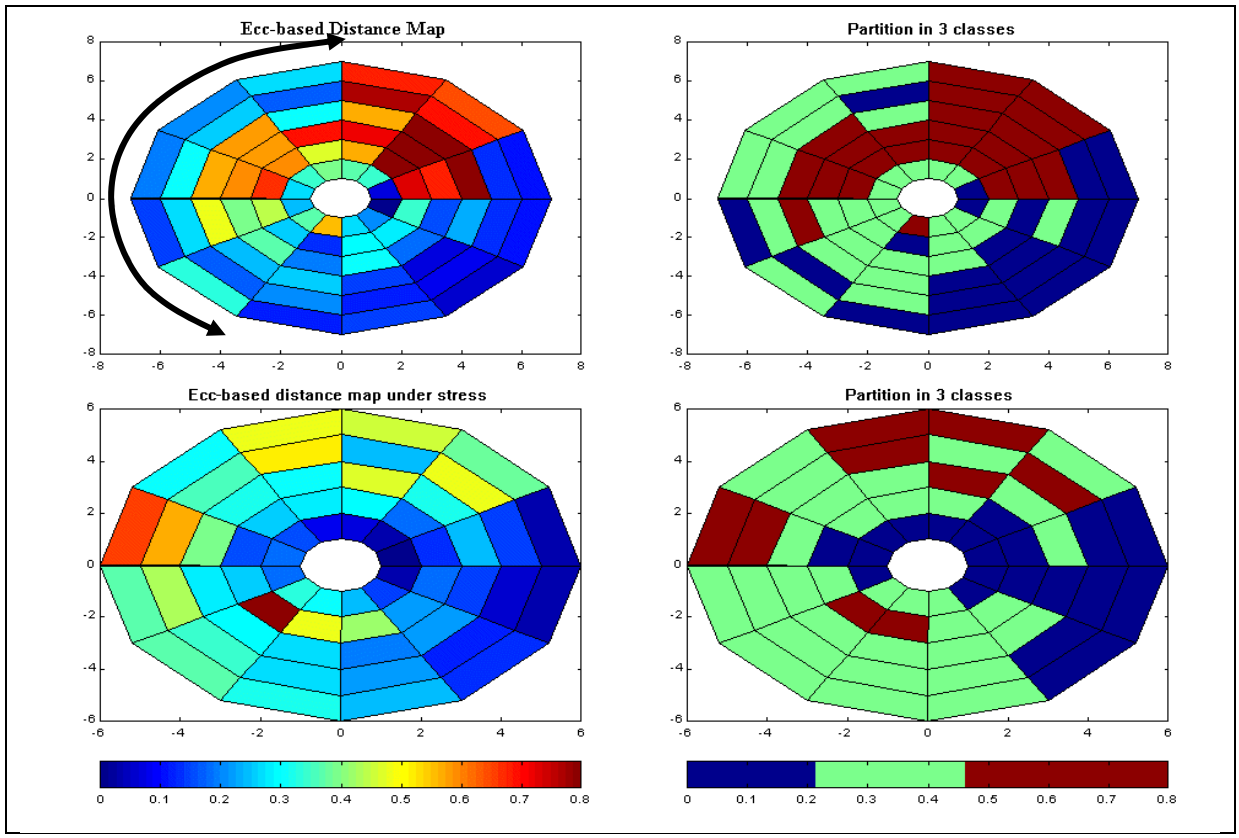


*Figure 27. Cartographies polaires au repos (en haut) et sous stimulation (en bas) illustrant la 'distance' du cas pathologique P3 au modèle de référence 'sain' pour le paramètre $E_{cc.}$ La région de nécrose a été estimée en TEP-FDG dans les régions s'étendant de 7 à 12h. Les cartographies de droite sont une version seuillée en 3 classes des cartographies de gauche (Extrait de [97]).*

Ces travaux ont fait l'objet de 3 publications dont 2 dans des revues internationales à comité de lecture, de la thèse de Meimei HAN et de 3 communications (liste ci-dessous). Dans le cadre d'une collaboration avec le Laboratoire D'Analyse des Systèmes de Santé (LASS) à Lyon et d'un projet soutenu par la région Rhône-Alpes, nous avons contribué à la généralisation de l'approche d'analyse de données fonctionnelles au cas multi-variables. Ce travail a fait l'objet de la thèse de Mathématiques Appliquées de Denis Clot (UCB Lyon 1, Décembre 2002) [98]. Un article est en cours de rédaction sur le sujet. L'objectif est triple :

1. Proposer au clinicien des cartographies du cœur qui résument les tendances principales de l'évolution des divers PSTD calculés au cours du cycle cardiaque
2. Synthétiser la variabilité de l'évolution des PSTD sur une population de sujets sains. Extraire de la connaissance sur le mouvement d'un cœur normal
3. Utiliser la connaissance préalablement acquise pour aider à la détection et à la localisation d'anomalies de la fonction contractile.

L'ACPF a été plus récemment utilisée dans un sens très proche par C. Tilmant pour la comparaison d'indices de la fonction myocardique, en particulier les déplacements centripètes et l'asynchronisme de contraction ventriculaire en échocardiographie [99].

**Bibliographie :**


- Revues à comité de lecture

M. Han, P. Clarysse, P. Croisille, I. E. Magnin, and D. Revel, "Aide à l'analyse de l'évolution spatio-temporelle de la déformation du myocarde," *Innovation et Technologie en Biologie et Médecine*, vol. 19, pp. 379-388, 1998.

L. Khouas, P. Clarysse, D. Friboulet, and C. Odet, "Fast 2D vector field visualization using a 2D texture synthesis based on an autoregressive filter. Application to cardiac imaging," *Machine Graphics and Vision*, vol. 7, pp. 751-764, 1998.

- Articles longs de congrès

F. Sottilini, P. Clarysse, D. Revel, and I. E. Magnin, "LV myocardial wall motion estimation with tagged cine MRI (SPAMM)," Computers In Cardiology, Vienna, Austria, pp. 529-532, 1995.

M. Han, P. Clarysse, P. Croisille, I. E. Magnin, and D. Revel, "Computer aided diagnosis of the myocardial ischemia based on a spatio-temporal deformation features analysis," Computers In Cardiology, Cleveland, Ohio, pp. 749-752, 1998.

F. Vincent, P. Clarysse, P. Croisille, and I. E. Magnin, "An elasticity-based region model and its application to the estimation of the heart deformation in tagged MRI.," International Conference on Image Processing (ICIP), Vancouver, BC, Canada, pp. 629-632, 2000.

- Thèses

M. Han, "Analyse exploratoire de la déformation spatio-temporelle de myocarde à partir de l'imagerie par Résonance Magnétique de marquage tissulaire," thèse de doctorat *CREATIS*, Institut National des Sciences Appliquée, Lyon, 201p, 1999.

### 4.3. INTEGRATION DE DONNEES CARDIAQUES MULTI-MODALITES

**Mots clés :** imagerie anatomique, imagerie fonctionnelle, mise en correspondance d'images, fusion d'information

Comme le montrent plusieurs études récentes, une meilleure définition de la viabilité myocardique requiert l'étude conjointe des informations de métabolisme, de perfusion et de la fonction myocardique issues des modalités d'imagerie spécifiques. Ceci nécessite d'être en mesure de mettre en correspondance des données de nature diverse, acquises dans des géométries éventuellement très différentes et dont les caractéristiques en termes de résolutions spatiales et temporelles, notamment, peuvent être notablement différentes. Il existe des difficultés supplémentaires liées aux caractéristiques propres du cœur en particulier le nombre limité de marqueurs anatomiques visibles et utilisables, et le mouvement permanent du cœur enchâssé dans la cage thoracique elle-même animée par le mouvement respiratoire. Le recalage des données images doit donc idéalement être à la fois spatial et tenir compte de la dynamique des structures. Nous avons développé des méthodes de recalage de données cardiaques TEP et IRM, rigides dans un premier temps, et une technique de génération de cartographies fonctionnelles individualisées du coeur. Nous avons également travaillé à l'évaluation de telles méthodes. Ces travaux sont menés en étroite collaboration avec le *Laboratory of Biomedical Engineering*, Helsinki University of Technology, Finlande. Ils ont été soutenus par une convention de coopération du CNRS avec la Finlande (1998-2001) et sont actuellement soutenus par un Programme International de Coopération Scientifique du CNRS (PICS n°1932).

Une des méthodes de recalage rigide proposée est basée sur la mise en correspondance des images de thorax transverses IRM et de transmission en TEP (voir images natives en Figure 28) [100]. Les surfaces des structures thoraciques et pulmonaires sont dans un premier temps extraites des images TEP de transmission et transverses IRM avec l'algorithme des pyramides déformables de Lötjönen *et al.* [101]. Cette segmentation repose sur un modèle général topologique et géométrique du thorax, incluant le torse, les poumons et l'enveloppe péricardique du cœur, qui est adapté aux données du patient à partir de déformations de forme libre. Une transformation rigide est alors estimée entre les 2 jeux de surfaces issues de la segmentation par la minimisation d'une distance entre les points du modèle de thorax extraits de la TEP et le modèle issu de l'IRM. Cette transformation est combinée à celle réalisant la réorientation des coupes IRM en petit axe par rapport aux coupes transverses. Le principe de la méthode de recalage est schématisé en Figure 29. La Figure 30 illustre un exemple de résultat de recalage. Des méthodes de recalage rigide de type iconique (basées sur les niveaux de gris des images), ne nécessitant pas de segmentation préalable, ont été également développées à titre de comparaison. Leur principe est assez classique. La similarité entre les deux images, basée sur les critères d'information mutuelle, de corrélation ou de rapport de corrélation, est maximisée dans un processus itératif et multi-résolutions [102, 103]. Nous discuterons ultérieurement des résultats respectifs de chaque type de méthode. Le recalage, associé à la segmentation des cavités ventriculaires cardiaques avec le GDE (voir section 4.1), permet de générer un modèle anatomique portant des informations fonctionnelles métaboliques (TEP 18F-FDG, fluorodésoxyglucose marqué au fluor18). Par ailleurs, le recalage de données IRM et magnétocardiographiques (MCG) a été réalisé par nos collègues finlandais à partir d'amers externes. Les densités de courant obtenues par la résolution du problème inverse en MCG ont ainsi été adjointes à notre modèle [104], [100] (Figure 31). A notre connaissance, c'est la première fois que l'appréciation simultanée de données métaboliques et électro-magnétiques du cœur *in vivo* a été réalisée en 3D. Une dizaine de cas ont été traités. Les résultats ont été jugés encourageants mais ont aussi montré les limites de

l'étude en particulier les nombreuses sources d'erreurs. Ce travail constitue une première étape vers la construction automatique de modèles anatomo-fonctionnels individualisés du cœur qui est le thème du programme PICS. Ces travaux ont fait l'objet de la thèse de Timo Mäkelä soutenue en Finlande en Mai 2003 [105] et en France en Juillet 2004 [102].

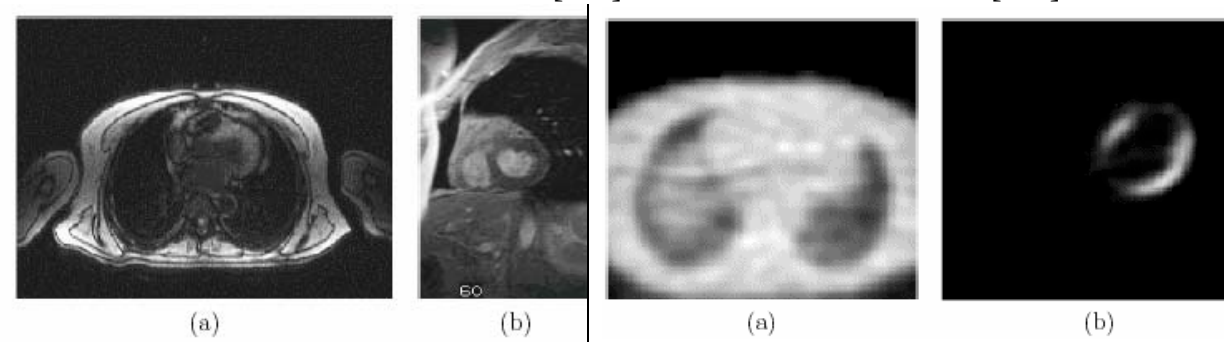


*Figure 28 : Images IRM transverses (a) et en petit axe (b). Images TEP de transmission (a) et d'émission 18F-FDG (b)*

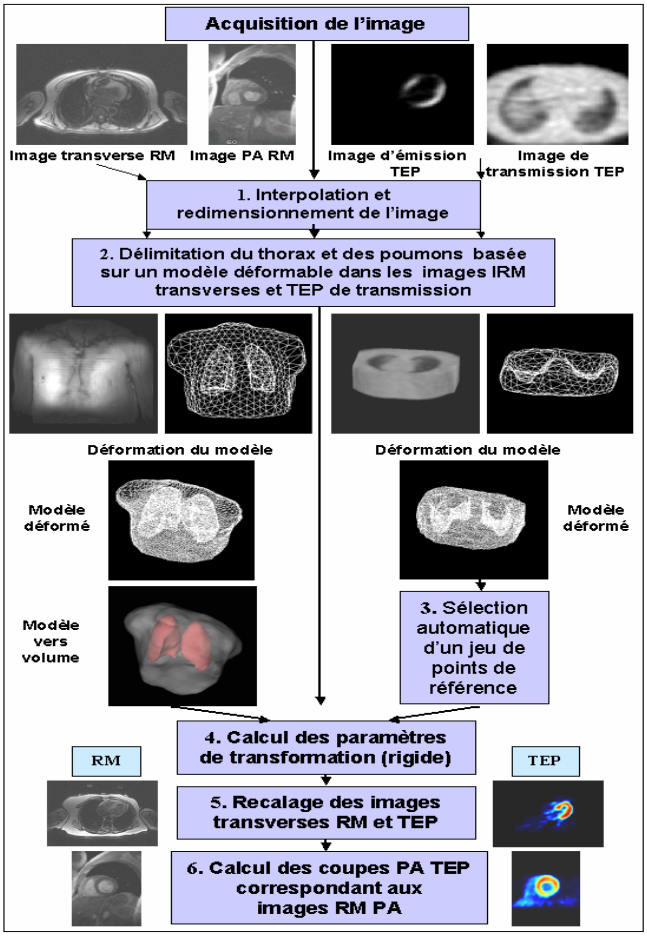


*Figure 29. Principales étapes de la méthode rigide de recalage d'images RM et TEP thoraciques et cardiaques basée sur les surfaces des structures anatomiques*

La problématique de traitement individualisé de données dans le domaine cardio-vasculaire est également le thème d'un réseau d'Excellence Européen (REX), dénommé *e-Heart*, qu'Isabelle Magnin a proposé à la communauté Européenne en 2003. Bien que bien noté, le réseau n'a pas été financé mais la démarche appuyée par un large consortium a néanmoins montré l'importance stratégique de cette problématique. Les équipes du consortium continuent d'échanger sur le site internet du projet: http://www.creatis.insa-lyon.fr/e-heart/.

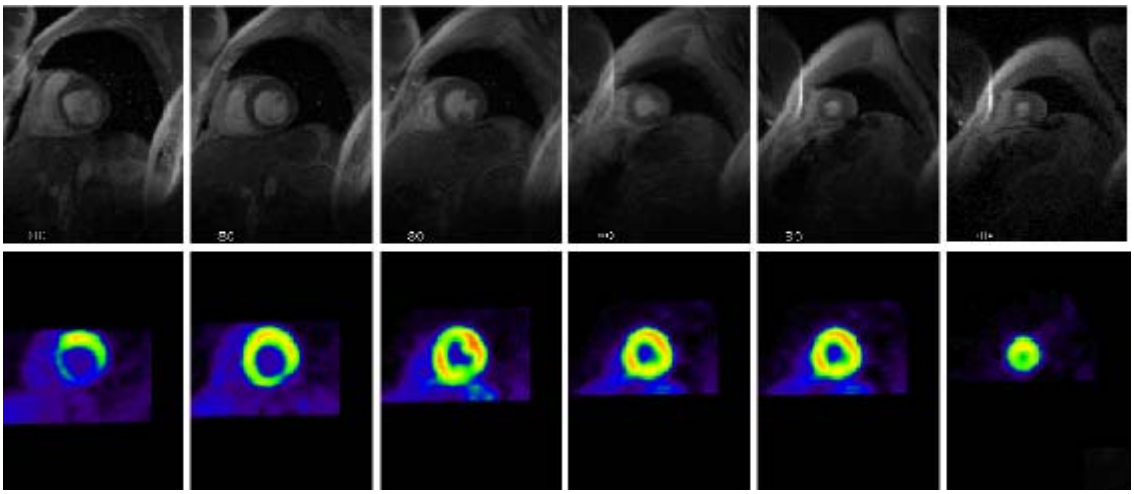

*Figure 30. Coupes IRM du cœur en petit axe (en haut) recalées avec les coupes TEP d'émission (en bas) pour un même cas.*

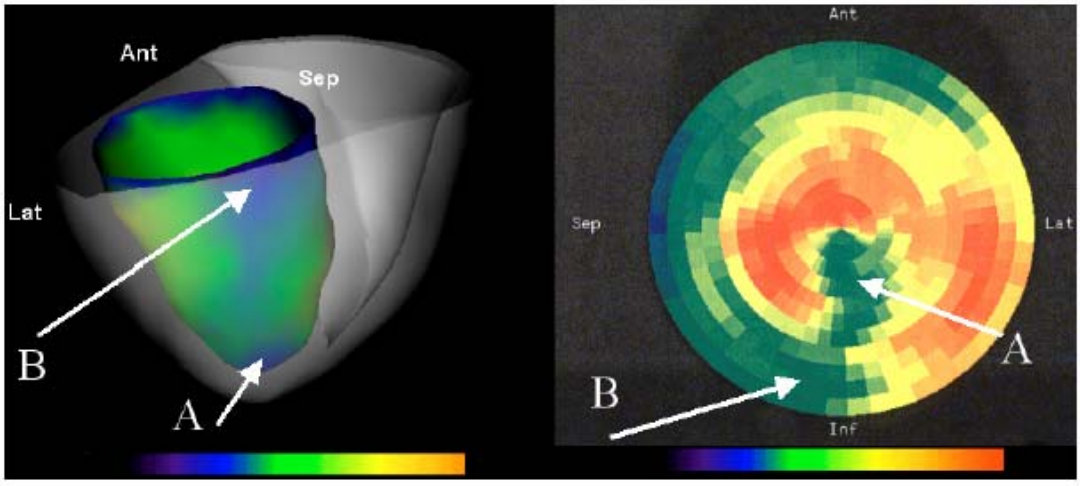


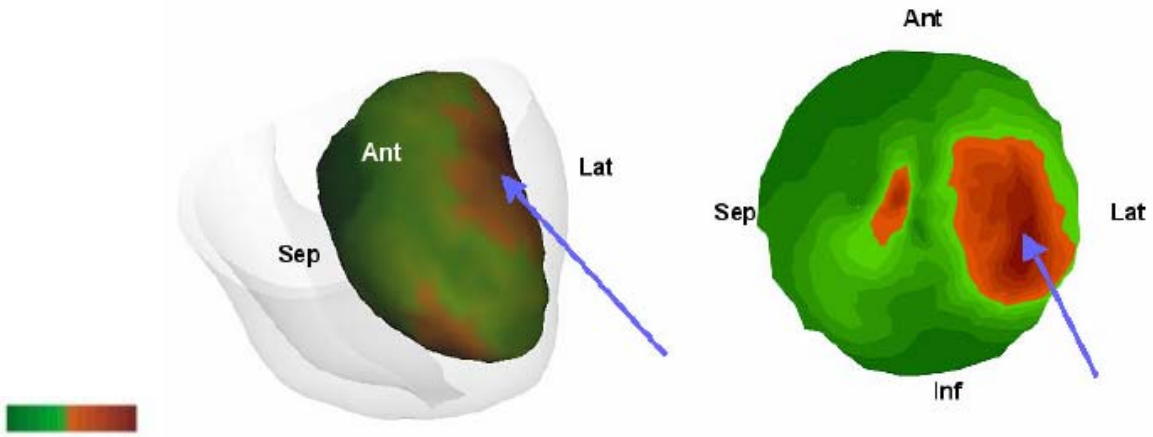


*Figure 31: Haut. Cartographies 3-D de la captation du fluorodésoxyglucose (gauche) sur le modèle de cœur biventriculaire du patient E2. La représentation polaire réalisée manuellement de l'image TEP-FDG correspondante est présentée à droite. Bas: Cartographies 3-D des valeurs de densité de courant plaquées sur le modèle de cœur biventriculaire du patient E2. A droite : représentation polaire 2D réalisée de façon interactive à partir de la surface interne en 3-D. Les flèches indiquent des zones qui se correspondent.*

Dans l'objectif d'évaluer le recalage en termes de précision, de robustesse et de temps de calcul, Nicoleta Pauna a développé une stratégie d'évaluation de techniques de recalage en imagerie cardiaque à partir de la simulation d'images TEP (thèse soutenue en Juin 2004) [103]. Cette évaluation repose sur la création d'un jeu de données d'images de référence TEP-IRM en quasi-parfaite correspondance. Pour cela, une acquisition 3D thoracique a été réalisée sur un sujet sain en IRM. Ces données sont segmentées manuellement et étiquetées en 9 classes (muscle, poumons, foie, graisse, rachis (os), myocarde du VG, cavité du VG, myocarde du VD et la cavité du VD). Le modèle numérique résultant est introduit dans un simulateur d'images TEP (SORTEO, simulation Of Realistic Transmission and Emission Object, CERMEP, Lyon) qui calcule les images TEP de transmission et d'émission de référence [106]. Un jeu de transformations rigides (tirage aléatoire) est appliqué aux données TEP simulées. Les couples constitués des données IRM originales et TEP simulées/transformées sont présentés à l'entrée de l'algorithme de recalage à évaluer. Les résultats de recalage sont ensuite quantitativement évalués à l'aide de métriques adaptées (erreur quadratique moyenne dans un volume d'intérêt) compte tenu de la connaissance des transformations entre les couples d'images. La stratégie d'évaluation est résumée Figure 32. Pour évaluer la robustesse des algorithmes vis-à-vis des caractéristiques des images (coeur normal ou pathologique), un jeu de données de référence supplémentaire pour un cœur pathologique a également été généré.

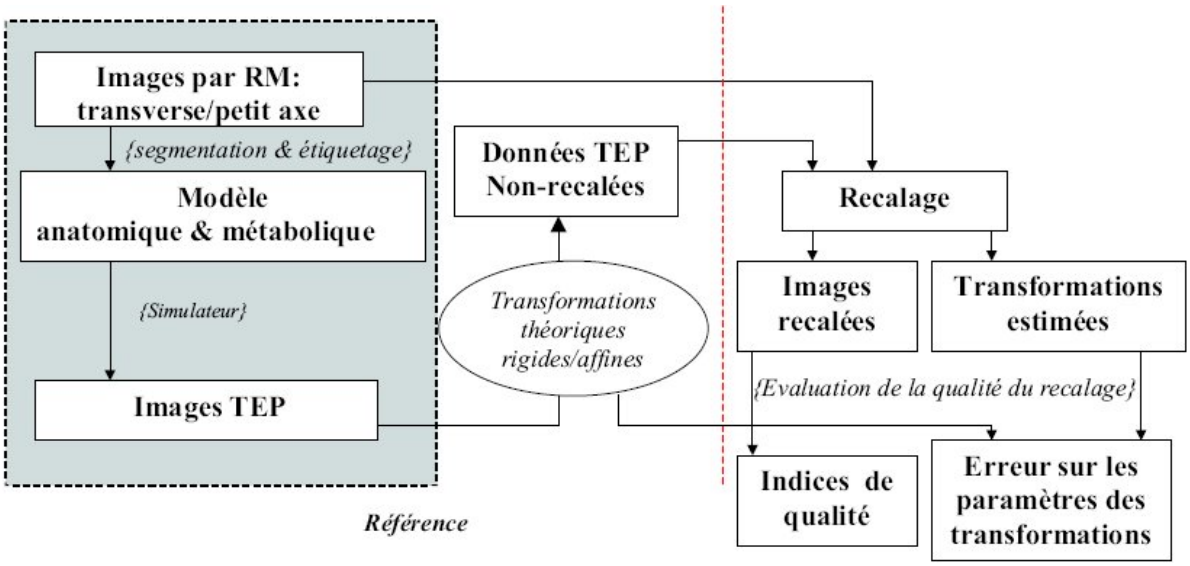


*Figure 32. Stratégie d'évaluation des méthodes de recalage d'images: vue générale*

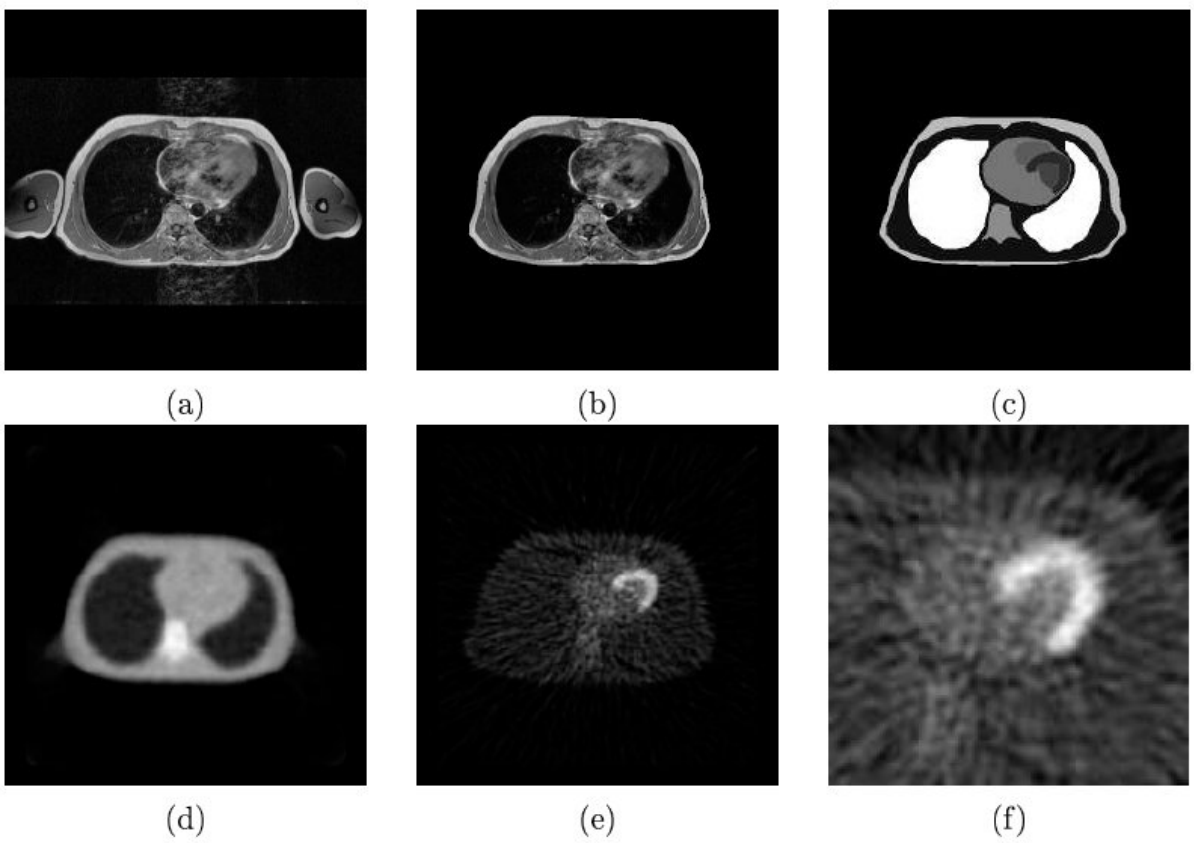


*Figure 33. Etapes de construction de la référence.(a) Image par RM réelle. (b) Image par RM sans les bras. (c) Image segmentée et étiquetée. (d) Image simulée du modèle (c) en TEP de transmission. (e) Image simulée en TEP d'émission. (f) Image simulée centrée sur le cœur en TEP d'émission*

Cette stratégie a été appliquée à l'évaluation de 3 méthodes de recalage rigide d'images 3D du thorax et du cœur. Ce sont :

- Une méthode de recalage iconique (identifiée par HMR, home made registration) développée dans le cadre de la thèse de N. Pauna dont les caractéristiques sont : transformation rigide à 6 paramètres (3 translations, 3 rotations), 3 mesures de similarité au choix (coefficient de corrélation (CC), information mutuelle (IM), rapport de corrélation (RC)), Interpolation par B-splines (linéaires à cubiques, principalement), optimisation par la méthode de Powel, stratégie multi-résolution
- Une méthode construite sur la librairie ITK (identifiée par IMP, Information Mutuelle Parzen) où la transformation est exprimée avec les quaternions, la métrique de similarité est l'information mutuelle estimée dans une fenêtre de Parzen ; l'interpolation est tri-linéaire et l'optimisation est une descente de gradient.
- La méthode de recalage de surface présentée précédemment (identifiée par SBR, surface based registration). Celle-ci ne sera évaluée que pour le recalage thoracique.

Des tests d'hypothèse ont été définis pour répondre statistiquement à la question : La méthode X permet-elle de recaler des images IRM et TEP du thorax/cœur avec une précision inférieure ou égale à la taille du voxel TEP ?

Pour le recalage d'images de thorax, les méthodes IMP, HMR+IM, HMR+RC sont les plus précises. Le test d'hypothèse rejette la méthode SBR (Précision de recalage attendue de 3.52 mm). Le temps de calcul est plus faible avec IMP compte tenu de l'utilisation des fenêtres de Parzen.

En ce qui concerne le recalage d'images de cœur normal et pathologique, on obtient les mêmes résultats (précision attendue de 2.43 mm) avec cependant la nécessité de définir un volume d'intérêt afin de réduire le domaine du recalage et de réorienter préalablement les images TEP compte tenu de l'orientation des images IRM en petit axe pour parvenir à des résultats (Figure 34). La méthode HMR+CC ne satisfait pas les tests statistiques.

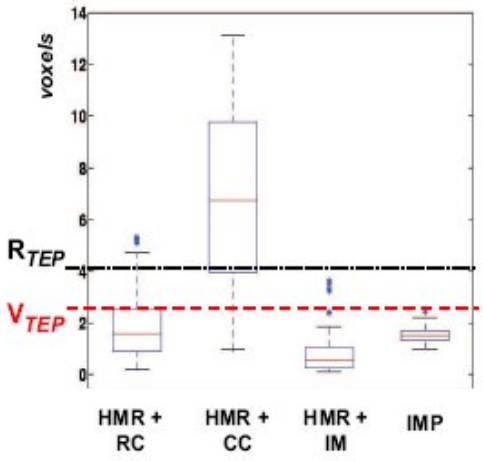


*Figure 34. Résultat de l'évaluation de la précision de la méthode de recalage HMR pour 3 mesures de similarité et de la méthode IMP pour la mise en correspondance d'images par RM et TEP de coeur. L'erreur RMS exprimée en mm est portée en ordonnée. La taille du voxel et la résolution physique de la caméra TEP sont respectivement égales à 2.43mm et 4.1mm.*

Plus largement, la problématique d'évaluation de méthodes est au cœur des recherches que j'anime au sein de l'Action Spécifique du CNRS 'ICoMIM' (Intégration de Connaissances et Modélisation en Imagerie Médicale) [70].

**Bibliographie :**

- Revues à comité de lecture

T. Mäkelä, O. Sipilä, P. Clarysse, N. Pauna, Q.-C. Pham, T. Katila, and I. E. Magnin, "A review of cardiac registration methods," *IEEE Transactions on Medical Imaging*, vol. 21, N°9, pp. 1011-1021, 2002.

T. Mäkelä, Q. C. Pham, P. Clarysse, J. Nenonen, J. Lötjönen, O. Sipilä, H. Hänninen, K. Lauerma, J. Knutti, T. Katila, and I. E. Magnin, "A 3D model-based registration approach for the PET, MR and MCG cardiac data fusion, Medical Image Analysis," *Medical Image Analysis*, vol. 7, pp. 377-389, 2003.

- Articles longs de congrès

T. Mäkelä, P. Clarysse, J. Lötjönen, O. Sipilä, H. Hänninen, J. Nenonen, K. Lauerma, J. Knuuti, T. Katila, and I. E. Magnin, "A method for registration of cardiac Magnetic Resonance and Positron Emission Tomography images for assessing myocardial viability," in *Understanding Cardiac Imaging Techniques from Basic Pathology to Image Fusion*, vol. 332, *NATO Science Series - Life and Behavourial Sciences*, P. Marzullo, Ed., Proceedings of the NATO Advanced Research Workshop on Understanding Cardiac Imaging Techniques : From Basic Pathology to Image Fusion ed. Pisa, Italy: IOS Press, 2001, pp. 155-165.

T. Mäkelä, Q.-C. Pham, P. Clarysse, J. Lötjönen, K. Lauerma, H. Hänninen, J. Knuuti, T. Katila, and I. E. Magnin, "A 3-D model-based approach for the PET-functional and MR-anatomical cardiac imaging data fusion," Springer, Lecture Notes In Computer Science, vol. 2230, Functional Imaging and Modeling of the Heart (FIMH'01), Helsinki, Finland, pp. 83-90, 2001.

N. Pauna, P. Croisille, N. Costes, A. Reilhac, T. Mäkelä, O. Cozar, M. Janier, and P. Clarysse, "A strategy to quantitatively evaluate MRI/PET cardiac rigid registration methods using a Monte Carlo simulator," Springer, Lecture Notes in Computer Science, vol. 2674, Functional Imaging and Modeling of the Heart (FIMH'03), Lyon, France, pp. 194-204, 2003.

M. Pollari, J. Lötjönen, T. Mäkelä, N. Pauna, A. Reilhac, and P. Clarysse, "Evaluation of cardiac PET-MRI registration methods using a numerical breathing phantom," IEEE International Symposium on Biomedical Imaging (ISBI), Arlington, VA, USA, pp. 1447-1450, 2004.

- Thèses

T. Mäkelä, "Data registration and fusion for cardiac applications," PhD thesis Helsinki University of Technology, Espoo, 2003.

T. Mäkelä, "Mise en correspondance en imagerie cardiaque multimodale: vers un modèle anatomo-fonctionnel individualisé du coeur," thèse de Doctorat *CREATIS*, Institut National des Sciences Appliquée, Lyon, 119p, 2004.

N. Pauna, "Evaluation des méthodes de mise en correspondance en imagerie multimodale IRM/TEP thoracique et cardiaque," thèse de Doctorat *CREATIS,* Université Claude Bernard Lyon 1, Lyon, 123p, 2004.

# 5. PROJET DE RECHERCHE

## 5.1. COMMENTAIRES PRELIMINAIRES

L'imagerie rapide pour l'étude de la dynamique des organes est en plein essor actuellement. En IRM, la qualité et la rapidité d'obtention des images par les séquences dynamiques les plus récentes ont ainsi considérablement augmenté en une dizaine d'années et 2 générations successives d'imageurs. Les dernières séquences IRM de marquage tissulaire présentent ainsi un marquage persistant et fin tout en permettant d'acquérir davantage de phases du cycle cardiaque dans un temps d'examen plus réduit (Figure 35). Des évolutions sont encore à attendre même si des compromis restent nécessaires entre la vitesse d'acquisition et le rapport signal à bruit ou le risque d'artefacts [91]. La versatilité de l'IRM permet d'étudier de multiples aspects de l'anatomie et de la fonction cardiaque et vasculaire: anatomie du cœur et des vaisseaux (angiographie par RM 3D), fonction contractile (séquence ciné TrueFISP en apnée ou en respiration libre avec post-synchronisation respiratoire et cardiaque), perfusion, viabilité avec les séquences de rehaussement tardif pour la détection des régions nécrosées. Les récents tomodensitomètres à rayons X multi-détecteurs permettent également l'analyse précise de l'anatomie cardiaque et de la fonction contractile myocardique et même, cela reste encore à démontrer, de la perfusion [38]. L'imagerie isotopique et l'imagerie ultrasonore offrent aussi des alternatives intéressantes. Les outils de post-traitement sont cependant un élément déterminant pour l'exploitation quantitative des images.

Néanmoins, le transfert dans un contexte de recherche médicale et/ou clinique des outils de post-traitement développés est un processus long et difficile principalement pour les raisons suivantes :

1. L'intérêt et les apports de l'outil doivent être démontrés à la fois au niveau scientifique et médical (recherche médicale et/ou clinique)
2. L'utilisation effective repose sur la confiance attribuée par le clinicien dans l'outil. Cette confiance repose généralement sur une validation menée conjointement par le binôme (médecin-ingénieur) à partir de données issues d'un protocole de recherche clinique
3. L'outil doit pouvoir être utilisé par le partenaire médical sans connaissances approfondies des méthodes, de l'informatique…

Une plus large diffusion dans un cadre industriel, par exemple, requiert une certification par un organisme (Normes ISO).

Les contributions apportées jusqu'à présent sont d'ordre méthodologique mais elles sont motivées par les problèmes pratiques posés par l'exploitation raisonnée des informations portées par les images. Jusqu'à présent, nous pensons avoir démontré la pertinence et l'intérêt des méthodes développées, comme la méthode GDE de segmentation par modèle a priori, l'ACPF pour l'analyse de paramètres cardiaques et les techniques de recalage multi-modalités. Chacune constitue un élément qui participe à l'édification d'un *modèle intégratif anatomique et fonctionnel du cœur* auquel nous aspirons. Il est désormais possible d'obtenir une quantification de la déformation segmentaire en 3D et au cours du cycle cardiaque grâce à la technique d'IRM de marquage tissulaire, en particulier, à la condition de disposer des programmes de post-traitement ad-hoc.

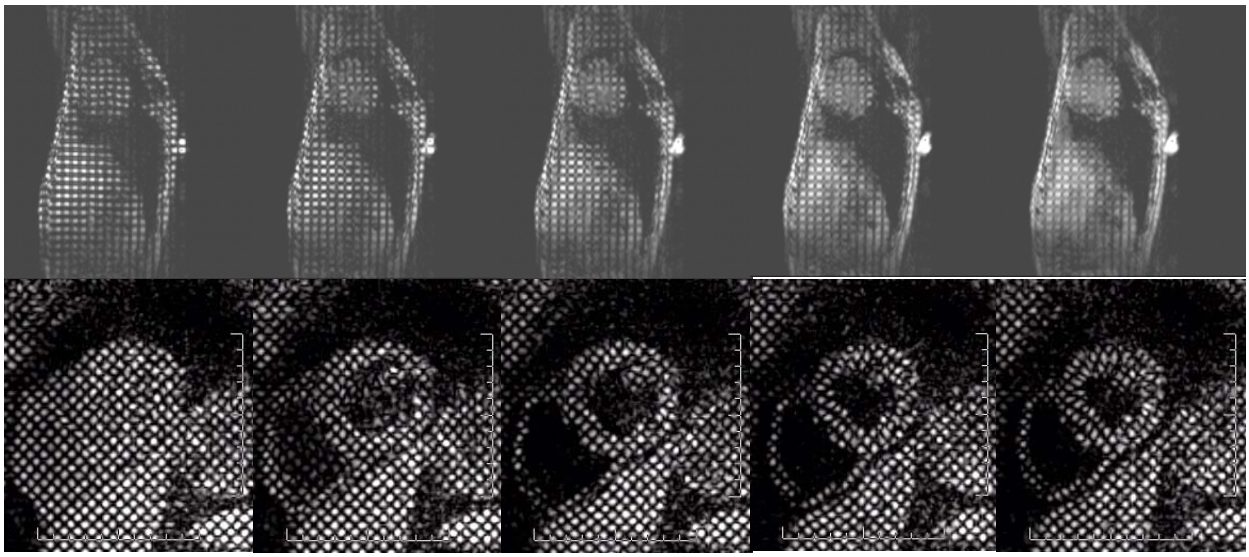

*Figure 35. Ligne du haut : Série de 5 images par RM obtenues sur un imageur Siemens 1.5T de la précédente génération avec des séquences en écho de gradient et un motif de marquage SPAMM en grille. Ligne du bas : Série d'images acquise avec une nouvelle séquence CSPAMM spiral [29] .*

### 5.2. PROJET DE RECHERCHE : ANALYSE INDIVIDUALISEE EN IMAGERIE ANATOMIQUE ET FONCTIONNELLE CARDIOVASCULAIRE ASSISTEE PAR LES MODELES

Notre objectif est de développer les méthodes conduisant à l'analyse individualisée des données anatomiques et fonctionnelles du système cardiovasculaire à partir d'une imagerie multi-modalités (Figure 36). Ces méthodes reposent sur un modèle générique du thorax et de ses principales structures intégrant des données *a priori* anatomiques et fonctionnelles du cœur et des vaisseaux (Figure 37). On considère ainsi une hiérarchie de modèles anatomo-fonctionnels. Nos travaux les plus récents en recalage d'images multi-modalités ont montré, en statique, ce à quoi un tel modèle pouvait ressembler (voir section 4.3). Les modalités considérées en premier lieu sont l'IRM, la TEP et la MCG mais d'autres modalités plus répandues comme l'échocardiographie et la TESP ne sont pas exclues.

L'enjeu majeur concerne :

1. la construction d'un *modèle anatomique du système cardiovasculaire* plus complet, intégrant les 4 cavités cardiaques, les principaux gros vaisseaux et les coronaires, la prise en compte des caractéristiques structurelles des tissus myocardiques comme l'architecture fibreuse du myocarde. L'environnement du cœur peut également être considéré par la connexion avec un modèle anatomique du thorax et de ses structures.
2. l'intégration dans ces modèles d'informations fonctionnelles, relatives à la physiologie du cœur : mécanique de déformation du myocarde, perfusion myocardique et propagation du potentiel électrique d'activation de la contraction. Les modèles considèrent un niveau de description que l'on peut qualifier de *tissulaire* sur une échelle allant de la molécule à l'organe.
3. Les méthodes d'individualisation du modèle anatomo-fonctionnel ainsi constitué aux données multi-modalités acquises. Cette étape conduit au calcul de paramètres quantitatifs spatio-temporels des fonctions cardiaques étudiées pour le patient considéré. Il s'agit d'un *problème inverse.*

Un tel outil permettra dans un contexte clinique de mieux appréhender et synthétiser l'état fonctionnel du cœur de chaque patient à partir de la somme considérable de données multi-modalités enregistrées que l'on souhaite pleinement exploiter. La fonction mécanique sera considérée en premier lieu.

## 1. Dynamique cardiaque

Compte tenu de nos précédents développements, le modèle GDE constitue une base intéressante sur laquelle construire notre modèle générique. Du point de vue de l'anatomie cardiaque, le modèle bi-ventriculaire a été étendu à 4 cavités et inclus l'abouchement des principaux vaisseaux et les branches principales des coronaires (Figure 37(b) et Figure 38). Nous cherchons également à lui associer l'information sur la structure fibreuse du myocarde. Nous proposons ensuite d'étendre le modèle GDE par la prise en compte explicite de la dimension temporelle (3D+temps). Les données d'entrée sont des séquences anatomiques 3D+temps et/ou des séquences IRM de marquage tissulaire. Ceci peut s'envisager en considérant le flux de la fonction intensité des images au cours de la séquence toujours dans un cadre de déformation élastique linéaire ou non-linéaire (travaux en collaboration avec le laboratoire de Mathématiques Appliquées de Lyon, MAPLY). Ce travail est le thème de recherche de la thèse de J. Shaerer (1ère année). Le modèle GDE peut s'appliquer à la segmentation d'autres structures dans d'autres modalités. Nous explorons ses potentialités dans le cadre de la segmentation de données ultrasonores 3D (collaboration avec Didier Vray, Creatis) et sur des données TEP cardiaques.

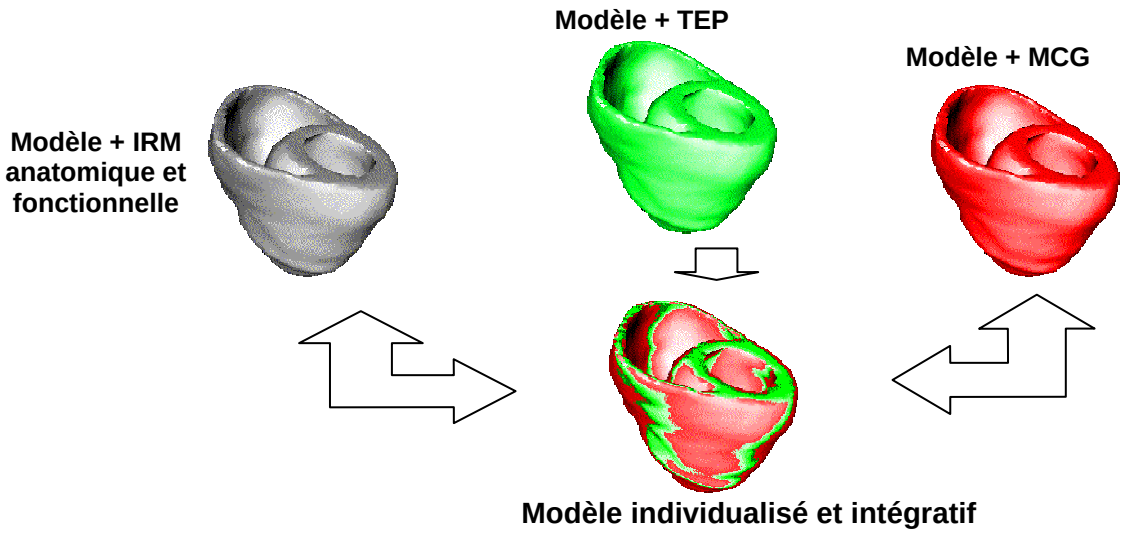


*Figure 36. Modèle individualisé intégrant les informations anatomiques et fonctionnelles en provenance des différentes modalités d'imagerie*

(a) (b)

*Figure 37. Modèles de thorax (Collaboration Lab. Biomedical Engineering, HUT, Finland) (a) et de cœur, vaisseaux et coronaires (b) issus de données de référence acquises en IRM (Creatis, Lyon)*

Parallèlement, des travaux menés dans le cadre du stage post-doctoral de Julien Milles (Bourse Internationale de Recherche de la Région Rhône-Alpes, 2003-2004) s'appuient sur le même modèle pour la segmentation du cœur dans des séquences d'IRM de marquage tissulaire et sur une technique d'estimation de mouvement de type fréquentiel ne nécessitant pas l'extraction du motif de marquage. Cette dernière, assez proche de la méthode IRM-HARP, a été développée par le Professeur Theo Arts (CARIM, Maastricht University) avec qui nous avons collaboré dans le cadre du post-Doctorat. Les premiers résultats très intéressants ont été présentés à ISBI'04 [107]. Ceci permet d'envisager une analyse de la déformation myocardique avec très peu d'intervention humaine et en un temps réduit. Le calcul des paramètres quantitatifs de mouvement et la construction des cartographies associées sont en cours dans le cadre d'un stage de Master.

L'estimation conjointe formes/mouvement dans des séquences d'images est étudiée également par B. Delhay (2$^{ième}$ année de thèse) par des techniques de mise en correspondance d'images non-rigide 3D+temps. Dans ce cadre, la dimension temporelle est considérée différemment des dimensions spatiales par l'introduction de contraintes spécifiques traduisant la continuité et la périodicité et certaines informations a priori disponibles. Des résultats très préliminaires ont été présentés à ICIP'2004 [108]. Un contexte différent de ces développements concerne la reconstruction d'images avec compensation de mouvement en tomographie dynamique du thorax et du cœur [109, 110] (Collaboration initiée avec le CEA-LETI). En effet, la technique pourrait être utilisée pour fournir les estimées de mouvement nécessaires à l'algorithme de reconstruction d'images en vue d'améliorer la qualité des images en limitant l'effet des artefacts cinétiques. Un autre domaine d'application est la radiothérapie des structures thoraciques qui devrait bénéficier des techniques de compensation de mouvement pour améliorer le traitement des zones tumorales en épargnant le plus possible les structures saines environnantes. Cet aspect sera considéré dans le groupe de recherche en Image et Modélisation pour la radiothérapie et l'hadronthérapie (RIME, David Sarrut, CLB, LIRIS, IPNL, Creatis) en cours de constitution.

### 2. Intégration d'information multi-modalités

Plus largement, les méthodes développées visent à intégrer dans un même modèle de référence les informations issues d'une imagerie multi-modalités. Ainsi, d'autres informations fonctionnelles pourraient faire l'objet d'une intégration dans le modèle comme des données

d'IRM de rehaussement tardif, des données métaboliques issues d'acquisitions en TEP dynamiques, des données de l'activité électro-magnétique de la MCG, au travers de notre collaboration avec la finlande. Cette intégration doit s'appuyer sur le modèle générique de GDE dynamique associé à des techniques de mise en correspondance spécifiques à chaque modalité.

### 3. Evaluation des méthodes

R. Haddad (thèse, 3ième année) construit actuellement un modèle anthropomorphique de cœur battant destiné à constituer une référence pour évaluer les méthodes de segmentation, de recalage et d'estimation de mouvement développées. Ce modèle est constitué d'une représentation géométrique des principales structures cardiaques (Ventricules gauche et droit, oreillettes gauche et droite, péricarde) et vasculaires (abouchement des principales veines et artères, réseau des coronaires) (Figure 38), des images natives ayant servis à la définition de ces structures et d'un modèle de mouvement identifié à partir des images. Il est construit à partir d'acquisitions en IRM 3D et ciné sur un même volontaire sain. Un modèle multimodal via des simulations de différentes modalités d'imagerie est aussi envisageable et constituerait la version dynamique du modèle précédemment présenté pour l'évaluation de méthodes de recalage TEP-IRM (section 4.3). Dans ce but, les structures thoraciques (cage thoracique, poumons, diaphragme) doivent être également prises en compte dans le modèle.

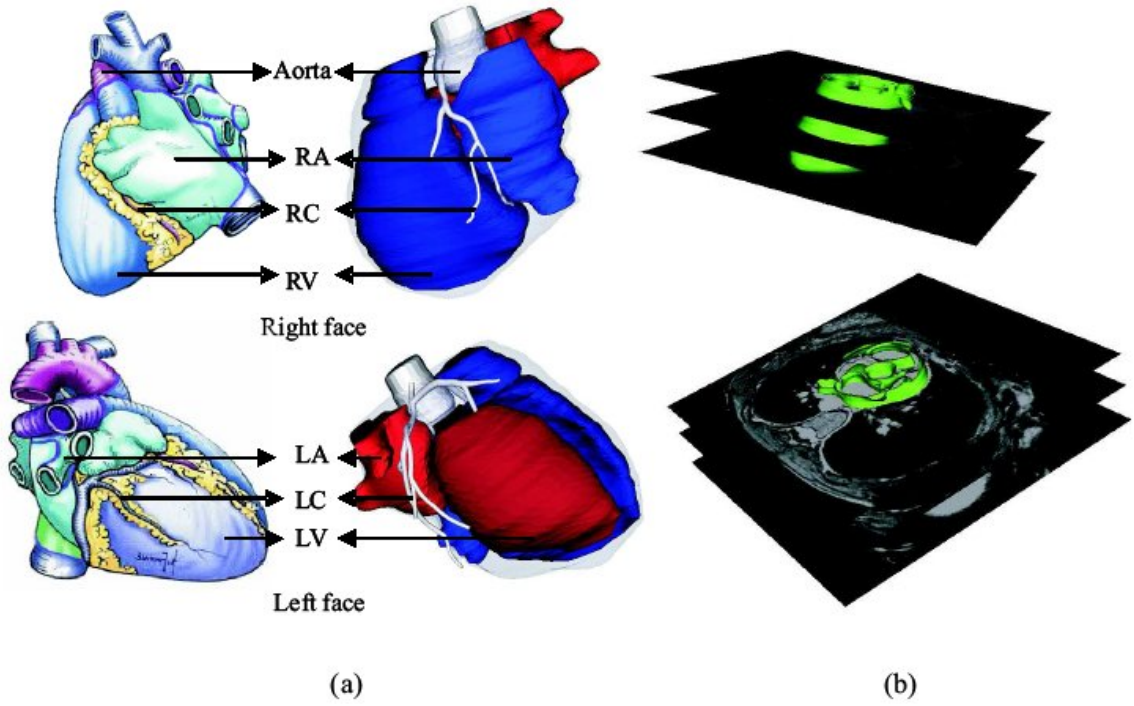


*Figure 38. Modèle anatomique de cœur. (a) correspondance du modèle avec un atlas anatomique. (b) Le modèle plongé dans les images par RM natives.*

## 5.3. LES ATOUTS ET LES MOYENS

### b. Plateau d'imagerie Lyonnais

Nous disposons à Lyon d'un plateau d'imagerie très riche composé entre autres de 2 IRM cliniques et d'une IRM destinée à la recherche. Ces imageurs sont récents et dotés des séquences IRM les plus performantes pour l'étude de la fonction et de la perfusion myocardiques, notamment. On dispose également d'une caméra TEP (CERMEP) et

d'échographes de dernière génération. La plateforme Animage permet d'envisager de réaliser le même type de traitements sur le petit animal.

### c. Partenariat et collaborations

L'ampleur de ce projet requiert l'implication d'une équipe pluri-displinaire de chercheurs et de doctorants, la continuité des partenariats en cours et l'établissement de nouvelles collaborations.

*Au niveau local*

Le projet concerne directement le thème SDV 'Athérosclérose et conséquences: Ischémie Myocardique' à Creatis. La problématique d'estimation de mouvement dans des séquences d'images est aussi un sujet central dans le thème STIC « Imagerie dynamique » à Creatis. Des travaux sont menés sous la direction de Denis Friboulet pour l'estimation du mouvement du cœur dans des séquences ultrasonores. Du fait des spécificités de cette modalité, les techniques employées sont différentes mais ils existent des points communs qui justifient une interaction. Au sein de l'équipe, de nombreux développements ont portés sur l'extraction d'arborescences vasculaires (Maciej Orkisz) et sur le calcul de cartographies de perfusion (Bruno Neyran) qui seront exploités dans le cadre du projet. Nous collaborons avec le Laboratoire de Mathématiques Appliquées de Lyon (MAPLY, CNRS UMR 5585) en mécanique des milieux continus. Au niveau Lyonnais, des collaborations sont envisagées avec l'Institut de Médecine Théorique (IMTH, HCL Lyon).

*Au niveau national et international*

Au niveau national et international, nous pouvons compter sur les relations établies dans le cadre des différents projets auxquels nous avons pris part : Action incitative inter GDR-PRC « Cœur battant » du CNRS (1998-2001), préparation du Réseau d'Excellence Européen 'e-heart' soumis en 2003 dans le cadre du 6$^{ème}$ PCRD. Pour les partenariats actuels, un Programme International de Coopération Scientifique du CNRS (PICS n°1932, 2002-2005) est en cours avec nos partenaires finlandais sur le thème 'Modélisation individualisée 4D de l'anatomie et de la fonction cardiaque à partir d'une imagerie multi-modalités'. Il nous a permis d'aboutir à la version 'statique' du modèle d'intégration. Nous collaborons également avec l'équipe de Théo Arts à l'Université de Maastricht sur l'analyse de la mécanique cardiaque en IRM de marquage tissulaire. Par ailleurs, nous sommes partenaires du projet CardioSense3D : Patient-specific Cardiac Simulation (suite du projet ICEMA, Images of Cardiac Electro-Mechanical Activity) de l'INRIA.

### d. Mise à disposition des méthodes

*Plateforme logicielle*

Un logiciel d'analyse d'images cardiaques est en cours de développement (B. Regrain, IE CNRS) à partir de la plate-forme logicielle commune du laboratoire (CreaTools). Basé sur un navigateur de fichiers DICOM, Il est destiné à recevoir les développements relatifs à l'estimation de la perfusion et de la fonction contractile en premier lieu. Un tel logiciel doit permettre une homogénéisation et la pérennisation des codes, une mise à disposition plus rapide des nouveaux développements et leur démonstration. Mais cet outil devrait également faciliter l'interaction avec les partenaires médicaux et les évaluations de méthodes.

*Grilles de calcul*

Par ailleurs, la lourdeur de certains calculs rend impossible la restitution de résultats dans des temps compatibles avec la routine clinique. C'est pourquoi nous réalisons le portage de certaines applications sur des architectures de ferme de PC et de grille de calcul. C'est le cas notamment pour le modèle GDE pour lequel la segmentation d'une phase demande environ 3 minutes sur un PENTIUM M à 1.7GHz et le traitement de dix phases demande près d'une demi-heure. Le recours à des fermes de PC ou aux grilles de calcul devrait réduire significativement le temps de calcul. Cela permettra également une mise à disposition des méthodes plus large et permettra leur évaluation à plus grande échelle. L'implantation de la segmentation d'images cardiaques sur grilles de calcul est réalisée dans le cadre de l'ACI « Analyse Globalisée des données d'imagerie radiologique » (AGIR, http://www.aci-agir.org/) du ministère. La segmentation est également une des applications portée sur la grille de calcul du projet Européen EGEE (Enabling Grids for E-sciencE, http://public.eu-egee.org/).

**Bibliographie en cours:**

- Revues avec comité de lecture


Pham, Q.-C., Vincent, F., Clarysse, P., Pousin, J., Croisille, P., Katila, T. and Magnin, I.E. Segmentation and tracking of the heart ventricles from MRI using a 3D elastic active region model, en révision pour *IEEE Trans. Med. Imaging*.

Pauna N., Croisille P., Costes N., Reilhac A., Mäkelä T., Janier M., Clarysse P., A rigorous strategy to quantitatively evaluate MR/PET thorax/cardiac rigid registration methods using a Monte Carlo simulator, en révision pour *IEEE Trans. Med. Imaging*

Clot D., Croisille P., Clarysse P., Functional data analysis of spatio-temporal deformation parameters derived from tagged MRI, en préparation pour *IEEE Trans. Biomed. Eng.*

Milles J., Clarysse P., Arts T., van Susteren A., Croisille P., Stuber M., Magnin I.E., Automated 2D segmentation of the left ventricle in cardiac tagged MRI using image and displacement information, en preparation pour MEDIA.


- Articles longs de congrès


Germain C., Breton V., Clarysse P., Gaudeau Y., Glatard T., Jeannot E., Legré Y., Loomis C., Montagnat J., Moureaux J-M., Osorio A., Pennec X., Texier R., Grid-enabling medical image analysis, accepté à BIOGRID'05.

Rana Haddad, Patrick Clarysse, Maciej Orkisz, Pierre Croisille, Didier Revel, Isabelle E. Magnin, A realistic anthropomorphic numerical model of the beating heart, accepté à FIMH'05.

Bertrand Delhay, Patrick Clarysse, Jyrki Lötjönen, Toivo Katila and Isabelle E. Magnin, Evaluation of two free form deformation based motion estimators in cardiac and chest imaging, accepté à FIMH'05.


- Thèses en cours

R. Haddad, "Modèle Dynamique Anthropomorphique de Cœur Battant", 3ème année

B. Delhay, "Segmentation et suivi de mouvement dans des séquences temporelles d'images", 2ème année

J. Schaerer, "Segmentation spatio-temporelle par modèle déformable 3D+temps", 1ère année

# 6. CONCLUSION

Après avoir introduit le contexte de nos recherches et mis en évidence les difficultés, nous avons présenté une sélection de nos contributions dans le domaine de l'analyse d'images cardiaques. Les publications associées sont disponibles en fin de ce mémoire. Ces travaux sont pour la plupart le fruit d'une recherche commune dans le cadre de co-encadrements de thèses (au nombre de cinq soutenues, et trois en cours). Nous pensons avoir acquis au cours de ces années une expérience et des connaissances pluridisciplinaires dans ce contexte. Notre objectif est de parvenir à une meilleure diffusion de ces développements et de systématiser leur évaluation par une approche rigoureuse. L'imagerie cardiaque est un domaine extrêmement riche en problématiques cliniques et fondamentales. D'un point de vue technologique, l'évolution importante, ces dernières années, des systèmes d'acquisition permet d'envisager des progrès considérables dans la compréhension des phénomènes physio-pathologiques et une meilleure prise en charge des pathologies cardiaques. L'analyse quantitative des informations complémentaires obtenues requiert cependant le développement parallèle de méthodes de post-traitement. Le champ reste encore très ouvert pour parvenir à une exploitation exhaustive et utile, aussi bien en recherche médicale qu'en clinique, de toute l'information disponible. Mais le succès d'une telle entreprise requiert nécessairement une collaboration étroite entre les diverses spécialités impliquées : physiciens de l'imagerie, cardiologues, radiologues et physiologistes, spécialistes du traitement du signal et des images, mathématiciens de la modélisation, principalement.

# 7. BIBLIOGRAPHIE


[1] C. Boesch, "The 2003 Nobel Prize for MRI: significance and impact," *Journal of Magnetic Resonance Imaging*, vol. 19, pp. 177-179, 2004.

[2] A. N. Mazzadi, "Apport de l'imagerie fonctionnelle à l'étude des couplages entre la perfusion, le métabolisme glucidique et la fonction contractile dans l'ischémie myocardique," PhD thesis, Claude Bernard - Lyon 1, 136p, 2003.

[3] P. Takala, "Cardiac exercise studies with bioelectromagnatic mapping," PhD thesis, Helsinki University of Technology, Espoo, p, 2001.

[4] H. Hänninen, P. Takala, M. Mäkijärvi, J. Montonen, P. Korhonen, L. Oikarinen, K. Simelius, J. Nenonen, T. Katila, and L. Toivonen, "Recording locations in multichannel magnetocardiography and body surface potential mapping sensitive for regional exercise-induced ischemia," *Basic Research in Cardiology*, vol. 96, pp. 405-414, 2001.

[5] B. Neyran, M. Janier, C. Casali, D. Revel, and E. Canet-Soulas, "Mapping myocardial perfusion with intravascular MR contrast agent: robustness of deconvolution methods at various blood flows," *Magnetic Resonance in Medecine*, vol. 48, N° 1, pp. 166-179, 2002.

[6] S. Carme, "Modélisation de la perfusion quantitative en Imagerie par Resonance Magnétique (IRM) cardiaque *in-vivo*," PhD thesis, Institut National des Sciences Appliquées, Lyon, 258p, 2004.

[7] N. M. Wilke, M. Jerosch-Herold, A. Zenovich, and A. E. Stillman, "Magnetic resonance first-pass myocardial perfusion imaging: clinical validation and future applications," *Journal of Magnetic Resonance Imaging*, vol. 10, pp. 676-685, 1999.

[8] J. Barkhausen, P. Hunold, M. Jochims, and J. F. Debatin, "Imaging of myocardial perfusion with magnetic resonance," *Journal of Magnetic Resonance Imaging*, vol. 19, pp. 750-757, 2004.

[9] M. Jerosch-Herold, R. T. Seethamraju, C. M. Swingen, N. M. Wilke, and A. E. Stillman, "Analysis of myocardial perfusion MRI," *Journal of Magnetic Resonance Imaging*, vol. 19, pp. 758-770, 2004.

[10] R. Tennant and C. J. Wiggers, "The effect of coronary occlusion on myocardial contraction," *Am. J. Physiol.*, vol. 112, pp. 351--361, 1935.

[11] D. Friboulet, "Analyse d'Images et modélisation en imagerie cardiaque," PhD thesis, Université Claude Bernard Lyon 1, Institut National des Sciences Appliquées, Lyon, HDR, 111p, 2001.

[12] E.-P. d'Alché, *Comprendre La physiologie cardiovasculaire*. Paris: Flammarion, 1999.

[13] A. F. Frangi, W. J. Niessen, and M. A. Viergever, "Three-Dimensional modeling for functional analysis of cardiac images, a review," *IEEE Transactions on Medical Imaging*, vol. 20, N° 1, pp. 2-25, 2001.

[14] U. Sigwart and P. H. Heintzen, "Ventricular Wall Motion," in *International Symposium Lausanne*. Stuttgart, New York: Georg Thieme Verlag, 1984, pp. 327.

[15] G. B. J. Mancini, S. F. DeBoe, E. Anselmo, S. B. Simon, M. T. LeFree, and R. A. Vogel, "Quantitative regional curvature analysis : An application of shape determination for the assessment of segmental left ventricular function in man," *Am. Heart J.*, vol. 113, N° 2, pp. 326-334, 1987.

[16] J. S. Duncan, F. A. Lee, A. W. M. Smeulders, and B. L. Zaret, "A Bending Energy Model for Measurement of Cardiac Shape Deformity," *IEEE Transactions on Medical Imaging*, vol. 10, N° 3, pp. 307-320, 1991.

[17] P. Shi, A. Sinusas, R. T. Constable, E. Ritman, and J. S. Duncan, "Point-tracked quantitative analysis of LV motion from 3D image sequences," *IEEE Transactions on Medical Imaging*, vol. 19, N° 1, pp. 36-50, 2000.

[18] C. Nastar and N. Ayache, "Frequency-based nonrigid motion analysis : application to four dimensional medical images," *IEEE Transactions on Pattern Analysis and Machine Intelligence*, vol. 18, N° 11, pp. 1067-1079, 1996.

[19] P. Clarysse, D. Friboulet, and I. E. Magnin, "Tracking geometrical descriptors on 3-D deformable surfaces: application to the left-ventricular surface of the heart," *IEEE Transactions on Medical Imaging*, vol. 16, N° 4, pp. 392-404, 1997.

[20] E. L. Ritman, R. A. Robb, and L. D. Harris, *Imaging Physiological Functions: Experience with the Dynamic Spatial Reconstructor*. New York: Praeger, 1985.

[21] R. R. Robb, *Three dimensional biomedical imaging*, vol. I. Tomography. Boca Raton, Florida: CRC Press, 1985.

[22] S. Pujadas, G. P. Reddy, O. Weber, J. J. Lee, and C. B. Higgins, "MR Imaging assessment of cardiac function," *Journal of Magnetic Resonance Imaging*, vol. 19, pp. 789-799, 2004.
[23] A. Planat, "Estimation de Mouvement par Maillage Actif Multiéchelle avec Prise en Compte des Discontinuités: Application à l'Imagerie Cardiaque en Résonance Magnétique," PhD thesis, CREATIS, INSA de Lyon, 201p, 1999.
[24] S. Benayoun and N. Ayache, "Dense non-rigid motion estimation in sequences of medical images using differential constraints," *International Journal of Computer Vision*, vol. 26, N° 1, pp. 25-40, 1998.
[25] J. M. Gorce, D. Friboulet, and I. E. Magnin, "Estimation of three-dimensional cardiac velocity fields: Assessment of a differential method and application to 3D CT data," *Medical Image Analysis*, vol. 1, N° 3, pp. 245-261, 1997.
[26] E. A. Zerhouni, D. M. Parish, W. J. Rogers, A. Yang, and E. P. Shapiro, "Human heart: tagging with MR imaging - A method for noninvasive assessment of myocardial motion," *Radiology*, vol. 169, pp. 59-63, 1988.
[27] L. Axel and L. Dougherty, "Heart wall motion: improved method of spatial modulation of magnetization for MR imaging," *Radiology*, vol. 183, pp. 745-750, 1989.
[28] A. A. Amini and J. L. Prince *Measurement of cardiac deformations from MRI: physical and mathematical models*, vol. 23: Kluwer Academic Publishers, 2001.
[29] S. Ryf, K. V. Kissinger, M. A. Spiegel, P. Börnert, W. J. Manning, P. Boesiger, and M. Stuber, "Spiral MR myocardial tagging," *Magnetics Resonance Imaging*, vol. 51, pp. 237-242, 2004.
[30] N. F. Osman, W. S. Kerwin, E. R. McVeigh, and J. L. Prince "Cardiac motion tracking using CINE harmonic phase (HARP) magnetic resonance imaging," *Magnetic Resonance in Medecine*, vol. 42, N° 6, pp. 1048-1060, 1999.
[31] N. F. Osman, E. R. McVeigh, and J. L. Prince "Imaging heart motion using harmonic phase MRI," *IEEE Transactions on Medical Imaging*, vol. 19, N° 3, pp. 186-202, 2000.
[32] N. F. Osman and J. L. Prince "Visualizing myocardial function using HARP MRI," *Physics in Medicine and Biology*, vol. 45, N° 6, pp. 1665-1682, 2000.
[33] J. Garot, D. A. Bluemke, N. F. Osman, C. Rochitte, E. R. McVeigh, E. A. Zerhouni, J. L. Prince , and J. Lima, "Fast determination of regional myocardial strain fields from tagged cardiac images using harmonic phase (HARP) magnetic resonance imaging," *Circulation*, vol. 101, pp. 981-988, 2000.
[34] N. J. Pelc, R. J. Herfkens, A. Shimakawa, and D. R. Enzmann, "Phase contrast cine magnetic resonance imaging," *Magnetic Resonance Quaterly*, vol. 7, pp. 229-254, 1991.
[35] M. Markl, F. P. Chan, M. T. Alley, K. L. Wedding, M. T. Draney, C. J. Elkins, D. W. Parker, R. Wicker, C. A. Taylor, R. J. Herfkens, and N. J. Pelc, "Time-resolved three-dimensional phase-contrast MRI," *Journal of Magnetic Resonance Imaging*, vol. 17, pp. 499-506, 2003.
[36] R. D. White, "MR and CT assessment for ischemic cardiac disease," *Journal of Magnetic Resonance Imaging*, vol. 19, pp. 659-675, 2004.
[37] K. Saito, M. Saito, S. Komatu, and K. Ohtomo, "Real-time four-dimensional imaging of the heart with multi-detector row CT," *Radiographics*, vol. 23, pp. e8-e11, 2003.
[38] Y. Koyama, T. Mochizuki, and J. Higaki, "Computed tomography assessment of myocardial perfusion, viability and function," *Journal of Magnetic Resonance Imaging*, vol. 19, pp. 800-815, 2004.
[39] D. Pellerin, O. Dubourg, D. Coisne, F. Extramania, S. Witchitz, and C. Veyrat, "Apport de l'imagerie doppler du myocarde pour l'étude des cardiomyopathies," *Archives des Maladies du Coeur et des Vaisseaux*, vol. 91, N° supplément, pp. 51-58, 1998.
[40] J. D'hooge, A. Heimdal, F. Jamal, T. Kukulski, B. Bijnens, F. Rademakers, L. Hatle, P. Suetens, and G. R. Sutherland, "Regional strain and strain rate measurements by cardiac ultrasound: principles, implementation and limitations," *European Journal Echocardiography*, vol. 1, pp. 154-170, 2000.
[41] E. D. Angelini, "Spatio-temporal analysis of three-dimensional real-time ultrasound for quantification of ventricular function," PhD thesis, Columbia University, 183p, 2003.
[42] C. Bonciu, R. Weber, and C. Léger, "4D reconstruction of the left ventricle during a single heart beat from ultrasound imaging," *Image and Vision Computing*, vol. 19, pp. 401-412, 2001.
[43] J. Kisslo, B. Firek, T. Ota, D. H. Kang, C. E. Fleishman, G. Stetten, J. Li, C. J. Ohazama, D. Adams, C. Landolfo, T. Ryan, and O. T. von Ramm, "Real-time volumetric echocardiography: the technology and the possibilities," *Echocardiography*, vol. 17.8, pp. 773-779, 2000.
[44] A. Fenster, D. B. Downey, and H. N. Cardinal, "Three-dimensional ultrasound imaging," *Physics in Medicine and Biology*, vol. 46, pp. R67-R99, 2001.

[45] G. E. Mailloux, F. Langlois, P. Y. Simard, and M. Bertrand, "Restoration of the velocity field of the heart from two-dimensional echocardiograms," *IEEE Transactions on Medical Imaging*, vol. 8, N° 2, pp. 143-153, 1989.
[46] P. Baraldi, A. Sarti, C. Lamberti, A. Prandini, and F. Sgallari, "Evaluation of differential optical flow techniques on synthesized echo images," *IEEE Transactions on Biomedical Engineering*, vol. 43, N° 3, pp. 259-272, 1996.
[47] S. Malassiotis and M. G. Strintzis, "Tracking the Left Ventricle in Echocardiographic Images by Learning Heart Dynamics," *IEEE Transactions on Medical Imaging*, vol. 18, N° 3, pp. 282-290, 1999.
[48] G. Jacob, J. A. Noble, C. Behrenbruch, A. D. Kelion, and A. P. Banning, "A shape-space-based approach to tracking myocardial borders and quantifying regional left-ventricular function applied in echocardiography," *IEEE Transactions on Medical Imaging*, vol. 21, N° 3, pp. 226-238, 2002.
[49] D. Comaniciu, X. S. Zhou, and S. Krishnan, "Robut real-time myocradial border tracking for echocardiography: An information fusion approach," *IEEE Transactions on Medical Imaging*, vol. 23, N° 7, pp. 849-860, 2004.
[50] F. Frouin, A. Delouche, H. Raffoul, H. Diebold, E. Abergel, and B. Diebold, "Factor analysis of the left ventricle by echocardiography (FALVE): a new tool for detecting regional wall motion abnormalities," *European Journal Echocardiography*, vol. 5, pp. 335-346, 2004.
[51] E. D. Angelini, A. Laine, S. Takuma, J. W. Holmes, and S. Homma, "LV volume quantification via spatio-temporal analysis of real-time 3D echocardiography," *IEEE Transactions on Medical Imaging*, vol. 20, N° 6, pp. 457-498, 2001.
[52] L. E. J. Thomson, R. J. Kim, and R. M. Judd, "Magnetic resonance imaging for the assessment of myocardial viability," *Journal of Magnetic Resonance Imaging*, vol. 19, pp. 771-788, 2004.
[53] T. Mäkelä, O. Sipilä, P. Clarysse, N. Pauna, Q.-C. Pham, T. Katila, and I. E. Magnin, "A review of cardiac image registration methods," *IEEE Transactions on Medical Imaging*, vol. 21, N° 9, pp. 1011-1021, 2002.
[54] C. A. R. Boyd and D. Noble, *The logic of life: the challenge of integrative Physiology*. New York: Oxford University Press, 1993.
[55] N. Ayache, *Special Volume: Computational Models for the Human Body*, vol. XII: Elsevier, 2004.
[56] J. B. Bassingthwaighte, "Strategies for the Physiome project," *Annals of Biomedical Engineering*, vol. 28, pp. 1043-1058, 2000.
[57] L. Glass, P. J. Hunter, and A. D. McCulloch, *Theory of Heart*. New York: Springer-Verlag, 1991.
[58] A. McCullough, J. B. Bassingthwaighte, P. J. Hunter, and D. Noble, "Computational biology of the heart: from structure to function," *Progress in Biophysics and Molecular Biology*, vol. 69, pp. 151-572, 1998.
[59] D. H. van Campen, J. M. Huyghe, P. H. M. Bovendeerd, and T. Arts, "Biomechanics of the heart muscle," *European J. Mechanics, A/Solids*, vol. 13, N° 4-suppl, pp. 19-41, 1994.
[60] F. B. Sachse, *Computational cardiology*: Springer, 2004.
[61] R. C. P. Kerckhoffs, P. H. M. Bovendeerd, J. C. S. Kotte, F. W. Prinzen, K. Smits, and T. Arts, "Homogeneity of cardiac contraction despite physiological asynchrony of depolarization: a model study," *Annals of Biomedical Engineering*, vol. 31, N° 5, pp. 536-547, 2003.
[62] P. J. Hunter, A. D. McCulloch, and H. E. D. J. ter Keurs, "Modelling the mechanical properties of cardiac muscle," *Progress in Biophysics and Molecular Biology*, vol. 69, pp. 289-331, 1998.
[63] J. M. Guccione, K. D. Costa, and A. D. McCulloch, "Finite element stress analysis of left ventricular mechanics in the beating dog heart," *Journal of Biomechanicss*, vol. 28, N° 10, pp. 1167-1177, 1995.
[64] J. S. Duncan, P. Shi, R. T. Constable, and A. Sinusas, "Physical and geometrical modeling for image-based recovery of left ventricular deformation," *Progress in Biophysics and Molecular Biology*, vol. 69, pp. 333-351, 1998.
[65] X. Papademetris, A. J. Sinusas, D. P. Dione, and J. S. Duncan, "Estimation of 3D left ventricular deformation from echocardiography," *Medical Image Analysis*, vol. 5, pp. 17-28, 2001.
[66] Q.-C. Pham, F. Vincent, P. Clarysse, P. Croisille, and I. E. Magnin, "A FEM-based deformable model for the 3D segmentation and tracking of the heart in cardiac MRI," vol. 2nd International Symposium on Image and Signal Processing and Analysis (ISPA 2001), Pula, Croatia, pp. 250-254, 2001.

[67] Q.-C. Pham, "Segmentation en imagerie cardiaque multimodale conduite par un modèle réaliste du cœur," PhD thesis, INPG, Grenoble, Signal-Image-Parole, 148p, 2002.
[68] M. Sermesant, C. Forest, X. Pennec, H. Delingette, and N. Ayache, "Deformable biomechanical models: application to 4D cardiac image analysis," *Medical Image Analysis*, vol. 7, pp. 475-488, 2003.
[69] M. Sermesant, "Modèle électromécanique du coeur pour l'analyse d'image et la simulation (Electromechanical Model of the Heart for Image Analysis and Simulation)," PhD thesis, Université de Nice Sophia Antipolis, p, 2003.
[70] P. Clarysse, F. Frouin, M. Garreau, A. Lalande, J. Rousseau, D. Sarrut, and C. Vasseur, "Intégration de Connaissances et Modélisation en Imagerie Médicale," *Innovations et Technologies en Biologie et Médecine - RBM*, vol. 25, pp. 139-149, 2004.
[71] Y. Bamberger, *Mécanique de l'Ingénieur II: Milieux déformable*. Paris: Hermann, 1981.
[72] J. Montagnat, H. Delingette, and N. Ayache, "A review of deformable surfaces: topology, geometry and deformation," *Image and Vision Computing*, vol. 19, N° 14, pp. 1023-1040, 2001.
[73] P. G. Ciarlet, *Elasticité tridimensionnelle*, vol. 1. Paris: Masson, 1985.
[74] F. Vincent, P. Clarysse, P. Croisille, and I. E. Magnin, "Segmentation et suivi de mouvement d'objets déformables par région active," vol. GRETSI'99, Vannes, France, pp. 163-166, 1999.
[75] F. Vincent, "Gabarits déformables élastiques pour la segmentation et le suivi de mouvement du cœur en Imagerie par Résonance Magnétique," PhD thesis, INSA LYON, Lyon, 120p, 2001.
[76] B. Faugeras and J. Pousin, "Variational asymptotic derivation of an elastic model arising from the problem of 3D automatic segmentation of cardiac images.," *Analysis and Applications*, vol. 2, N° 4, pp. 1-33, 2004.
[77] J. Pousin and Y. Rouchdy, "Constraint 3D Elastic Model for the segmentation in cardiac MRI," *CRAS*, pp. Submitted, 2004.
[78] D. Vray, A. Discher, J. Lefloc'h, W. Mai, P. Clarysse, Q. C. Pham, J. Montagnat, and M. Janier, "3D quantification of ultrasound images : application to mouse embryo imaging in vivo," IEEE International Ultrasonics Symposium, Munich, Germany, pp. 1557-1560, 2002.
[79] B. Qiu, P. Clarysse, J. Montagnat, M. Janier, and D. Vray, "Comparison of 3D deformable models for in vivo measurements of mouse embryo from 3D ultrasound images," IEEE International Ultrasonics Symposium, Montréal (Canada)2004.
[80] P. J. Besl and R. C. Jain, "Invariant surface characteristics for 3D object recognition in range images," *Computer Vision, Graphics and Image Processing: Graphical Models and Image Processing*, vol. 33, pp. 33-80, 1986.
[81] D. Friboulet, I. E. Magnin, C. Mathieu, A. Pommert, and K. H. Hoehne, "Assessment and visualization of the curvature of the left ventricle from 3D medical images," *Computerized Medical Imaging and Graphics*, vol. 17, N° 4/5, pp. 257--262, 1993.
[82] P. T. Sander and S. W. Zucker, "Inferring surface trace and differential structure from 3D images," *IEEE Transactions on Pattern Analysis and Machine Intelligence*, vol. 12, N° 9, pp. 833-854, 1990.
[83] J. J. Koenderink and A. J. van Doorn, "Surface shape and curvature scales," *Image and Vision Computing*, vol. 10, N° 8, pp. 557-565, 1992.
[84] C. Dorai and A. K. Jain, "COSMOS-A representation scheme for 3D free-form objects," *IEEE Transactions on Pattern Analysis and Machine Intelligence*, vol. 19, N° 10, pp. 1115-1130, 1997.
[85] C. Dorai and A. K. Jain, "Shape spectrum based view grouping and matching of 3D free-form objects," *IEEE Transactions on Pattern Analysis and Machine Intelligence*, vol. 19, N° 10, pp. 1139-1146, 1997.
[86] A. Matheny and D. B. Goldgof, "The use of three- and four-dimensional surface harmonics for rigid and non rigid shape recovery and representation," *IEEE Transactions on Pattern Analysis and Machine Intelligence*, vol. 7, N° 10, pp. 967-981, 1995.
[87] P. Clarysse, C. Basset, L. Khouas, P. Croisille, D. Friboulet, C. Odet, and I. E. Magnin, "Two-dimensional spatial and temporal displacement and deformation field fitting from cardiac magnetic resonance tagging," *Medical Image Analysis*, vol. 4, pp. 253-268, 2000.
[88] L. Khouas, P. Clarysse, D. Friboulet, and C. Odet, "Fast 2D vector field visualization using a 2D texture synthesis based on an autoregressive filter. Application to cardiac imaging," *Machine Graphics and Vision*, vol. 7, N° 4, pp. 751-764, 1998.

[89] P. Clarysse, L. Bracoud, P. Croisille, and I. E. Magnin, "Integrated Quantitative Analysis of Tagged Magnetic Resonance Images," Springer, vol. LNCS 2230, FIMH'01, Helsinky, Finland, pp. 69-75, 2001.
[90] F. Vincent, P. Clarysse, P. Croisille, and I. E. Magnin, "An elasticity-based region model and its application to the estimation of the heart deformation in tagged MRI.," vol. International Conference on Image Processing (ICIP), Vancouver, BC, Canada, pp. 629-632, 2000.
[91] L. Axel, A. Montillo, and D. Kima, "Tagged Magnetic Resonance Imaging of the Heart: A Survey," *Medical Image Analysis*, pp. To appear, 2005.
[92] M. Han, "Analyse exploratoire de la déformation spatio-temporelle du myocarde à partir de l'imagerie par résonance magnétique de marquage tissulaire," PhD thesis, Lyon, 201p, 1999.
[93] W. G. O'Dell, C. C. Moore, W. C. Hunter, E. A. Zerhouni, and E. R. McVeigh, "Three-dimensional myocardial deformations: calculation with displacement field fitting to tagged MR images," *Radiology*, vol. 195, N° 3, pp. 829-835, 1995.
[94] M. A. Guttman, E. A. Zerhouni, and E. R. McVeigh, "Analysis of cardiac function from MR Images," *IEEE Computer Graphics and Application*, vol. 17, N° 1, January-February, pp. 30-38, 1997.
[95] J. O. Ramsay and B. W. Silverman, *Functional Data Analysis*. New York: Springer, 1997.
[96] J. O. Ramsay and B. W. Silverman, *Applied functional data analysis*: Springer, 2002.
[97] P. Clarysse, M. Han, P. Croisille, and I. E. Magnin, "Exploratory analysis of the spatio-temporal deformation of the myocardium during systole from tagged MRI," *IEEE Transactions on Biomedical Engineering*, vol. 49, N° 11, pp. 1328-1339, 2002.
[98] D. Clot, "Méthodologie de fouille de données pour la modélisation dans les processus d'aide à la décision complexe - Application à l'analyse des paramètres de déformation du coeur," PhD thesis, Université Claude Bernard - Lyon 1, Lyon, Doctorat, 207p, 2002.
[99] C. Tilmant, "Estimation d'indices de contractilité myocardique par analyse d'images echocardiographiques," PhD thesis, Université Blaise Pascal, Clermont Ferrand, France, Doctorat, 205p, 2004.
[100] T. Mäkelä, Q. C. Pham, P. Clarysse, J. Nenonen, J. Lötjönen, O. Sipilä, H. Hänninen, K. Lauerma, J. Knutti, T. Katila, and I. E. Magnin, "A 3D model-based registration approach for the PET, MR and MCG cardiac data fusion," *Medical Image Analysis*, vol. 7, N° 3, pp. 377-389, 2003.
[101] J. Lötjönen, P.-J. Reissman, I. E. Magnin, and T. Katila, "Model extraction from Magnetic Resonance volume data using the deformable pyramid," *Medical Image Analysis*, vol. 3, N° 4, pp. 387-406, 1999.
[102] T. Mäkelä, "Mise en correspondance en imagerie cardiaque multimodale: vers un modèle anatomo-fonctionnel individualisé du coeur," PhD thesis, Institut National des Sciences Appliquées de Lyon, Lyon, 119p, 2004.
[103] N. Pauna, "Evaluation des méthodes de mise en correspondance en imagerie multimodale IRM/TEP thoracique et cardiaque," PhD thesis, Université Claude Bernard Lyon 1, Lyon, 123p, 2004.
[104] J. Nenonen, K. Pesola, H. Hänninen, K. Lauerma, P. Takala, T. Mäkelä, M. Mäkijärvi, J. Knutti, L. Toivonen, and T. Katila, "Current-density estimation of exercise-induced ischemia in patients with multivessel coronary artery disease," *Journal of Electrocardiology*, vol. 34, N° Supplement, pp. 37-42, 2001.
[105] T. Mäkelä, "Data registration and fusion for cardiac applications," PhD thesis, Helsinki University of Technology, Espoo, p, 2003.
[106] A. Reilhac, C. Lartizien, N. Costes, S. Sans, C. Comtat, R. N. Gunn, and A. C. Evans, "PET-SORTEO: A Monte Carlo-based simulator with high count rate capabilities," *IEEE Transactions on Nuclear Science*, vol. 51, N° 1, pp. 46–52, 2004.
[107] J. Milles, P. Clarysse, A. van Susteren, P. Croisille, I. E. Magnin, and T. Arts, "Automatic 2D segmentation of the left ventricle in tagged cardiac MRI using motion information," vol. IEEE International Symposium on Biomedical Imaging (ISBI), Arlington, VA, USA, pp. 153-156, 2004.
[108] B. Delhay, P. Clarysse, S. Bonnet, P. Grangeat, and I. E. Magnin, "Combined 3D object motion estimation in medical sequences," vol. International Conference on Image Processing (ICIP), Singapore, pp. 1461-1464, 2004.
[109] S. Roux, "Modèle dynamique en tomographie - Application à l'imagerie cardiaque," PhD thesis, Université Joseph Fourier, Grenoble, Doctorat, 145p, 2004.

[110] P. Grangeat, A. Koenig, T. Rodet, and S. Bonnet, "Theoretical framework for a dynamic cone-beam reconstruction algorithm based on a dynamic particle model," *Physics in Medicine end Biology*, vol. 47, pp. 2611-2625, 2002.

# PARTIE B :
# SYNTHESE DES ACTIVITES

# 1. RESUME DES ACTIVITES DE RECHERCHE

### 1.1. PERIODE 1988-1992 (THESE)

Notre travail de thèse a porté sur le développement d'un système d'aide au repérage en imagerie stéréotaxique cérébrale. Sa principale fonctionnalité était de permettre la mise en correspondance d'une imagerie pré-opératoire en IRM ou en Tomodensitométrie avec des images per-opératoires acquises en radiographie standard en condition stéréotaxique par l'intermédiaire de marqueurs externes positionnées dans les fixations d'un cadre stéréotaxique de Talairach. Ce travail a été réalisé au Laboratoire de Biophysique de la Faculté de Médecine de Lille et au Centre d'Automatique de Lille (actuellement LAGIS). Le système a été validé et installé en salle d'opération du service de neurochirurgie du CHU de Lille. Depuis son installation, il permis de réaliser plus de 1000 interventions. Son extension à la radiochirurgie multifaisceaux, développée par David Gibon dans le cadre de sa thèse, a permis la réalisation du traitement de plus de 2500 patients. Ma thèse a été soutenue en décembre 1991. J'ai poursuivi mon activité de recherche dans ce domaine quelques mois en tant qu'ATER à l'Université de Sciences et Technologies de Lille.

### 1.2. PERIODE 1992 A AUJOURD'HUI

A l'issu du concours CNRS 1992, j'ai été recruté en tant Chargé de Recherche et affecté au Laboratoire de Traitement de Signal et Ultrasons qui deviendra Creatis. J'appartiens à la section 30 (Thérapeutique, médicaments et bioingénierie : concepts et moyens, ex section 22) du département des Sciences de la Vie du CNRS. De formation STIC, mon activité de recherche est toutefois orientée vers une thématique médicale.

Mes travaux de recherche ont pour objectif le développement de nouvelles méthodes d'analyse d'images médicales multi-modalités, anatomiques et fonctionnelles, dans les buts d'*améliorer la connaissance du fonctionnement du muscle cardiaque*, et d'aider le praticien hospitalier dans la *détection et l'évaluation de pathologies cardiaques* en particulier les pathologies ischémiques.

Les travaux de cette période sont présentés dans la première partie de ce document.

# 2. SITUATION DES ACTIVITES DANS L'UNITE

Depuis mon arrivée au Laboratoire CREATIS (Centre de REcherche et d'Applications en Traitement de l'Image et du Signal), j'ai été intégré au thème scientifique « **Imagerie Dynamique** » sous la responsabilité d'Isabelle Magnin. Ce thème a pour objectif le développement de nouveaux modèles pour la segmentation, l'estimation de mouvement, et la caractérisation de phénomènes évolutifs complexes à partir d'images médicales. De part ma position de chercheur SDV-STIC, j'ai été impliqué dans les développements liés à des problématiques SDV, en particulier en imagerie cardiaque. J'ai été ainsi amené à prendre la co-responsabilité avec Marc Janier du projet médical « **Imagerie Fonctionnelle de l'Ischémie et de ses Conséquences** ». Ce projet avait pour objectif la caractérisation des différents états des tissus ischémiés à partir d'une exploration en imagerie multi-modalités (Tomographie par Emission de Positons, Imagerie par Résonance Magnétique, échocardiographie) du métabolisme, de la perfusion et de la fonction contractile. Mon activité de recherche a donc été entièrement orientée par les recherches menées dans ce projet. Dans la nouvelle structure validée par le CNRS en 2002 (voir organigramme en page suivante), je suis co-responsable avec Pierre Croisille du sous-thème SDV « **Ischémie myocardique »** et responsable du thème STIC « Imagerie dynamique » (avec Maciej Orkisz, responsable adjoint) en remplacement d'Isabelle Magnin, devenue Directeur de l'Unité.

**Services communs :**

**Secrétariat de direction** :
- B. Chimenton, TCH Insa
- F. Berkaï, AJT CNRS

**Accueil, Secrétariat de 4 Equipes** :
- F. Berkaï , AJT Cnrs

Secrétariat site hospitalier :
- C. Castelli, ADT UCBL

Gestion :
- S. Tilleul, TCH CNRS
- S. Riahi, ADA Insa (contractuelle)

**CREATIS-INSERM Unité 630, CNRS UMR 5515**

**Directeur : Isabelle Magnin, DR Inserm**

**Directeur-adjoint : Didier Revel, PUPH UCB**

**Effectif global : 125 personnes**

**Cellule de valorisation**

Responsable:G. Courbebaisse, IR Insa

P. Seillé, Ingénieur contractuel
E.Davilla, Ingénieur contractuel

| **Imagerie dynamique** | **Imagerie volumique** | **Imagerie ultrasonore** | **Imagerie isotopique** | **Microarchitecture et tissu osseux** | **Athérosclérose et conséquences Responsable : Didier Revel (ETP : 12)** | | |
|---|---|---|---|---|---|---|---|
| | | | | | **Lumière et paroi vasculaire** | **Ischémie myocardique** | **Ischémie cérébrale** |
| Resp.:**P. Clarysse**,CR CNRS | Resp. : R.Prost, PR | Responsable : | Responsable : | Responsable : | co-responsables : | co-responsables : | co-responsables : |
| Adj. : M. Orkisz, PR | Adj. : C. Odet, PR | D. Vray, PR | D. Sappey-Marinier, MCUPH | F. Peyrin, DR Inserm | Ph. Douek, PUPH | P. Croisille, MCUPH | N. Nighoghossian, PUPH |
| --- | --- | --- | --- | --- | *(C. Cachard, PR)* | *(P. Clarysse,CR Cnrs)* | Y.Berthezène, PUPH |
| I. Magnin, DR Inserm | Y.M. Zhu, CR Cnrs | C. Cachard, PR | --- | *(C. Odet, PR Insa)* | --- | --- | --- |
| M. Wiart, CR Cnrs | O. Basset, PR | G. Gimenez, PR | C.Lartizien, CR Cnrs | *(H. Benoit-CattinMCU)* | G. Finet, PUPH | M. Janier, PUPH | J.-C. Froment, PUPH |
| D. Friboulet, PR | H.Benoit-Cattin, MCU | Ph.Delachartre, MCU | | *(C. Muller, MCU)* | F. Turjman, PUPH | D. Revel, PUPH | M. Wiart, CR Cnrs |
| B. Neyran, MCU | C. Muller, MCU | E. Brusseau, CR Cnrs | | | J. Azencot, MCU | *(B. Neyran, MCU)* | |
| M. Robini, MCU | | | | | J.M. Serfaty, MCUPH | | |
| | | | | | *(I.Magnin,DR Inserm)* | | |
| | | | | | *(D. Vray, PR)* | | |
| | | | | | *(M. Orkisz, PU)* | | |
| - 3 post-docs | - 1 post-doc | | - 1 post-doc | | | | |
| - 8 doctorants | - 11 doctorants | - 10 doctorants | - 2 doctorant | - 4 doctorants | - 4 doctorants | - 3 doctorants | - 4 doctorants |

**Services communs : Informatique**

Responsables. : H. Benoit-Cattin, MCU - P. Croisille, MCUPH - F. Bellet, IR Cnrs
J.-P. Roux, IR UCBL – B. Regrain, IE Cnrs – S. Dubois, TCH Insa – A. Pélossier, ADT Insa –

*Figure 38. Organigramme de l'Unité CREATIS*

# 3. AUTRES ACTIVITES

## 3.1. ACTIVITES D'ENSEIGNEMENT ET DE DIFFUSION

### 3.1.1. Encadrements

Les différentes responsabilités d'encadrement que j'ai exercées sont listées ci-après :

- ***Thèses soutenues :***

**PAUNA** Nicoletta, 'Evaluation des méthodes de mise en correspondance en imagerie multimodale IRM/TEP thoracique et cardiaque'. Numéro d'Ordre : UCBL66-2004, Université Claude Bernard LYON 1 en co-tutelle avec l'Université de Cluj, Roumanie, **2004**. Jury : I. Magnin (Pdt), B. Gibaud (R), R. Ciupa (R), M. Janier (Dir.), O. Cozar (Dir.), P. Clarysse (Co-Dir), A. Georgescu. *Co-encadrement à 40% avec M. Janier et O. Cozar.*

Actuellement en Post-Doc à l'IPNL, Lyon.

**MÄKELÄ** Timo, double Thèse et co-tutelle

- 'Data registration and fusion for cardiac applications', Helsinki University of Technology, Mai **2003.** Oponent : N. Ayache (INRIA).
- 'Mise en correspondance en imagerie cardiaque multimodale : vers un modèle anatomo-fonctionnel individualisé du cœur'. Numéro d'Ordre : ISAL106, INSA LYON, **2004.** Jury : P. Cinquin (R, Pdt), N. Ayache (R), T. Katila (Dir.), I. E. Magnin (Dir.), P. Clarysse (Co-Dir.), U. Ruotsalainen. Co-encadrement à 50% en collaboration avec les partenaires Finlandais.

Actuellement hospitalo-universitaire à l'hôpital de Oulu, Finlande.

**PHAM** Quoc-Cuong, Segmentation en imagerie cardiaque multimodale conduite par un modèle réaliste du cœur, INPG, 2002. Jury : J-M. Chassery (Pdt), F. Heitz (R), H. Delingette (R), I. E. Magnin (Dir.), P. Clarysse (Co-Dir.), J. Pousin, P. Croisille, T. Katila. INPG, 2002. Co-encadrement à 80% avec I. Magnin.

Actuellement chercheur au CEA, Saclay.

**VINCENT** Fabrice, Gabarits déformables élastiques pour la segmentation et le suivi de mouvement du cœur en Imagerie par Résonance Magnétique. Numéro d'ordre : 01ISAL0079, INSA LYON, **2001.** Jury : J. Pousin (Pdt), N. Ayache (R), Ph. Cinquin (R), I. Magnin (Dir), P. Clarysse (Co-Dir), P. Croisille. Co-encadrement à 80% avec I. Magnin.

Actuellement ingénieur société Théralys.

**HAN** Meimei, Analyse exploratoire de la déformation spatio-temporelle du myocarde à partir de l'Imagerie par Résonance Magnétique de Marquage tissulaire. Numéro d'Ordre : ISALY004, INSA LYON, **1999.** Jury : I. Magnin (Pdt), M. Lamure (R), J-G. Postaire (R), P. Clarysse (Dir.), P. Croisille, D. Revel, J. Rousseau. Co-encadrement à 80% avec I. Magnin.

Actuellement ingénieur entreprise Bombardier, Montréal, Canada

- ***Thèses en cours :***

**HADDAD** Rana, 3ème année thèse Images & Systèmes, Modèle anthropomorphique de cœur battant. Co-encadrement avec I. Magnin.

**DELHAY** Bertrand, 2ème année thèse Images & Systèmes, Estimation conjointe forme et mouvement en 3D – Application au mouvement du thorax et du cœur. Co-encadrement avec I. Magnin.

**SCHAERER** Joël, 1ère année thèse Instrumentation, Système, Signal & Image, Modèle spatio-temporel pour la segmentation de structures en mouvement – application à l'imagerie du cœur. Co-encadrement avec I. Magnin.

- ***Post-Doctorats :***

**MILLES** Julien, nationalité Française, Univ. Maastricht, Pays-Bas. 'Segmentation automatique du ventricule gauche dans des images par résonance magnétique de marquage tissulaire'. Co-encadrement à 50% avec T. Arts, **2003-2004 .**

**QIU** Bo, nationalité Chinoise, Creatis, 'Segmentation 3D en imagerie ultrasonore'. Co-encadrement à 50% avec D. Vray, **2003-2004.**

- ***DEA (2002-2004)***

2004 : Josiane **YANKAM NJIWA** (I&S): "Recalage non rigide en imagerie du thorax et du cœur"

2004 : Sonia **CHOUBRAC** (I&S): "Estimation de mouvement en IRM de marquage tissulaire"

2003 : Li **ZHOU** (I&S), 50%, : "Estimation du mouvement cardiaque à partir de séquences rapides d'images échographiques"

2003 : Bertrand **DELHAY** (I&S) : "Estimation de champs de déplacement 3D en tomographie dynamique du thorax. Développement d'une méthode intégrant la notion d'objet"

2002 : Rana **HADDAD** (I&S) : "Extraction des contours ventriculaires dans des images par Résonance Magnétique de Marquage tissulaire"

2002 : Evguénia **REVOUNKOVA** (I&S) : "Développement d'une méthode d'estimation d'un champ dense de mouvement - application à la tomographie dynamique", en collaboration avec le LETI-CEA Grenoble

Soit plus de 10 encadrements depuis 1994 et 3 actuellement en cours.

- ***Stages de fin d'études (2002-2004):***

2004 : Dan **ONICA**, étudiant de l'Université d'Oradea, Roumanie. Logiciel d'estimation de mouvement.

2003 : Ovidiu **PANTEA**, étudiant de l'Université d'Oradea, Roumanie. Visualisation de champs de mouvements 3D.

2002 : Sébastien **BAIMONT** CPE-Lyon. Développement de l'interface du logiciel de boite à outils mouvement. En collaboration avec M. Orkisz.

2002 : Andrea **VLADU**, Ovidiu **PANTEA,** étudiants de l'Université d'Oradea, Roumanie. Extension de la boite à outils mouvement.

Soit une dizaine de stagiaires depuis 1993.

### 3.1.2. Enseignement

Mes différentes interventions en enseignement ont été les suivantes:

**Etablissement :**

1. Centre d'Actualisation Scientifique et Technique (CAST), Villeurbanne
2. INSA de Lyon, Département Génie Electrique et Télécommunications
3. INSA de Lyon, Master Instrumentation, Système, Signal & Image (ISSI), Master Recherche en Informatique (MRI)

**Discipline :**

1. Traitement d'images
2. Traitement du signal, processeurs DSP
3. Estimation de mouvement, modèles déformables, recalage d'images

**Niveau:**

1. Formation Continue
2. 2ème cycle, 1ère année cycle Ingénieur
3. 3ème cycle

**Nature** (CM, TD, TP) **et volume** (nombre annuel moyen d'heures effectuées) **:**

1. CM(4), TP(6)
2. TD(13), TP(24)
3. CM(19)

***Commentaires*** : depuis 2003, mes interventions ne concernent plus que les DEA/Master pour environ 23h de cours par an. Le cours d'estimation de mouvement (7h en Master Instrumentation, Système, Signal & Image) débute par les notions de base en estimation de mouvement dans des séquences d'images puis comporte principalement 3 volets : détection de mouvement, méthodes d'estimation quantitative du flux optique, prise en compte des discontinuités de mouvement. Le cours de recalage (6h en Master Recherche en Informatique) concerne les méthodes non rigides de recalage d'images et l'évaluation de méthodes de traitement d'images, en particulier des méthodes de recalage.

### 3.1.3. Organisation de séminaires ou congrès

Nous avons co-organisé avec Isabelle Magnin, Johan Montagnat et nos collègues Finlandais, Jukka Nenonen et Toivo Katila, les première (Helsinki, Novembre 2001) et seconde (Lyon, Juin 2003) éditions du workshop international "Functional Imaging and Modeling of the Heart" (FIMH). Les actes du workshop ont été publiés chez *Springer* dans la série *Lecture Notes in Computer Science*, vol 2230, ISBN 3-540-42861-5, Novembre 2001 et vol. 2674, ISBN 3-540-40262-4, Juin 2003

### 3.1.4. Diffusion de connaissances

- J'ai été invité à présenter les applications en imagerie cardio-vasculaire de la fusion d'images aux Journées de Recherche en Imagerie Médicale à Nantes les 21-23 Mai 2003.

- Nous avons développé en collaboration avec des chercheurs étrangers le serveur WWW « Special Interest Group on Cardiac Motion Analysis », basé à CREATIS, dont l'objectif était de faciliter les relations entre les chercheurs de diverses disciplines dans le domaine de l'estimation et l'analyse du mouvement du cœur. Ce serveur, créé en 1997 à l'issu de la 2nd IEEE EMBS International Summer School on Biomedical Imaging (Ile de Berder, 1996), repose sur une base de données pluridisciplinaire de références bibliographiques que chacun pouvait consulter et faire évoluer (http://creatis.insa-lyon.fr/sigcma).
- D'autres interventions sont indiquées dans la liste des travaux.

### 3.2. PARTENARIAT ET VALORISATION

- LETI-CEA, Grenoble, contrat n° 7D20-1B000330, Etude prospective en imagerie pour la tomographie dynamique, 11.4KEuros, 2001.

### 3.3. ENCADREMENT, ANIMATION ET ADMINISTRATION DE LA RECHERCHE

#### 3.3.1. Animation de projets

- Responsable Français d'un PICS du CNRS (PICS n°1932) avec le Laboratory of Biomedical Engineering, Helsinki University of Technology, Finlande, 2003-2005
- Co-responsable avec Frédérique Frouin (INSERM-U494) de l'Action Spécifique du CNRS ICoMIM (Intégration de Connaissances et Modélisation en Imagerie Médicale), 2002-2003
- Co-responsable avec Laurent Desbat (UJF, Grenoble) du projet "ADéMo : Modélisation et suivi spatio-temporel pour le diagnostic et le traitement" dans le cadre des thématiques de Recherche de la Région RA, 2000-2003.
- Coordinateur adjoint de Isabelle Magnin pour le projet: "Vision quantitative et imagerie médicale" dans le cadre d'un programme de recherche de la Région Rhône-Alpes intitulé "Santé et HPC", 1997-2000.
- Animation en collaboration avec Isabelle Magnin et Nicolas Rougon (INT-Evry) du Groupe de Travail #4 (Modèles déformables dynamiques) du GDR-PRC ISIS du CNRS jusqu'en 2001. J'ai été, dans ce cadre, impliqué dans deux des opérations du GT4, et responsable de l'une d'elles. Responsable du pôle 3 "Estimation et modélisation du comportement dynamique du cœur" de l'action incitative inter GDR-PRC ISIS/ALP-AMI/MSPC "Cœur Battant" coordonnée par Isabelle Magnin.

#### 3.3.2. Responsabilité dans la direction d'équipe

- Co-responsable avec Pierre Croisille du sous-thème SDV « *Imagerie fonctionnelle de l'ischémie myocardique et de ses conséquences* » à CREATIS depuis 1998. L'équipe comprend 5 permanents du laboratoire, 3 doctorants.
- Responsable du thème STIC "*Imagerie dynamique*", depuis 2002 (Resp. adjoint Maciej Orkisz). L'équipe comprend 7 permanents, 8 doctorants et 3 post-doctorants.

#### 3.3.3. Divers

***a) Au niveau International***

- **Référé de Journaux**: IEEE Trans. Med. Imaging, IEEE Trans. Image Processing, IEEE Trans. Biomed. Eng, IEEE Trans. ITB, MEDIA, J. of Mathematical Imaging and Vision,

Pattern Recognition Letter, Investigative Radiology, Journal of Electronic Imaging, J. Computing and Information Technology (CIT), Innov. Techn. Biol. Med.

• **Référé de Conférences**: ICPR'02, ISBI, ICIP, FIMH, IISPA, ISPA, RFIA, GRETSI, Forum des Jeunes Chercheurs en GBM.

• **Comités de programme** : Participation à la création de la conférence internationale FIMH (3ième édition en 2005), Membre du comité scientifique de FIMH, ISPA, SURGETICA.

***b) Au niveau national***

- Membre de la commission d'Emergence N°5, «Chirurgie micro-invasive et robotisée » de l'INSERM
- Membre de la Société Française de Génie Biologique et Médical (SFGBM)
- Membre des commissions de spécialistes (61ième section) de Lyon 2 (jusqu'à 2004), UCB-Lyon1, de l'UST de Lille (1998-2001) et de l'INSA de Lyon (jusqu'en 1997)
- **Jurys de thèse externes: 2**
    - **Allouche** Cyril, 'Reconstruction, recalage et modélisation 4D du mouvement du ventricule gauche du cœur humain pour le traitement d'images médicales, Thèse de l'Université de Paris XI, Janvier 2002
    - **Hila Benhajel** Kaouthar, 'Etude et modélisation de la fonction cardiaque par analyse numérique d'images', Thèse de l'Université Paris XII Val de Marne, Décembre 2003.

***c) Au niveau du laboratoire***

- Membre du Conseil de Direction à CREATIS
- Correspondant Formation de l'Unité jusqu'en 2001

### 3.4. ACTIVITES INTERNATIONALES

J'ai été amené à visiter plusieurs laboratoires Européens (Univ. Saragosse, Univ. Karlsruhe, Univ. Leuven) dans le cadre de la préparation de la proposition du réseau d'excellence e-Heart présenté par Isabelle Magnin à la Communauté Européenne en Avril 2003 (priorité IST, e-health) et qui n'a malheureusement pas été sélectionné. Ce réseau reste virtuellement actif via sa liste de diffusion et le site web associé (http://www.creatis.insa-lyon.fr/eheart). La conférence biannuelle FIMH (Functional Imaging and Modeling of the Heart), que nous avons initiée, est la manifestation associée à ce réseau. La troisième édition (FIMH 2005) aura lieu à Barcelone du 2 au 4 Juin 2005 (http://www.cilab.upf.edu/fimh/).

J'ai effectué plusieurs séjours au Biomedical Engineering Laboratory, Université Techonologique d'Helsinki, Finlande. Nous avons une collaboration qui fonctionne depuis plusieurs années qui a été soutenue de 1999 à 2001 dans le cadre d'une convention de coopération scientifique entre le CNRS et l'Académie des Sciences de Finlande et qui est soutenue depuis par un Programme International de Coopération Scientifique (PICS n°1932) du CNRS. Le Biomedical Engineering Laboratory a une structure similaire à celle de CREATIS : il comprend des médecins et des ingénieurs. De plus, le groupe Finlandais travaille également sur l'imagerie du cœur mais à partir de modalités différentes et complémentaires des nôtres (Magnétocardiographie, Electrocardiographie). Des échanges de doctorants ont pu avoir lieu dans ce cadre et plusieurs publications communes ont été produites.

Enfin, dans le cadre d'un post-doctorat, nous avons initié une collaboration avec Théo Arts de l'université de Maastricht au Pays-Bas autour de l'analyse du mouvement du cœur.

# 4. PUBLICATIONS PERSONNELLES

- ***Publications en révision***

Pauna N., Croisille P., Costes N., Reilhac A., Mäkelä T., Janier M., Clarysse P., A strategy to quantitatively evaluate MR/PET thorax/cardiac rigid registration methods using a Monte Carlo simulator, en révision pour *IEEE Trans. Med. Imaging*

- ***Publications avec comité de lecture***

[J-17] Germain C., Breton V., Clarysse P., Gaudeau Y., Glatard T., Jeannot E., Legré Y., Loomis C., Montagnat J., Moureaux J-M., Osorio A., Pennec X., Texier R., Grid-enabling medical image analysis, *Journal of Clinical Monitoring and Computing*, Special Issue, A paraitre.

[J-16] J. Luo, Y. M. Zhu, P. Clarysse, and I. Magnin, "Correction of Bias Field in MR Images Using Singularity Function Analysis," *IEEE Transactions on Medical Imaging*, vol. 24, N° 8, pp. 1067-1085, 2005.

[J-15] P. Clarysse, F. Frouin, M. Garreau, A. Lalande, J. Rousseau, D. Sarrut, and C. Vasseur, "Intégration de Connaissances et Modélisation en Imagerie Médicale," *Innovations et Technologies en Biologie et Médecine - RBM*, 25(3), pp. 139-149, 2004

[J-14] Mäkelä T., Pham Q-C, Clarysse P., Nenonen J., Lötjönen J., Sipilä O., Hänninen H., Lauerma K., Knutti J., Katila T., Magnin I.E. A 3D model-based registration approach for the PET, MR and MCG cardiac data fusion, *Medical Image Analysis*, Vol. 7, N° 3 , pp. 377-389, September 2003.

[J-13] Clarysse P., Han M., Croisille P., Magnin I. E., Exploratory analysis of the spatio-temporal deformation of the myocardium during systole from tagged MRI, *IEEE Trans. Biomed. Eng., Vol.49, N°. 11, 2002, 1328-1339*

[J-12] Mäkelä, T., Sipilä, O, Clarysse, P., Pauna, N., Pham, Q-C., Katila, T., Magnin, I.E. A review of cardiac registration methods, *IEEE Trans. Med. Imaging*., Vol. 21, N° 9, September 2002

[J-11] Clarysse P., Basset C., Khouas L., Croisille P., Friboulet D., Odet C. and Magnin I.E. (2000) 2D spatial and temporal displacement and deformation field fitting from cardiac MR tagging. *Medical Image Analysis*, 4, pp. 253-268, 2000.

[J-10] Verhnet, H., Revel D., Arteaga C., Clarysse P., Sottilini F., Roux J.P., Canet E., Predictive value of regional left ventricular circumferential shortening in jeopardized myocardium : a 2D SPAMM Cine-MR imaging study in a canine model, *Invest Radiol*, Vol. 34, N° 10, pp. 621-628, 1999.

[J-9] Khouas, L., Clarysse, P., Friboulet, D. and Odet, C. (1998) Fast 2D vector field visualization using a 2D texture synthesis based on an autoregressive filter. Application to cardiac imaging. *Machine GRAPHICS & VISION*, 7, 4, 751-764.

[J-8] Han, M., Clarysse, P., Croisille, P., Magnin, I.E., Revel, D. (1998) Aide à l'analyse de l'évolution spatio-temporelle de la déformation du myocarde. ITBM, 19, 5, 379-388.

[J-7] Clarysse P., Friboulet D., Magnin I. E., "New shape descriptors for 3D deformable object tracking. Application to the left-ventricular surface of the heart", *IEEE T. Med. Imaging*, Vol. 16, N°4, pp. 392-404, 1997.

[J-6] Reissman P-J., Clarysse P., Magnin I.E., "Modélisation et mise en correspondance avec la pyramide neuractive", *Traitement du Signal*, Vol. 14, N°4, pp. 395-403, 1997.

[J-5] Orkisz M., Clarysse P., "Estimation du flot optique en présence de discontinuités: une revue", *Traitement du Signal*, Vol. 13, N°5, pp. 489-513, 1996.

[J-4] Rousseau J., Clarysse P., Blond S., Gibon D., Vasseur C., Marchandise X., "Validation of a new method for stereotactic localization using MR Imaging", *Journal of Computer Assisted Tomography*, Vol. 15, N°2, pp. 291-296, March/April 1991

[J-3] Clarysse P., Gibon D., Rousseau J., Blond S., Vasseur C., Marchandise X., "A computer assisted system for 3D frameless localization in stereotaxic MRI", *IEEE Trans. Medical Imaging*, Vol. 10, N°4, pp. 523-529, December 1991

[J-2] Rousseau J., Gibon D., Clarysse P., Pruvo J.P., Blond S., Marchandise X., "Une méthode de repérage stéréotaxique par IRM", *J. Med. Nucl. Biophy*., Vol. 16, N°4, pp. 374-379, 1992

[J-1] Rousseau J., Clarysse P., Gibon D., Blond S., Bradaï N., Marchandise X., "A frameless method for 3D MRI- and CT- guided stereotaxic localization", *Neuroradiology*, Vol. 2, pp. 35-41, 1992

- ***Actes de Workshops organisés***

[FIMH-01] Proceedings of the First international Workshop on Functional Imaging and Modeling of the Heart (FIMH), T. KATILA, I.E. MAGNIN, P. CLARYSSE, J. MONTAGNAT, et J. NENONEN editors, Springer, *Lecture Notes in Computer Science*, vol. 2230, ISBN 3-540-42861-5, nov 2001.

[FIMH-03] Proceedings of the Second international Workshop on Functional Imaging and Modeling of the Heart (FIMH'03), I.E. MAGNIN, J. MONTAGNAT, P. CLARYSSE, J. NENONEN et T. KATILA, editors, Springer, *Lecture Notes in Computer Science*, vol. 2674, ISBN 3-540-40262-4, 2003.

- ***Communications invitées dans des congrès***

Clarysse P. « Fusion d'images : applications en imagerie cardio-vasculaire », Journées de Recherche en Imagerie Médicale, 12ème Forum des Jeunes Chercheurs en GBM, Nantes, 21-23 Mai 2003.

Clarysse P. "Overview of Medical Image Processing" dans le cadre de la 8th Summer School on Image Processing, Zagreb, Croatia, July 7-16, 2000.

Clarysse P. Revel D., Magnin I.E., "Segmentation d'images par résonance magnétique multi-phases et multi-coupes du cœur par une approche de régions déformables", Rencontre Annuelle du Futuroscope "Les techniques d'imagerie cardiovasculaire du futur", Poitiers, 1997

Clarysse P., "Recent and future trends in cardiac image processing", 2nd IEEE EMBS International Summer School on Biomedical Imaging, Ile de Berder, 1996

- ***Communications dans des conférences internationales avec actes***

[C-34] Elisabeth Brusseau, Ghada Said, Patrick Clarysse, Modèle numérique d'estimation 2D de la déformation des tissus mous biologiques à partir d'images échographiques radiofréquence: Résultats sur simulations numériques et données expérimentales, accepté à GRETSI 2005

[C-33] Rana Haddad, Patrick Clarysse, Maciej Orkisz, Pierre Croisille, Didier Revel, Isabelle E. Magnin, A realistic anthropomorphic numerical model of the beating heart, accepté à FIMH'05.

[C-32] Bertrand Delhay, Patrick Clarysse, Jyrki Lötjönen, Toivo Katila and Isabelle E. Magnin, Evaluation of two free form deformation based motion estimators in cardiac and chest imaging, accepté à FIMH'05.

[C-31] Germain C., Breton V., Clarysse P., Gaudeau Y., Glatard T., Jeannot E., Legré Y., Loomis C., Montagnat J., Moureaux J-M., Osorio A., Pennec X., Texier R., Grid-enabling medical image analysis, accepté à BIOGRID'05.

[C-30] B. Delhay, P. Clarysse, S. Bonnet, P. Grangeat, and I. E. Magnin, "Combined 3D object motion estimation in medical sequences," International Conference on Image Processing (ICIP), Singapore, 2004

[C-29] Qiu B., Clarysse P., Montagnat J., Janier M., Vray D., Comparison of 3D Deformable Models For in vivo Measurements of Mouse Embryo from 3D Ultrasound Images, IEEE International Ultrasonics Symposium, Montréal (Canada), August 24-27, 2004

[C-28] J. Milles, P. Clarysse, A. van Susteren, P. Croisille, I. E. Magnin, and T. Arts, "Automatic 2D segmentation of the left ventricle in tagged cardiac MRI using motion information," IEEE International Symposium on Biomedical Imaging (ISBI), Arlington, VA, USA, pp. 153-156, 2004

[C-27] M. Pollari, J. Lötjönen, T. Mäkelä, N. Pauna, A. Reilhac, and P. Clarysse, "Evaluation of cardiac PET-MRI registration methods using a numerical breathing phantom," IEEE International Symposium on Biomedical Imaging (ISBI), Arlington, VA, USA, pp. 1447-1450, 2004

[C-26] N. Pauna, P. Croisille, N. Costes, A. Reilhac, T. Mäkelä, O. Cozar, M. Janier, P. Clarysse, « A Strategy to quantitatively evaluate MRI/PET cardiac rigid registration methods using a Monte Carlo simulator », Springer LNCS 2674, Proceedings of FIMH'03, Lyon, France, pp. 194-204, Juin 2003

[C-25] T. Mäkelä, M. Pollari, J. Lötjönen, N. Pauna, A. Reilhac, P. Clarysse, I. Magnin, T. Katila, , « Evaluation and comparison of surface and intensity based rigid registration methods for thorax and cardiac MR and PET images », Springer LNCS 2674, Proceedings of FIMH'03, Lyon, France, pp. 224-233, Juin 2003

[C-24] I. Dydenko, S. Chehbi, D. Friboulet, P. Clarysse, I. E. Magnin, "Using an elastic deformable template for the segmentation of ultrasound cardiac radio frequency images based on the

velocity information", IEEE International Ultrasonics Symposium, München, Germany, pp. 1749-1752, october 2002.

[C-23] D. Vray, A. Discher, J. Lefloc'h, W. Mai, P. Clarysse, Q.C. Pham, J. Montagnat, M. Janier, "3D Quantification of Ultrasound Images : Application to Mouse Embryo Imaging In Vivo", IEEE International Ultrasonics Symposium, Munich, Germany, pp. 1557-1560, October 2002.

[C-22] P. Clarysse, P. Croisille, L. Bracoud and I. Magnin, "Integrated Quantitative Analysis of Tagged Magnetic Resonance Images", Springer LNCS 2230, FIMH'01, November 15-16, 2001, pp. 69-75, 2001

[C-21] T. Mäkelä, Q. C. Pham, P. Clarysse, J. Lötjönen, K. Laeuerma, H. Hänninen, J. Knuuti, T. Katila, I. Magnin, "A 3D model-based approach for the PET-functional and MR-anatomical cardiac imaging data fusion", Springer LNCS 2230, FIMH'01, November 15-16, 2001, pp. 83-90, 2001

[C-20] T. Mäkelä, P. Clarysse, J. Lötjönen, O. Sipilä, K. Lauerma, H. Hänninen, J. Nenonen, J. Knuuti, T. Katila, and I. E. Magnin, "A new method for the registration of cardiac PET and MR images using deformable model based segmentation of the main thorax structures," Medical Image Computing and Computer Assisted Intervention (MICCAI 2001), Utrecht, The Netherlands, pp. 557-564, 2001

[C-19] P. Clarysse, C. Lavorel, A. Glière, P. Grangeat, I. E. Magnin, "Un modèle de thorax respirant pour l'évaluation d'algorithmes de reconstruction d'organes en mouvement par tomographie virtuelle", GRETSI'01, Toulouse, France, 10-13 Septembre 2001

[C-18] Q.C. Pham, F. Vincent, P. Clarysse, P. Croisille, I.E. Magnin, "A FEM-Based Deformable Model for the 3D Segmentation and Tracking of the Heart in Cardiac MRI", ISPA-2001, Pula, Croatia, June19-21, pp. 250-254, 2001

[C-17] QC. Pham, F. Vincent, P. Clarysse, P. Croisille, I.E. Magnin, "Heart segmentation in MRI using A 3D prior biventricular deformable model", Forum des Jeunes Chercheurs en GBM 2001, Compiègne, France, 5-6 Juin 2001, pp.70-71, 2001.

[C-16] T. Mäkelä, P. Clarysse, J. Lötjönen, O. Sipilä, H. Hänninen, J. Nenonen, K. Lauerma, J. Knuuti, T. Katila, and I. E. Magnin, "A method for registration of cardiac Magnetic Resonance and Positron Emission Tomography images for assessing myocardial viability," in *Understanding Cardiac Imaging Techniques from Basic Pathology to Image Fusion*, vol. 332, *NATO Science Series - Life and Behavourial Sciences*, P. Marzullo, Ed., Proceedings of the NATO Advanced Research Workshop on Understanding Cardiac Imaging Techniques : From Basic Pathology to Image Fusion ed. Pisa, Italy: IOS Press, 2001, pp. 155-165.

[C-15] Vincent F., Clarysse P., Croisille P. and Magnin I.E. (2000) An elasticity-based region model and its application to the estimation of the heart deformation in tagged MRI. accepté à ICIP-2000, Vancouver, BC, Canada, September 10 - 13, 2000.

[C-14] Vincent F., Clarysse P., Croisille P. and Magnin I.E. (1999) Segmentation et suivi de mouvement d'objets déformables par région active. GRETSI'99, Vannes, France, 13-17 Septembre 1999.

[C-13] Benoit-Cattin H., Planat A., Joachimsmann P., Baskurt A., Clarysse P., Magnin I. E. "On the coding of active quadtree mesh", IEEE International Conference on Image Processing, Washington, Illinois, USA, October 4-7, 1998.

[C-12] Han M., Clarysse P., Croisille P., Behloul F., Magnin I. E., Revel D. "Computer aided diagnosis of the myocardial ischemia based on a spatio-temporal deformation features analysis", Computers In Cardiology, Cleveland, Ohio, USA, September 13-16, pp.749-752, 1998.

[C-11] Han M., Clarysse P., Croisille P., Magnin I. E., Revel D. "Aide à l'analyse de l'évolution spatio-temporelle de la déformation du myocarde", 9ième Forum Jeunes Chercheurs GBM, Brest, France, May 14-15, 1998

[C-10] Clarysse P., Reismann P-J., Lefebvre S., Baudin O., Revel D. "Region-based segmentation of multi-slice and multi-phase cardiac Magnetic Resonance Images", World Congress On Medical Physics and Biomedical Engineering, Vol. 35, N°2, p. 684, Nice, France, September 14-19, 1997

[C-9] Boudraa A., Clarysse P. "Fast fuzzy gray level image segmentation method", World Congress On Medical Physics and Biomedical Engineering, Vol. 35, N°2, p. 686, Nice, France, September 14-19, 1997

[C-8] Sottilini F., Clarysse P., Revel D., Magnin I. E., "LV myocardial wall motion estimation with tagged cine MRI (SPAMM)", Computers In Cardiology, Vienna, Austria, pp. 529-532, September 10-13, 1995

[C-7] Clarysse P., Poupon F., Barbier B., Magnin I.E, "3D boundary extraction of the left ventricle by a deformable model with a priori information", IEEE International Conference on Image Processing, Washington, D. C., USA, pp. 492-495, October 22-25, 1995

[C-6] Clarysse P., Jaouen O., Magnin I. E., Morvan J-M., "Interpolation 3D des parois cardiaques à partir de données discrètes", Journées Thématiques GDR 134-GRAISYHM Région Nord-Pas de Calais. Thème: Mouvement 3D d'objets non rigides, Lille, France, 4-5 Mai 1995

[C-5] Clarysse P., Friboulet D., Magnin I. E., "Time-evolution analysis of differential features on 3D surfaces of the heart walls", IEEE Medical Imaging Conference, Norfolk, Virginia (USA), pp. 1807-1811, November 3-5 1994

[C-4] Gorce J. M., Friboulet D., Clarysse P., Magnin I. E., "Three-dimensional velocity field estimation of moving cardiac walls", Proc. Computers In Cardiology, Bethesda, Maryland(USA), pp. 489-492, September 25-28 1994

[C-3] Clarysse P., Jaouen O., Magnin I. E., Morvan J. M., "3D representation and deformation analysis of the heart walls from X-rays and MR Images", Proc. Computers In Cardiology, Bethesda, Maryland(USA), pp. 657-660, September 25-28 1994

[C-2] Clarysse P., Friboulet D., Magnin I. E., "Curvature assessment of the heart walls in 3D dynamic imaging", Proc. Computers In Cardiology, London (UK), pp. 607-610, September 5-8, 1993

[C-1] Magnin I. E., Mathieu C., Friboulet D., Clarysse P., "Intérêt de l'imagerie cardiaque 3D. Acquisition, segmentation, quantification", Proc. Symposium Echocardiographie et analyse d'images ventriculaires, Dijon, France, pp. 119-132, 25-26 Mars 1993

- ***Communications sans actes***

David Sarrut, Serge Miguet, Fabrice Vincent, Patrick Clarysse, Matthieu Exbrayat, Lionel Brunie, Markus Fleute, Laurent Desbat, Isabelle Magnin, "Requêtes complexes et hybrides dans des bases d'images médicales distantes. Une illustration en imagerie cardiaque", ASTI'2001, Paris, France, 24-27 Mai 2001

F. Vincent, P. Clarysse, P. Croisille, and I. E. Magnin, “Segmentation of the heart from MR image sequences using a 3D active model,” Biomedical Engineering Society Annual Meeting, Seattle, Washington, USA, 2000.

P. Clarysse, M. Han, P. Croisille, and I. E. Magnin, “Exploratory analysis of the spatio-temporal deformation of the myocardium during systole from tagged MRI,” Biomedical Engineering Society Annual Meeting, Seattle, Washington, USA, 2000.

Clarysse, P., Canet E., Croisille P., Janier M., Neyran B. "Imagerie fonctionnelle multi-modalités de l'ischémie myocardique et de ses conséquences", VIIème colloque de la section 22 du CNRS, Paris, Avril 2000.

Clarysse P., Friboulet D., Magnin I.E., Revel D., "Suivi temporel de surfaces déformables - Application à la surface endocardique du VG", VIème Colloque "Thérapeutique et médicaments, de la recherche à la découverte", section 22 du CNRS, Reims, France, Mars 1997

Clarysse P., "Applications de la géométrie en traitement d'images", Journées de Géométrie Sous-Variétés et Applications, UCB Lyon I, 17-18 Mai 1995

Clarysse P., "Evolution temporelle de la courbure 3D des surfaces des parois cardiaques", Vème Colloque "Thérapeutique et médicaments, de la recherche à la découverte", section 22 du CNRS, Montpellier, France, pp. 13, 5-6 Décembre 1994

Clarysse P., Friboulet D., Magnin I. E., "Calcul de la courbure 3D des parois cardiaques en imagerie dynamique", IVème Colloque "Thérapeutique et médicaments, de la recherche à la découverte", section 22 du CNRS, Strasbourg, France, 1-2 Décembre 1993

Clarysse P., Rousseau J., Blond S., Gibon D., Dubois P., "Méthode de repérage par IRM", IIème Congrès sur la Recherche en Imagerie Médicale, Bordeaux, France, 10-12 Octobre 1990

- ***Séminaires***

"Traitement d’images et infographie en imagerie du cœur", Séminaire du LIGIM, Lyon, 1997.

"Imagerie Médicale : Principes et Aide à l’interprétation des Images", Ecole Centrale de Lyon, Janvier 2000.

# 5. SELECTION DE PUBLICATIONS

Les publications [1] et [2] sont relatives aux travaux en recalage d'images cardiaques et de nos efforts en faveur de la construction d'un modèle anatomique et fonctionnel individualisé du cœur. Les publications [3] à [5] sont des contributions à l'estimation (approche surfacique [4], IRM de marquage tissulaire [5]) et l'analyse du mouvement du cœur ([3]).


[1] Mäkelä T., Pham Q-C, Clarysse P., Nenonen J., Lötjönen J., Sipilä O., Hänninen H., Lauerma K., Knutti J., Katila T., Magnin I.E. A 3D model-based registration approach for the PET, MR and MCG cardiac data fusion, *Medical Image Analysis*, Vol. 7, N° 3 , pp. 377-389, September 2003.

[2] Mäkelä, T., Sipilä, O, Clarysse, P., Pauna, N., Pham, Q-C., Katila, T., Magnin, I.E. A review of cardiac registration methods, *IEEE Trans. Med. Imaging*., Vol. 21, N° 9, September 2002

[3] Clarysse P., Han M., Croisille P., Magnin I. E., Exploratory analysis of the spatio-temporal deformation of the myocardium during systole from tagged MRI, *IEEE Trans. Biomed. Eng., Vol.49, N°. 11, 2002, 1328-1339*

[4] Clarysse P., Basset C., Khouas L., Croisille P., Friboulet D., Odet C. and Magnin I.E. (2000) 2D spatial and temporal displacement and deformation field fitting from cardiac MR tagging. *Medical Image Analysis*, 4, pp. 253-268, 2000.

[5] Clarysse P., Friboulet D., Magnin I. E., "New shape descriptors for 3D deformable object tracking. Application to the left-ventricular surface of the heart", *IEEE T. Med. Imaging*, Vol. 16, N°4, pp. 392-404, 1997.

Available at www.ComputerScienceWeb.com
POWERED BY SCIENCE DIRECT®

Medical Image Analysis 7 (2003) 377–389

MEDICAL IMAGE ANALYSIS

www.elsevier.com/locate/media

# A 3-D model-based registration approach for the PET, MR and MCG cardiac data fusion

Timo Mäkelä[a,b,c,*], Quoc Cuong Pham[b], Patrick Clarysse[b], Jukka Nenonen[a,c], Jyrki Lötjönen[d], Outi Sipilä[e], Helena Hänninen[f], Kirsi Lauerma[e], Juhani Knuuti[g], Toivo Katila[a,c], Isabelle E. Magnin[b]

[a]*Laboratory of Biomedical Engineering, Helsinki University of Technology, P.O.B. 2200, FIN-02015 HUT Helsinki, Finland*
[b]*CREATIS, INSA, Batiment Blaise Pascal, 69621 Villeurbanne Cedex, France*
[c]*BioMag Laboratory, Helsinki University Central Hospital, P.O.B. 503, FIN-00029 HUS Helsinki, Finland*
[d]*VTT Information Technology, P.O.B. 1206, FIN-33101 Tampere, Finland*
[e]*Department of Radiology, Helsinki University Central Hospital, P.O.B. 340, FIN-00029 HUS Helsinki, Finland*
[f]*Division of Cardiology, Helsinki University Central Hospital, P.O.B. 340, FIN-00029 HUS Helsinki, Finland*
[g]*Turku PET Centre, c/o Turku University Central Hospital, Box 52, FIN-20521 Turku, Finland*

**Abstract**

In this paper, a new approach is presented for the assessment of a 3-D anatomical and functional model of the heart including structural information from magnetic resonance imaging (MRI) and functional information from positron emission tomography (PET) and magnetocardiography (MCG). The method uses model-based co-registration of MR and PET images and marker-based registration for MRI and MCG. Model-based segmentation of MR anatomical images results in an individualized 3-D biventricular model of the heart including functional parameters from PET and MCG in an easily interpretable 3-D form.


## 1. Introduction

Ischemic diseases and their dramatic consequence, the myocardial infarct, are the leading cause of mortality in industrial countries. From the physio-pathological point of view, ischemia results from a disequilibrium between myocardial perfusion, metabolism and contractile function. Following an ischemic event, the question of myocardial viability arises. Both ischemia diagnosis and viability estimation rely on the joint analysis of the perfusion, metabolism and contractile function, each of which being quantified with specific imaging modalities (Fig. 1). Consequences onto the electric and magnetic activity of the heart have also been observed. Therefore, computer-based methods are required to automatically perform multi-modal cardiac image registration in 3-D. This is the purpose of this work.

Anatomical (structural) information of the heart is usually provided by magnetic resonance imaging (MRI) and ultrasound (US). Metabolism can be analyzed with positron emission tomography (PET), perfusion with thallium single photon emission computed tomography (SPECT), MRI, or PET, and contractile function by using MRI and US. Fluorodeoxyglucose (FDG) PET imaging is

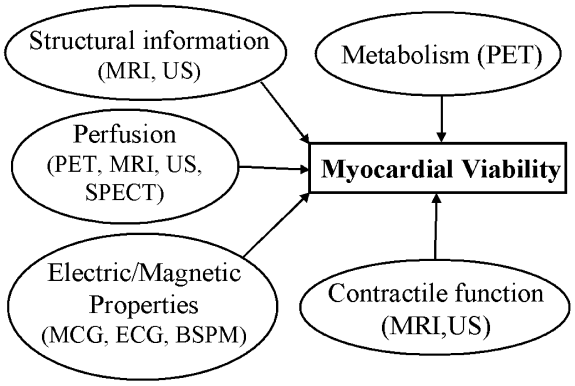


Fig. 1. Variety of imaging modalities required for the cardiac viability assessment.

*Corresponding author. Tel.: +358-9-451-3174; fax: +358-9-451-3182.
*E-mail address:* timo.makela@hut.fi (T. Mäkelä).

1361-8415/03/$ – see front matter 
doi:10.1016/S1361-8415(03)00012-4

considered as the gold standard to determine viable areas of the heart (Hartiala and Knuuti, 1995). The electrical activity of the heart creates both an electric and a magnetic field and can be measured by using electrocardiography (ECG) and magnetocardiography (MCG), respectively (Siltanen, 1988). In MCG and ECG *inverse problems*, a current distribution inside of the heart is estimated from noninvasively measured signals by solving a regularized inverse problem (Hämäläinen and Nenonen, 1999; MacLeod and Brooks, 1998). Thus, multichannel MCG and ECG studies can be applied in locating abnormal electrical activity in the heart (Nenonen et al., 2001). The MCG signals are generated by the same bioelectric currents as the ECG, but the MCG may show ischemia-induced deviations from the normal direction of depolarization and repolarization in a different way than ECG (Hänninen et al., 2001). In the literature, electrical activity and metabolism have usually been studied separately, principally because the acquisition system are quite different and involve different specialists. From the physiopathological point of view, it is clear that all the activities are related one to each other. Therefore, our objective here was to allow for the study of the correlation between the electrical (MCG data) and metabolic (PET imaging) activities which may reveal new aspects of hearts complex pathological processes. To our knowledge, this kind of comparison has not been done before. The presented 3-D method gives good possibilities especially for visual comparison of data from different imaging modalities. Whereas PET imaging is used to study the cardiac metabolism, the multichannel ECG and MCG mappings allow a comprehensive study of the electromagnetic fields of the heart. These mapping techniques give unique additional information on the electromagnetic manifestations of myocardial ischemia and viability. At present, the nuclear imaging modalities are mainly used in elective manner, applied only rarely in clinical decisions concerning cardiac care unit patients, whereas ECG monitoring is widely used in emergency care units. In the future, technical development will hopefully allow the MCG mapping function as clinical tool without need for shielding. Multichannel ECG and MCG studies, used with standard torso models (to obtain individual torso model one needs usually MR images), could then give estimation of ischemia (and viability). The 3-D model based approaches could be first used with functional data from ECG and/or MCG, and then be extended during the clinical studies with other modalities, such as MR and nuclear medicine studies. In this paper, we will use MRI for obtaining the heart's anatomy. Myocardial functional data are issued from FDG-PET for the metabolism and MCG data for the heart's electrical activity.

In viability studies, mental registration of the information from different imaging modalities is routinely performed by clinicians. Automatic registration, based on computer programs, is however expected to offer better accuracy, repeatability, and to save time. Registration of cardiac images is a more complex problem than brain image registration because of the mixed motions of the heart and the thorax structures. Moreover, as compared to the registration of brain images, the heart exhibits much fewer accurate anatomical landmarks and the images are usually acquired with lower resolution. A review of cardiac image registration approaches can be found in (Mäkelä et al., 2002a). These methods are usually based on manual intervention (Behloul et al., 2001; Waiter et al., 2000), automatic registration of thorax surfaces (Pallotta et al., 1995; Gilardi et al., 1998; Yu et al., 1995; Tai et al., 1997; Cai et al., 1999; Mäkelä et al., 2001a) or heart surfaces (Faber et al., 1991; Sinha et al., 1995; Andersson et al., 1995; Declerck et al., 1997; Thirion, 1995, 2001; Nekolla et al., 2000). Another category of methods relies on the matching of image intensities (Hoh et al., 1993; Bettinardi et al., 1993; Slomka et al., 1995; Eberl et al., 1996; Dey et al., 1999; Carrillo et al., 2001; Lötjönen and Mäkelä, 2001). In (Behloul et al., 2001), maximal myocardial deformation from tagged MRI and FDG-PET metabolism were combined using neuro-fuzzy rules to generate polar maps representing the viability. The registration was performed manually with the help of the long axis angles defined in the MRI protocol. In the 'MunichHeart' software, endocardial and epicardial contours were manually delineated in short axis (SA) MR images and registered with the same contours extracted from PET or SPECT using the maximum count detection algorithm (Nekolla et al., 1998, 2000).

In this work, we propose a method for extracting an individualized 3-D anatomical heart model which combines myocardial metabolic data from PET and electrical measurements from MCG. A first approach of the method was presented in (Mäkelä et al., 2001b). Here, it is improved by adding functional MCG results to the model. The method provides a 3-D geometric representation of the heart onto which functional information can be displayed. The data are presented in Section 2. An overview of the approach is given in Section 3, and the different steps are described in Section 4. The extraction of an individualized heart model is explained in Section 5. The construction of functional cartographies are described in Section 6. Results are presented in Section 7 and discussed in Section 8.

## 2. Cardiac imaging protocol

The cardiac data were composed of MR and PET images and MCG data of 10 patients (identified by P1 to P10) suffering from 3 vessels coronary artery disease, diagnosed with coronary angiography and regional dyskinesia in cineangiograms (Lauerma et al., 2000). The mean age was 69 (8 men, 2 women). All patients underwent MR and fluorine-18-deoxyglucose (FDG) PET imaging within 10 days. MCG measurements were also acquired.

- *MR images*. The MR data were acquired with a 1.5 T Siemens Magnetom Vision imager (Siemens, Erlangen, Germany) at the Department of Radiology in Helsinki University Central Hospital (HUCH). A series of 39 ECG-gated contiguous transaxial images was acquired during free respiration using a TurboFLASH sequence (Fig. 2(a)). The pixel size and the slice thickness were 1.95×1.95 mm and 10 mm, respectively. Five ECG-gated breath-hold cine SA sections were also acquired (Fig. 2(b)). The pixel size for SA slices was 1.25×1.25 mm and the slice thickness 7 mm with a gap of 15 mm between slices. About 15 time points were taken for each section with a repetition time of 40 ms.
- *PET images*. The static cardiac PET data were acquired with a Siemens ECAT 931/08-12 (Siemens/CTI, Knoxville, TN, USA) PET scanner at the Turku PET Centre (Turku, Finland). A series of 15 contiguous transmission and emission images were acquired (Fig. 2(c) and (d)). Transmission images were used for attenuation correction of emission images and also provided structural information that was utilized for registration purposes. The emission image, which can be assumed to be in good registration with the transmission image (Kim et al., 1991), gives absolute quantification of glucosis uptake. For both transmission and emission images, the pixel size and the slice thickness were 2.41×2.41 mm and 6.75 mm, respectively.
- *MCG data*. The MCG measurements were performed at rest and after stress with the 67-channel cardiomagnetometer (4-D NeuroImaging, Helsinki, Finland) at the BioMag Laboratory (Montonen et al., 2000) at HUCH. Acute ischemia was induced by exercise testing with a non-magnetic stress ergometer (Hänninen et al., 2001), pedaled in supine position.

The ST-segment difference signals of averaged post-stress and rest recordings were used in computing current density estimates (CDE) (Nenonen et al., 2001). In this work, the depolarization (QRS complex) data at rest was utilized. Patient-specific boundary-element torso models were acquired from magnetic resonance images, including the triangulated thorax and LV surfaces (Lötjönen et al., 1999, Pham et al., 2001). The torso was assigned a constant electrical conductivity of 0.2 S/m. Discrete CDE values were computed on the LV at midwall locations. The ill-posed inverse problem was regularized with three different methods (Tikhonov regularization with an identity or a surface Laplacian operator, and a maximum a posteriori estimator, MAP; for details, see (Nenonen et al., 2001)). In the present study, we selected MCG results obtained with the MAP estimator.

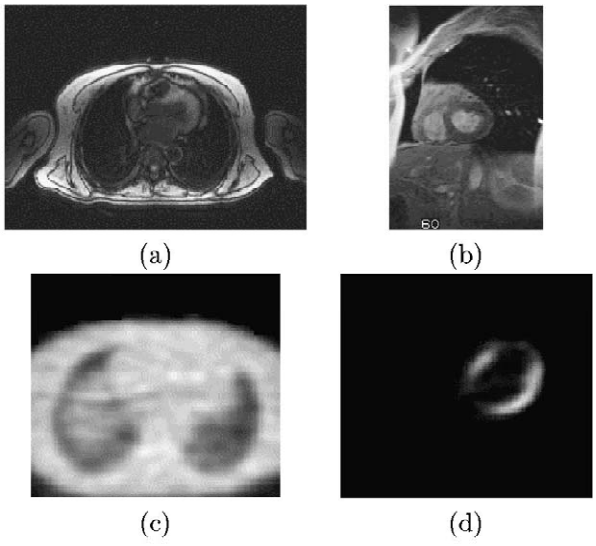


Fig. 2. (a) Transaxial and (b) SA MR images, (c) transmission and (d) emission PET images.

## 3. Method overview

The aim of the overall approach is to extract a 3-D anatomical model of the heart from patient MR images and to incorporate functional data, such as FDG uptake, information of the magneto-electric properties of the heart and other clinically relevant parameters to the model. The process is summarized in Fig. 3.

First, MR transaxial images were co-registered (rigid transformation) with the PET transmission image (Mäkelä et al., 2001a). The obtained registration parameters were used to register transaxial MR images and the PET emission image. PET slices that correspond to SA MR images were calculated by using MR header information. Then, a 3-D biventricular deformable model was initialized in the SA MR images to segment the myocardium. The deformed model was transformed into the registered SA PET image to obtain FDG uptake values. The model was also transformed to the transaxial MR image and MCG values were calculated for the LV midwall locations. The main steps of the method are described in the following sections.

## 4. Registration

### 4.1. PET-MRI registration

The rigid registration method for cardiac PET and MR images was fully described in (Mäkelä et al., 2001a). The registration method is based on the matching of the thorax and lungs surfaces which are visible in both PET transmission and MR transaxial images. The registration protocol first matches PET transmission and transaxial MR images by using a surface-based registration algorithm and then computes the SA PET slices corresponding to the SA MR slices. The emission and transmission PET and transaxial MR images were first interpolated to the same isotropic

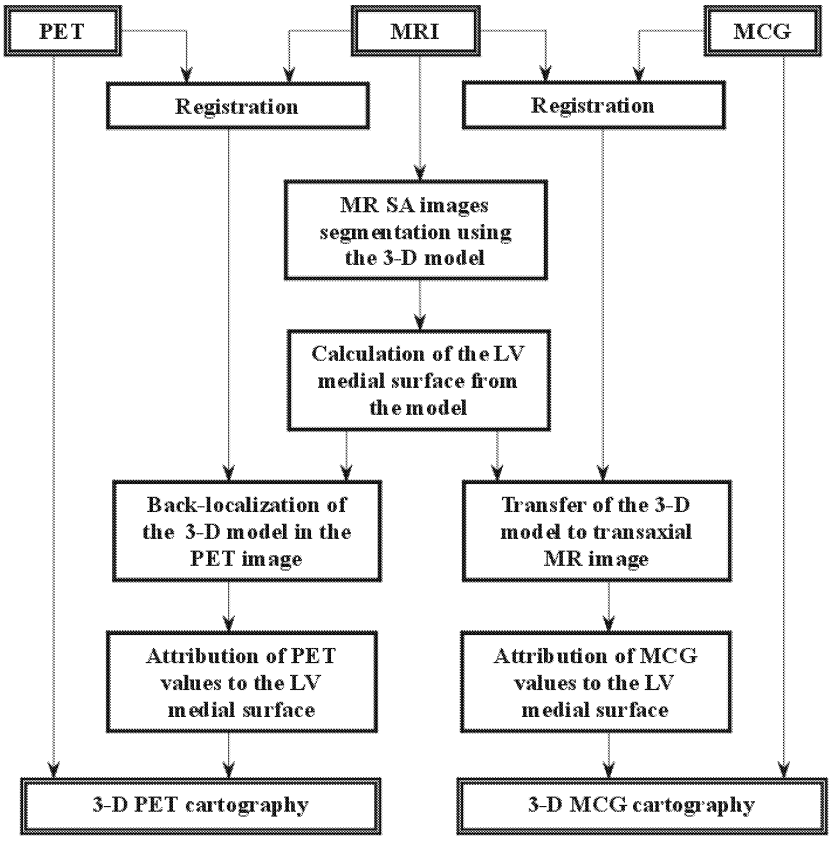


Fig. 3. Extraction of the 3-D anatomical and functional model of the heart including PET-FDG uptake and MCG values: main steps of the process.

voxel dimensions using tri-linear interpolation. Then, the PET transmission and emission images, which had smaller physical dimensions than MR image, was set to the geometric center of the MR image space. The thorax and lung surfaces were segmented from PET transmission image using the deformable model based segmentation method proposed in (Lötjönen et al., 1999). Segmentation of the thorax structures (thorax and lungs surfaces) was based on the elastic deformation of a topologic and geometric prior model using a multiresolution approach. A thorax model including a full triangulated thorax and the lungs surfaces was used with MR images (Fig. 4(a)) while with the PET transmission images, the model was truncated (Fig. 4(b)). The initialization of the models can be made in three ways in our software: (1) manually, (2) matching bounding boxes set around the model and binarized (thresholded) volume, or (3) making rigid registration with the model and binarized volume. In this work, the initialization was done manually. However, we have also used successfully the second approach in more than 50 cases as the thorax is segmented from MR images. Although the bounding boxes do not allow any rotation correction, it has performed well because subjects are always lying on the bed in an approximately same orientation. The segmentation algorithm can cope initialization errors up to a few degrees and several centimeters as demonstrated also in the original article (Lötjönen et al., 1999).

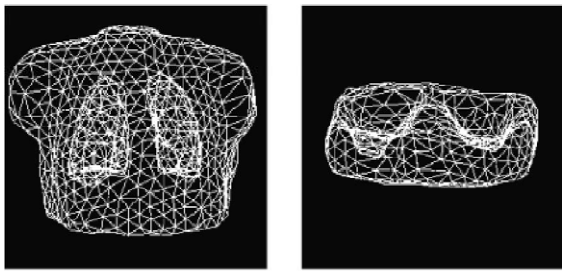


Fig. 4. Geometric and topologic prior model of the thorax for the (a) MR and (b) PET transmission image segmentation.

The free-form based deformation algorithm adapts the prior model to locally fit the salient edges in the image within a minimization process. The energy to be minimized is

$$E_{\text{total}} = E_{\text{image}} + \gamma E_{\text{model}}, \quad (1)$$

where $E_{\text{image}}$ represents the matching error between the prior model and the partial edges in the data volume. $E_{\text{model}}$ tends to preserve the model's shape by restricting the deformation of the prior model. It describes the deviation of the model's surface normals from their original orientation. The image energy results from a

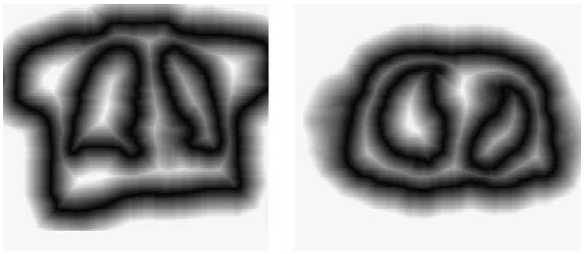

Fig. 5. MR distance maps. The registration algorithm minimizes the distance of the thorax surface points in PET relatively to this distance map.

distance map (Borgefors, 1988) built upon edges extracted either by a Canny–Deriche method (Canny, 1986) or image thresholding (Fig. 5). In order to select edges corresponding to the model, oriented distance maps (Lötjönen et al., 1999) were computed. The parameter $\gamma$ sets the contribution of the two energy components. A multiresolution process speeds up the minimization process and improves the convergence. Figs. 6(a) and (b) show segmentation results for the thorax structures in MR and PET transmission images.

The parameters of the rigid transformation parameters (three translations, three rotations) between the two image sets are derived from the minimization of the distance between the point set from segmented PET transmission image surfaces and a distance map (Borgefors, 1988) built upon the segmented transaxial MR surfaces (Fig. 5). The uniformly distributed nodes of the deformable model were used as point set from PET transmission image surface. PET transmission and MR transaxial images are acquired in a similar geometry; the model is therefore initialized in a position close to the registration solution. The minimization algorithm is more detailed in (Mäkelä et al., 2001a).

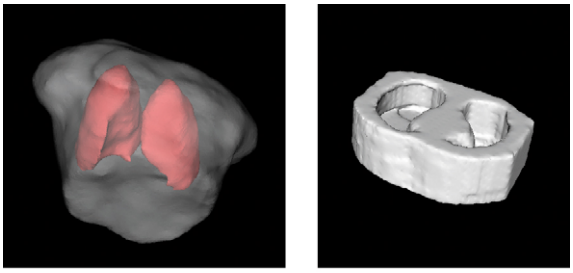

(a) (b)

Fig. 6. Segmented (a) MR and (b) PET transmission images.

PET emission image was registered with transaxial MR image using the computed registration parameters. The PET transmission image was thus used as a linking mediator to register PET emission image to MR image coordinates.

After registration of the PET emission image with the transaxial MR image, the SA PET slices that corresponded to the SA MR images were computed using MR header information of transaxial and SA MR images (Fig. 7). Note that, as PET acquisition was not gated in this study, the PET images were registered with the SA MR data at end-diastole. This cardiac instant best corresponds to the average PET image.

### 4.2. MCG–MRI registration

MCG measurements were registered with MRI data by using external markers. The position of the MCG recording system with respect to the patient is determined by attaching three marker coils (magnetic dipoles) to the skin. The magnetic fields produced by the coils are then used to compute the sensor locations relatively to the marker coils (Montonen et al., 2000). The three marker coils were also used to define the MCG sensor coordinates with respect to the MCG markers, a set of nine external marker positions which were selected for registering the MCG sensor system to MR images (Fig. 8).

The locations of the MCG markers were defined by attaching a cross-shaped object consisting of two silicone strips of rubber on the skin of the thorax. The separation between neighboring MCG markers was 5 cm in the head-feet direction and 10 cm in the left-right direction. The locations of the MCG markers and the small marker

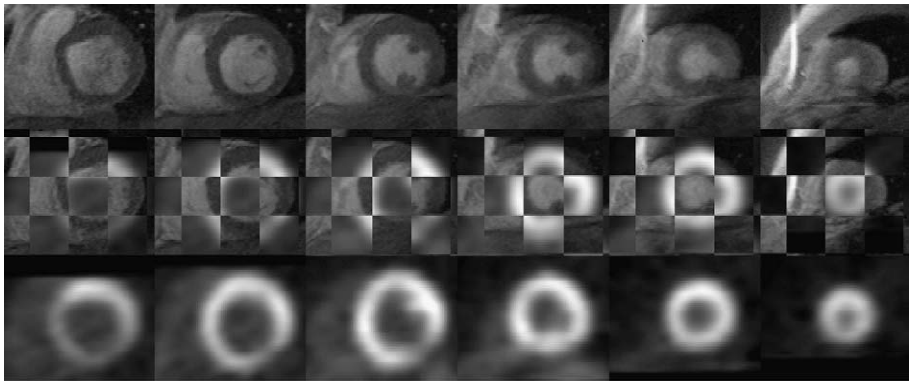

Fig. 7. A stack of registered end-diastolic SA MR (top) and PET emission (bottom) image slices for the P1 case. In the middle row, the images were overlaid in block format to visualize registration results.

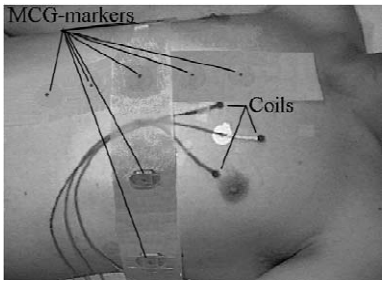


Fig. 8. Placements of the nine MCG markers and three marker coils on the chest in a typical patient study. The round pieces of plastic in two silicone strips of rubber denote the MCG marker locations. Their centerpoints are digitized, and the pieces are removed from the strips before stamping the locations with ink visible in UV light. The three marker coils are used to define the MCG sensor coordinates in respect to the MCG markers.

coils were defined with a 3-D digitization system (3SPACE ISOTRAK II; Polhemus, Colchester, VT, USA). The digitized MCG marker positions were stamped with non-toxic ink, visible only in ultraviolet light. Prior to MR imaging, the nine MRI markers were placed on the stamped positions on the skin. The MRI markers were constructed from two perpendicular tubes filled with 1 mmol/l $MnCl_2$ fluid, inserted inside a piece of plastic of $4.0 \times 4.0 \times 0.7$ cm. The cross-shaped figure of a marker was well visible in the MR images. The MRI markers were located manually from MR images, using a dedicated software. The nine marker coordinate sets $(x, y, z)$ in the MCG and MRI coordinate systems, respectively, were registered using a non-iterative least-squares method (Arun et al., 1987). Only rigid transformations including global rotations and translations were considered. MCG–MRI registration protocol has been applied to more than 50 patient studies (Pesola et al., 2000). With our patient studies we have obtained the root mean square (RMS) error of the nine registered markers to be about 6 mm. The registration error includes various error sources such as the effect of breathing, reattachment of the markers between MCG and MR measurements, localization of the markers from MR images and shape changes in thorax between the measurements because of the flexibility of the shoulders and the skin (Mäkelä et al., 2002b). One of the reasons why the RMS error values are relatively low in our measurements is that the markers in our protocol were attached in positions which were not very sensitive to different alignment errors.

## 5. Capturing the heart anatomy

MR images provide relevant information on the cardiac anatomy. In this section, we present a method for extracting a 3-D individualized anatomical model of the heart from MR short axis images, based on an Elastic Active Region Model (ARM) which is an extension of our previous work (Pham et al., 2001). Several groups have proposed superficial deformable models to segment the cardiac chambers in three dimensions (McInerney and Terzopoulos, 1996). More recently, Montagnat and Delingette (2000) introduced simplex meshes for segmenting the LV surfaces from 4-D cardiac sequences in MR, SPECT and ultrasound imaging. The reader can find in (Frangi et al., 2001) a good review of 3-D heart modeling approaches used for the purpose of segmentation. Contrary to superficial models, the ARM relies on a volumetric deformation of a geometric heart model. It allows to simultaneously extract the LV and RV endocardial surfaces, as well as the epicardium, while enforcing regularity between these surfaces. In addition, it is formulated in the mechanical framework of elastic bodies that is often used in the context of motion estimation (Papademetris et al., 2001). The ARM is also closely related to the work of Sermesant et al. (2001) who introduced an electro-mechanical model of the heart. In this model, the contraction is controlled by simulating the propagation of electrical waves and taking into account the interaction with ultrasound images. Nevertheless, in this work, the objective is not to provide a complete biomechanical model of the heart, but to accurately segment MR cardiac images by means of a simple but natural description of the heart. The segmentation process can be divided in two main steps. First, the template is spatially positioned by registering it with the image to be segmented. Then, starting from this initial configuration, it is elastically deformed to fit the cardiac structures. Each step will be described in the following.

### 5.1. The 3-D biventricular template

A priori information on the shape of the object of interest strongly constrains the segmentation. We thus developed a 3-D geometric accurate representation of the heart ventricles. This volumetric template was created from a MR reference dataset. The heart of a healthy volunteer was imaged using a cine-MR protocol and the end-diastolic time frame was selected, as we only focus on the images corresponding to the end-diastole. A medical expert interactively delineated the epi- and endocardial contours of the two ventricles on each of the 2-D short axis slices. The corresponding surfaces were then reconstructed and the interior meshed with tetrahedra using the GHS3D software (INRIA, Gamma Project, France). The 3-D biventricular template is shown in Fig. 9.

### 5.2. Interpolating 3-D MR volumes

In order to take advantage of a fully three-dimensional interaction between the model and the short axis images of the heart, 3-D isotropic volumes were interpolated from stacks of 2-D short axis slices. SA images present a good spatial resolution in the acquisition plane, but a poor one in the transversal direction. For the studied cases, the inter-

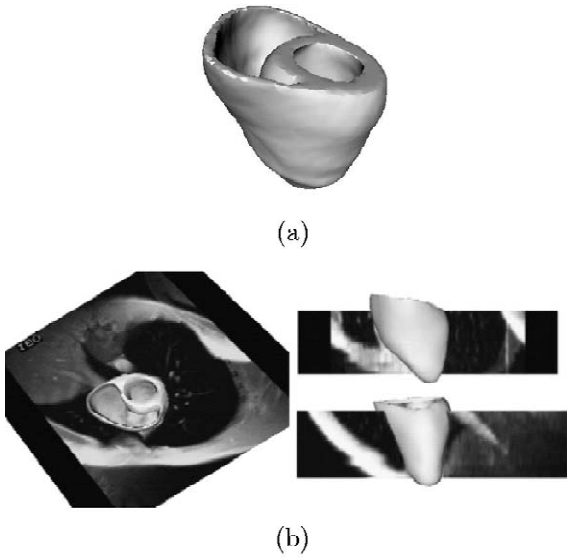

Fig. 9. (a) 3-D prior biventricular model (19 524 nodes, 94 402 tetrahedral elements), (b) model immersed in the MR data.

slice distance was 15 mm, whereas the pixel size was less than 1.5 mm. In such conditions, we experimentally observed that the shape based interpolation technique (Grevera and Udupa, 1996) gave better results than polynomial interpolations on our data.

### 5.3. The model initialization as a registration step

The model is rigidly positioned with respect to the image to be as close as possible to the cardiac structures to be segmented. This is done by searching for the 6 parameters of the rigid spatial transformation $T$ (3 translations, 3 rotations) applied to the model, that minimizes the following energy:

$$E_{\text{ini}}(T) = E_{\partial\Omega}(T)\, E_W(T). \tag{2}$$

Like in (Pluim et al., 2000), the energy to be minimized is a product of an energy based on an intensity criterion and an energy deriving from the image gradient. Here, $E_{\partial\Omega}(T)$, computed on the boundary of the template, represents a distance from the model to detected contours in the image. In practice, we take the mean square Euclidean distance from the boundary nodes to the image edges. The region energy $E_W(T)$ is a similarity measure between the image intensities. It is estimated in a floating meshed domain $W$ surrounding the template ($\Omega \subset W$) and can either be the sum of the square intensity differences (SSD) sampled on the nodes of $W$, or the mutual information (MI) between the two gray level distributions. In most of the cases, good results are obtained with the SSD criterion which is known to be efficient in the monomodal case (Fitzpatrick and Maurer, 2000). The total initialization energy is minimized using the Powell's optimization method (Press et al., 1988) which does not require the computation of the function's gradient. Fig. 10 shows initialization results for two patients.

### 5.4. The deformation model

The second step of the segmentation process is seen as the deformation of an elastic body submitted to an external force field. The myocardium is modeled as a linear elastic continuous medium. Under the small deformation assump-

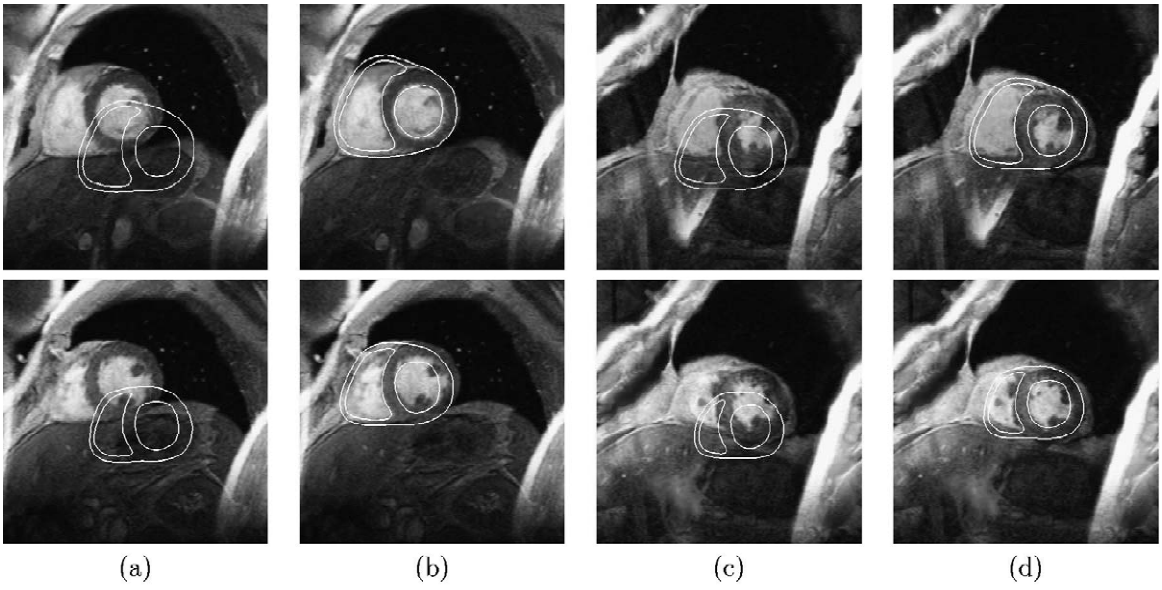

Fig. 10. Initialization step. (a) Patient P1, before registration, (b) patient P1, after registration, (c) patient P2, before registration, (d) patient P2, after registration. First row: basal cross-section; second row: mid-ventricular level.

tion, the linearized form of the Green–Lagrange strain tensor is used:

$$[\epsilon] = \frac{1}{2}(\nabla \mathbf{u} + \nabla \mathbf{u}^{\mathrm{T}}), \tag{3}$$

where **u** denotes the displacement vector. The stress is related to the strain by the constitutive law of the material. For a homogeneous isotropic material, it takes the form

$$\boldsymbol{\sigma} = \mathbf{R}\boldsymbol{\varepsilon} = \mathbf{RSu}, \tag{4}$$

where $\boldsymbol{\sigma} = (\sigma_{11},\sigma_{22},\sigma_{33},\sigma_{12},\sigma_{23},\sigma_{31})^{\mathrm{T}}$ and $\boldsymbol{\varepsilon} = (\varepsilon_{11},\varepsilon_{22},\varepsilon_{33},\varepsilon_{12},\varepsilon_{23},\varepsilon_{31})^{\mathrm{T}}$ are, respectively, the stress and the strain vectors, **R** the elasticity matrix depending on two mechanical parameters (either the Lamé coefficients $\lambda$ and $\mu$, or the Young modulus $E$ and the Poisson ratio $\nu$), and **S** a differential operator. If we note $\Omega$ the considered domain, $\partial\Omega$ its boundary, and **t** the superficial external forces applied on the boundary, the equilibrium state corresponds to the minimum of the following potential energy:

$$E_{\mathrm{glob}}(\mathbf{u}) = \underbrace{\frac{1}{2}\int_{\Omega} \boldsymbol{\sigma}\boldsymbol{\varepsilon}\, \mathrm{d}\mathbf{x}}_{E_{\mathrm{elast}}(\mathbf{u})} - \alpha \underbrace{\int_{\partial\Omega} \mathbf{t}(\mathbf{I}+\mathbf{u})\cdot\mathbf{u}\, \mathrm{d}\mathbf{s}}_{E_{\mathrm{data}}(\mathbf{u})}. \tag{5}$$

The first term $E_{\mathrm{elast}}(\mathbf{u})$ is an elastic energy which regularizes the deformations imposed by the external energy $E_{\mathrm{data}}(\mathbf{u})$, evaluated in the deformed configuration (if we assume that the displacements are small). In the case of large displacements, the geometric non-linearity should be taken into account by updating the elastic energy during the deformation process. The external force field deriving from the image is chosen such that it tends to attract the model's boundary towards salient features existing in the image. One way to compute a 3-D force field is to calculate the gradient of a potential image $\mathbf{t}(\mathbf{x}) = -\nabla P(\mathbf{x})$ which can be, for example, either the norm of the image gradient, an edge map extracted with a Canny–Deriche operator and smoothed with a gaussian filter, or a distance map (chamfer or Euclidean distance). The Gradient Vector Flow (GVF), proposed by Xu and Prince (1998), directly provides a force field which allows a better convergence, especially in the case of concavities. In our experiments, the GVF computed from the norm of the image gradient was used in most of the cases.

Eq. (5) is discretized using the Finite Element Method (FEM) with linear basis functions (Zienkiewicz and Taylor, 1987). The energy to be minimized thus becomes

$$E_{\mathrm{glob}}(\mathbf{U}) = \frac{1}{2}\mathbf{U}^{\mathrm{T}}\mathbf{K}\mathbf{U} + \alpha\mathbf{F}\cdot\mathbf{U}, \tag{6}$$

with **U** being the global displacement vector, **F** the global force vector and **K** the stiffness matrix. A minimum is reached for

$$\mathbf{KU} = \mathbf{F}. \tag{7}$$

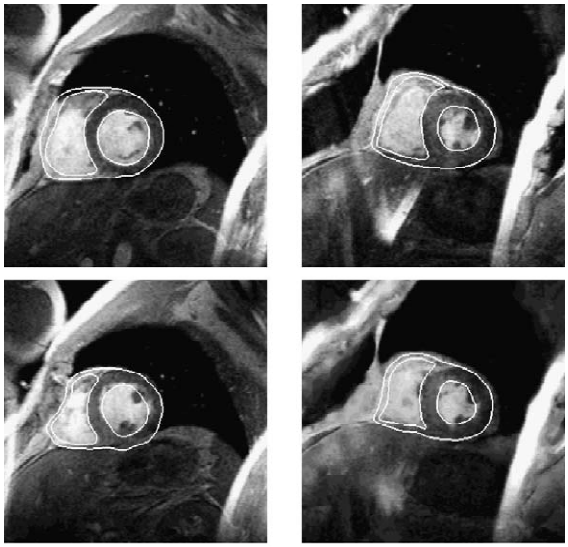

(a) (b)

Fig. 11. Segmentation results. (a) Patient P1, (b) patient P2. First row: basal slice; second row: mid-ventricular level.

As **F** is a function of the displacement, Eq. (7) is solved iteratively using a semi-implicit Euler scheme. Final segmentation results after the model deformation are shown in Fig. 11 for the two same cases.

## 6. Functional model of the heart

### 6.1. FDG-PET cartography

After the registration and segmentation steps, functional data was attributed to the elements and nodes of the 3-D biventricular model. Also some parameters with clinical interest was derived from MR imaging. First, the model was labeled so that it was possible to separate the right and left ventricles and obtain internal and external surfaces. Moreover, cavity volumes, myocardial mass and local wall thickness were computed. In order to enrich the model with metabolic information, the model was transformed into the registered PET-FDG emission image. A LV medial surface was automatically calculated between LV endo- and epicardial surfaces (Fig. 12).

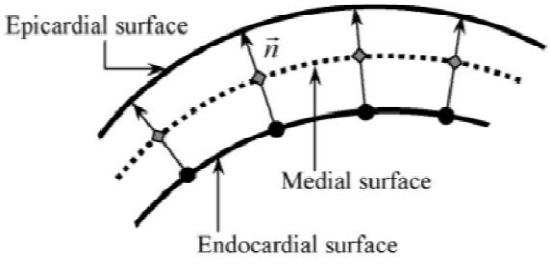


Fig. 12. Calculation of the medial surface using the segmented epicardial and endocardial surfaces.

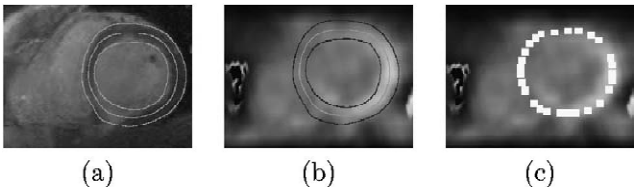


Fig. 13. (a) Intersection of endocardial (inner contour), epicardial (outermost contour) and calculated medial (middle contour) surfaces with a MR SA slice, (b) the same contours are shown in the corresponding registered PET SA image (medial contour in the middle) and (c) the mean value of the FDG-uptake was computed at the medial surface nodes in a small neighborhood.

The medial surface nodes were calculated by, first computing the 3-D normal to each node of the endocardial surface and, secondly, calculating the middle point of the segment normal to the endocardial surface and its intersection with the epicardial surface (Fig. 13(a)). Surfaces were transformed to registered PET emission image and a FDG uptake mean value was computed at each node of the medial surface (Fig. 13(b), middle contour) in a $5\times5\times5$ neighborhood, which corresponds to $6.25\times6.25\times6.25$ mm physical dimensions (Fig. 13(c)).

### 6.2. Magneto-electric cartography

MCG inverse current–density estimates were calculated for the nodepoints of the medial surface. To this aim, the medial surface was transformed from MR SA plane to transaxial MR coordinate system by using MR header information. The MCG measurements were regularized with a MAP estimator.

## 7. Results

### 7.1. FDG-PET cartography

Fig. 14(left) and Fig. 15(left) illustrate the FDG metabolic activity over the LV medial surface for 2 cases. Right ventricular and epicardial surfaces are shown in transparency. In Fig. 14(right) and Fig. 15(right), the corresponding PET bull's eye (polarmap) presentations are shown for a qualitative evaluation of the 3-D displays (Siemens software, Turku PET Centre). Bull's eye images are commonly used method for displaying functional information of the heart. The center corresponds to the

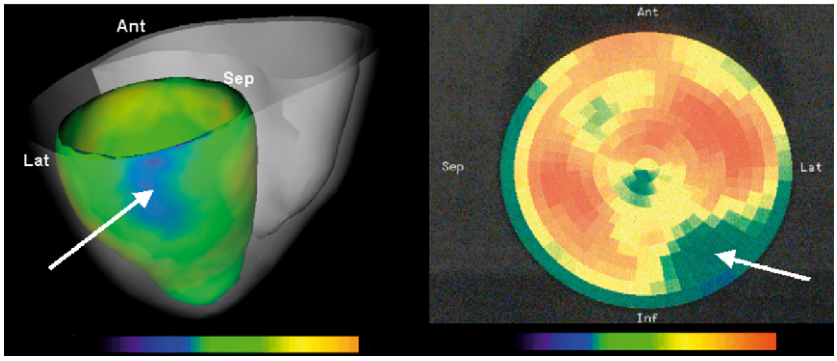


Fig. 14. 3-D representation of the FDG PET uptake values on the biventricular heart model (left) for patient P1. Interactively made bull's eye representation (Siemens software) of the corresponding PET image is presented on the right. The polarmap shows PET values at mid-wall location. Scar area can be seen in dark green at the basal level of the 3-D display (arrows).

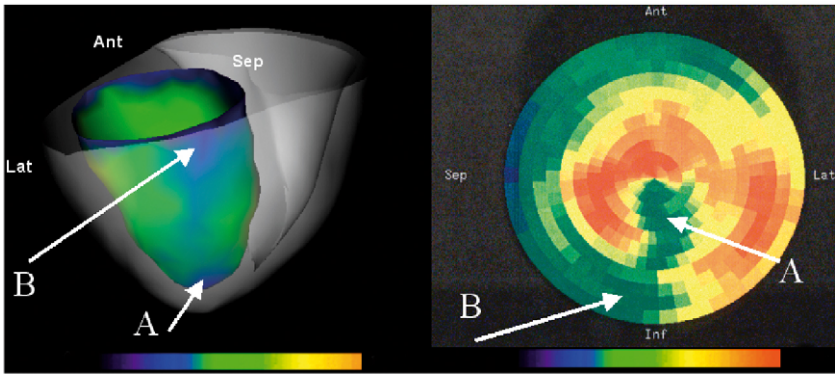


Fig. 15. Left: 3-D representation of the FDG PET uptake values on the biventricular heart model for patient P2. Right: corresponding bull's eye representation (Siemens software) with values estimated at mid-wall location. The low LV FDG uptake areas (arrows A, B) can be seen clearly in darker colors in the figures.

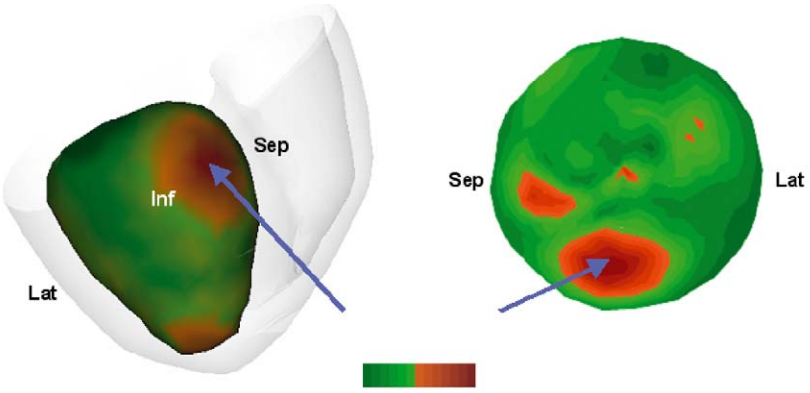


Fig. 16. Left: 3-D representation of the MCG values on the biventricular heart model for patient P1. Right: interactively made corresponding bull's eye representation calculated from the 3-D medial surface. Highest current magnitudes can be seen in red at the basal level of the presentations (arrows) and lowest current magnitudes in dark green.

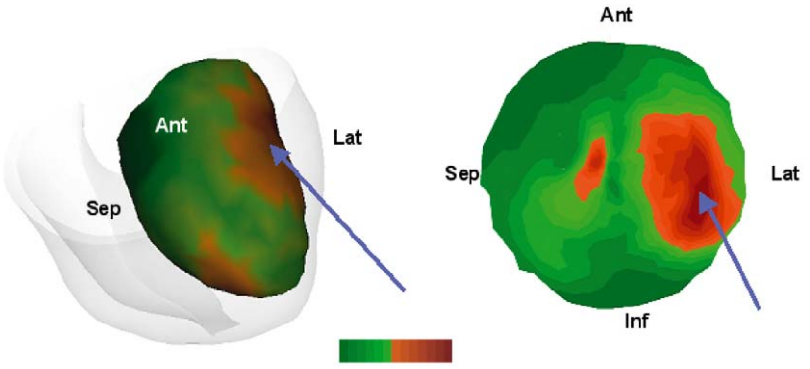


Fig. 17. Left: 3-D representation of the MCG values on the biventricular heart model for patient P2. Right: interactively made corresponding bull's eye representation calculated from the 3-D medial surface.

apex and the outermost ring represents the basal slice. In such polarmaps, metabolic activity is estimated at left-ventricular mid-wall.

The corresponding low LV FDG uptake areas can clearly be seen in both the bull's eye images (dark green in Figs. 14 and 15(right)) and in the 3-D model displays (arrows in Figs. 14 and 15(left)). Visualizations of the 3-D model were performed using the VTK software library.[1]

### *7.2. Magneto-electric cartography*

MCG results are presented on the medial surface for P1 in Fig. 16 and P2 in Fig. 17. For both cases, the 3-D visualization is presented on the left and the corresponding bull's eye representation computed from the extracted 3-D medial surface on the right. The MCG results were computed from the resting state data at a single time instant in the middle of the QRS complex. The results have to be regarded illustrative in that sense that the electrical activity in the right ventricle was neglected in the inverse calculations.

[1]The visualization Toolkit (VTK), http://www.kitware.com.

## 8. Discussion and conclusion

In this paper, we presented a new approach for the combination of anatomical and functional data from various cardiac imaging modalities. It relies on the registration of thorax structures (thorax surfaces) which are extracted from MR anatomical and PET transmission images. In order to provide 3-D displays of the heart that are easily interpretable by the physician, an individualized 3-D biventricular heart model is extracted from the SA MR images. The various geometrical and functional parameters can therefore be represented onto this model through the LV medial surface (Figs. 14–17). Following our previous efforts, we show in this paper the ability of the method to integrate information about the magneto-electric activity of the heart from MCG. The fusion of metabolic data from PET and magneto-electrical potential onto the same individualized 3-D heart model from MRI has been illustrated on two pathological cases. With such an approach, the localization of metabolic and conduction defects is straightforward since the biventricular model allows for the unambiguous identification of myocardial territories. Within the same framework, it is natural to envisage the inclusion of other complementary functional data such as

information related to the myocardial deformation or perfusion (Behloul et al., 2001).

The reliability of the method mainly depends on the accuracy of the rigid PET-MRI registration. The registration results of 10 cases were visually inspected by a medical expert. Nine over the 10 available cases were considered to provide satisfactory correspondence results. In the remaining bad case, unexpected artifacts were observed in FDG-PET data. In a previous paper (Mäkelä et al., 2001a), we proposed a quantification of the registration accuracy based on the calculation of a distance between segmented surfaces in PET and MRI. The mean distance was 3 mm with a maximum of 4 mm. This is only an indication of the performance of the registration algorithm since it highly depends upon the segmentation of the thorax structures. It also provides a simple mean to detect possible registration failure. A more systematic and accurate validation of the registration method is currently conducted through image simulations. Also intensity based methods, like mutual information, are potential alternative to determine registration parameters in this kind of registration methods where the PET transmission image is used as a linking mediator to register PET emission image to MR image coordinates. In some cases, intensity based methods can even allow to register the emission image directly with the anatomical image.

PET imaging devices have typically 4–10 mm spatial resolution (Hartiala and Knuuti, 1995). In general, the ability of our 3-D model based method to detect functional abnormalities is limited by the spatial resolution of the PET imaging device. In MCG, accuracies of 5 to 25 mm have been reported by comparing the MCG localization results to: (i) cardiac surgery, (ii) catheter ablation, (iii) the results of invasive electrophysiological studies, (iv) ECG localization results, and (v) physiological knowledge (X-ray or MRI). Besides patient studies, the ability of the MCG to locate artificial current dipoles has been tested with physical thorax phantoms. A non-magnetic pacing catheter in a realistically shaped thorax phantom resulted in equal accuracies of 5–10 mm between MCG and ECG mapping data (Fenici et al., 1998). On the other hand, the same catheter in 15 patients showed significantly better localization accuracy with MCG data (7 mm) than with simultaneously recorded ECG mapping data (25 mm) (Pesola et al., 1999).

The MCG results in this work were evaluated on the median LV surface during the cardiac depolarization. The resting-state MCG data in the peak of the QRS contains contributions from both ventricles, while the LV contribution dominates. In this study the RV was not included in the inverse MCG computations. The main motivation to use only the LV surface came from our previous study where we investigated the MCG data after physical exercise test in the same patient population (Nenonen et al., 2001). In that study the ST segment was analyzed and difference signals were computed (post-exercise minus rest). This difference was associated with exercise-induced ischemia which was known to arise in the left ventricle on the basis of PET and MRI (Lauerma et al., 2000). While the whole MCG (and ECG) source imaging methodology is still under rapid development (Hämäläinen and Nenonen, 1999) the results show that MCG, due to a millisecond time resolution, may be able to provide new valuable information on cardiac function, especially when constrained with accurate anatomy from MRI and combined with other medical imaging data.

The temporal correspondence of the PET and MR images has been overcome by assuming the correspondence between the MR transaxial, end-diastolic SA images, and the PET acquisitions, as it is usually admitted in clinical practice. In fact, transaxial MR images were obtained with a snapshot technique during free respiration while PET measurements were accumulated during a relatively long period of time (about 10 min). This might generate differences in the thorax and lungs shape and, consequently, cause registration errors. ECG-gated PET with non-rigid registration could certainly help to better handle the temporal correspondence problem.

The results of the automatic extraction of the biventricular model using the ARM were quite satisfactory for the two processed cases as shown in Fig. 11. This step, which is independent of the others, is important since (i) it extracts an individualized anatomical model from which volumes, masses, wall thickness can be derived, (ii) it provides the region of interest where the functional parameters from PET and MCG are estimated. We are currently quantifying the performance of the ARM in terms of accuracy (as compared to manual tracing) and robustness, especially as a function of model initialization. In addition, acquisition sequences such as stimulated echo sequences (e.g. TrueFISP, bFFE, Fiesta) provide better resolution and contrast and may improve the reliability and the accuracy of the segmentation results.

The medial surface seems to us the most straightforward way to obtain functional cartographies preventing from border effects that could occur from slight mis-registration. In this work, we implemented a simple geometrical approach to compute this surface. Other methods such as the centersurface (Bolson et al., 1995) could also be applied. In order to keep the volumetric property of the model, the next step will consist in the anatomical re-parameterization of the heart's geometry so that the functional parameters can be easily depicted on the myocardial borders as well as inside the wall by interactively peeling the model, for instance.

In conclusion, we have presented a model-based approach for the combination onto patient-specific heart model of both anatomical and diverse functional data from multimodality cardiac imaging. In this work, one of the main purposes was to automatically register metabolic PET and electromagnetic measurements from MCG. Similar approach could also be used to combine other modalities

such as SPECT and multichannel ECG studies. We believe that the presented approach can help the radiologist or cardiologist to rapidly apprehend the functional state of the myocardium through 3-D intuitive cartographies. It is therefore possible to accurately compare the different imaged functions (metabolism, magneto-electric activity) in the context of physio-pathological studies on the ischemic diseases, for instance, which consequences on the cardiac muscle are complex and not yet fully understood. In order to enrich the model, other parameters related to the heart motion and perfusion will be integrated in the near future.

## Acknowledgements

This study was partly granted by the Scientific Department of the French Embassy in Finland, the Region Rhône Alpes, through the ADéMO project and The Foundation of Technology in Finland. This work was performed within the framework of the joint incentive action 'Beating Heart' of the research groups ISIS, ALP and MSPC of the French National Center for Scientific Research (CNRS).

## References

Andersson, J.L.R., Bagnhammar, B., Schneider, H., 1995. Accurate attenuation correction despite movement during PET imaging. J. Nucl. Med. 36 (4), 670–678.

Arun, K.S., Huang, T.S., Blostein, S.D., 1987. Least-squares fitting of two 3-D point sets. IEEE Trans. Pattern Anal. Machine Intell. 9 (5), 698–700.

Behloul, F., Lelieveldt, B.P.F., Boudraa, A., Janier, M., Revel, D., Reiber, J.H.C., 2001. Neuro-fuzzy systems for computer-aided myocardial viability assessment. IEEE Trans. Med. Imaging 20 (12), 1302–1313.

Bettinardi, V., Gilardi, M., Lucignani, G., Landoni, C., Rizzo, G., 1993. A procedure for patient repositioning and compensation for misalignment between transmission and emission data in PET heart studies. J. Nucl. Med. 34 (1), 137–142.

Bolson, E., Sheehan, F., Legget, M., Jin, H., McDonald, J., Sampson, P., Martin, R., Bashein, G., Otto, C., 1995. Applying the centersurface model to 3-D reconstructions of the left ventricle for regional function analysis. In: Computers in Cardiology. IEEE Computer Society, Long Beach, CA, pp. 63–66.

Borgefors, G., 1988. Hierarchical chamfer matching: a parametric edge matching algorithm. IEEE Trans. Pattern Anal. Machine Intell. 10 (6), 849–865.

Cai, J., Chu, J., Recine, D., Sharma, M., Nguyen, C., Rodebaugh, R., Saxena, A., Ali, A., 1999. CT and PET lung image registration and fusion in radiotherapy treatment planning using the chamfer-matching method. Int. J. Radiat. Oncol. Biol. Phys. 43 (4), 883–891.

Canny, J., 1986. A computational approach to edge detection. IEEE Trans. Pattern Anal. Machine Intell. 8 (6), 679–698.

Carrillo, A., Duerk, J., Lewin, J., Wilson, D., 2001. Semiautomatic 3-D image registration as applied to interventional MRI liver cancer treatment. IEEE Trans. Med. Imaging 19 (3), 175–185.

Declerck, J., Feldmar, J., Goris, M., Betting, F., 1997. Automatic registration and alignment on a template of cardiac stress and rest reoriented SPECT images. IEEE Trans. Med. Imaging 16 (6), 727–737.

Dey, D., Slomka, P., Hahn, L., Kloiber, R., 1999. Automatic three-dimensional multimodality registration using radionuclide transmission CT attenuation maps: a phantom study. J. Nucl. Med. 40 (3), 448–455.

Eberl, S., Kanno, I., Fulton, R., Ryan, A., Hutton, B., Fulham, M., 1996. Automated interstudy image registration technique for SPECT and PET. J. Nucl. Med. 37 (1), 137–145.

Faber, T., McColl, R., Opperman, R., Corbett, J., Peshock, R., 1991. Spatial and temporal registration of cardiac SPECT and MR images: methods and evaluation. Radiology 179 (3), 857–861.

Fenici, R., Nenonen, J., Pesola, K., Korhonen, P., Lötjönen, J., Mäkijärvi, M., Poutanen, V.P., Keto, P., Katila, T., 1998. Non-fluoroscopic localization of an amagnetic stimulation catheter by multichannel magnetocardiography. PACE 22, 1210–1220.

Fitzpatrick, J., Hill, D., Maurer, C., 2000. Image registration. In: Handbook of Medical Imaging, Vol. 2. SPIE Press, pp. 375–435.

Frangi, A.F., Niessen, W.J., Viergever, M.A., 2001. Three-dimensional modeling for functional analysis of cardiac images, a review. IEEE Trans. Med. Imaging 20 (1), 2–25.

Gilardi, M.C., Rizzo, G., Savi, A., Landoni, C., Bettinardi, V., Rossetti, C., Striano, G., Fazio, F.N., 1998. Correlation of SPECT and PET cardiac images by a surface matching registration technique. Comput. Med. Imag. Graph. 22, 391–398.

Grevera, G.J., Udupa, J.K., 1996. Shape-based interpolation of multi-dimensional grey-level images. IEEE Trans. Med. Imaging 15 (6), 881–892.

Hämäläinen, M., Nenonen, J., 1999. Magnetic source imaging. In: Encyclopedia of Electrical Engineering, Vol. 12. Wiley, New York, pp. 464–479.

Hänninen, H., Takala, P., Mäkijärvi, M., Montonen, J., Korhonen, P., Oikarinen, L., Simelius, K., Nenonen, J., Katila, T., Toivonen, L., 2001. Recording locations in multichannel magnetocardiography and body surface potential mapping sensitive for regional exercise-induced ischemia. Basic Res. Cardiol. 96, 405–414.

Hartiala, J., Knuuti, J., 1995. Imaging of heart by MRI and PET. Ann. Med. 27, 35–45.

Hoh, C., Dahlbom, M., Harris, G., Choi, Y., Hawkins, R., Philps, M., Maddahi, J., 1993. Automated iterative three-dimensional registration of positron emission tomography images. J. Nucl. Med. 34 (11), 2009–2018.

Kim, R., Aw, T., Bacharach, S., Bonow, R., 1991. Correlation of cardiac MRI and PET images using lung cavities as landmarks. In: Proceedings of the IEEE Conference on Computers in Cardiology, pp. 49–52.

Lauerma, K., Niemi, P., Hänninen, H., Janatuinen, T., Voipio-Pulkki, L., Knuuti, J., Toivonen, L., Mäkelä, T., Mäkijärvi, M., Aronen, H., 2000. Multimodality MR imaging assessment of myocardial viability, combination of first-pass and late contrast enhancement to wall motion dynamics and comparison with FDG-PET. Radiology 217, 729–736.

Lötjönen, J., Mäkelä, T., 2001. Elastic matching using a deformation sphere. In: Niessen, W., Viergever, M. (Eds.), Medical Image Computing and Computer-Assisted Intervention. Lecture Notes in Computer Science 2208. Springer, Berlin, pp. 541–548, MICCAI01.

Lötjönen, J., Reissman, P.-J., Magnin, I.E., Katila, T., 1999. Model extraction from magnetic resonance volume data using the deformable pyramid. Medical Image Analysis 3 (4), 387–406.

MacLeod, R.S., Brooks, D.H., 1998. Recent progress in inverse problems in electrocardiology. IEEE Eng. Med. Biol. 17 (1), 73–82.

Mäkelä, T., Clarysse, P., Lötjönen, J., Sipilä, O., Lauerma, K., Hänninen, H., Nenonen, J., Knuuti, J., Katila, T., Magnin, I.E., 2001a. A method for registration of cardiac magnetic resonance and positron emission tomography images for assessing myocardial viability. In: Understanding Cardiac Imaging Techniques – from Basic Pathology To Image Fusion, Vol. 322. IOS Press, pp. 155–165.

Mäkelä, T., Clarysse, P., Lötjönen, J., Sipilä, O., Lauerma, K., Hänninen, H., Pyökkimies, E.-P., Nenonen, J., Knuuti, J., Katila, T., Magnin, I.E., 2001b. A new method for the registration of cardiac PET and MR images using deformable model based segmentation of the main thorax

structures. In: Medical Image Computing and Computer-Assisted Intervention (MICCAI'01). Lecture Notes in Computer Science (LNCS), Vol. 2208. Springer, Berlin, pp. 557–564.

Mäkelä, T., Clarysse, P., Sipilä, O., Pauna, N., Pham, Q., Katila, T., Magnin, I.E., 2002a. A review of cardiac image registration methods. IEEE Trans. Med. Imaging 21 (9), 1011–1021.

Mäkelä, T., Lötjönen, J., Sipilä, O., Lauerma, K., Nenonen, J., Katila, T., Magnin, I.E., 2002b. Error analysis of registering of anatomical and functional cardiac data using external markers. In: Nowak, H., Haueisen, J., Giesler, F., Huonker, R. (Eds.), Biomag 2002, Proceedings of the 13th International Conference on Biomagnetism, pp. 842–845.

McInerney, T., Terzopoulos, D., 1996. Deformable models in medical image analysis: a survey. Medical Image Analysis 1 (2), 91–108.

Montagnat, J., Delingette, H., 2000. Space and time shape constrained deformable surfaces for 4D medical image segmentation. In: Medical Image Computing and Computer-Assisted Intervention (MICCAI'00). Lecture Notes in Computer Science (LNCS), Vol. 1935. Springer, Berlin, pp. 196–205.

Montonen, J., Ahonen, A., Hämäläinen, M., Ilmoniemi, R., Laine, P., Nenonen, J., Paavola, M., Simelius, K., Simola, K., Katila, J.T., 2000. Magnetocardiographic functional imaging studies in biomag laboratory. In: Biomag96, Proceedings of the 10th International Conference on Biomagnetism, pp. 494–497.

Nekolla, S., Miethaner, C., Nguyen, N., Ziegler, S., Schwaiger, M., 1998. Reproducibility of polar map generation and assessment of defect severity and extent assessment in myocardial perfusion imaging using positron emission tomography. Eur. J. Nucl. Med. 25, 1313–1321.

Nekolla, S., Ibrahim, T., Balbach, T., Klein, C., 2000. Coregistration and fusion of cardiac magnetic resonance and positron emission tomography studies. In: Understanding Cardiac Imaging Techniques – from Basic Pathology To Image Fusion. IOS Press, pp. 144–154.

Nenonen, J., Pesola, K., Hänninen, H., Lauerma, K., Takala, P., Mäkelä, T.J., Mäkijärvi, M., Knuuti, J., Toivonen, L., Katila, T., 2001. Current – density estimation of exercise-induced ischemia in patients with multivessel coronary artery disease. J. Electrocardiogr. 34 (suppl.), 37–42.

Pallotta, S., Gilardi, M.C., Bettinardi, V., Rizzo, G., Landoni, C., Striano, G., Masi, R., Fazio, F., 1995. Application of a surface matching image registration technique to the correlation of cardiac studies in positron emission tomography by transmission images. Phys. Med. Biol. 40, 1695–1708.

Papademetris, X., Sinusas, A.J., Dione, D.P., Duncan, J.S., 2001. Estimation of 3D left ventricular deformation from echocardiography. Medical Image Analysis 5, 17–28.

Pesola, K., Nenonen, J., Fenici, R., Lötjönen, J., Mäkijärvi, M., Fenici, P., Korhonen, P., Lauerma, K., Valkonen, M., Toivonen, L., Katila, T., 1999. Bio-electromagnetic localization of a pacing catheter in the heart. Phys. Med. Biol. 44, 2565–2578.

Pesola, K., Lötjönen, J., Nenonen, J., Magnin, I., Lauerma, K., Fenici, R., Katila, T., 2000. The effect of geometry and topology differences in boundary element models on magnetocardiographic localization accuracy. IEEE Trans. Biomed. Eng. 47 (9), 1237–1247.

Pham, Q.C., Vincent, F., Clarysse, P., Croisille, P., Magnin, I.E., 2001. A FEM-based deformable model for the 3-D segmentation and tracking of the heart in cardiac MRI. In: Image and Signal Processing and Analysis ISPA 2001, pp. 250–254.

Pluim, J., Maintz, J., Viergever, M., 2000. Image registration by maximization of combined mutual information and gradient information. IEEE Trans. Med. Imaging 19 (8), 809–814.

Press, W., Flannery, B., Teukolsky, S., Vetterling, W., 1988. Numerical Recipes in C. Cambridge University Press, Cambridge.

Sermesant, M., Coudière, Y., Delingette, H., Ayache, N., Désidéri, J., 2001. An electro-mechanical model of the heart for cardiac image analysis. In: Medical Image Computing and Computer-Assisted Intervention (MICCAI'01). Lecture Notes in Computer Science (LNCS), Vol. 2208. Springer, Berlin, pp. 224–231.

Siltanen, P., 1988. Comprehensive Electrocardiology. Pergamon Press, Oxford, Chapter on Magnetocardiography.

Sinha, S., Sinha, U., Czernin, J., Porenta, G., Schelbert, H., 1995. Noninvasive assessment of myocardial perfusion and metabolism: feasibility of registering gated MR and PET images. Am. J. Roentgenol. 36, 301–307.

Slomka, P., Gilbert, A., Stephenson, J., Cradduc, T., 1995. Automated alignment and sizing of myocardial stress and rest scans to three-dimensional normal templates using an image registration algorithm. J. Nucl. Med. 36, 1115–1122.

Tai, Y.-C., Lin, K., Hoh, C., Huang, S., Hoffman, E., 1997. Utilization of 3-D elastic transformation in the registration of chest X-ray CT and whole body PET. IEEE Trans. Nucl. Med. 44 (4), 1606–1612.

Thirion, J.-P., 1995. Fast non-rigid matching of 3-D medical images. Research Report 2547. INRIA.

Thirion, J.-P., 2001. Perfusion and motion from gated SPECT. In: Understanding Cardiac Imaging Techniques – From Basic Pathology to Image Fusion. IOS Press, pp. 84–93.

Waiter, G.D., Al-Mohammad, A., Norton, M.Y., Redpath, T.W., Welch, A., Walton, S., 2000. Regional myocardial wall thickening assessed at rest by ECG gated (18)F-FDG positron emission tomography and by magnetic resonance imaging. Heart 84, 332–333.

Xu, C., Prince, J.L., 1998. Snakes, shapes, and gradient vector flow. IEEE Trans. Image Process. 7 (3), 359–369.

Yu, J.N., Fahey, F.H., Gage, H.D., Eades, C.G., Harkness, B.A., Pelizzari, C.A., 1995. Intermodality, retrospective image registration in the thorax. J. Nucl. Med. 36 (12), 2333–2338.

Zienkiewicz, O., Taylor, R., 1987. The Finite Element Method. McGraw-Hill, New York.

# A Review of Cardiac Image Registration Methods

Timo Mäkelä*, *Student Member, IEEE*, Patrick Clarysse, Outi Sipilä, Nicoleta Pauna, Quoc Cuong Pham, Toivo Katila, *Member, IEEE*, and Isabelle E. Magnin, *Member, IEEE*

***Abstract*—In this paper, the current status of cardiac image registration methods is reviewed. The combination of information from multiple cardiac image modalities, such as magnetic resonance imaging, computed tomography, positron emission tomography, single-photon emission computed tomography, and ultrasound, is of increasing interest in the medical community for physiologic understanding and diagnostic purposes. Registration of cardiac images is a more complex problem than brain image registration because the heart is a nonrigid moving organ inside a moving body. Moreover, as compared to the registration of brain images, the heart exhibits much fewer accurate anatomical landmarks. In a clinical context, physicians often mentally integrate image information from different modalities. Automatic registration, based on computer programs, might, however, offer better accuracy and repeatability and save time.**

***Index Terms*—Cardiac image registration, computed tomography (CT), magnetic resonance imaging (MRI), positron emission tomography (PET), single-photon emission computed tomography (SPECT), ultrasound (US).**

## NOMENCLATURE

| | |
|---|---|
| CC | Correlation coefficient. |
| CT | X-ray computed tomography. |
| ECG | Electrocardiography. |
| ED | End-diastolic. |
| ES | End-systolic. |
| FDG | Fluorodeoxyglucose. |
| ICP | Iterative closest point. |
| LA | Long axis. |
| LV | Left ventricle. |
| MRI | Magnetic resonance imaging. |
| PET | Positron emission tomography. |
| rms | Root mean square. |
| SA | Short axis. |
| SAD | Sum of absolute differences. |
| SPECT | Single-photon emission computed tomography. |
| SSC | Stochastic sign change. |
| SSD | Sum of squared intensity differences. |
| SVD | Singular value decomposition. |
| US | Ultrasound. |
| VIR | Variance of intensity ratio. |

Manuscript received November 3, 2001; revised July 6, 2002. This work was supported in part by the Scientific Department of the French Embassy in Finland, the Region Rhône Alpes, the ADéMO project, and The Foundation of Technology in Finland. *Asterisk indicates corresponding author.*

*T. Mäkelä is with the Laboratory of Biomedical Engineering, Helsinki University of Technology, P.O. Box 2200, FIN-02015 HUT, Finland, and CREATIS, UMR CNRS #5515, 69621 Villeurbanne Cedex, France (e-mail: timo.makela@hut.fi).

P. Clarysse, N. Pauna, Q. C. Pham, and I. E. Magnin are with CREATIS, UMR CNRS #5515, 69621 Villeurbanne Cedex, France.

O. Sipilä is with the Department of Radiology, Helsinki University Central Hospital, FIN-00029 HUS, Finland.

T. Katila is with the Laboratory of Biomedical Engineering, Helsinki University of Technology, FIN-02015 HUT, Finland, and BioMag Laboratory, Helsinki University Central Hospital, FIN-00029 HUS, Finland.

Digital Object Identifier 10.1109/TMI.2002.804441

## I. INTRODUCTION

DIFFERENT imaging modalities bring complementary information that can be advantageously used to establish a diagnosis or assist the clinician for a therapeutic gesture. To locally compare two or more measurements of different nature, a number of registration algorithms have been developed, especially in brain imaging.

In the widespread ischemic heart diseases, the consequence of reduced blood flow to the heart muscle can be studied using several medical imaging modalities, each of which gives a specific view of this complex phenomenon. The first consequence is a deterioration of the myocardial perfusion, which can be analyzed with nuclear medicine imaging techniques (SPECT and PET) or with MRI [1], [2]. The deficit of perfusion induces metabolic changes in myocardial tissues highlighted using FDG PET studies [1]. A further consequence of a myocardial ischemia is the reduced capacity of the heart to eject blood into the body. This can be evaluated by analyzing the myocardial contractile function using MRI or US. Recent studies have demonstrated the interest of concurrently analyzing those different aspects in order to assess the myocardial viability, which will determine the proper therapeutic action [3], [4]. Therefore, there is a growing interest in the development of cardiac image registration methods that could bring into the same anatomical reference all the available functional measurements.

Cardiac image registration is a more complex problem than brain image registration, in particular because of the nonrigid and mixed motions of the heart and the thorax structures. Moreover, as compared to the brain, the heart exhibits fewer accurate anatomical landmarks. Also, cardiac images are usually acquired with a lower resolution than brain images. Fig. 1 illustrates a typical acquisition protocol with ECG-gated cardiac MRI. This highlights certain problems induced by the spatiotemporal image acquisition that hamper image registration.

In clinical practice, physicians mentally integrate information from different images acquired from a patient, often with different imaging modalities. Images are shown in various orientations and positions and at different scales. Semi-interactive registration methods rely on the expert's ability to interactively select corresponding slices using anatomical knowledge. In cardiac image registration, the semi-interactive methods are often used to register gated SA images [5], [6].

Several survey papers have been published in the field of medical image registration [7]–[10]. Also, some review articles

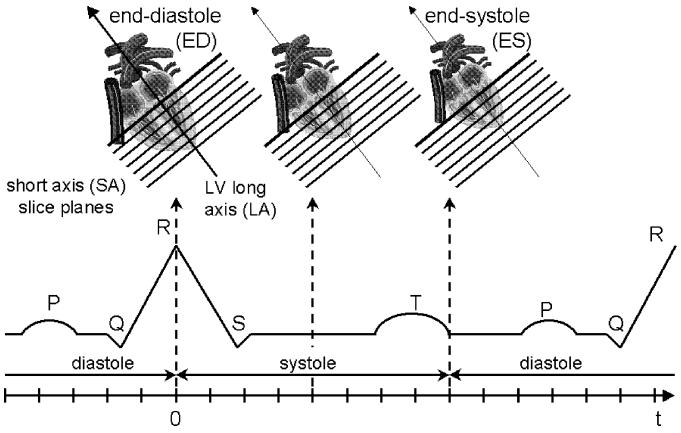


Fig. 1. Illustration of a classical acquisition of SA images with a ECG-gated cine MR sequence. The same slice is acquired at successive time points of the cardiac cycle. However, due to the motion of the heart, we do not observe the same anatomical region within the same slice. Moreover, several cardiac cycles are required to reconstruct slices. When possible, patients are asked to retain their breath (15–20 s) during acquisition.

and books closely related to medical image registration and fusion can be mentioned, such as [11]–[17]. Very few review papers focusing on cardiac image registration have been published [18], [19]. Gilardi *et al.* [18] reviewed the techniques and clinical applications for the integration of multimodal biomedical images of the heart. Habboosh *et al.* [19] briefly discussed the aspects of cardiac PET and MRI correlation. In the review article of Maintz *et al.* [8], registration methods for cardiac images were also referenced in a separate section.

This paper aims to provide a survey concerning cardiac image registration, including the most recent articles and discussing also implementation and validation issues. For the four-dimensional (4-D) registration of intramodality cardiac images, the problem is often addressed in a cardiac motion tracking framework. In this survey, the 4-D motion tracking problem is not considered at the methodological level. Instead, we refer to some recent papers in this field [14], [20]–[23].

In this paper, cardiac image registration methods are divided into two main categories: 1) those based on geometric image features (Section II-A) and 2) those based on voxel similarity measures (Section II-B). The geometric image feature-based methods are divided into registration of *a set of points* and *edges or surfaces*. Registration methods based on voxel similarity measures include *moments and principal-axes methods, intensity difference and correlation methods,* and *methods based on mutual information*. After presenting the current status of cardiac image registration methods, we discuss implementation issues, such as interpolation and optimization (Section II-C). Validation of the registration methods is presented in Section III. The overview of cardiac and thorax registration methods and their main parameters are summarized in Table I. Some of the brain, thorax, and abdominal image registration articles are referenced when methods have been, or can easily be, applied to heart image registration.

In the reviewed papers, mainly MR, CT, PET, and SPECT imaging modalities have been considered. There are very few references related to registration with cardiac US images. This is due to the characteristics of the US images that make them difficult to process automatically. Moreover, despite the existence of three-dimensional (3-D) echocardiographic systems [24], two-dimensional (2-D) image acquisitions are routinely performed. At most, a collection of radial planes is acquired, resulting in a quite different geometry as compared to the other imaging modalities.

## II. Cardiac Image Registration: Principles and Applications

### A. Registration Methods Based on Geometric Image Features

Registration methods based on geometric image features can be divided into registration of *a set of points* and registration of *edges or surfaces*.

*1) Point-Based Registration:* Point-based registration methods often uses external markers or anatomical landmarks. Corresponding point sets are usually manually defined in the reference and floating images. The advantages of the point-based registration methods are that they can be applied to any imaging modalities where markers or landmarks are visible and that the calculation of the registration parameters between two point sets is usually fast. A noniterative least squares method can be used to register corresponding point sets [12], [25]. The method uses an SVD of a 3 by 3 covariance matrix to find a unique solution for the registration parameters between two point sets. In cardiac image registration, the method has been used, e.g., in phantom experiments for validating rigid registration error [26].

Registration methods based on *external skin markers* (fiducial markers) are widely applied in medical image registration because they allow matching of any imaging modalities in which the positions of markers can be accurately defined. Registration based on skin markers is independent of the alteration in the image patterns, induced by the pathologies [18]. Skin markers must be easy to use and accurate to reattach, but they should not interfere with the diagnostic content of the images. Since the flexibility of the body can cause errors in registration, it is important to choose relatively stable parts of the body for markers placement [27]. Ideally, markers should not be removed between imaging sessions to ensure the same placements in different modalities [28]. Registration of external skin markers does not guarantee registration of the heart within the body, since heart position changes with body position, respiration, and cardiac contraction [29]. The disadvantage of the skin markers is also that they cannot be utilized retrospectively. External markers have been applied especially as a gold standard method in phantom measurements to validate the accuracy of rigid cardiac and thorax registration methods [26], [30]–[33] and in clinical images, e.g., to validate the accuracy of rigid registration of head images [34]. For rigid thorax CT and SPECT image registration, the combination of both external markers and landmarks has also been utilized [35], [36].

In *landmark-based registration,* corresponding anatomical points have to be visible in both registered images. For heart images, there are usually only few spatially accurate anatomical landmarks. In pathological conditions, such as ischemia, the functional alterations can also hide anatomical landmarks [18].

TABLE I
OVERVIEW OF EVALUATED CARDIAC AND THORAX IMAGE REGISTRATION METHODS

| Reference | Modalities | Object | Trans. | Struc. | Method | Valid. | Error | Error type |
|---|---|---|---|---|---|---|---|---|
| **Registration methods based on geometric image features** | | | | | | | | |
| Point-based registration | | | | | | | | |
| Wirth *et al.* [42] | CT-MR | Thorax | Elastic | Landmarks | Interpolation & Elastic funct. | - | - | - |
| Thorax surface based registration | | | | | | | | |
| Yu *et al.* [33] | CT-PET | Thorax | Rigid | T & L | "head-and-hat" | P | (x,y) 2.3 mm, (y) 3.0 mm | mean (rms) |
| Cai *et al.* [46] | CT-PET | Lungs | Rigid | T & L | Chamfer | P & Pa.& S | (x,y) 2-3 mm, (y) 3-4 mm, (rot.)1.5° | mean |
| Pallotta *et al.* [26] | PET-PET | Heart | Rigid | T & L | Chamfer | P & S | 3 mm, (rot.) 1 °<br>2.19 ± 0.52 mm | mean (rms)<br>mean (rms)±s.d. |
| Gilardi *et al.* [31] | SPECT-PET | Heart | Rigid | T & L | Chamfer | P & Pa. | (x,y) 3 mm, 5 mm (z) | (x,y) mean (rms), (z) mean |
| Mäkelä *et al.* [47] | MR-PET | Heart | Rigid | T & L | Chamfer | Surfaces | (x,y,z) 2.8 ± 0.5 mm | mean |
| Heart surface based registration | | | | | | | | |
| Faber *et al.* [29] | MR-SPECT | Heart | Rigid | HS | "head-and-hat" | P | 2.7 mm | mean (rms) |
| Sinha *et al.* [40] | MR-PET | Heart | Rigid | HS | "head-and-hat" | L | 1.95 mm ± 1.6 mm | mean (rms) |
| Nekolla *et al.* [57] | PET-SPECT | Heart | Rigid | HS | - | Surfaces | 2.5 mm | mean |
| Declerck *et al.* [50] | SPECT-SPECT | Heart | Elastic | HS | ICP | Pa. | - | - |
| **Registration methods based on voxel similarity measures** | | | | | | | | |
| Intensity difference and correlation methods | | | | | | | | |
| Gallippi *et al.* [75] | MR-MR (time series) | Heart | Rigid & Elastic | - | *C* | M | 1.23 ± 0.06 mm<br>3.25 ± 1.04 mm | left-right (mean)<br>anterior-poster. (mean) |
| Bidaut *et al.* [37] | MR-MR (perfusion) | Heart | Rigid | - | *SSD* | L | 3.0 mm (x), 1.6 mm (y), 2.2 mm (z) | mean (rms) (maximum) |
| Bacharach *et al.* [76] | PET-PET | Heart | Rigid | - | *CC* | M | (x,y,z) 1 mm, (rot.) 1.5 ° | mean |
| Turkingston *et al.* [71] | PET-PET | Heart | Rigid | - | *C* | P | (x, y) 1.7 mm, (z) 4.2 mm | mean |
| Klein *et al.* [23] | PET-PET | Heart | Elastic (4-D) | - | LS | P | (x) 1.9 mm, (y) 2.4 mm, (z) 6.8 mm | mean (max.) |
| Hoh *et al.* [67] | MR-SPECT | Heart | Rigid | - | *SAD, SSC* | M | (x,y) 0.5 ± 0.5 mm, (z) 1.1 ± 1.1 mm, (rot) 0.9 ± 1.1 ° | mean ± s.d. |
| Dey *et al.* [32] | CT-SPECT | Heart & Thorax | Rigid | - | *SAD*<br>*VIR* | P<br>P | 2.5 ± 1.2 mm<br>3.3 ± 1.3 mm | mean (rms)<br>mean (rms) |
| Eberl *et al.* [30] | SPECT-SPECT | Heart | Rigid | - | *SAD* | P | 3.1 ± 1.7 mm<br>1.3 ° (rot) | mean ± s.d. |
| Slomka *et al.* [66] | SPECT-SPECT | Heart | Affine | - | *SAD* | P | 1.5 mm(x,y,z)<br>2.0° (rot), 5.3 % (size) | mean (max.) |
| Mutual information | | | | | | | | |
| Carrillo *et al.* [38] | MR-MR | Abdom. | Rigid | - | MI | L | (x,y,z) 3.05 mm | mean |

Object = Main object to be registered.
Trans. = Transformation method.
Struc. = Structures used in registration (T = Thorax, L = Lungs, HS = heart surfaces).
Method = Method used in registration (C = cross-correlation, LS = least squares voxel difference, MI = mutual information).
Valid. = Validation method (P = Phantom, Pa. = Patient, S = Simulated images, M = Misaligned images, L = Landmarks).
Error: rot. = Rotational error.
Error type: s.d. = Standard deviation.

Landmarks have been exploited to estimate rigid registration error in [30], [31], [35], [37], and [38]. Savi *et al.* [39] rigidly registered cardiac PET and US images by using homologous anatomical landmarks (the two papillary muscles and the inferior junction of the right ventricle) of the heart. Rigid US-PET image registration was first performed in a plane identified by three landmarks. The obtained registration parameters were then applied to the whole PET volume. Sinha *et al.* [40] validated the rigid heart surface-based cardiac MR and PET image registration method by analyzing registration error using cardiac landmarks (papillary muscles, the insertion point of the right ventricle into the septum, the most inferior aspect of the septum, and the most inferior aspect of the lateral wall). Identification of landmarks was prone to errors because of their finite width and complex shapes. Especially in multimodal cardiac image registration, the accurate localization of the same anatomical landmarks can be difficult. Sometimes automatically detected points and lines can be used as landmarks [41]. Wirth *et al.* [42] utilized landmark-based elastic registration to register a thorax MR image to the coordinates of a CT image of the same subject. In this method, 36 corresponding landmarks in thorax and lung surfaces were elastically matched, and the rest of the points were mapped using interpolation or elastic mapping functions. The method registered corresponding points well, but general validation of the method accuracy was not performed.

*2) Edge- and Surface-Based Registration:* The chamfer matching method [43], [44] is often used to register surfaces and point sets. In this method, the sum of the distances between the transformed points and a distance map built upon the segmented surface using the chamfer distance transformation is minimized [45]. For cardiac image registration, chamfer

matching methods have mainly been utilized for rigid registration methods based on the thorax structures [26], [31], [46], [47]. Also the ICP algorithm of Besl *et al.* [48] has been used to elastically register surfaces and lines [49], [50]. In the ICP method, the distances between structures are explicitly computed at every iteration of the registration algorithm and the sum of distances minimized. The "head-and-hat" algorithm [51], [52] has also been commonly proposed to register medical images and was first presented to register brain images. This algorithm models the contours from one of the images (usually higher resolution) as a surface (the "head") and the contours of the other image set as a series of points (the "hat"). The algorithm then determines the optimum rigid transformation, which minimizes the mean squared deviation between the points of the hat and the surfaces of the head by using the Powell minimization algorithm [53], [54]. The "head-and-hat" method has been applied for registering surfaces from cardiac MR and PET images [40] and thorax CT and PET images [33].

*a) Registration methods based on thorax surfaces:* Cardiac image registration methods based on the registration of the thorax surfaces have been proposed because it is often difficult to extract structural information from the heart surfaces directly. Thorax and lung surfaces are, in general, well visible in MR and CT images and in PET and SPECT transmission images. In the registration methods based on the thorax surfaces, every surface point that is involved in registration should have a unique corresponding point in the other image. In practice, this usually means that the axial extension in the reference study must be greater than in the study to be matched [18]. Sometimes, artificial edges of the images have to be excluded from the registration parameters' calculation. Surfaces from the transmission images have been utilized for intramodality registration of cardiac PET images [26] and for intermodality registration of cardiac PET and SPECT images [31], MR and PET images [47], and thorax CT and PET images [33], [46], [55]. Thorax and lung surfaces have often been obtained using the simple thresholding method of Yu *et al.* [33], where a threshold value of 50% of the maximum soft-tissue value was selected to segment the PET and SPECT transmission images [31], [46] and thorax CT images [33], [46]. Also, deformable models have been applied to segment thorax structures from PET transmission and MR images [47]. In this rigid registration method, chamfer matching was used to register segmented surfaces from PET transmission image with the MR transaxial image. Also, SA PET images were calculated from registered transaxial images by using header information between MR transaxial and SA images.

*b) Registration methods based on heart surfaces:* Registration of the heart surfaces may result in better registration of the area of interest [31]. The choice of the surfaces to be registered (e.g., epicardial and/or endocardial) is important. Faber *et al.* [29] presented a method for the intersubject rigid registration of 4-D gated cardiac SPECT perfusion images to the coordinates of the gated MR image. Left ventricular ED and ES endocardial surfaces were automatically detected from both image modalities using a model-based surface detector [56]. The best single transformation was searched to register SPECT ED and ES surfaces with corresponding surfaces in an MR image. Registration of the center of mass of the surfaces was used as an initial alignment, and the "head-and-hat" algorithm [51], [52] was used to find more accurate registration parameters. After registration, quadrilinear interpolation was applied to the SPECT image to obtain a temporal correlation with time frames of an MR image. Sinha *et al.* [40] presented a method to register gated cardiac FDG PET images to the coordinates of gated MR images. In this method, contours of the left ventricular wall were defined from both imaging modalities by using an interactive algorithm with morphologic operators. Registration parameters were defined by using the "head-and-hat" surface matching approach [51]. In the MunichHeart software [57], endocardial and epicardial contours were manually delineated from SA MR images and registered with the same contours extracted from PET or SPECT images using the maximum count detection algorithm [58]. Declerck *et al.* [49], [50] presented an automated elastic registration method to align images from rest and stress myocardial perfusion SPECT studies. In this method, feature points of the cardiac SPECT image surfaces were extracted using a Canny–Deriche edge detector [59], [60]. The features were then registered using the ICP method [48]. Images were also elastically registered with a template image by using local spline transformations. The method was also applied to cardiac SPECT perfusion followup studies [61]. Thirion *et al.* [62], [63] presented a deformable model-based elastic registration method for intramodality registration of diastolic and systolic CT or SPECT images. Andersson *et al.* [64] utilized heart edge information for the cardiac PET emission images to rigidly reduce movement artifacts. The method was also applied to rigidly realign cardiac PET emission and transmission images [65].

### *B. Registration Methods Based on Voxel Similarity Measures*

Registration methods based on voxel similarity measures can be divided into methods based on *moments and principal axes, intensity difference and correlation methods*, and methods based on *mutual information*.

*1) Methods Based on Moments and Principal Axes:* Image registration methods based on moments and principal axes use statistical factors derived from image data [7]. Moments describe the spatial distribution of the mass (intensity) of the image. Methods based on the principal axes register images by bringing the principal axes of the inertia tensors of corresponding objects in the images into coincidence. Accurate registration based on principal axes requires that the entire object be present in both imaging sets. Therefore, applications of these methods are limited. The principal-axes approach has been used to initially register myocardial SPECT stress and rest scans to templates [66], using SAD and SSC methods (see Section II-B2) to obtain more accurate registration. For the registration of thorax images, the principal-axes approach was proposed as an initial registration between CT and transmission SPECT images [32], while SAD and VIR measures (see Section II-B2) were applied to obtain the final registration.

*2) Intensity Difference and Correlation Methods:* Image intensity difference and correlation methods attempt to determine the best registration by maximizing the similarity between images that differ primarily because of different image-acquisition conditions, like noise [7]. The assumption of these methods is usually that pixel values in the registered images are strongly

correlated. Therefore, these methods are particularly powerful for intramodality registration methods.

*a) Intramodality registration:* Hoh *et al.* [67] compared the SAD and SSD similarity measures for the rigid registration of cardiac PET emission images. In the SAD method, registered images are subtracted pixel-by-pixel, and the mean value of the sum of the absolute intensity difference of all the pixels in the subtracted image is computed. The SSD is similar to the SAD measure, but the squared intensity difference is calculated instead of the absolute difference. The SSD is the optimum measure when registered images differ only by Gaussian noise [12], [68]. In the paper by Hoh *et al.* [67], the effect of various defects and misalignments was simulated. No significant differences in the translation or rotation errors of the SAD and SSD algorithms were found. Slomka *et al.* [66] compared the SAD and SSC methods for affine registration of SPECT emission images to templates. An initial registration was obtained using alignment of the principal axes. Registered images were first subtracted, and the SSC was determined by counting along each pixel row the number of times the pixel gray level in the subtracted images went from negative to positive or from positive to negative [67]. At the optimum registration, there is a maximum of total sign changes. Slomka *et al.* [66] argued that the SAD provided better results than the SSC. This method was later enhanced and proposed for voxel-by-voxel quantification of SPECT images as a clinical tool [69]. In the enhanced method, not only did the registration algorithm compensate for shape differences by affine registration, but also a template erosion technique was used (role similar to warping adjustments) for fine tuning of the registration. The SSD-based similarity measure has also been applied in rigid motion correction (caused mainly by breathing) of gated heart perfusion MR images [37]. Perfusion MR imaging often takes more than 3 min. Breath holding is not possible during the imaging protocol, nor can respiratory gating be used since a high temporal resolution is needed. Therefore, dynamic gated heart images and temporal resolution are degraded by respiratory-induced movements during the whole sequence [37]. In the recent paper by Klein *et al.* [23], [70], a novel affine 4-D registration algorithm was proposed for motion compensation of gated cardiac PET emission images to give better estimation of perfusion and metabolic parameters. The method registers different cardiac PET emission image time frames with the end- diastolic time frame. It uses nonuniform elastic material model (12-parameter global affine motion model) and iteratively calculates registration parameters of the model using a cost function that combines a least squares voxel difference measure with penalty terms assuming constant velocity and an affine model. The method does not require the precise a priori segmentation of the object.

Turkingston *et al.* [71] utilized cross-correlation measure for the rigid alignment of dynamic cardiac PET images to cardiac templates. The method used only translations, assuming that the orientation of the heart remains the same during the study. The cross-correlation technique has also been proposed for rigid motion correction of cardiac SPECT images [72], [73]. Bettinardi *et al.* [74] utilized the cross-correlation measure to rigidly register two PET transmission images for patient repositioning. Cross-correlation measure was also used for the correction of the patient motion in the PET heart studies with the help of PET transmission images, taken before and after emission imaging [74]. Gallippi *et al.* [75] utilized modified correlation measure to match local brightness statistics of the registered images. The method was applied to rigidly register intramodality cardiac MR or US time series images. Bacharach *et al.* [76] utilized CC measure to rigidly register two cardiac PET emission scans of the same subject acquired at different times. The method was based on the registration of corresponding transmission data sets. The optimum alignment was defined as the one that produced the maximum value of the CC between the two data sets. CC is an optimal measure for registration in the case of a linear relationship between the intensity values in the images to be registered [11], [12], [68], [77]. This is seldom the case between different image modalities, and the CC is thus mainly used for intramodality registration.

*b) Intermodality registration:* In the paper by Dey *et al.* [32], SAD and VIR methods were compared for the rigid registration of thorax CT and SPECT images. In the VIR method, the sum of the normalized standard deviations is calculated to define registration parameters. The method was first proposed by Woods *et al.* [78], [79] for registering intramodality brain PET images [78] and intermodality brain PET and MR images [79]. In the latter, the VIR algorithm minimizes the normalized standard deviation of PET voxel values for each MR intensity value, but the method could also be used for these images vice versa [12]. Dey *et al.* [32] utilized SPECT transmission image as a linking mediator to register thorax CT and SPECT emission images. In this VIR method, the Simplex algorithm was applied for the minimization of the cost function, while in the original VIR method [79], the Newton–Rhapson method [54] was used. An approximate image alignment was made using a technique based on the principal-axes transformation [80]. VIR provided better convergence than SAD and may perform better for CT and SPECT image registration, but the method was only tested on phantom images. In the paper by Eberl *et al.* [30], the SAD, SSC, VIR, and *sum of pixel-by-pixel product* measures were compared for rigid registration of intramodality cardiac SPECT emission images or intermodality cardiac PET and SPECT emission images. SAD was recognized to be the most accurate and reliable method. The use of SAD and VIR thus depends on the type of images to be registered.

In [81], the cross-correlation measure was utilized to rigidly register cardiac MR and PET emission images by using PET transmission image as a linking mediator for registration. Edge information and a region growing algorithm were combined to segment lung cavities from both MR and PET transmission images. The segmented cavities were then utilized as landmarks for registration. Matching of the center of mass of segmented cavities was exploited as an initial registration, and the cross-correlation function was employed for maximizing overlapping areas of the lung cavities for accurate registration. The method was validated only qualitatively, using visual inspection.

*3) Mutual Information:* Mutual information is an information theory measure of the statistical dependence between two random variables or the amount of information that one variable contains about the other [11], [12], [82]–[84]. Mutual information can be qualitatively considered as a measure of how well one image explains the other. The mutual information is maxi-

mized at the optimal alignment [77]. No assumptions are made regarding the nature of the relation between the image intensities in the registered images [82]. Therefore, the mutual information method is promising in particular for intermodality registration.

Intermodality registration differs from intramodality registration because different medical imaging modalities usually have different intensity characteristics and different resolutions, noise characteristics, and fields of view. Several normalized versions of the mutual information has been proposed because changes in overlap of very low-intensity regions of the image can disproportionately contribute to the mutual information measure [10]–[12].

Registration based on mutual information has been proposed to register thorax CT and PET images, rigidly [85] and elastically [86]. In the latter, the rigid registration method [85] was first applied as an initialization prior to the elastic registration. A nonlinear thin-plate-spline warping was done using lung contours detected on PET transmission scans and CT volumes. Nonlinear deformation significantly improved the alignment of PET with breath-hold CT. Carrillo *et al.* [38] used mutual information,VIR, and the CC methods for registering abdominal thorax MR images. Results were compared with the manual registration method. The best registration results were obtained using the mutual information with the Powell minimization algorithm. In [87], a method that associates mutual information, gradient information, and the smoothness of the registration transformation was presented to elastically register intrapatient cardiac MR and PET images. A rigid thorax surface-based cardiac registration method [47] was used for the initial registration of the images.

### C. Implementation: Interpolation and Optimization

In a registration process, the image interpolation and minimization algorithm are key points. We give hereafter some comments on these important topics.

*1) Interpolation:* Interpolation is required when an image needs to be translated, rotated, scaled, warped, or otherwise deformed before it can match a reference image or an atlas [88]. In volumetric imaging, interpolation is often used to compensate for nonisotropic data sampling. This is typically the case with cardiac and thorax images where the in-slice resolution can be much higher (e.g., 1 mm) than the interslice resolution (e.g., 8 mm). In intermodality registration, one image may be of substantially lower resolution than the other, and in cardiac image registration, lower resolution images (e.g., SPECT or PET) are often transformed to the sample space of the higher resolution modality (e.g., CT or MR) [29], [40]. To obtain the same isotropic voxel dimension in cardiac and thorax image registration, trilinear interpolation is often used [47], [88]. Nekolla *et al.* [57] created a scaled isotropic set from individual SA MR and PET images using a cubic interpolation. In [37], bicubic interpolation was used for interpolation of SA MR perfusion images. Faber *et al.* [29] used quadrilinear interpolation to interpolate a 4-D SPECT image to the coordinates of a corresponding MR image. For cardiac nuclear medicine images, cubic convolution interpolation method has been recognized as efficient [89].

*2) Optimization:* For rigid 3-D image registration, the optimal transformation usually minimizes a cost function with six degrees of freedom (three translations and three rotations), giving a six-dimensional parameter space. Elastic registration algorithms have more degrees of freedom, in which case the parameter space has correspondingly more dimensions [10]–[12]. Because the heart is a nonrigid moving object, elastic registration is ideally needed. An exhaustive search to find the global minimum of the cost function is usually computationally too extensive and time consuming. Nonoptimal optimization methods, like Powell [53], [54] and Simplex [54], [90] methods, are applied to find an optimum faster than with the exhaustive search. The Powell method has been selected for the minimization of cardiac image registration methods in [29], [33], [38], and [46] and for thorax image registration methods in [32], [85], and [86]. The Simplex method has been used for cardiac image registration in [30], [66], [67], and [69].

Multiresolution methods can be implemented to increase the probability of finding the global optimum in the parameter space and to make the registration procedure faster. In the multiresolution approach, the images are first registered at a low resolution, and the transformation solution is applied to the next resolution level. The process is repeated until the highest resolution level is reached. For cardiac image registration, the multiresolution approach has been applied in [26], [37], [47], and [86]. To our knowledge, no comparative studies on the performance of minimization methods for cardiac image registration have been published to date.

## III. Validation of Registration Methods

A method can not be accepted as a clinical tool without careful validation. Validation of registration accuracy is a difficult task because the ground truth (i.e., gold standard) is generally not available [11], [12], [91]. Registration methods are often validated using external markers, anatomical landmarks, or external fiducial frames as the gold standards [91]. Visual inspection is the most obvious method for evaluation of the registration accuracy but can be considered as an informal and insufficient approach.

A direct comparison of the measurements reported in the literature is not straightforward because of the nonunique definition of accuracy and of the different methods adopted to measure it [31]. In cardiac image registration, the main interest is the registration accuracy in the heart area (target registration error) [12]. The mean and rms errors are commonly used measures for registration errors [11], [12], [91]. In rigid-body registration, error in the parameters of the spatial transformation model, such as errors in $x$-axis translation, are also commonly reported. However, the decomposition of a rigid-body movement into elementary rotations and translations is not unique, i.e., the result depends on the order of the elementary operations [92].

To reduce registration errors caused by cardiac movement and respiration, ECG gating and breath holding (or breath gating) are sometimes used. The problem for cardiac image registration of ECG-gated cine MR images is often that the same anatomical region is not observed within the same slice of the cine images. Recent MRI "slice following" techniques should make temporal registration easier, showing the same anatomical locations of the heart through cine image sequence. In thorax surface-based

cardiac registration methods, movement of the thoracic wall and diaphragm is quite different in magnitude in all directions. Movements can lead to distortions and asymmetrical position changes that can cause errors while determining the registration parameters [93]. The movements near the diaphragm are largest, reaching several centimeters [94]. Cardiac PET and SPECT images are often integral images through time (static images). This causes extra difficulties for registering, e.g., with gated MR images. In the case where both registered images are integral images through time, the errors caused by breathing and cardiac motion can be considered to be similar in both images [31].

In registration methods in which a transmission image (PET, SPECT) is used as a linking mediator to register corresponding emission image, the assumption is that the patient does not move during and between image acquisition. Because the image-acquisition times in cardiac PET and SPECT transmission and emission images are often several minutes, movement artifacts often occur. In modern PET imaging scanners, emission and transmission images are acquired without taking the patient out of the scanner between acquisitions. Yu *et al.* [95] argue that careful application of laser alignment is an adequate method of registration in the PET imaging systems where the patient is taken out of the scanner between transmission and emission acquisitions during the uptake period. Methods have also been presented for the rigid registration of PET emission and transmission images [74], [96]. If the movement between SPECT transmission and the emission image is more than 2–3 cm, it can also seriously affect the attenuation correction of the emission image and, thus, its quality [97].

### A. Phantom Studies

Phantom studies are important for the estimation of the registration accuracy because a phantom can remain perfectly still and can be displaced and sometimes even rotated with considerable accuracy. Phantom-based validation is utilized especially for estimating the accuracy of intramodality registration methods. For registration methods based on thorax surfaces, the registration accuracy has been usually validated using thorax phantoms [26], [30]–[33], [35], [46], [74]. For example, the Alderson thorax phantom [31], [98], a physical torso phantom with lungs, cardiac, and spine inserts (Data Spectrum) [32] and Jaszczak thorax phantom (Data Spectrum) [35] have been applied. In [71], a heart phantom was used. Simulations of images and different error sources can be used to estimate cardiac registration accuracy [26], [55]. Klein *et al.* [23], [70] utilized a mathematical cardiac phantom [99] to validate a 4-D motion correction algorithm of cardiac PET images. Integrated imaging devices such as combined PET/CT scanners [100], [101] could also provide gold standards for registration [94].

The accuracy of thorax surface-based registration methods depends on the modalities and structures to be registered. Pallotta *et al.* [26] compared the registration accuracy of the method where segmented PET transmission images were linking mediators to register corresponding PET emission images. A synthetic thorax phantom was used to validate the registration accuracy by using only external thorax surfaces (E), internal lung surfaces (I), or both thorax and lungs (EI). Seven markers were positioned to the external surfaces of the synthetic thorax phantom. Average values for the mean residual marker displacement over ten experiments were $3.41 \pm 1.41$ mm, $2.27 \pm 0.76$ mm, and $2.19 \pm 0.52$ mm for E, I, and EI surfaces, respectively. The rotational error was smaller than $1.5^\circ$ in each case. The result indicated that the more the surfaces were integrated in the registration, the more accurate the result.

### B. Registration Accuracy

*1) Intramodality Registration:*

*a) MRI:* Bidaut *et al.* [37] rigidly registered intramodality gated heart perfusion MR images by using SSD measure and obtained 3.0-mm accuracy in $x$, 1.6-mm accuracy in $y$, and 2.2-mm accuracy in $z$ directions. Gallippi *et al.* [75] utilized correlation measure and warping to register cardiac MR time-series images. Mean left–right registration error of $1.23 \pm 0.06$ mm and mean anterior–posterior error of $3.25 \pm 1.04$ mm were reported. With intramodality mutual information-based registration of abdominal MR images, Carrillo *et al.* [38] reported 3-mm accuracy by using anatomical landmarks.

*b) PET:* Hoh *et al.* [67] registered cardiac PET emission images using SAD and SSC measures. For both methods, accuracy was typically $0.5 \pm 0.5$ mm in the inplane direction, $1.1 \pm 1.1$ mm in the interplane direction, and $0.9 \pm 1.1^\circ$ for all rotational directions. Turkingston *et al.* [71] used cross-correlation measure for the alignment of dynamic cardiac PET emission scans to templates and showed that the rigid registration technique was reliable within one voxel ($1.7 \times 1.7 \times 4.2$ mm$^3$). Pallotta *et al.* [26] obtained with synthetic thorax phantom $2.19 \pm 0.52$ mm rms error for rigid registration of cardiac PET emission images with $1.5^\circ$ rotational error, while using both thorax and lung surfaces from corresponding transmission images for registration. Klein *et al.* [23], [70] reported a 1.9-, 2.4-, and 6.8-mm maximum registration error for the $x$, $y$, and $z$ directions, respectively, after the use of a 4-D PET motion compensation algorithm. For theCC-based PET transmission image registration of corresponding cardiac PET emission images, Bacharach *et al.* [76] reported 1-mm accuracy in $x$, $y$, and $z$ directions and $1.5^\circ$ in the three angles of rotation.

*c) SPECT:* Eberl *et al.* [30] rigidly registered intramodality SPECT emission images by using SAD measure and obtained $2.1 \pm 1.2$ mm accuracy by using a phantom experiment.

*2) Intermodality Registration:*

*a) MR-PET:* Sinha *et al.* [40] reported a $1.95 \pm 1.6$ mm$^2$ accuracy for a rigid heart surface-based registration method of ECG-gated cardiac MR and FDG PET images. This error was estimated only in the ($x$, $y$) plane using 80 internal landmarks from six volunteer scans. In [47], a $2.8 \pm 0.5$ mm error was reported for the rigid registration of cardiac MR and PET images. The reported error was a surface distance registration error between thorax and lung surfaces. The measure depended also on deformable model-based segmentation results, but provided also a reasonable measure of the registration accuracy of the MR and PET cardiac (thorax) images.

*b) MR-SPECT:* For rigid heart surface-based registration of MR and SPECT images, Faber *et al.* [29] reported a 2.7-mm registration accuracy.

*c) CT-PET:* In the rigid thorax and lung CT and PET image registrations, where a PET transmission image was used as a linking mediator to register PET emission image to CT image coordinates, accuracy of 1–3 mm in the transaxial plane and 2–4 mm in the longitudinal direction was reported in [33], [46], and [55], with about 1.5° rotational error [46].

*d) CT-SPECT:* For the rigid registration of thorax CT and SPECT emission images with the help of SPECT transmission images, the VIR and SAD methods were found to have about the same accuracy (about 3.5 mm), but VIR provided better convergence [32].

*e) PET-SPECT:* For rigid cardiac PET and SPECT image registration based on the segmentation of thorax and lung surfaces from transmission images, the accuracy was reported to be on the order of 3 mm in longitudinal direction and 5 mm in the transaxial plane [31]. For rigid cardiac PET and SPECT emission image registration based on SAD measure, Eberl *et al.* [30] reported $3.1 \pm 1.7$ mm accuracy. Nekolla *et al.* [57] rigidly registered heart surfaces from PET and SPECT images, and a mean distance between the two registered heart surfaces was less than 2.5 mm. The surface distance error measure depended on segmentation results but provided a reasonable measure of the registration accuracy.

## IV. Conclusion

Registration of different cardiac imaging modalities is the preliminary and mandatory step to combining anatomical and functional cardiac information. The integration of multiple complementary data into a common reference allows a more comprehensive analysis of the cardiac functions and pathologies. The accurate spatial coregistration of different imaging modalities also provides additional useful clinically relevant information, or information relevant to cardiac research, which is not available while looking at images from a single modality.

We have presented a survey of various cardiac image registration methods, which were coarsely divided into registration methods based on *geometric image features* and *voxel similarity measures*. In the first category, registration relies on the extraction of geometric features; in the latter, preliminary extraction of the features is not needed.

The choice of a cardiac registration method is difficult since, at the present time, no general fully automatic method exists that could handle the wide variety of encountered clinical situations (modalities, acquisition protocols, etc.). Moreover, it should also be driven by the evaluation of the methods' performances with the same common databases for which the ground truth is available. Such a reference does not exist either. We give hereafter some critical comments about the main categories of cardiac image registration methods.

1) External skin marker-based registration of cardiac images does not guarantee registration of the heart within the body, since heart position changes with body position (e.g., prone or supine), respiration, and cardiac contraction [29]. Also, skin markers cannot be utilized retrospectively.
2) Landmark-based registration of the heart is also difficult because there are few spatially accurate anatomical landmarks in cardiac images. Landmarks can also be less visible with certain modalities and in some pathological conditions, such as ischemia.
3) Thorax surface-based methods can be used if it is not possible to obtain structural information from the heart surfaces directly. In thorax surface,based cardiac image registration methods, it is recommended to use both thorax and lung surfaces, which are well visible in thorax MR and CT images and in PET and SPECT transmission images [26]. Still, these methods are prone to errors induced by respiration and different movement artifacts [94].
4) Registration of the heart surfaces directly will result in the better registration of the area of interest. The choice of the surfaces to be registered (e.g., epicardial and/or endocardial) is important and depends on the application and modalities to be used. Gated acquisitions combined with breath-hold (or breath-gated) image acquisition [94] give in many cases acceptable results even with rigid cardiac registration methods.
5) The voxel similarity measures, compared to geometric image feature-based registration methods, have the important advantage that they do not require a priori extraction of the registered features (e.g., segmentation). The use of image intensity difference and correlation methods relies on the assumption that pixel values in the registered images are strongly correlated. This is usually not the case with intermodality registration. In modern information-theoretic voxel similarity methods, like mutual information, no assumptions are made regarding the nature of the relation between the image intensities in the registered images [82]. These methods are particularly promising for the intermodality cardiac image registration. Because of the recent development of the mutual information-based methods, applications to cardiac image registration are still rare. One of the aims of recent research in the voxel similarity measure-based registration area has been to devise general algorithms that will work on a wide variety of image types, without application-specific preprocessing [12].

Rigid cardiac image registration generally does not describe the spatial relationship between images adequately. Elastic (nonrigid) cardiac image registration is needed especially because of cardiac motion; between end-diastole and end-systole (during cardiac cycle), the heart valvular plane moves 9–14 mm toward the apex and the myocardial walls thicken from approximately 10 to over 15 mm [23], [102], [103]. Also, the problems due to imaging conditions, different movement artifacts, and elasticity of the body, lungs, and heart cause different tissue deformations that are not possible to compensate for using rigid registration methods. There is considerable research going on in extending the use of intensity-based registration algorithms to nonrigid transformations [12].

Deformable model-based approaches (deformable registration algorithms) for cardiac image registration are particularly promising for elastic 4-D registration of the cardiac images (e.g., to compensate for movement artifacts) [23], [70]. Model-based approaches can also lead to the integration of information from different imaging modalities into an individualized heart model,

including anatomical and functional information [69], [104]. This kind of model can be applied in computer-assisted diagnosis, treatment planning, and surgery. Data fusion techniques, based, i.e., on neural networks and fuzzy logic, can be used to interpret and summarize the large amount of information from registered images and to help establish a diagnostic or select a therapy [4], [105]. Methods combining similarity measures with a priori knowledge from geometric models can also provide new possibilities, especially for elastic registration [87], [106].

The validation of the registration accuracy is particularly important. Virtual and physical phantoms may provide the gold standard for validation. Also, image databases may in the future provide a source for the objective comparison of different cardiac registration methods.

Cardiac image registration remains a challenge because of the numerous specific problems mainly related to the different motion sources (patient, respiration, heart) and to the specificity of each imaging modality. Up to now, no general method is able to automatically register any modality with any other modality. Cardiac image registration methods also always require a compromise among accuracy, precision, reliability, robustness, and issues such as automation, interactivity, speed, patient-friendliness, etc. It is also important to keep in mind that the registration techniques and results should be useful and usable in clinical practice.

## ACKNOWLEDGMENT

The authors are grateful to the anonymous reviewers for their suggestions to improve this paper.

## REFERENCES

[1] J. Hartiala and J. Knuuti, "Imaging of heart by MRI and PET," *Ann. Med.*, vol. 27, pp. 35–45, 1995.

[2] N. Wilke, M. Jerosch-Herold, A. E. Stillman, K. Kroll, N. Tsekos, H. Merkle, T. Parrish, X. Hu, Y. Wang, J. Bassingthwaighte, R. J. Bache, and K. Ugurbil, "Concepts of myocardial perfusion imaging in magnetic resonance imaging," *Magn. Res. Quart.*, vol. 10, pp. 249–286, 1994.

[3] H. R. Schelbert, "Metabolic imaging to assess myocardial viability," *J. Nucl. Med.*, vol. 35, pp. 8–14, 1994.

[4] F. Behloul, B. P. F. Lelieveldt, A. Boudraa, M. Janier, D. Revel, and J. H. C. Reiber, "Neuro-fuzzy systems for computer-aided myocardial viability assessment," *IEEE Trans. Med. Imag.*, vol. 20, pp. 1302–1313, Dec. 2001.

[5] F. Behloul, M. Janier, P. Croisille, C. Poirier, A. Boudraa, R. Unterreiner, J. Mason, and D. Revel, "Automatic assessment of myocardial viability based on PET-MRI data fusion," in *Int. Conf. IEEE Engineering in Medicine and Biology Soc.*, 1998, pp. 429–495.

[6] G. D. Waiter, A. Al-Mohammad, M. Y. Norton, T. W. Redpath, A. Welch, and S. Walton, "Regional myocardial wall thickening assessed at rest by ECG gated (18)F- FDG positron emission tomography and by magnetic resonance imaging," *Heart*, vol. 84, pp. 332–333, 2000.

[7] C. Maurer and J. M. Fizpatrick, "A review of medical image registration," *Interact. Image-Guided Neurosurg.*, pp. 17–44, 1993.

[8] J. B. A. Maintz and M. A. Viergever, "A survey of medical image registration," *Med. Image Anal.*, vol. 2, no. 1, pp. 1–36, 1998.

[9] P. A. van den Elsen, E.-J. D. Pol, and M. A. Viergever, "Medical image matching—A review with classification," *IEEE Eng. Med. Biol.*, vol. 12, no. 2, pp. 16–39, 1993.

[10] D. L. G. Hill, P. G. Batchelor, M. H. Holden, and D. J. Hawkes, "Medical image registration," *Phys. Med. Biol.*, vol. 46, no. 1, pp. 1–45, 2001.

[11] J. V. Hajnal, D. L. G. Hill, and D. J. Hawkes, *Medical Image Registration*. Boca Raton, FL: CRC Press, 2001.

[12] J. M. Fitzpatrick, D. L. G. Hill, and C. R. Maurer, *Handbook of Medical Imaging*. Bellingham, WA: SPIE Press, 2000, vol. 2, ch. Image Registration, pp. 375–435.

[13] I. N. Bankman, *Handbook of Medical Imaging: Processing and Analysis*: Academic Press, 2000.

[14] A. F. Frangi, W. J. Niessen, and M. A. Viergever, "Three-dimensional modeling for functional analysis of cardiac images, a review," *IEEE Trans. Med. Imag.*, vol. 20, pp. 2–25, Jan. 2001.

[15] M. Audette, F. Ferrie, and T. Peters, "An algorithmic overview of surface registration techniques for medical imaging," *Med. Image Anal.*, vol. 4, no. 4, pp. 201–217, Feb. 2000.

[16] H. Lester and S. R. Arridge, "A survey of hierarchical nonlinear medical image registration," *Pattern Recognit.*, vol. 32, pp. 129–149, 1998.

[17] L. G. Brown, "A survey of image registration techniques," *ACM Comput. Surv.*, vol. 24, no. 4, pp. 325–376, 1992.

[18] M. C. Gilardi, G. Rizzo, A. Savi, and F. Fazio, "Registration of multimodal biomedical images of the heart," *Q. J. Nucl. Med.*, vol. 40, no. 1, pp. 142–150, 1996.

[19] A. W. Habboosh, "A review of MRI and PET correlation," in *Proc. IEEE Conf. Bioengineering*, 1992, pp. 16–17.

[20] G. Z. Yang, P. Burger, J. Panting, P. D. Gatehouse, D. Rueckert, D. J. Pennel, and D. N. Firmin, "Motion and deformation tracking for short-axis echo-planar myocardial perfusion imaging," *Med. Image Anal.*, vol. 2, no. 3, pp. 285–302, Mar. 1998.

[21] J. C. McEachen II, A. Nehorai, and J. S. Duncan, "Multiframe temporal estimation of cardiac nonrigid motion," *IEEE. Trans. Med. Imag.*, vol. 9, pp. 651–665, Apr. 2000.

[22] X. Papademetris, A. J. Sinusas, D. P. Dione, and J. S. Duncan, "Estimation of 3D left ventricular deformation from echocardiography," *Med. Image Anal.*, vol. 5, pp. 17–28, 2001.

[23] G. J. Klein and R. H. Huesman, "Four-dimensional processing of deformable cardiac PET data," *Med. Image Anal.*, vol. 6, pp. 29–46, 2002.

[24] T. R. Nelson, D. B. Downay, D. H. Pretorius, and A. Fenster, *Three-Dimensional Ultrasound*. Philadelphia, PA: Lippincott Williams & Wilkins, 1999.

[25] K. S. Arun, T. S. Huang, and S. D. Blostein, "Least-squares fitting of two 3-D point sets," *IEEE Trans. Pattern Anal. Machine Intell.*, vol. PAMI-9, pp. 698–700, May 1987.

[26] S. Pallotta, M. C. Gilardi, V. Bettinardi, G. Rizzo, C. Landoni, G. Striano, R. Masi, and F. Fazio, "Application of a surface matching image registration technique to the correlation of cardiac studies in positron emission tomography by transmission images," *Phys. Med. Biol.*, vol. 40, pp. 1695–1708, 1995.

[27] Q. Li, L. Zamorano, Z. Jiang, F. Vinas, and F. Diaz, "The application accuracy of the frameless implantable marker system and analysis of related affecting factors," in *Lecture Notes in Computer Science 1496: Medical Image Computing and Computer-Assisted Intervention, MICCAI98*, W. M. Wells, A. Colchester, and S. Delp, Eds., 1998, pp. 253–260.

[28] O. Sipilä, "Methodological aspects for improving clinical value of SPECT and MRI," Ph.D. dissertation, Helsinki Univ. Technol., Helsinki, Finland, 2000.

[29] T. L. Faber, R. W. McColl, R. M. Opperman, J. R. Corbett, and R. M. Peshock, "Spatial and temporal registration of cardiac SPECT and MR images: Methods and evaluation," *Radiology*, vol. 179, no. 3, pp. 857–861, 1991.

[30] S. Eberl, I. Kanno, R. R. Fulton, A. Ryan, B. F. Hutton, and M. J. Fulham, "Automated interstudy image registration technique for SPECT and PET," *J. Nucl. Med.*, vol. 37, no. 1, pp. 137–145, 1996.

[31] M. C. Gilardi, G. Rizzo, A. Savi, C. Landoni, V. Bettinardi, C. Rossetti, G. Striano, and F. N. Fazio, "Correlation of SPECT and PET cardiac images by a surface matching registration technique," *Comput. Med. Imag. Graph.*, vol. 22, pp. 391–398, Dec. 1998.

[32] D. Dey, P. J. Slomka, L. J. Hahn, and R. Kloiber, "Automatic three-dimensional multimodality registration using radionuclide transmission CT attenuation maps: A phantom study," *J. Nucl. Med.*, vol. 40, no. 3, pp. 448–455, 1999.

[33] J. N. Yu, F. H. Fahey, H. D. Gage, C. G. Eades, B. A. Harkness, and C. A. Pelizzari, "Intermodality, retrospective image registration in the thorax," *J. Nucl. Med.*, vol. 36, no. 12, pp. 2333–2338, Dec. 1995.

[34] J. West, J. M. Fitzpatrick, M. Y. Wang, B. M. Dawant, C. R. Maurer Jr., R. M. Kessler, R. J. Maciunas, C. Barillot, D. Lemoine, A. Collingnon, F. Maes, P. Suetens, D. Vandermeulen, P. A. van den Elsen, S. Napel, T. S. Sumanaweera, B. Harkness, P. F. Hemler, D. L. G. Hill, D. J. Hawkes, C. Studholme, J. B. A. Maintz, M. A. Viergever, G. Malandain, X. Pennec, M. E. Noz, G. Q. Maguire Jr., M. Pollack, C. A. Pelizzari, R. A. Robb, D. Hanson, and R. P. Woods, "Comparison and evaluation of retrospective intermodality image registration techniques," *J. Comput. Assist. Tomogr.*, vol. 21, pp. 554–566, 1997.

[35] E. L. Kramer, M. E. Noz, J. J. Sanger, A. J. Megibow, and G. Q. Maguire, "CT-SPECT fusion to correlate radiolabeled monoclonal antibody uptake with abdominal CT findings," *Radiology*, vol. 172, no. 10, pp. 861–865, 1989.

[36] H. Loats, "CT and SPECT image registration and fusion for spatial localization of metastatic processes using radiolabeled monoclonals," *J. Nucl. Med.*, vol. 34, pp. 562–566, 1993.

[37] L. M. Bidaut and J.-P. Vallee, "Automated registration of dynamic MR images for the quantification of myocardial perfusion," *J. Magn. Res. Imag.*, vol. 13, pp. 648–655, 2001.

[38] A. Carrillo, J. L. Duerk, J. S. Lewin, and D. L. Wilson, "Semiautomatic 3-D image registration as applied to interventional MRI liver cancer treatment," *IEEE Trans. Med. Imag.*, vol. 19, pp. 175–185, Mar. 2001.

[39] A. Savi, M. C. Gilardi, G. Rizzo, M. Pepi, C. Landoni, C. Rossetti, G. Lucignani, A. Bartonelli, and F. Fazio, "Spatial registration of echocardiographic and positron emission tomographic heart studies," *Eur. J. Nucl. Med.*, vol. 22, no. 3, pp. 243–247, 1995.

[40] S. Sinha, U. Sinha, J. Czernin, G. Porenta, and H. R. Schelbert, "Noninvasive assessment of myocardial perfusion and metabolism: Feasibility of registering gated MR and PET images," *Amer. J. Roentgenol.*, vol. 36, pp. 301–307, 1995.

[41] X. Pennec, N. Ayache, and J.-P Thirion, *Handbook of Medical Imaging: Processing and Analysis*. New York: Academic, 2000, ch. Landmark-based registration using features identified through differential geometry, pp. 499–513.

[42] M. A. Wirth, C. Choi, and A. Jennings, "Point-to-point registration of nonrigid medical images using local elastic transformation methods," in *IEEE Int. Conf. Image Processing and Its Applications*, 1997, pp. 780–784.

[43] G. Borgefors, "Distance transformation in digital images," *Comput. Vision Graph. Image Process.*, vol. 48, pp. 344–371, 1986.

[44] ——, "Hierarchical chamfer matching: A parametric edge matching algorithm," *IEEE Trans. Pattern Anal. Machine Intell.*, vol. 10, pp. 849–865, Nov. 1988.

[45] M. Van Herk, *Handbook of Medical Imaging: Processing and Analysis*. New York: Academic, 2000, ch. Image registration using chamfer matching, pp. 515–527.

[46] J. Cai, J. C. Chu, D. Recine, M. Sharma, C. Nguyen, R. Rodebaugh, A. Saxena, and A. Ali, "CT and PET lung image registration and fusion in radiotherapy treatment planning using the chamfer-matching method," *Int. J. Radiat. Oncol. Biol. Phys.*, vol. 43, no. 4, pp. 883–891, 1999.

[47] T. J. Mäkelä, P. Clarysse, J. Lötjönen, O. Sipilä, K. Lauerma, H. Hänninen, E.-P Pyökkimies, J. Nenonen, J. Knuuti, T. Katila, and I. E. Magnin, "A new method for the registration of cardiac PET and MR images using deformable model based segmentation of the main thorax structures," in *Lecture Notes in Computer Science 2208: Medical Image Computing and Computer-Assisted Intervention, MICCAI01*, W. J. Niessen and M. Viergever, Eds., 2001, pp. 557–564.

[48] P. J. Besl and N. D. McKay, "A method for registration of 3-D shapes," *IEEE Trans. Pattern Anal. Machine Intell.*, vol. 14, pp. 239–256, Feb. 1992.

[49] J. Declerck, J. Feldmar, M. L. Goris, and F. Betting, "Automatic registration and alignment on a template of cardiac stress and rest SPECT images," INRIA, Res. Rep. 2770, 1996.

[50] ——, "Automatic registration and alignment on a template of cardiac stress and rest reoriented SPECT images," *IEEE Trans. Med. Imag.*, vol. 16, pp. 727–737, Dec. 1997.

[51] C. A. Pelizzari, G. T. Y. Ghen, D. R. Spelbring, R. R. Weichselbaum, and C. T. Chen, "Accurate three-dimensional registration of CT, PET and/or MR images of the brain," *J Comput. Assist. Tomogr.*, vol. 13, no. 1, pp. 20–26, 1989.

[52] D. N. Levin, C. A. Pelizzari, G. T. Y. Chen, C.-T. Chen, and M. D. Cooper, "Retrospective geometric correlation of MR, CT and PET images," *Radiology*, vol. 169, no. 3, pp. 817–823, 1988.

[53] M. J. Powell, "An iterative method of finding stationary values of a function of several variables," *Comp. J.*, vol. 5, pp. 147–151, 1962.

[54] W. H. Press, S. A. Teukolsky, W. T. Vetterling, and B. P. Flannery, *Numerical Recipes in C: The Art of Scientific Computing*, 2nd ed. Cambridge, U.K.: Cambridge Univ. Press, 1992.

[55] Y.-C. Tai, K. P. Lin, C. K. Hoh, S. C. Huang, and E. J. Hoffman, "Utilization of 3-D elastic transformation in the registration of chest X-ray CT and whole body PET," *IEEE Trans. Nucl. Sci.*, vol. 44, pp. 1606–1612, Aug. 1997.

[56] T. L. Faber, E. M. Stokely, R. M. Peshock, and J. R. Corbett, "A model based four-dimensional left ventricular surface detector," *IEEE Trans. Med. Imag.*, vol. 10, pp. 321–329, Sept. 1991.

[57] S. Nekolla, T. Ibrahim, T. Balbach, and C. Klein, *Understanding Cardiac Imaging Techniques—From Basic Pathology to Image Fusion*. Amsterdam, The Netherlands: IOS Press, 2001, vol. 322, ch. Coregistration and fusion of cardiac magnetic resonance and positron emission tomography studies, pp. 144–154.

[58] S. Nekolla, C. Miethaner, N. Nguyen, S. Ziegler, and M. Schwaiger, "Reproducibility of polar map generation and assessment of defect severity and extent assessment in myocardial perfusion imaging using positron emission tomography," *Eur. J. Nucl. Med.*, no. 25, pp. 1313–1321, 1998.

[59] J. Canny, "A computational approach to edge detection," *IEEE Trans. Pattern Anal. Machine Intell.*, vol. PAMI-8, pp. 679–698, Nov. 1986.

[60] R. Deriche, "Using Canny's criteria to derive a recursively implemented optimal edge detector," *Int. J. Comput. Vision*, vol. 1, pp. 167–187, 1987.

[61] J.-P Thirion, *Understanding Cardiac Imaging Techniques—From Basic Pathology to Image Fusion*. Amsterdam, The Netherlands: IOS Press, 2001, ch. Perfusion and motion from gated SPECT, pp. 84–93.

[62] ——, "Fast non-rigid matching of 3-D medical images," INRIA, Res. Rep. 2547, 1995.

[63] ——, "Image matching as a diffusion process: An analogy with Maxwell's demons," *Med. Image Anal.*, vol. 2, no. 3, pp. 243–260, 1998.

[64] J. L. R. Andersson, "A rapid and accurate method to realign PET scans utilizing image edge information," *J. Nucl. Med.*, vol. 36, no. 4, pp. 657–669, 1995.

[65] J. L. R. Andersson, B. E. Bagnhammar, and H. Schneider, "Accurate attenuation correction despite movement during PET imaging," *J. Nucl. Med.*, vol. 36, no. 4, pp. 670–678, 1995.

[66] P. J. Slomka, A. H. Gilbert, J. Stephenson, and T. Cradduc, "Automated alignment and sizing of myocardial stress and rest scans to three-dimensional normal templates using an image registration algorithm," *J. Nucl. Med.*, vol. 36, pp. 1115–1122, 1995.

[67] C. K. Hoh, M. Dahlbom, G. Harris, Y. Choi, R. A. Hawkins, M. E. Philps, and J. Maddahi, "Automated iterative three-dimensional registration of positron emission tomography images," *J. Nucl. Med.*, vol. 34, no. 11, pp. 2009–2018, 1993.

[68] P. A. Viola, "Alignment by maximization of mutual information," Ph.D. dissertation, Massachusetts Inst. Technol., Cambridge, MA, 1995.

[69] P. J. Slomka, P. Radau, G. A. Hurwitz, and D. Dey, "Automated three-dimensional quantification of myocardial perfusion and brain SPECT," *Comput. Med. Imag. Graph.*, no. 25, pp. 153–164, 2001.

[70] G. J. Klein, B. W. Reutter, and R. H. Huesman, "Four-dimensional affine registration models for respiratory-gated PET," *IEEE Trans. Med. Imag.*, vol. 48, pp. 756–760, Mar. 2002.

[71] T. G. Turkington, T. R. DeGrado, M. W. Hanson, and R. E. Coleman, "Alignment of dynamic cardiac PET images for correction of motion," *IEEE Trans. Nucl. Sci.*, vol. 44, pp. 235–242, Apr. 1997.

[72] M. K. O'Connor, K. M. Kanal, M. W. Gebhard, and P. J. Rossman, "Comparison of four motion correction techniques in SPECT imaging of the heart: A cardiac phantom study," *J. Nucl. Med.*, vol. 39, pp. 2027–2034, 1998.

[73] M. K. O'Connor, "Evaluation of motion-correction techniques in cardiac SPECT," *J. Nucl. Med.*, vol. 41, no. 7, p. 1298, 2000.

[74] V. Bettinardi, M. C. Gilardi, G. Lucignani, C. Landoni, and G. Rizzo, "A procedure for patient repositioning and compensation for misalignment between transmission and emission data in PET heart studies," *J. Nucl. Med.*, vol. 34, no. 1, pp. 137–142, 1993.

[75] C. M. Gallippi and G. E. Trahey, "Automatic image registration for MR and ultrasound cardiac images," in *Lecture Notes in Computer Science 2082: Information Processing in Medical Imaging, IPMI01*, M. F. Insana and R. M. Leahy, Eds., 2001, pp. 141–147.

[76] S. L. Bacharach, M. A. Douglas, R. E. Carson, P. J. Kalkowski, N. M. Freedman, P. Perrone, and R. O. Bonow, "Three-dimensional registration of cardiac positron emission tomography attenution scans," *Comput. Vision, Graph. Image Process.*, vol. 34, no. 2, pp. 311–321, 1993.

[77] D. L. G. Hill and D. J. Hawkes, *Handbook of Medical Imaging: Processing and Analysis*. New York: Academic, 2000, ch. Across-modality registration using intensity-based cost functions, pp. 537–553.

[78] R. P. Woods, S. R. Cherry, and J. C. Mazziotta, "Rapid automated algorithm for aligning and reslicing PET images," *J. Comput. Assist. Tomogr.*, vol. 17, no. 4, pp. 620–633, 1992.

[79] R. P. Woods, J. C. Mazziotta, and S. R. Cherry, "MRI-PET registration with automated algorithm," *J. Comput. Assist. Tomogr.*, vol. 17, no. 4, pp. 536–546, 1993.

[80] N. Alpert, J. Bradshaw, D. Kennedy, and J. Correia, "The principal axes transformation—A method for image registration," *J. Nucl. Med.*, vol. 31, no. 1, pp. 717–721, 1990.

[81] R. Kim, T. Aw, S. Bacharach, and R. Bonow, "Correlation of cardiac MRI and PET images using lung cavities as landmarks," in *Proc. IEEE Conf. Computers in Cardiology*, 1991, pp. 49–52.

[82] F. Maes, A. Collignon, D. Vandermeulen, G. Marchal, and P. Suetens, "Multimodality image registration by maximization of mutual information," *IEEE Trans. Med. Imag.*, vol. 16, pp. 187–198, Apr. 1997.

[83] W. M. Wells, P. Viola, H. Atsumi, S. Nakajima, and R. Kikinis, "Multi-modal volume registration by maximization of mutual information," *Med. Image Anal.*, vol. 1, no. 1, pp. 35–51, 1996.

[84] R. P. Woods, *Handbook of Medical Imaging: Processing and Analysis*. New York: Academic, 2000, ch. Within-modality registration using intensity-based cost functions, pp. 529–536.

[85] P. J. Slomka, D. Dey, C. Przetak, and R. Baum, "Automated 3-D spatial integration of 18-F FDG wholebody PET with CT," *J. Nucl. Med.*, vol. 41, no. 6, p. 59P, 2000.

[86] ——, "Automated nonlinear 3-D registration of 18-F FDG wholebody PET with thoracic CT," *J. Nucl. Med.*, vol. 42, no. 5, p. 11P, 2001.

[87] J. Lötjönen and T. J. Mäkelä, "Elastic matching using a deformation sphere," in *Lecture Notes in Computer Science 2208: Medical Image Computing and Computer-Assisted Intervention, MICCAI01*, W. Niessen and M. Viergever, Eds., 2001, pp. 541–548.

[88] P. Thévenaz, T. Blu, and M. Unser, *Handbook of Medical Imaging: Processing and Analysis*. New York: Academic, 2000, ch. Image interpolation and resampling, pp. 393–418.

[89] M. Haddad, "Impact of reorientation algorithms on quantitative myocardial SPECT perfusion imaging," *J. Nucl. Med.*, vol. 39, no. 11, pp. 1864–1869, 1998.

[90] J. Nelder and R. A. Mead, "A simplex method for function minimization," *Comp. J.*, vol. 7, pp. 308–313, 1965.

[91] R. P. Woods, *Handbook of Medical Imaging: Processing and Analysis*. New York: Academic, 2000, ch. Validation of registration accuracy, pp. 491–497.

[92] ——, *Handbook of Medical Imaging: Processing and Analysis*. New York: Academic, 2000, ch. Spatial transformation models, pp. 465–490.

[93] M. Dahlbom and S.-C. Huang, *Handbook of Medical Imaging: Processing and Analysis*. New York: Academic, 2000, ch. Physical and biological bases of spatial distortions in positron emission tomography images, pp. 439–448.

[94] G. W. Goerres, E. Kamel, T.-N. H. Heidelber, M. R. Schwitter, C. Burger, and G. K. von Schulthess, "PET-CT image co-registration in the thorax: Influence of respiration," *Eur. J. Nucl. Med.*, vol. 29, no. 3, pp. 351–360, 2002.

[95] J. N. Yu, F. H. Fahey, H. D. Gage, C. G. Eades, and J. W. Keyes, "Evaluation of emission-transmission registration in thoracic PET," *J. Nucl. Med.*, vol. 35, no. 11, pp. 1777–1781, 1994.

[96] W. L. Costa, D. R. Haynor, and T. K. Lewellen, "Registration of segmented attenuation and emission data in PET," in *Proc. Nucl. Science Symp. Medical Imaging Conf.*, 1994, pp. 1407–1411.

[97] C. D. Stone, J. W. McCormick, D. R. Gilland, K. L. Greer, R. E. Coleman, and R. J. Jaszczak, "Effect of registration errors between transmission and emission scans on a SPECT system using sequential scanning," *J. Nucl. Med.*, vol. 39, no. 2, pp. 365–373, 1998.

[98] S. W. Alderson, L. H. Lanzl, M. Rollins, and J. Spira, "An instrumented phantom system for analog computation of treatments plans," *Amer. J. Roentgenol. Radium Ther. Nucl. Med.*, vol. 87, pp. 185–195, 1962.

[99] P. H. Pretorius, W. Xia, M. A. Kinag, B. M. W. Tsui, T. S. Pan, and B. J. Villegas, "Evaluation of right and left ventricular volume and ejection fraction using a mathematical cardiac torso phantom," *J. Nucl. Med.*, vol. 38, no. 10, pp. 1528–1535, 1997.

[100] T. Beyer, D. W. Townsend, T. Brun, P. E. Kinahan, M. Charron, R. Roddy, and J. Jerin, "A combined PET/CT scanner for clinical oncology," *J. Nucl. Med.*, vol. 41, no. 8, pp. 1369–1379, 1999.

[101] J. Patton, D. Delbeke, and M. P. Sandler, "Image fusion using an integrated, dual-head coincidence camera with X-ray tube-based attenuation maps," *J. Nucl. Med.*, vol. 41, no. 8, pp. 1364–1368, 2000.

[102] W. J. Rogers, E. P. Shapiro, J. L. Weiss, M. B. Buchalter, F. E. Rademakers, M. L. Weisfeldt, and E. A. Zerhouni, "Quantification of and correction for left ventricular systolic long-axis shortening by magnetic resonance tissue tagging and slice isolation," *Circulation*, vol. 84, no. 2, pp. 721–731, 1991.

[103] W. G. O'Dell, C. C. Moore, W. C. Hunter, E. A. Zerhouni, and E. R. McViegh, "Three-dimensional myocardial defomations: Calculation with displacement field fitting to tagged MR images," *Radiology*, vol. 195, pp. 829–835, 1995.

[104] T. J. Mäkelä, Q. C. Pham, P. Clarysse, J. Lötjönen, K. L. H. Hänninen, J. Nenonen, J. Knuuti, T. Katila, and I. E. Magnin, "A 3-D model-based approach for the PET-functional and MR-anatomical cardiac imaging data fusion," in *Lecture Notes in Computer Science 2230: 1st Int. Workshop Functional Imaging and Modeling of the Heart, FIMH 2001*, T. Katila, I. E. Magnin, P. Clarysse, J. Montagnat, and J. Nenonen, Eds., 2001, pp. 83–90.

[105] C. Muller, M. Rombaut, and M. Janier, "Dempster shafer approach for high level data fusion applied to the assessment of myocardial viability," in *Lecture Notes in Computer Science 2230: 1st Int. Workshop Functional Imaging and Modeling of the Heart, FIMH 2001*, T. Katila, I. E. Magnin, P. Clarysse, J. Montagnat, and J. Nenonen, Eds., 2001, pp. 104–112.

[106] T. McInerney and D. Terzopoulos, "Deformable models in medical image analysis: A survey," *Med. Image Anal.*, vol. 1, no. 2, pp. 91–108, 1996.

# Exploratory Analysis of the Spatio–Temporal Deformation of the Myocardium During Systole From Tagged MRI

Patrick Clarysse*, Meimei Han, Pierre Croisille, and Isabelle E. Magnin, *Member, IEEE*

***Abstract*—Myocardial contractile function is, with perfusion, one of the main affected factors in ischemic heart diseases. In this paper, we propose an original framework based on functional data analysis for the quantitative study of spatio–temporal parameters related to the myocardial contraction mechanics. The mechanical strains in the left-ventricular (LV) myocardium are computed from tagged magnetic resonance imaging cardiac sequences. A statistical functional model of the normal contractile function of the LV is build from the study of eight examinations on healthy subjects. We show that it is possible to detect abnormal strain patterns comparatively to this model, by generating distance maps at rest and under pharmacological stress. We demonstrate the consistency of the results for the circumferential deformation parameter on healthy and pathological data sets.**

***Index Terms*—Cardiac motion analysis, functional data analysis, spatio–temporal data analysis.**

## NOMENCLATURE

| | |
|---|---|
| EV | Elementary volume. |
| LV | Left ventricle |
| MR(I) | Magnetic resonance (imaging) |
| NCR | Normal contraction reference (model) |
| PCOM | Principal component |
| PET | Positron emission tomography |
| SPAMM | Spatial modulation of the magnetization |
| STDP | Spatio–temporal deformation parameter |
| $p(t)$ | One STDP which is a continuous function of the time variable |
| $x_i(t), i = 1 \cdots N$ | Designates the $N$ measurements of $p(t)$ from which the mean curve $\overline{x} = (1/N)\sum_{i=1}^{N} x_i(t)$ has been subtracted. |

Manuscript received January 16, 2001; revised June 20, 2002. This work was supported by the Région Rhône-Alpes under Grant "Santé et HPC." and in part by a grant from the Lipha Santé Company, a subsidiary of the group MERCK KGaA. *Asterisk indicates corresponding author.*

*P. Clarysse is with the CREATIS, French National Center for Scientific Research Unit #5515, INSA Bâtiment Blaise Pascal, 69621 Villeurbanne Cedex, France (e-mail: patrick.clarysse@creatis.insa-lyon.fr).

M. Han is with Bombardier Transport, 800, bld. René-Lévesque Ouest, Montréal, Québec, Canada.

P. Croisille and I. E. Magnin are with the CREATIS, French National Center for Scientific Research Unit #5515, 69621 Villeurbanne Cedex, France.

Digital Object Identifier 10.1109/TBME.2002.804587

## I. INTRODUCTION

SINCE the early works of Tennant and Wiggers in 1935 [1], it is well known that ischemic heart diseases induce abnormal myocardial contractile function. Much of progress in the physiopathology of the heart has been made since then. In the 1980s, new concepts have emerged from the observation that, in some situations, contractile function can recover from a revascularization procedure [2]. Ischemia can be seen as a consequence of a disequilibrium between myocardial metabolism, perfusion, and contractile function due to a blood flow deficit in some myocardial territory. Better understanding of the complex pathological mechanism can be achieved thanks to the increasing performances of medical imaging techniques. Tagged MRI [3] is a very useful and non invasive technique to quantitatively explore the local contractile function. The analysis of parameters extracted from MR tagging data has already been conducted by several groups [4]–[7]. However, most of these studies usually consider parameter statistics at few locations within the myocardium at the end-diastolic and end-systolic phases. According to most recent works [8]–[11], it is now possible to extract contraction parameters all over the myocardium and for several successive phases of the cardiac cycle. In this paper, we propose an original framework for the systematic and exhaustive analysis of spatio–temporal deformation parameters (STDP) of the myocardium, extracted from MR tagging data. The acquired images are processed to extract spatio–temporal deformation parameters over a set of LV contiguous myocardial regions throughout the systolic phase of the cardiac cycle. These STDPs are then analyzed using functional data analysis methods [12]. Functional data analysis of individual data sets is first considered. Then, several healthy data sets are simultaneously analyzed to provide a *normal contraction reference model*. Pathological cases can be compared with this model in order to highlight abnormal strain patterns. The framework and the methods are described in Section II. The results are presented in Section III and discussed in the last section of the paper.

## II. MATERIAL AND METHOD

### A. Imaging Data

Eight healthy subjects (S1 to S8) have been investigated using MR tagging at the Johns Hopkins Hospital, Baltimore, USA. The acquisitions have been conducted on a 1.5-tesla (T) MR scanner (Signa, GE Medical Systems, Milwaukee, WI) using ECG-gated (on end-diastole) gradient echo sequences. Ten to twelve frames were acquired within a breath-hold with a tem-

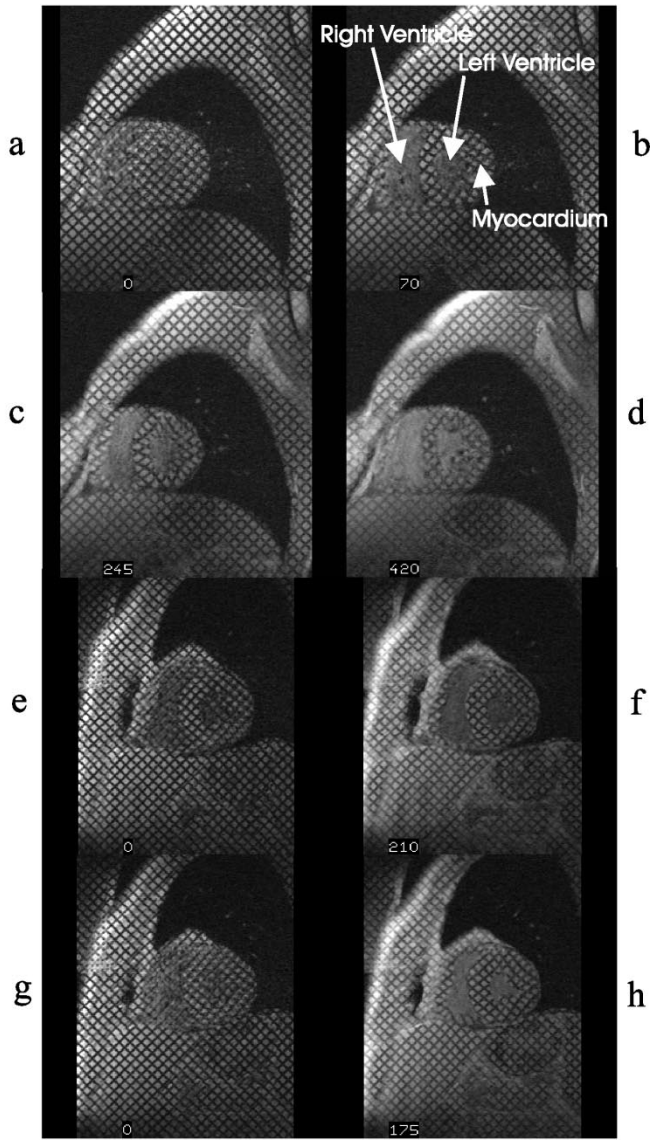


Fig. 1. (a)–(d) A sequence of four SPAMM images from end-diastole (time 0) to end-systole (time 420 ms) for a healthy subject. (e)–(f) End-diastolic and end-systolic images for a patient at rest. (g)–(h) End-diastolic and end-systolic images for the same patient under Dobutamine induced stress.

poral resolution of 32.5 ms. Tags were applied in three orthogonal directions (six short-axis slices, six radial long-axis slices) to allow three–dimensional deformation estimation according to the imaging protocol described in [8].

Six patients (P1 to P6) were studied at the Cardiologic Hospital in Lyon, France. The acquisitions were performed on a 1.5-T MR scanner (Siemens, Erlangen, Germany) using a fast ECG-gated (end-diastole) segmented gradient echo sequence. Five to seven short-axis slices were acquired to cover up the LV at rest and under pharmacological stress (Dobutamine) with a two–dimensional (2-D) SPAMM grid tagging pattern [13] (Fig. 1). Seven to nine cardiac phases have been acquired for the examination at rest while only six to seven phases could be acquired under stress because of the increased heart rate. Patients were required to hold their breath (from 15–22 s) during image acquisition. Tags have a 45° inclination. The tag spacing is 6–7 mm, the tag thickness is approximately 1.5 mm and the time between two consecutive frames ranges from 35 to 40 ms. Note that as the tagging pattern persists for times on the order of the $T1$ relaxation time, only the systolic part (400 ms) of the cardiac cycle can be reasonably analyzed. The characteristics of the MR acquisitions are summed up in Table I. Tagged images can be seen in Fig. 1. Also, fluorodesoxyglucose PET (FDG-PET) images have been acquired for each patient with an Ecat Exact HR+ PET camera (Siemens-CTI, Erlangen, Germany). They highlight the location of reduced metabolic activity and necrosed regions where the contractile function should be affected.

### *B. Spatio–Temporal Deformation Parameters (STDP)*

This large image data set is processed to extract the tag lines and compute the displacement field within the myocardium using the FINDTAGS software [14], [15].[1] The displacement field is estimated through the least-square fit of the tag displacements by a harmonic series in a prolate spheroidal coordinate system [8]. Several other methods have been proposed to estimate the displacement field from tag points [9], [10], [16]–[18] and could provide similar input parameters to the analyzing procedure presented in this paper. The strain parameters are derived frame by frame in a radial–circumferential coordinate system from the displacement field. Those parameters are the circumferential $E_{cc}$ and radial $E_{rr}$ deformation components, the lowest eigen value of the deformation tensor $E$, which corresponds to the maximum shortening at midwall, and the angle between the principal direction associated to the eigen value and the local circumferential direction. The function $p(t)$ will refer to any of those parameters. To simplify further analysis, the LV myocardial wall is subdivided into EVs according to the circumferential, radial and longitudinal directions. The partitioning relies on the definition of the LV long axis, as a rotation axis, and an anatomical landmark, located at the junction between the right ventricles and LVs at the basal level, which determines the origin of the circumferential partition (Fig. 2). This partition allows a one-to one correspondence between the EVs of two different LVs. In this study, the myocardial partition is fixed over time and the LV geometry is normalized relatively to the LV size to allow STDP comparisons between LVs. The mean value of STDP, $p(t)$, is computed over each EV and at each frame. The temporal evolution of a parameter's value over the whole myocardium can be visualized using a planar representation of the myocardium as displayed in Fig. 2. The polar representation (bull's eye), which is a very popular representation mode in cardiology, will be used to display diagnostic results (Figs. 2, 9, and 10).

### *C. Functional Analysis of STDPs*

Our concern being to analyze STDPs through populations of patients taking into account their temporal behavior, we investigate a possible methodology among available methods. The PCOM analysis is a very common approach for multidimensional exploratory data analysis. PCOM analysis geometrically consists in searching the optimal coordinate system (the

[1]Analysis software was used courtesy of Dr. E. Zerhouni of the Johns Hopkins University School of Medicine.

TABLE I
DESCRIPTION OF THE MR ACQUISITIONS PERFORMED ON HEALTHY SUBJECTS AND PATIENTS DURING A BREATH-HOLD. FOV MEANS FIELD OF VIEW; TR, TE, NEX, SA AND LA STANDS FOR REPETITION TIME, ECHO TIME, NUMBER OF EXCITATION, SHORT AXIS AND LONG AXIS, RESPECTIVELY

| | MRI Sequence Parameters | FOV (mm) | matrix size | slice thickness (mm) | SA slices | LA slices | phases | Temporal res. (ms) | Tagging |
|---|---|---|---|---|---|---|---|---|---|
| Healthy subjects (8) | TR=6.5 ms TE=2.3 ms flip angle=15° NEX=1 | 360 | 256x110 | 8 | 5-6 | 6 | 10-12 | 32.5 | 3D stripes |
| Patients (6) | TR=70 ms with echo sharing TE=4 ms flip angle=15° NEX=1 | 280 | 256x154 | 8 | 5-6 | - | 7-9 (rest) 6-7 (stress) | 35-40 | 2D grid |

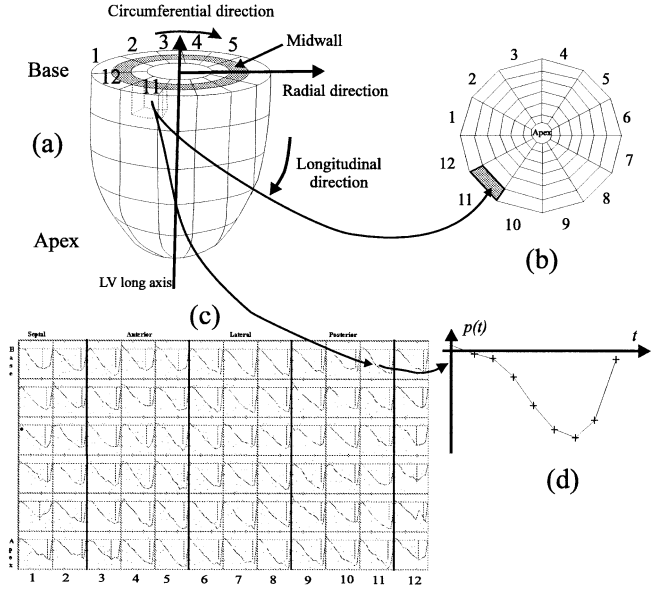


Fig. 2. (a) Partition of the LV myocardial wall into EVs. (b) Polar map representation of one myocardial layer (midwall here) used for diagnostic purposes of the contractile function. (c) Planar representation of one myocardial layer (midwall here). In each EV, mean value of the deformation parameters is computed for several successive timepoints. (d) Linear interpolation of the discrete samples of parameter $p(t)$ (arbitrary unit) in the EV.

PCOMs) that best represents the extent of a cloud of points. Representing the data points in this system highlights the proximity between individuals. Usually, the first (first–third) PCOMs are sufficient to sum up information and produce meaningful 2-D graphical representations of the clouds of individuals and parameters. If the data set is representative, groups of individuals and correlated variables emerge. In this study, the configuration of the data is different since each parameter (STDP) varies in space and time (Fig. 2). The measure of one deformation parameter in a specific myocardial EV over the cardiac systole and through a population of subjects provides a set of time series. In their book *Functional data Analysis* [12], Ramsay and Silverman define functional data as the repeated measure of a continuously evolving quantity. This definition exactly fits our input data sets at each EV. We propose to adapt functional data analysis methods to analyze the myocardial deformation through a population of subjects.

*1) Functional Data Analysis:*

*Principle:* The problem can be stated as follows. In a given EV, we observe a parameter (STDP) which is supposed to be a continuous function $p$ of a variable $t$ (time) varying in the $[a, b]$ interval of $\Re$. Let the $x_i$, $i = 1 \cdots N$ be the $N$ repetitions of the measurement of $p(t)$ through a population of $N$ subjects from which the mean curve has been subtracted. The $x_i$ are also functions of time. In order to explain the variation of parameter function $p(t)$ from the $\{x_i, i = 1 \cdots N\}$ data set, we seek for a set of $q$ orthogonal functions $\{\varepsilon_\alpha(t), \alpha = 1 \cdots q\}$ such that

$$\langle \varepsilon_\alpha, \varepsilon_\beta \rangle = \int_a^b \varepsilon_\alpha(t)\varepsilon_\beta(t)\,dt = 0, \quad \forall \alpha, \beta = 1 \cdots q, \alpha \neq \beta \tag{1}$$

and

$$\|\varepsilon_\alpha\|^2 = \int_a^b \varepsilon_\alpha^2\,dt = 1, \qquad \forall \alpha = 1 \cdots q$$

where $\|.\|$ is the $\mathcal{L}^2$ norm and $\langle . \rangle$ stands for the inner product [12]. This problem turns out to be equivalent to the eigen function problem (see the Appendix-A for the intermediate steps)

$$V\zeta = \lambda\zeta. \tag{2}$$

The functions $\zeta_\alpha(t)$, $\alpha = 1 \cdots q$, $\|\zeta_\alpha\| = 1$ are the first $q$ eigen functions associated with the $q$ eigen values $\lambda_\alpha$, $\alpha = 1 \cdots q$. The eigen functions are the *functional principal components* and the approach is called "*functional principal component analysis*" [12].

The computation of the functional PCOMs relies on a basis expansion of both the input curves and the functional PCOMs (see Appendix-B) which leads to the eigen analysis (9). The coefficients of the basis expansion are deduced from the eigen vectors of the $Q$ matrix.

The contribution of each functional PCOM, $\zeta_\alpha(t)$, is evaluated from the eigen values of the $Q$ matrix by: $\Lambda_\alpha = 100\lambda_\alpha / \sum_i \lambda_i \%$. In the system of the functional

PCOMs, each curve $x_i$ has coordinates represented by its scores

$$f_i = (f_{i1} f_{i2} \cdots f_{im}) = C_i W B_m \tag{3}$$

where $B_m = [\boldsymbol{b}_1 \cdots \boldsymbol{b}_m]$ is the $K \times m$ coefficient matrix of the $m$ first functional PCOMs and $C_i$ is the $K$-vector of coefficients of $x_i$. The software we developed in this paper for the analysis of the myocardial contractile function is based on MATLAB (The MathWorks, Inc., Natick, MA) functions written by Ramsay and Silverman [12] for the analysis of functional data.

*2) Setting up the Reference Models:* We propose to build a functional PCOM-based model of the normal contraction from the available healthy data sets. In fact, two models are set up: a global one that does not make any explicit difference between myocardial EV locations and a local one that considers each EV independently.

*a) Mean Global NCR Model.* In each myocardial EV, deformation parameters are averaged through the eight normal cases. A Functional PCOM analysis is performed on this average case for each deformation parameter $p$ without accounting for the location of EVs. A mean curve and the resulting functional PCOMs constitutes the *global "normal contraction" reference (NCR) model*.

*b) Local NCR Model.* The deformation evolution can be quite different from one myocardial EV to another. A Functional PCOM analysis is performed for each myocardial EV and for each deformation parameter $p$ through the eight normal data sets. The set of all the mean curves and functional PCOMs at each myocardial EV constitutes the *local "normal contraction" reference (NCR) model*.

*3) Detection of Abnormal Strain Patterns:* Given an unknown new case, being potentially pathological, the aim is to compare its STDPs with the global or local NCR models. Each parameter curve of the myocardial EV of interest is expanded within the basis of the global/local NCR model using (3). Then, a distance between the new case and the global/local NCR model is computed using the scores. If we restrict the computations to the first two PCOMs related to one deformation parameter, the distance $d_{ev}$ for a particular EV, $ev$, is given by

$$d_{ev} = \left[ \left( f_{ev,1} \frac{\Lambda_1}{\Lambda_1 + \Lambda_2} \right)^2 + \left( f_{ev,2} \frac{\Lambda_2}{\Lambda_1 + \Lambda_2} \right)^2 \right]^{1/2} \tag{4}$$

where $f_{ev,1}$ and $f_{ev,2}$ are the scores related to the first and the second functional PCOMs, respectively. Additional terms can be added if other parameters are considered or if additional functional PCOMs are taken into account. The computation of such a distance for each myocardial EV results in a distance map giving the deviation of this new case from the global/local NCR model. Note that with the global NCR model, the distance is computed between each parameter curve of the unknown case and the couple {mean curve, Functional PCOMs} representing the global NCR model, while with the local NCR model, the distance computation is performed between the parameter curve and the corresponding model (mean curve plus functional PCOMs) for each EV. The experimental results given in the next section demonstrate that this method is an effective way to highlight local myocardial contraction dysfunctions. The approach is summed up in Fig. 3.

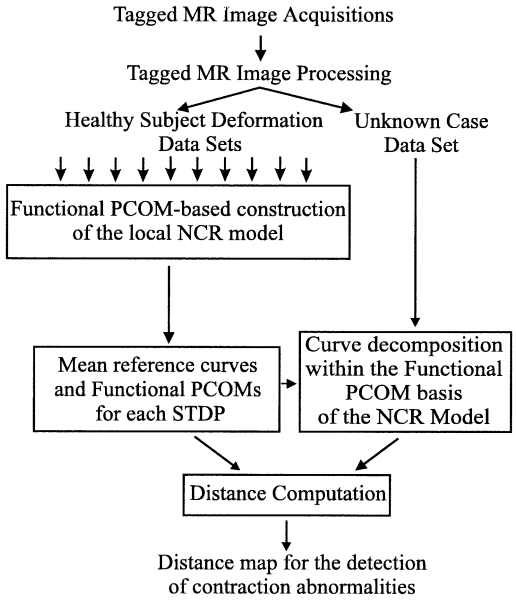


Fig. 3. Steps in determining contraction abnormalities using the local "normal contraction" reference (NCR) model.

## III. Results

Input data are preprocessed as described in the next subsection to prepare for functional analysis. Application of functional PCOM analysis to cardiac data is illustrated for a normal (S3) and a pathological (P3) cases. Then, global and local NCR models are built from the healthy data sets for the circumferential strain $(E_{cc})$. The detection of abnormal $E_{cc}$ evolution patterns is illustrated on two pathological cases using the previously build global and local NCR models. The distance maps obtained at rest and under pharmacological stress show the effect of the stimulation onto the $E_{cc}$ component of the deformation.

### A. Preprocessing of Data

As mentioned before, only a little bit more than the systolic phase is acquired. The values of the deformation parameters are computed frame by frame over the systolic phase to provide the discrete time samples of the time series. Each time series is converted into a continuous function $x_i(t)$ using a cubic B-spline model. Fig. 4(a) shows the approximated curves obtained for the $E_{rr}$ parameter of a normal subject at rest and under stress. The acquisitions are ECG-gated and time $t_0$ corresponds to the first frame acquisition time following tag creation. The temporal length of the curves naturally differs between rest and stress [Fig. 4(a)] so they have to be registered in time before comparison. The significant portions of the curves to be matched concern the systolic phase from end-diastole to end-systole.

Two methods were tested to automatically detect end-systolic time instant $t_{es}$. The first one is based on the current clinical definition stating that $t_{es}$ corresponds to the time when the LV cavity volume is the smallest. So, we estimate the LV volume from its contours throughout the cardiac cycle and select the

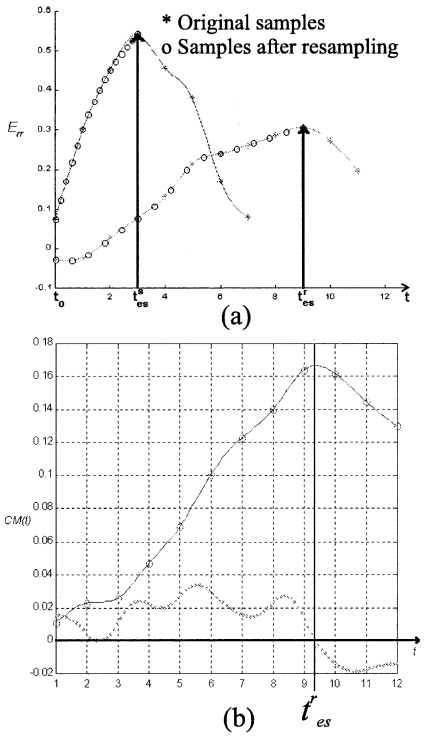


Fig. 4. STDP representation and end-systole detection. (a) Cubic B-spline representation of the evolution of the radial deformation $E_{rr}$ in a given EV of the LV of a normal subject at rest (gray curve) and under pharmacological stress (black curve). In order to match the temporal evolutions at rest and under stress, curves are resampled between $t_0$ (end-diastole) and $t^r_{es}, t^s_{es}$, respectively (end-systole). (b) The end systolic timepoint $t_{es}$ is defined as the time where the first derivative (dotted line) of the $CM(t)$ curve (solid line) cancels.

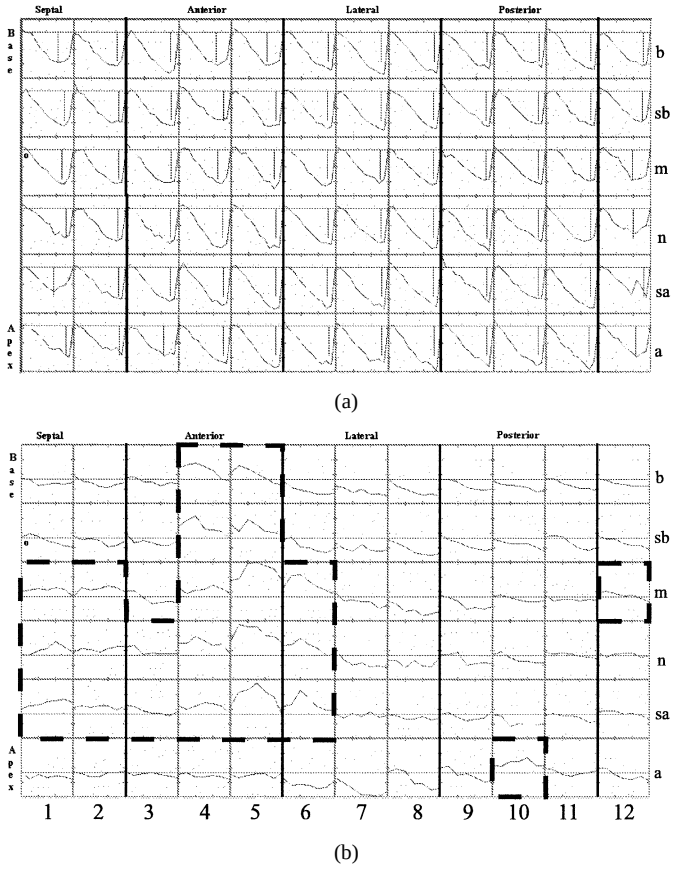


Fig. 5. Temporal evolution of the circumferential deformation $E_{cc}$ over 72 EVs of the LV midwall at rest. (a) Healthy subject S3 (extreme minimum value: $-0.24$). Detected end systolic time points are represented by vertical bars. The six longitudinal levels are referenced by the small letters: a (apical); sa (subapical); n and m (medium); sb (subbasal); b (basal). (b) Ischemic patient P3 with a septal and anterior necrosis. The abnormal regions, automatically detected by the program (see Section III-D), are circumscribed with the dashed lines.

time associated to the lowest value. The second method is based on electro-physiological considerations. According to cardiac physiology, it is clear that the mechanical contraction of the myocardium results from a propagating electrical activation wave. So, the maximum contraction time (defined as end-systole) of a myocardial region depends on its anatomical location. This leads us to propose a new local definition where $t_{es}$ is defined, region by region, as the maximum of the following curve:

$$CM(t) = |E_{cc}(t)| + |E_{rr}(t)|. \tag{5}$$

Within healthy regions, the typical evolution of $CM(t)$ resembles the one in Fig. 4(b). The maximum of this curve is calculated from its derivative. It is obvious that in some circumstances, in particular within pathological regions, this detection may fail. Therefore, if the value based on the maximum of the $CM(t)$ is less than one fourth the cardiac cycle or greater than two fifths of the cardiac cycle then the value based on the minimum of the cavity volume is chosen.

Once the $t_{es}$ values are determined for both states, the rest and stress curves within $(t_0, t^r_{es})$, $(t_0, t^s_{es})$, respectively, are mapped into a normalized time interval $(0, 1)$.

### *B. Application of Functional PCOM Analysis to Cardiac Data*

In this section, we illustrate the application of functional PCOM Analysis to the circumferential parameter $E_{cc}$ of the healthy case S3 and the pathological case P3 at midwall. The planar representation in Fig. 5 well demonstrates the differences between a healthy subject and a patient. The evolution of $E_{cc}$ is remarkably homogeneous all over the LV for the healthy subject at rest [Fig. 5(a)]. As this parameter is somehow related to the maximum shortening, it monotonously decreases during contraction. On the contrary, this evolution is greatly varying from one region to the other with the ischemic patient [Fig. 5(b)]. The expected monotonic decreasing evolution of $E_{cc}$ is observed in part of the lateral region and in the posterior region, especially from the basal to the medium level, but we clearly see the abnormal evolution of $E_{cc}$ in the anterior and septal territories. The physicians estimated that the ischemic region for patient P3 lies in the septal and antero-septal regions (sectors 12–3).

*1) Functional PCOM Analysis of Normal Case S3:* Fig. 6 shows the functional PCOM Analysis of the curves displayed in Fig. 5(a) regardless the anatomical position. The group of four plots represents the $E_{cc}$ mean curve to which the first four functional PCOMs are added ($+++$ curve) and subtracted ($---$ curve). The cumulative contribution of the first four components rises to about 92%, thus representing the most part of the variation. The graph below, named score plane, shows the 2-D distribution of the EVs in the plane related to the first two functional

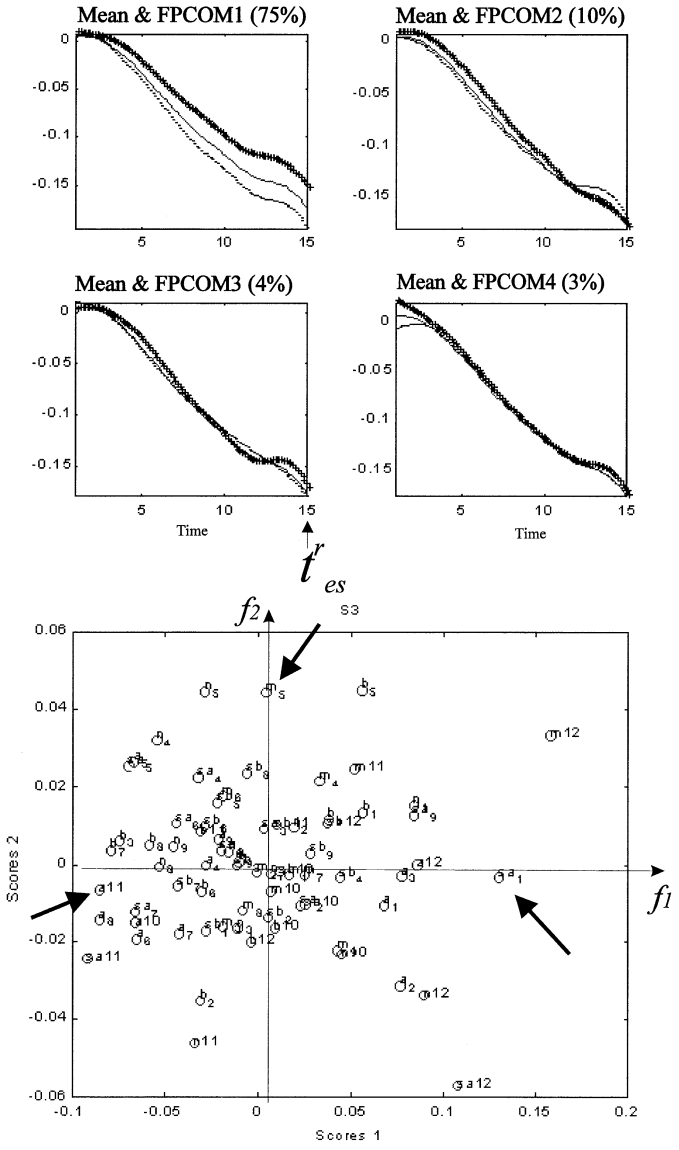


Fig. 6. Functional PCOM analysis of the $E_{cc}$ parameter for healthy case S3 at midwall and at rest. (top) Mean curve added $(+++)$ and subtracted $(---)$ to the first four functional PCOMs. (bottom) Score plane related to the first two PCOMs. Each dot represents one particular myocardial EV (see legend of Fig. 5 for EVs labels).

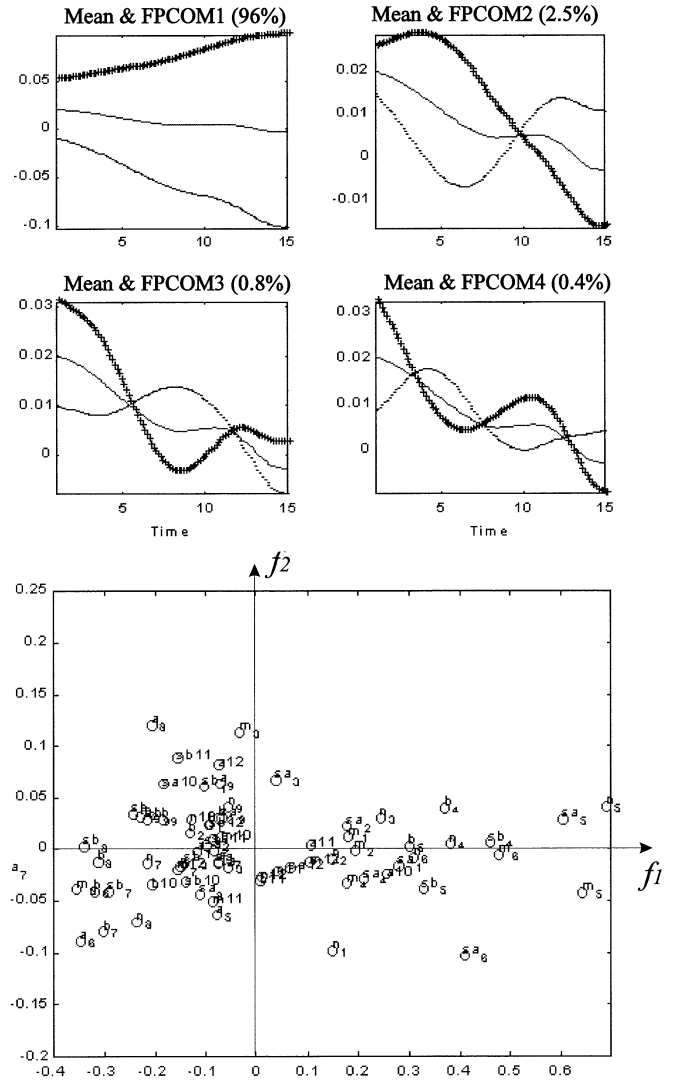


Fig. 7. Functional PCOM analysis of the $E_{cc}$ parameter for pathological case P3 at midwall and at rest. (top) Mean curve added $(+++)$ and subtracted $(---)$ to the first four functional PCOMs. (bottom) Score plane related to first two PCOMs.

PCOMs. The mean $E_{cc}$ curve shows a global decreasing evolution. The first functional PCOM is a globally increasing function. This means that, during the cardiac cycle, the variation between individuals (myocardial EVs) becomes larger. Curves that mostly follow the first functional PCOM resemble the $(+++)$ curve. For instance, the curve in EV "sa1" (subapical and septal EV) has smaller magnitude and, therefore, presents a high contribution of FPCOM1. This can also be seen in the score plane where "sa1" is located at an extreme right position on the horizontal axis. On the contrary, curves with a more accentuated negative variation than the mean curve are rejected to the left part of the score plane (see for instance "a11"). Those curves with the most negative variation are closer to the $(---)$ curve.

The second functional component has a smaller contribution (9.93%) and presents two phases in its evolution with opposite signs. The first phase represents a growing dispersion which attains a maximum at timepoint 6, cancels and inverts at timepoint 11. Curves that mostly follow this evolution exhibit a high $f_2$ score. For instance, curve "m5" evolves slower compared with the mean curve at the beginning but, in the second part of the curve, it compensates for its delay by a sharp increase. Third and fourth components represent lower contributions to the evolution with respectively 3.87% and 3.34%. Component FPCOM3 exhibits three zero-crossings that represent a more complex variation around the mean.

*2) Functional PCOM Analysis of Pathological Case P3:* Fig. 7 shows the results obtained with the pathological case P3. The first four functional PCOMs represent 99.62% of the total variation. Obviously, the dispersion between curves is much more important in this case. The first component added with the mean $E_{cc}$ curve illustrates this well, the curves being located between a positive increasing function $(+++$ curve) and a negative decreasing function $(---$ curve). The other components represent more or less complex variations around the mean. The score space experiences a higher dispersion of

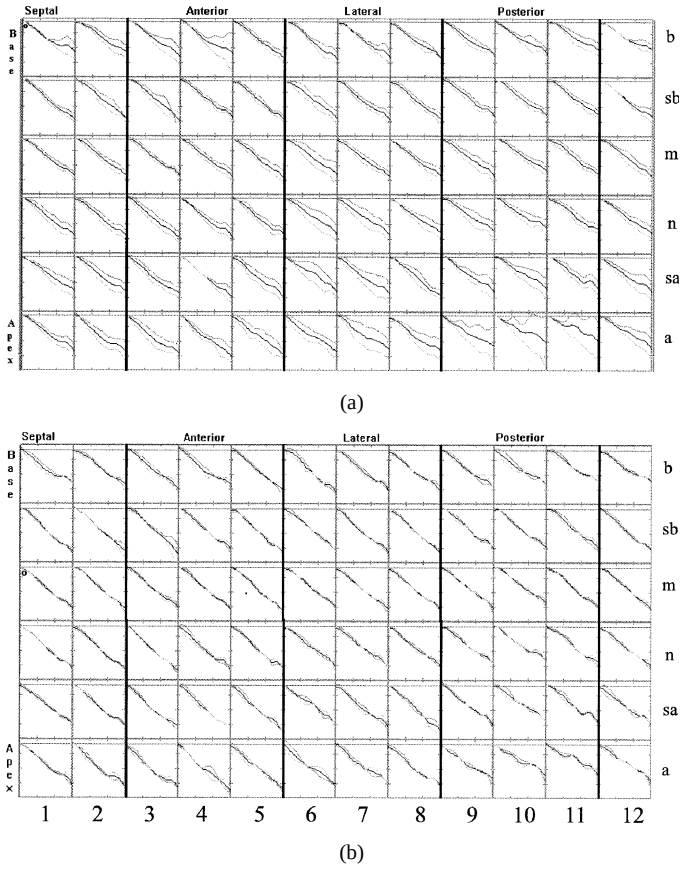


Fig. 8. *Local* NCR (NCR) model for the $E_{cc}$ parameter at rest. (a) First functional PCOM of the local NCR model at midwall. (b) Second functional PCOM. Mean curves are in black.

the $E_{cc}$ curves as compared with the score space for the healthy subject S3 (Fig. 6).

### C. Building the NCR Models

The first four functional PCOMs obtained for the averaged normal heart are very similar to the ones of the S3 case (Fig. 6) (this is the reason why they are not represented here). But, the averaging implies even less variations. The contribution of the first four functional PCOMs is 80.2%, 10.5%, 4.2%, 1.6%, respectively. The mean curve and the four functional PCOMs define the global NCR model.

With the local NCR model, the functional PCOM analysis is independently performed in each myocardial EV on the curves of the eight healthy subject data sets. Fig. 8 illustrates the first two functional PCOMs obtained by such an analysis over the myocardium at midwall and at rest. These two functional PCOMs represent the major part of the variation in each EV. Almost the same variations as those reported in Section III-B for the healthy case S3 can be observed here. It can be noticed that higher discrepancies exist at the apical level with FPCOM1.

### D. Abnormal Contractile Evolution Pattern Detection

The interest of the proposed functional approach is demonstrated through the detection of abnormal evolution patterns of the circumferential deformation parameter $E_{cc}$.

*1) Detection Using the Global NCR Model:* Fig. 9 gives the results obtained by comparing a new healthy case S9, which has not participated to the construction of the global NCR model [Fig. 9(a)] and two pathological cases P1 [Fig. 9(c)] and P3 [Fig. 9(b)] to the global NCR model. The score planes on the left part of the figure show the position of the patients' EVs (in red) relatively to those of the global NCR model (in blue). Note that due to the averaging through the healthy data sets, the EV cloud of the global NCR model is compact. For S9, the EV distribution is very close to the reference. On the contrary, the distributions are more spread with P1 and especially P3. On the right part of Fig. 9, distance maps show the proximity to the global NCR model using a polar representation. Color map ranges from blue to red where red represents the greatest distance (i.e., a more acute abnormal strain pattern) to the NCR model according to the definition given in (4). For the P3 case [Fig. 9(b)], the greatest distances are observed in the antero-lateral regions and in the medium-septal area (yellow). This can be directly evaluated by the visual inspection of the original $E_{cc}$ parameter curves in Fig. 5(b) where red to yellow regions are traced out with dashed lines. We can easily see that, indeed, those regions are the farthest from the normal case S3 [Fig. 5(a)] and the reference model.

*2) Detection Using the Local NCR Model:* The distance map computed for the P3 case at rest is given in Fig. 10(a). It is very similar to the one obtained with the global NCR model [Fig. 9(b)]. In fact, the great coherency in STDP data observed through the available healthy cases does not imply great differences between the local and global NCR models. The consistency among individuals of the normal strain patterns has also been observed in a study on more than 30 healthy volunteers [11]. In order to test the consistency of the model, we built eight models taking seven data sets out of the eight available. For each of these models, we computed the distance maps for the excluded case. If the model is consistent then the results among the eight tests should be similar. Table II gives the mean and standard deviation of the distance to the origin of the score plane over all the EVs, for each test case. The same information is given for the pathological cases P3 and P4 in Table III.

It is interesting to see how this distance map evolves under pharmacological stress. Stress activates the contractile function so that regions that are less contractile at rest may recover an improved function under stress if viable. Fig. 10(b) illustrates the distance map under pharmacological stress for the P3 case. Greatest distances are observed at basal and subbasal level in the septum. Also, one abnormal region is detected in the postero-septal region at the subbasal level. The abnormal strain patterns observed in the antero-lateral territory at rest are no longer highlighted under stress. Also, contraction defects are much less pronounced under stress with the P1 case [Fig. 10(c)]. A problem subsists at the apex in the anterior region and in the medium-septal region.

## IV. Discussion and Conclusion

We investigated the contribution of functional data analysis methods for the interpretation and comparison of evolution patterns of myocardial strain parameters obtained through tagged MRI. The results illustrate the potentialities of the functional

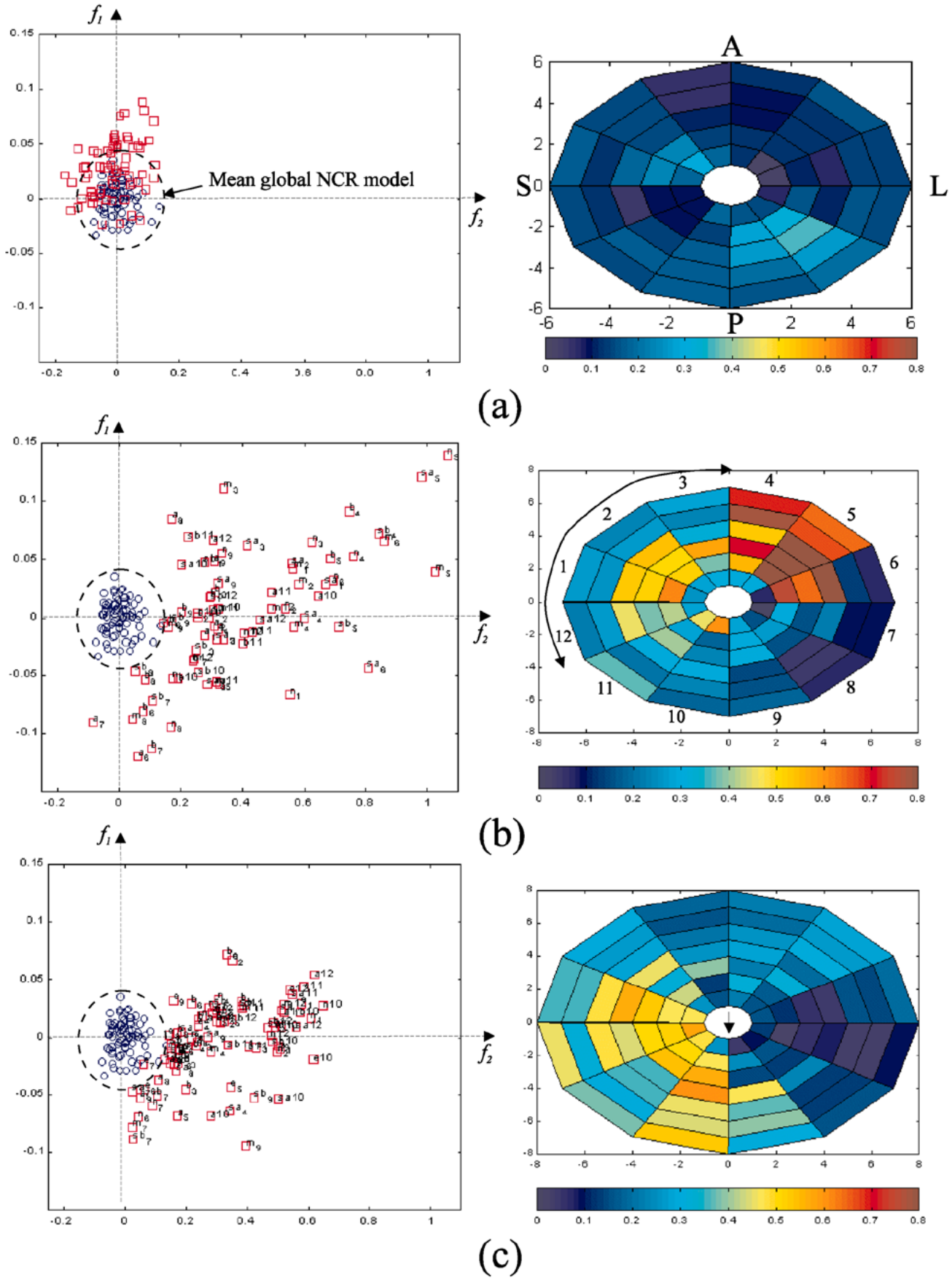


Fig. 9. Abnormal $E_{cc}$ pattern detection on three cases using the global NCR model at rest. The relative position of the myocardial EVs for the global NCR model and the three cases is given in the score planes on the left. Reference is in blue and the three cases are in red. The distance maps are displayed on the right. Red is for the greatest distances to the NCR model. (a) Results for a new healthy case S9, which was not included into the construction of the global NCR model. Mean distance is 0.081 with a standard deviation of 0.06 (b) Results for the pathological case P3. (c) Results for the pathological case P1. For P1 and P3, the extent of the nonviable region, estimated by the physician, is indicated with black arrows.

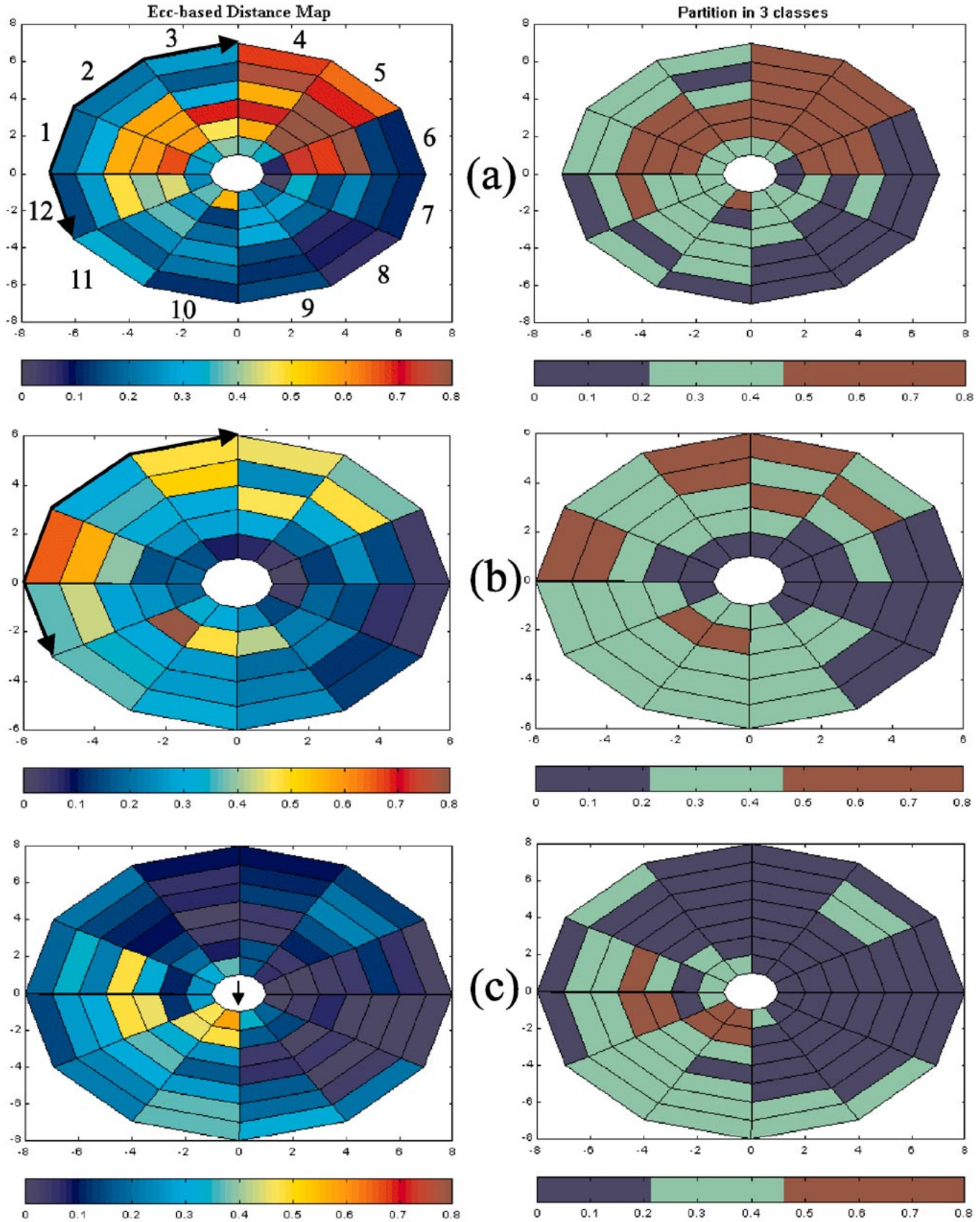


Fig. 10. Diagnostic maps ($E_{cc}$) using the local NCR model at rest and under stress. (a) Distance map for the pathological case P3 at midwall, at rest. (b) Distance map for the pathological case P3 at midwall under stress (5 levels). (c) Distance map for the pathological case P1 at midwall under stress. On the right, the continuous distance map is partitioned into three classes according to the distance of the EVs to the local NCR model. Highest distances are in red. The estimated extent of the necrosed region is indicated with black arrows.

TABLE II
MEAN AND STANDARD DEVIATION OF THE DISTANCE OF THE EVS TO THE ORIGIN OF THE SCORE PLANE FOR THE EIGHT TEST MODELS

| | S1 | S2 | S3 | S4 | S5 | S6 | S7 | S8 |
|---|---|---|---|---|---|---|---|---|
| Mean | 0.073 | 0.072 | 0.066 | 0.096 | 0.078 | 0.108 | 0.071 | 0.116 |
| Std. Dev. | 0.066 | 0.06 | 0.049 | 0.083 | 0.054 | 0.085 | 0.059 | 0.102 |

TABLE III
MEAN AND STANDARD DEVIATION OF THE DISTANCE OF THE EVS TO THE ORIGIN OF THE SCORE PLANE FOR PATHOLOGICAL CASES P3 AND P4 FOR EACH TEST MODEL. "TMX" REFERS TO TEST MODEL EXCLUDING NORMAL DATA SET SX. "ALL" REFERS TO THE MODEL THAT INCLUDES THE EIGHT DATA SETS

| | | TM1 | TM2 | TM3 | TM4 | TM5 | TM6 | TM7 | TM8 | All |
|---|---|---|---|---|---|---|---|---|---|---|
| P3 | Mean | 0.375 | 0.383 | 0.384 | 0.377 | 0.388 | 0.369 | 0.383 | 0.379 | 0.383 |
| | Std. Dev. | 0.251 | 0.256 | 0.258 | 0.257 | 0.253 | 0.246 | 0.253 | 0.254 | 0.255 |
| P4 | Mean | 0.401 | 0.411 | 0.412 | 0.403 | 0.414 | 0.398 | 0.409 | 0.404 | 0.410 |
| | Std. Dev. | 0.097 | 0.105 | 0.104 | 0.098 | 0.101 | 0.113 | 0.101 | 0.0994 | 0.1 |

PCOM analysis technique for synthesizing the evolution in a set of curves. In particular, the combination of the mean curve and the functional components, and the score plane representation are efficient ways to depict the main characteristics of the evolution of the deformation parameters over the myocardium (Figs. 6 and 7). In practice, we consider the first two functional PCOMs. Interpreting the contribution of the higher components (third and fourth) is more difficult as all these components are added. Within the context of computer aided diagnosis of the myocardial contractile function, we proposed to build a model of the normal contraction pattern (NCR model) through the functional analysis of healthy subject data sets. The contraction patterns for a new case can be compared with those of the model. As an illustration of this idea, a global and a local reference models of the normal evolution pattern of the circumferential parameter $E_{cc}$ have been built based upon the analysis of eight normal data sets. The differences of an unknown case with the model are highlighted using specific distance maps which are established at rest and under stress. For the P3 case, the polar maps in Figs. 9(b) and Fig. 10(a) are in agreement with the parameter evolution depicted in Fig. 5(b). This means that the model was able to correctly and automatically estimate the EVs where the parameter evolution diverges from the reference. This is also true for the P1 case. Fig. 10(b) and (c) illustrates the modifications induced under pharmacological stress. In a first step toward a more immediate overview of the main differences, distance maps can be crudely segmented into three regions using simple thresholding: regions close to the NCR model, at medium distance and far from the NCR model. It may happen that pharmacological stress implies a significant increase of the contractile function in some EVs. This may result in great distances if using (4) straightforwardly. Therefore, if the stress value is far from the reference but located in the "normal" (negative) half FPCOM1 plane then it is considered as normal. The thresholded maps are shown on the right part of Fig. 10.

The complementary experiments involving a truncated reference database showed that the results are consistent. In each healthy test case, the distance remains small and similar from case to case (Table II, standard deviation less than 2% on the mean values). With the pathological cases P3 and P4, we found that the results obtained with each test model were very similar and a significant difference in value is obtained as compared with the healthy cases (Table III, standard deviation 0.6% on the mean values for both cases).

According to the physicians, a necrosed region was identified by visual inspection of the PET data in sectors 1, 2, 3, and 12 of the septum for all levels of the P3 case. This is not in total agreement with our findings although we observe that the largest distances are located in a portion of the septum under stress. In the same way, a necrosis has been detected at the apex in the posterior region for the P1 case which corresponds to the highest detected contractile defect under stress [Fig. 10(c)].

The work presented in this paper is a first step toward a better understanding of the complex normal and pathological myocardial motion. Far from drawing definite conclusions about the ability of the proposed approach for automatically determining contraction abnormalities, we have however demonstrate that it provides coherent results and that the functional framework is a reliable candidate for the analysis of the spatio–temporal deformation parameters provided by Tagged MRI. The approach relies on the assumptions that, first, MR tagging provides meaningful comparable strain patterns—this has been previously shown by several studies [7], [19], [20], [11]—and, second, common strain patterns exist for the normal human LV. A recent study has characterized the normal systolic ranges of strain evolution [11] through a database of healthy volunteers. This tends to support the pertinence of a model based approach to the detection of LV dysfunctions. Due to technical constraints, this study focused on the systolic phase of the cardiac cycle. Cascaded acquisition of tagged MR images can be performed in order to reconstruct the LV motion over the whole heart cycle [21]. Also, the CSPAMM technique [22] improves the grid contrast making the motion assessment over the entire cardiac cycle possible. In this case, the same functional approach can be applied to the parameters over the whole cardiac cycle. The extracted functional components of

the NCR model would, therefore, include information about parameter evolution through both systole and diastole. Also, the practical part of this paper has only concerned the circumferential strain $E_{cc}$. In a diagnostic system of the LV function, radial and longitudinal deformations should be included [23]. This can be envisaged for instance by the parallel functional analysis of these three parameters the results of which can be finally fused into a single diagnostic map.

## APPENDIX

### A. Derivation of the Functional PCOMs

All the measurements $x_i(t)$ of $x$ maximize the criteria

$$J_\alpha = \frac{1}{N}\sum_{i=1}^{N} f_{i\alpha}^2$$

where

$$f_{i\alpha} = \langle x_i(t),\, \varepsilon_\alpha(t)\rangle = \int_a^b x_i(t)\varepsilon_\alpha(t)\,dt, \quad i = 1\cdots N,\ \alpha = 1\cdots q. \tag{6}$$

It can be shown that this maximization problem is equivalent to the problem of the eigen analysis of a covariance operator $V$

$$\max_{\varepsilon_\alpha}\langle \varepsilon_\alpha,\, V\varepsilon_\alpha\rangle, \qquad \|\varepsilon_\alpha\| = 1$$

where

$$V\varepsilon_\alpha = \int_a^b v(t,\,s)\varepsilon_\alpha(s)\,ds = \langle v(t,\,.),\,\varepsilon_\alpha\rangle$$

and $v(t,\,s) = (1/N)\sum_{i=1}^{N} x_i(t)x_i(s)$ is the covariance function. This problem turns out to be equivalent to the eigen function problem

$$V\zeta = \lambda\zeta \tag{7}$$

with the normalization constraint $\|\zeta\| = 1$ on each eigen function $\zeta$. The functions $\zeta_\alpha(t)$, $\alpha = 1\cdots q$ are the first $q$ eigen functions (the functional PCOMs) associated with the $q$ eigen values $\lambda_\alpha$, $\alpha = 1\cdots q$.

### B. Computation of the Functional PCOMs

One approach to the computation of the functional PCOMs uses a basis function expansion. Each $x_i(t)$ is defined as a linear combination of the basis functions $\phi_k(t)$, $k = 1\cdots K$ such that

$$x_i(t) = \sum_{k=1}^{K} C_{ik}\phi_k(t)$$

where the $C_{ik}$ are the coefficients. Using a matrix notation

$$X(t) = \begin{bmatrix} x_1(t) \\ | \\ | \\ x_N(t) \end{bmatrix} = C \begin{bmatrix} \phi_1(t) \\ | \\ | \\ \phi_k(t) \end{bmatrix} = C\boldsymbol{\phi}(t).$$

Then, the covariance function becomes: $v(t,\,s) = (1/N)\boldsymbol{\phi}'(t)C'C\boldsymbol{\phi}(s)$ where $C'$ denotes the transpose matrix of $C$. Similarly, the eigen functions $\zeta$ are linear combinations of the $\phi_k$ functions

$$\zeta(t) = \sum_{k=1}^{K} b_k\phi_k(t) = \boldsymbol{\phi}'(t)\boldsymbol{b}$$

with $b_k$, the coefficients. Therefore, (7) becomes

$$\frac{1}{N}C'CW\boldsymbol{b} = \lambda\boldsymbol{b} \tag{8}$$

with

$$W = \int \boldsymbol{\phi}(t)\boldsymbol{\phi}'(t)\,dt.$$

The condition

$$\int \zeta^2(t)\,dt = 1$$

implies $\boldsymbol{b}'W\boldsymbol{b} = 1$. Let us introduce the normalized vector $\boldsymbol{u}$ such that $\boldsymbol{u} = W^{1/2}\boldsymbol{b}$ with $\|\boldsymbol{u}\| = 1$. Consequently, (8) reduces to

$$Q\boldsymbol{u} = \lambda\boldsymbol{u} \tag{9}$$

with

$$Q = N^{-1}W^{1/2}C'CW^{1/2}.$$

If the basis is orthogonal then $W = I$ and $Q = N^{-1}C'C$. Therefore, to derive the first $q$ eigen functions $\zeta_\alpha(t)$, $\alpha = 1\cdots q$, the $q$ eigen vectors $\boldsymbol{u_\alpha}$, $\alpha = 1\cdots q$ of the matrix $Q$ are computed. The coefficients $b_k$ of the eigen functions are then deduced.

## ACKNOWLEDGMENT

The authors are grateful to Dr. J. O. Ramsay and Dr. B. W. Silverman for providing us functional data analysis functions. The authors are grateful to the anonymous reviewers for their pertinent and constructive suggestions on several aspects of the manuscript. This work was performed within the joint incentive action "Beating Heart" of the research groups ISIS, ALP, and MSPC of the French National Center for Scientific Research (CNRS).

## REFERENCES

[1] R. Tennant and C. J. Wiggers, "The effect of coronary occlusion on myocardial contraction," *Amer. J. Physiol.*, vol. 112, pp. 351–361, 1935.
[2] S. Rahimtoola, "Coronary bypass surgery for chronic angina," *Circulation*, vol. 65, pp. 225–241, 1982.
[3] E. Zerhouni, D. Parish, W. Rogers, A. Yang, and E. P. Shapiro, "Human heart: Tagging with MR imaging—A method for noninvasive assessment of myocardial motion," *Radiology*, vol. 169, pp. 59–63, 1988.
[4] M. B. Buchalter, J. L. Weiss, W. L. Rogers, E. A. Zerhouni, M. L. Weisfeldt, R. Beyar, and E. P. Shapiro, "Noninvasive quantification of left ventricular rotational deformation in normal humans using Magnetic Resonance Imaging myocardial tagging," *Circulation*, vol. 81, pp. 1236–1244, 1990.
[5] N. R. Clark, N. Reichek, P. Bergey, E. A. Hoffman, D. Brownson, L. Palmon, and L. Axel, "Circumferential myocardial shortening in the normal human left ventricle. Assessment by Magnetic Resonance Imaging using spatial modulation of magnetization," *Circulation*, vol. 84, pp. 67–74, 1991.

[6] S. E. Maier, S. E. Fisher, G. C. McKinnon, O. M. Hess, H. P. Krayenbuehl, and P. Boesiger, "Evaluation of left ventricular segmental wall motion in hypertrophic cardiomyopathy with myocardial tagging," *Circulation*, vol. 86, pp. 1919–1928, 1992.
[7] J. Marcus, M. Götte, A. Van Rossum, J. Kuijer, R. Heethaar, L. Axel, and C. Visser, "Myocardial function in infarcted and remote regions early after infarction in man: Assessment by magnetic resonance tagging and strain analysis," *Magn. Reson. Med.*, vol. 38, pp. 803–810, 1997.
[8] W. O'Dell, C. Moore, W. Hunter, E. Zerhouni, and E. McVeigh, "Three-dimensional myocardial deformations: Calculation with displacement field fitting to tagged MR images," *Radiology*, vol. 195, no. 3, pp. 829–835, 1995.
[9] A. A. Amini, Y. Chen, R. W. Curwen, V. Mani, and J. Sun, "Coupled B-snake grids and constrained thin-plate splines for analysis of 2-D tissue deformations from tagged MRI," *IEEE Trans. Med. Imag.*, vol. 17, pp. 344–356, June 1998.
[10] P. Clarysse, C. Basset, L. Khouas, P. Croisille, D. Friboulet, C. Odet, and I. E. Magnin, "Two-dimensional spatial and temporal displacement and deformation field fitting from cardiac magnetic resonance tagging," *Med. Image Anal.*, vol. 4, no. 3, pp. 253–268, 2000.
[11] C. C. Moore, C. H. Lugo-Olivieri, E. R. McVeigh, and E. A. Zerhouni, "Three-dimensional systolic strain patterns in the normal human left ventricle: Characterization with tagged MR imaging," *Radiology*, vol. 214, no. 2, pp. 453–466, 2000.
[12] J. Ramsay and B. Silverman, *Functional Data Analysis*. New York: Springer, 1997, Statistics.
[13] T. J. Mosher and M. Smith, "A DANTE tagging sequence for the evaluation of translational sample motion," *Magn. Reson. Med.*, vol. 15, pp. 334–339, 1990.
[14] M. A. Guttman, J. L. Prince, and E. R. McVeigh, "Tag and contour detection in tagged MR images of the left ventricle," *IEEE Trans. Med. Imag.*, vol. 13, no. 1, pp. 74–88, 1994.
[15] M. A. Guttman, E. A. Zerhouni, and E. R. McVeigh, "Analysis of cardiac function from MR images," *IEEE Comput. Graph. Applicat. Mag.*, vol. 17, no. 1, pp. 30–38, 1997.
[16] T. Denney and E. McVeigh, "Model-free reconstruction of three-dimensional myocardial strain from planar tagged MR images," *J. Magn. Reson. Imag.*, vol. 7, no. 5, pp. 799–810, 1997.
[17] J. Park, D. Metaxas, and L. Axel, "Analysis of left ventricule wall motion based on volumetric deformable models and MRI-SPAMM," *Med. Image Anal.*, vol. 1, no. 1, pp. 53–71, 1996.
[18] J. Declerk, N. Ayache, and E. McVeigh, "Use of a 4D planispheric transformation for the tracking and the analysis of LV motion with tagged MR images,", Tech. Rep. RR-3535, INRIA, Oct. 1998.
[19] G. Geskin, C. Kramer, W. J. Rogers, T. M. Theobald, D. Pakstis, Y. L. Hu, and N. Reichek, "Quantitative assessment of myocardial viability after infarction by dobutamine magnetic resonance tagging," *Circulation*, vol. 98, no. 3, pp. 217–223, 1998.
[20] P. Croisille, C. Moore, and R. Judd, "Differentiation of viable and nonviable myocardium by the use of three-dimensional tagged MRI in 2-day-old reperfused canine infarcts," *Circulation*, vol. 99, pp. 284–291, 1999.
[21] J. Park, D. N. Metaxas, L. Axel, Q. Yuan, and A. S. Blom, "Cascaded MRI-SPAMM for LV motion analysis during a whole cardiac cycle," *Int. J. Med. Inform.*, vol. 55, no. 2, pp. 117–126, 1999.
[22] S. Fischer, G. McKinnon, S. E. Maier, and P. Boesiger, "Improved myocardial tagging contrast," *Magn. Reson. Med.*, vol. 30, no. 2, pp. 191–200, 1993.
[23] M. Han, P. Clarysse, P. Croisille, I. E. Magnin, and D. Revel, "Computer aided diagnosis of the myocardial ischemia based on a spatio–temporal deformation features analysis," in *Proc. IEEE Computers In Cardiology '98*, Cleveland, OH, 1998, pp. 749–752.
[24] H. Azhari, S. Oliker, W. J. Rogers, J. L. Weiss, and E. P. Shapiro, "Three-dimensional mapping of acute ischemic regions using artificial neural networks and tagged MRI," *IEEE Trans. Biomed. Eng.*, vol. 43, pp. 619–626, June 1996.

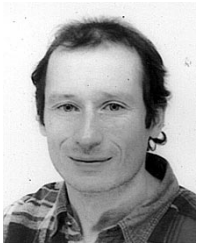

**Patrick Clarysse** received the Ph.D. degree in automatics from the University of Lille, Lille, France, in 1991.

Since 1992, he is with the French National Center for Scientific Research (CNRS) at CREATIS, UMR CNRS #5515, Lyon, France. His primary research interests are in the bioengineering and computer vision fields, and include boundary extraction, motion estimation and analysis, and deformable models with an application to the analysis of the heart function.

**Meimei Han** received the M.S. degree from the University of Tianjin, Tianjin, China, in 1988 and the Ph.D. degree from the National Institute of Applied Sciences (INSA), Lyon, France, in 1999. Her Ph.D. work concerned the analysis of the cardiac contractile function using MR tagging.

She is an engineer at Bombardier Transport, Montreal, QC, Canada.

**Pierre Croisille** received the M.D. and Ph.D. degrees from the University Claude Bernard Lyon 1, Lyon, France.

He is an Associate Professor in cardiovascular radiology in Lyon, France. After a research fellowship in radiology at the Johns Hopkins Hospital, Baltimore, MD, he has been working since 1996 at the Hospital Cardiologique L. Pradel, Lyon. His research work (CREATIS, Lyon, France) is focused on the use of cardiac MRI (functional imaging and wall motion estimation) as well as multimodal approaches (PET/MRI) to characterize ischemic myocardium.

**Isabelle E. Magnin** (M'85) received the engineering degree in 1977 and the "Doctorat d'état és Sciences" from INSA-Lyon Scientific and Technical University, France, in 1987.

She is a Researcher with the French National Institute for Health and Medical Research (INSERM). She is the Director of CREATIS, Lyon, France. Her main interest concerns modeling, medical image processing, dynamic imaging, and inverse problems. She is involved in more than 100 publications.

ELSEVIER

Medical Image Analysis 4 (2000) 253–268

MEDICAL IMAGE ANALYSIS

www.elsevier.com/locate/media

# Two-dimensional spatial and temporal displacement and deformation field fitting from cardiac magnetic resonance tagging☆

P. Clarysse*, C. Basset, L. Khouas, P. Croisille, D. Friboulet, C. Odet, I.E. Magnin

*CREATIS, UMR CNRS 5515, INSA Bâtiment 502, 69621 Villeurbanne Cedex, France*

Received 17 December 1998; received in revised form 29 June 1999; accepted 10 January 2000

**Abstract**

Tagged magnetic resonance imaging is a specially developed technique to noninvasively assess contractile function of the heart. Several methods have been developed to estimate myocardial deformation from tagged image data. Most of these methods do not explicitly impose a continuity constraint through time although myocardial motion is a continuous physical phenomenon. In this paper, we propose to model the spatio-temporal myocardial displacement field by a cosine series model fitted to the entire tagged dataset. The method has been implemented in two dimensions (2D)+time. Its accuracy was successively evaluated on actual tagged data and on a simulated two-dimensional (2D) moving heart model. The simulations show that an overall theoretical mean accuracy of 0.1 mm can be attained with adequate model orders. The influence of the tagging pattern was evaluated and computing time is provided as a function of the model complexity and data size. This method provides an analytical and hierarchical model of the 2D+time deformation inside the myocardium. It was applied to actual tagged data from a healthy subject and from a patient with ischemia. The results demonstrate the adequacy of the proposed model for this evaluation. 

*Keywords:* Two-dimensional spatial and temporal displacement; Displacement and deformation field fitting; Cardiac magnetic resonance tagging

## 1. Introduction

Myocardial ischemia is a frequently encountered pathological entity, which is caused by locally reduced blood flow due to the obstruction of arteries. The elastic mechanical properties of ischemic myocardium are altered and, thus, the injured territory is less contractile. Therefore, noninvasive estimation of myocardial contractility is of interest in order to detect regions with abnormal contraction and suspected failing arteries. The degree of abnormality is also of importance to determine the ability of the injured region to recover satisfactory contractile function after reperfusion.

In current clinical practice, physicians can obtain a crude estimate of the contractile function from cine magnetic resonance imaging (MRI), echographic ultrasound or SPECT images. In MRI, the contour of the endocardium and epicardium of the left ventricle (LV) are manually traced on the images and the wall thickness change between end-diastole and end-systole in the cardiac cycle can be estimated over the LV on a slice by slice basis. More advanced approaches to the determination of contractile function are based on specific MR imaging techniques. Phase contrast MRI (Pelc et al., 1991; Wedeen, 1992, Meyer et al., 1996; Zhu et al., 1997) exploits the phase shift of moving spins to compute the velocity at a specific point in three-dimensional (3D) space. This technique is theoretically able to provide a dense velocity field. However, measured velocity fields are often very noisy and need to be regularized. Also, in the existing methods, usually only 2D velocity fields are considered. Magnetic resonance (MR) tagging (Zerhouni et al., 1988; Axel and Dougherty, 1989) consists of positioning a regular saturation pattern onto the myocardial tissue by selective alteration of the tissue magnetic characteristics. This pattern is

☆Electronic Annexes available. See www.elsevier.com/locate/media.

*Corresponding author. Tel.: +33-4-7243-8148; fax: +33-4-7243-8526.

*E-mail address:* patrick.clarysse@creatis.insa-lyon.fr (P. Clarysse).

1361-8415/00/$ – see front matter 
PII: S1361-8415(00)00018-9

generated at the very beginning of an ECG-gated imaging sequence (Fig. 1(a)). Changes in shape of the saturated stripes in the image sequence reflect changes in shape of the underlying myocardial tissue (Fig. 1(b–f)). In order to image 3D motion, stripes are imposed in three orthogonal directions in space. With this imaging method, the accuracy of the estimated motion depends on the spatial resolution of the tagging pattern. The signal-to-noise ratio

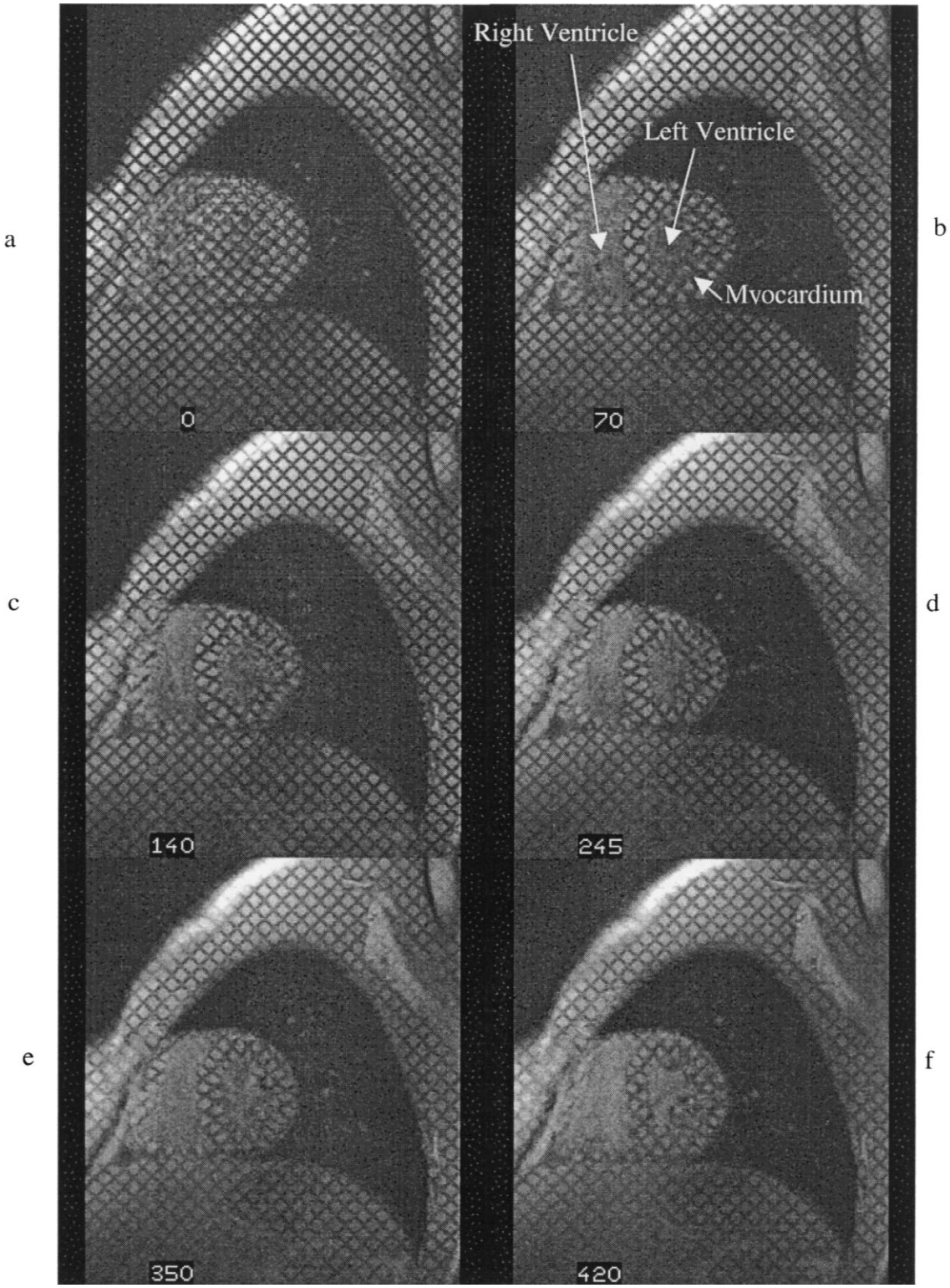


Fig. 1. MRI SPAMM sequence of the heart (short axis views) from end-diastole (a) to end-systole (f). The initial tagging pattern (a) deforms to conform the myocardial motion. The tagging pattern is extracted and processed to compute the displacement field inside the myocardium.

(SNR) limits the contrast of the tag lines. Atalar and McVeigh (1994) derived optimal values for the tag width and spacing. Due to T1 relaxation time, only a part of the cardiac cycle can be imaged.

Several methods have been proposed to estimate the motion of the myocardium from tagged MR images (see Section 2). Most of them compute the motion field (or displacement field) between one specific timepoint in the cardiac cycle and the initial timepoint for which the tag pattern is undeformed. It is necessary to repeat this task for each image of the sequence to track the motion over time. Other methods provide a discrete estimate of the displacement field between two timepoints. To compute deformation parameters such as strains, the derivatives of the displacement are, in such a case, numerically approximated.

Myocardial contraction can be considered a continuous process through time and space. It is essential to integrate a spatio-temporal continuity assumption into the motion reconstruction algorithm. A continuous model can, moreover, provide easy access to various kinematic parameters such as velocity and acceleration among others. In this paper, we propose a new model-based approach for the spatio-temporal displacement field fitting from cardiac MR tagged sequences. The model provides a hierarchical description of the motion and the accuracy of the reconstructed motion increases with the model order. The forward motion of the LV myocardium is modeled using a cosine series. From this model, it is possible to compute myocardial point trajectories and several parameters of interest, such as the Lagrangian deformation tensors, velocities, and accelerations. Section 2 presents a short review of the topic. The proposed method is detailed in Section 3. The ability of the 2D+time implementation of the method to accurately predict myocardial motion is evaluated both on actual cardiac data at the tag points and on a computer-generated model (Section 4). We deduce optimal time and space model orders as a function of tag spacing. The approach is applied to the MR tagged data of a healthy subject and of one patient with severe ischemia. Section 5 discusses the results and the properties of the method.

## 2. Related works based on MR tagging

The noninvasive estimation of heart motion using standard imaging techniques is a difficult problem due to the lack of point correspondence between image in a sequence and to the complex through-plane motion. The idea of MR tagging, originally introduced by Zerhouni et al. (1988) was to provide explicit point correspondences through the tags. A modification of the technique of the tag pattern generation was then proposed by Axel and Dougherty (1989) known as spatial modulation of the magnetization (SPAMM). Since then, MR tagging has been used to estimate the torsion and the circumferential-longitudinal shear (Buchalter et al., 1990), circumferential shortening (Clark et al., 1991), and radial displacements (Maier et al., 1992). However, these indices are generally computed in the slice plane and do not take into account the through-plane motion. In addition, only the deformation of the myocardium between end-diastole and end-systole is considered. Later studies have tried to estimate deformation in 3D and compute more reliable deformation descriptors. Moore et al. (1992) applied one set of radial tag planes parallel to the LV long axis, while five short axis image planes, orthogonal to the tag plane, are acquired. A second set of long axis image planes is acquired radially in accord with the previous tag planes and with tags parallel to the short axis image planes. Tag points are defined as the intersections of tags in the image and the epicardial/endocardial contours. The set of tag points defines a decomposition of the LV myocardium into volume elements. Mechanical strains are computed at the node of each volume element. However, this approach is unable to highlight transmural changes of the deformation. Young and co-workers (Young and Axel, 1992; Young et al., 1995) have developed a finite element model for the 3D reconstruction of the heart wall motion. Their method includes a geometric fit of the inner and outer surfaces to the endocardial contours within a prolate spheroidal coordinate system. This allows registration of one heart to another. Then, tag grid intersections (SPAMM) are used to reconstruct the displacements of the nodes (typically 16) of a 3D geometric model from the deformed state to the initial undeformed state. Each coordinate of the displacement is fitted using the adequate tag point set. In the last step, deformation of the model from the initial configuration at time $t$ is estimated in order to reconstruct the deformation from end-diastole to end-systole. Deformation inside the heart wall is linearly related to the one estimated at the nodes of the model. The method proposed by O'Dell and co-workers (O'Dell, 1995; O'Dell et al., 1995) follows a similar idea to fit a 3D displacement field. This fit is performed independently for the three coordinates of the displacement backward in time and once for each time frame. Three-dimensional displacements and deformations are estimated at a set of material points (LV mesh) defined within the heart wall in the first time frame. The method proposed by Park et al. (1996) is based on a deformable model in which parameters are piece-wise linear functions. These parameter functions have an intuitive meaning, such as radial contraction or twisting about the long axis. The forces needed for the dynamics of the deformable model are computed from both LV boundary points (which are not always reliable) and 2D intersections of tag lines. They are computed on the vertices of prismatic volume elements located on the inner and outer LV walls. The model parameters inside the LV wall are thus linear approximations of the ones on the LV boundaries. The deformation of the model is repeated once for each cardiac instant.

Denney and Prince's (1995) approach is based on a multidimensional stochastic model for the estimation of a dense displacement field. The displacement field is estimated at points of a 3D grid enclosing the LV. The discrete displacement field is estimated within the Fisher estimation framework under smoothness and incompressibility assumptions. The variance of the various stochastic processes is chosen empirically. There is no underlying parametric model of the obtained displacement field. Thus, the computation of strains involves discrete numerical differentiation (Denney and McVeigh, 1997).

Declerck et al. (1998a,b) modeled the motion of the LV using continuous spatio-temporal mapping. First, the LV myocardium is represented using a specially designed planispheric coordinate system. Within this coordinate system, the motion is modeled by affine functions whose parameter functions (dependent on space and time) are determined using a least mean square criterion and smoothing splines. The affine motion model is expected to capture locally the main components of the heart motion. This results in three intuitive parameters, the radial contraction, the rotation about the long axis, and the longitudinal contraction.

Radeva et al. (1997) proposed a 3D approach for the localization and tracking of SPAMM data. It is based on a deformable B-solid whose isoparametric curves are implicit snakes tracking the tag lines in the images. Amini et al. (1998) represent and track the tag pattern by coupled B-snake grids. Spline warps interpolate a dense vector field using displacement information at the intersections. Young (1998) also proposes a solution for the reconstruction of the 3D heart wall motion directly from tagged MR images.

## 3. Materials and method

Our approach was to reconstruct the spatio-temporal displacement field as a vector function of the spatial and temporal coordinates. Each tag set is able to assess the motion along a direction perpendicular to the tag lines. Therefore, we chose to reconstruct an accurate displacement field within a coordinate system relative to the tag orientation. Note that it is always possible to adapt this to a more specific anatomical system if needed. The mathematical expression of the reconstructed displacement field allows for the direct analytical derivation and leads to the computation of the spatio-temporal deformation tensors and other kinematic parameters such as velocities and accelerations. The displacement field can theoretically be reconstructed with increasing accuracy since the model is based on cosine series.

In this paper, we have considered the displacement field fitting problem in two space dimensions and in time.

### 3.1. Imaging protocol

Images were acquired on a 1.5T MR scanner (Siemens, Erlangen, Germany) using a fast ECG-gated segmented gradient echo sequence (TR=70 ms with echo sharing, TE=4 ms, Flip angle=15°, matrix=256×154, slice thickness=8 mm, FOV=280 mm, Acq=1, oversampling=27%). The tagging pattern is generated by a Dante pulse sequence (Mosher and Smith, 1994) with two series of tags oriented at ±45° and a tag spacing fixed to 8 mm (Fig. 1). The images were then processed using FindTags software (Guttman et al., 1994, 1997) to semi-automatically extract the tag lines in both orientations within the myocardium. The points of the tag lines are the input data of the algorithm described hereafter. Endocardial and epicardial contours were also extracted to circumscribe the myocardium for the computation of the displacement and for display purposes. Note that due to T1 relaxation and the technical limitations of the MR scanner, only a portion of the cardiac cycle (systole, ~400 ms) can be acquired since the tagging tends to disappear. Two examinations have been considered in this study: one healthy case (9 cardiac phases in a breath-hold) and one pathological case with a severe postero-lateral ischemia (EF=45%) at rest (9 cardiac phases in a breath-hold) and under pharmacological stress (using dobutamine, 6 cardiac phases in a breath-hold).

### 3.2. Mathematical formulation and notations

Let us consider the 2D spatial and temporal displacement field, $D$, formally defined by

$$\begin{aligned} D\colon \Omega \times R,\ \Omega \subset R^2 &\rightarrow \Omega' \subset R^2 \\ (P,t) &\mapsto \vec{D}(x,y,t) = (D_x(x,y,t), D_y(x,y,t)) \end{aligned}$$

As already pointed out, the problem of the estimation of the tag point $P'$ at time $t$, corresponding to the tag point, $P$, in the initial undeformed state at time $t_0$ (referred hereafter as the forward displacement field fitting) is ill-posed and can be related to the well-known aperture problem for optical flow estimation in computer vision (Fig. 2(a)). To alleviate this problem, one can consider only tag intersections. Displacement estimation using such a sparse information is less accurate and, moreover, this approach is not valid in 3D since intersections are out of the image plane during motion. Therefore, an inverse approach is used as in (Young and Axel, 1992; O'Dell, 1995; Declerck et al., 1998a,b), where an inverse displacement field is estimated. Considering a tag from a deformed state at time $t$ back to the initial undeformed tag at time $t_o$, it is possible to exactly determine the displacement component orthogonal to the axis of the initial tag (Fig. 2(b)). Thus, each tag set is used to estimate one component of the motion. Our approach consists of estimating the inverse displacement field $D' = (D'_x(x,y,t), D'_y(x,y,t))$ and using the so-obtained point correspondences to compute the direct displacement field, $D$. In the sequel, all '' notations will refer to variables relative to the so-called backward displacement field fit.

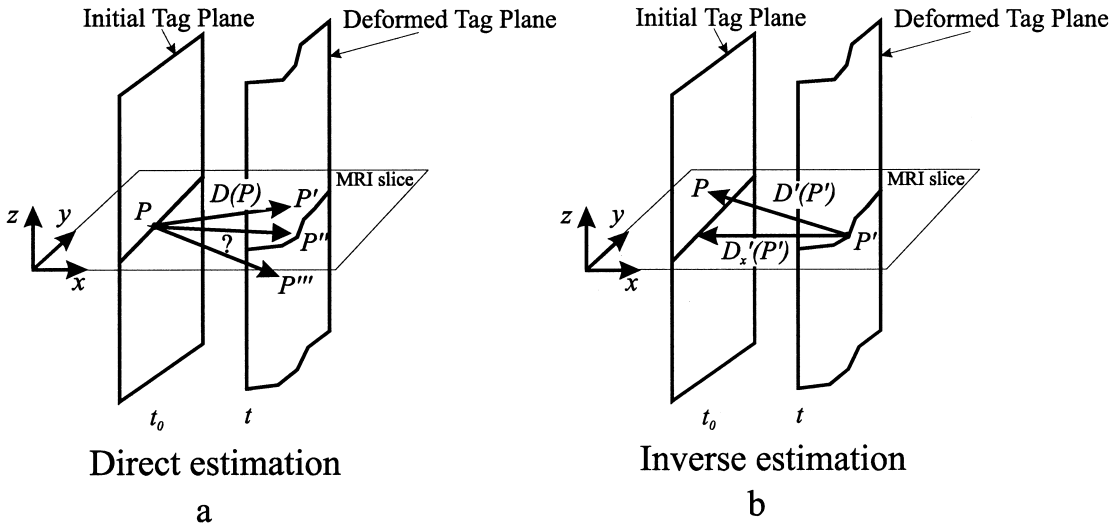


Fig. 2. Principle of the direct and inverse displacement estimations using MR tagging. (a) The forward approach consists in looking for the corresponding point $P'$ at time $t$ of each tag point $P$ of the initial frame at time $t_0$. (b) The backward approach estimates the projection of the displacement in the direction orthogonal to the tags from time $t$ to $t_0$.

### 3.3. Description of the model

#### 3.3.1. Reference coordinate system

Most of the approaches mentioned in Section 2, except the ones in (Denney and McVeigh, 1997) and (Radeva et al., 1997), use a reference coordinate system more or less adapted to the LV anatomy, such as the prolate-spheroidal or the planispheric coordinate system. The use of such a reference system allows the acquisition of motion parameters related to the anatomy of the LV at classical circumferential, radial and longitudinal coordinates. This generally requires the definition of anatomical landmarks such as the LV long axis, the LV cavity center, and other specific reference points. This is not an easy or error-free task. One advantage to use a coordinate system relative to the tag pattern is to uncouple the estimation of the three components of the motion. In this way, the accuracy is not dependent upon a specific anatomical system (see also the Discussion section in (Denney and Prince, 1995)). It can be used to estimate motion over the entire region of interest in the LV and also in the RV myocardium (Fayad et al., 1998). It is, however, possible to change the coordinate system afterward.

#### 3.3.2. Spatio-temporal displacement field modeling

The inverse spatio-temporal displacement field, $D'$, is modeled using cosine series. The component $D'_x$ of $D'$ has the following mathematical expression:

$$D'_x(x,y,t) = \sum_{k=0}^{K-1}\sum_{l=0}^{L-1}\sum_{m=0}^{M-1} A'_{x,k,l,m} \cos\left(\frac{\pi kx}{X}\right) \times \cos\left(\frac{\pi ly}{Y}\right)\cos\left(\frac{\pi mt}{T}\right). \quad (1)$$

The expression is similar for $D'_y$ with parameters $A'_{y,k,l,m}$:

$$D'_y(x,y,t) = \sum_{k=0}^{K-1}\sum_{l=0}^{L-1}\sum_{m=0}^{M-1} A'_{y,k,l,m} \cos\left(\frac{\pi kx}{X}\right) \times \cos\left(\frac{\pi ly}{Y}\right)\cos\left(\frac{\pi mt}{T}\right). \quad (2)$$

The coefficients $K$ and $L$ are, respectively, the $x$ and $y$ spatial orders, and $M$ is the temporal order. The $X$ and $Y$ parameters are the maximum sizes of the LV in the $x$ and $y$ directions, and $T$ is the amount of time between $t_0$, the creation time of the tagging pattern, and the acquisition time of the last image frame of the sequence. The coefficients $A'_{x,k,l,m}$ and $A'_{y,k,l,m}$ are the model's parameters to be estimated. Such a model is convenient for even functions and requires that the system origin be outside the myocardium region. In our case, this origin is located at one corner of the bounding box including the myocardium.

The direct spatio-temporal displacement field, $D$, is modeled using exactly the same mathematical expressions. It is characterized by the parameters $A_{x,k,l,m}$ and $A_{y,k,l,m}$, to be determined.

Theoretically, the accuracy of the reconstructed displacement field depends on the spatial and temporal orders of the model. This allows control of the accuracy of the reconstruction as well as further analysis of the distribution of the parameters for different cases.

#### 3.3.3. Estimation of the model's parameters

In an $(O,x,y)$ reference system, such that tag lines are either parallel or orthogonal to the system axes, the parameters of the inverse transform, $D'(P')$, with $P'$ belonging to the deformed (time $t$) tag lines, are estimated through the minimization of the Euclidean distance between the projection onto the coordinate axes of $D'(P')$ and the abscissa of the undeformed initial tag lines (Fig. 2(b)). The minimization of the two following error terms

leads to the separate computation of the estimated components, $\hat{D}'_x$ and $\hat{D}'_y$, of the inverse displacement field:

$$E_x^2 = \frac{1}{N_X}\sum_{t=t_o}^{t_f}\sum_{\mathrm{XTags}}\sum_{P'\in\mathrm{XTags}}\|x(P,t_0) - (x(P') + \hat{D}'_x(P'))\|^2, \tag{3}$$

$$E_y^2 = \frac{1}{N_Y}\sum_{t=t_o}^{t_f}\sum_{\mathrm{YTags}}\sum_{P'\in\mathrm{YTags}}\|y(P,t_0) - (y(P') + \hat{D}'_y(P'))\|^2, \tag{4}$$

where $N_X$ (respectively $N_Y$) is the total number of points for the set of tags orthogonal to the $x$ (respectively $y$) direction, and $t_f$ is the timepoint of the last image acquisition. Index XTags (respectively YTags) represents the set of the tags orthogonal to the $x$ (respectively $y$) direction. Replacing $\hat{D}'_x$ and $\hat{D}'_y$ by their expressions (1) and (2) in (3) and (4), we obtain the following system of two equations:

$$C_x = \sum_{t=t_o}^{t_f}\sum_{n=\min_x(t)}^{\max_x(t)}\sum_{o=1}^{O(n)}\Bigg[\sum_{k=0}^{K-1}\sum_{l=0}^{L-1}\sum_{m=0}^{M-1} - A'_{x,k,l,m}\cos\left(\frac{\pi k x'(\cdot)}{X}\right)\cdot\cos\left(\frac{\pi l y'(\cdot)}{Y}\right)\cdot\cos\left(\frac{\pi m t}{T}\right) - x'(\cdot) + x(n,t_0)\Bigg]^2, \tag{5}$$

$$C_y = \sum_{t=t_o}^{t_f}\sum_{n=\min_y(t)}^{\max_y(t)}\sum_{o=1}^{O(n)}\Bigg[\sum_{k=0}^{K-1}\sum_{l=0}^{L-1}\sum_{m=0}^{M-1} - A'_{y,k,l,m}\cos\left(\frac{\pi k x'(\cdot)}{X}\right)\cdot\cos\left(\frac{\pi l y'(\cdot)}{Y}\right)\cdot\cos\left(\frac{\pi m t}{T}\right) - y'(\cdot) + y(n,t_0)\Bigg]^2, \tag{6}$$

where $P'$ has $(x',y')$ coordinates and $(\cdot)$ stands for $(o,n,t)$. The indices $\min(t)$ and $\max(t)$ are, respectively, the minimum and the maximum indices of the tags at timepoint $t$. $O(n)$ defines the number of points for tags with the index, $n$.

To obtain the coefficients $A'$ of the model, we solve $\partial C_x/\partial A'_{x,i} = 0$ and $\partial C_y/\partial A'_{y,i} = 0$, $\forall i$. The details of the computations are given in Appendix A. Finally, the result is a system of $I$ linear equations for each component, $x$ and $y$, of the form (see Appendix A)

$$\sum_{j=0}^{I} A'_j B_{i,j} - C_i = 0, \quad i = 1,\ldots,I, \tag{7}$$

with $I = KLM$. The solution of (7) is obtained using the singular value decomposition (Press et al., 1988), which is a robust method for the estimation of least mean square problems with potentially singular matrices. The coefficients $A'_{x,k,l,m}$ and $A'_{y,k,l,m}$ of the backward model are now available.

The parameters of the direct displacement field $D(P)$ are computed according to the same scheme using the point correspondences given by $D'(P')$.

### 3.4. Estimation of the initial location of the tagging pattern

Usually, the first image of the temporal sequence is acquired at $t_1$, a short time period after the creation of the tagging pattern ($t_1 \sim 10$ ms). Therefore, the tags have already moved. The distance terms in the minimization of (3) and (4) require the initial tag abscissas at $t_0$ which are not known a priori. The user could be asked for the tag spacing and initial abscissas but this is not very accurate. We computed the optimal estimates of these parameters through the minimization of the following quadratic term (given for tags orthogonal to the $x$ direction) which is the sum of the differences between the estimated coordinates of the tag points and the actual ones in the first frame at $t_1$:

$$E_{ox} = \sum_{\mathrm{XTags}}\sum_{P}\left[\hat{X}_0 + (i_{\mathrm{XTags}} \times \hat{s}_{x_0}) - x(P,t_1)\right]^2 \tag{8}$$

where $\hat{X}_0$ is the estimated abscissa of the first left tag (index 0) at $t_0$, $i_{\mathrm{XTags}}$ is the index of the current tag and $\hat{s}_{x_0}$ is the estimated tag spacing along $x$. This leads to a linear system solved for $\hat{X}_0$ and $\hat{s}_{x_0}$. A similar approach is used to estimate $\hat{Y}_0$ and $\hat{s}_{y_0}$ for tags orthogonal to the $y$ direction.

### 3.5. Deformation parameters

The mathematical expression of the direct displacement field allows the computation of spatio-temporal parameters that characterize the motion and deformation of the LV myocardium. One can easily derive the velocity field given by

$$V_x(x,y,t) = \frac{\partial D_x}{\partial t}, \quad V_y(x,y,t) = \frac{\partial D_y}{\partial t}, \tag{9}$$

and the acceleration field

$$\gamma_x(x,y,t) = \frac{\partial V_x}{\partial t} = \frac{\partial^2 D_x}{\partial t^2}, \quad \gamma_y(x,y,t) = \frac{\partial V_y}{\partial t}. \tag{10}$$

The deformation field requires the computation of the deformation tensor, $\varepsilon$, which is given by

$$\varepsilon(x,y,t) = \frac{1}{2}(\nabla D^{\mathrm{T}} + \nabla D + \nabla D^{\mathrm{T}}\nabla D), \tag{11}$$

where

$$\nabla D = \begin{pmatrix} \frac{\partial D_x}{\partial x} & \frac{\partial D_x}{\partial y} \\ \frac{\partial D_y}{\partial x} & \frac{\partial D_y}{\partial y} \end{pmatrix}$$

is the gradient of the displacement.

The principal deformations are obtained by the

diagonalization of the $\varepsilon$ tensor. All these parameters are very useful for analyzing the contractile function of the myocardium.

## 4. Simulation experiments

The performance of the method were evaluated both on the tag points extracted from clinical data and on a computer-generated model of the moving LV myocardium.

### 4.1. Error of fit on tag points

We quantitatively evaluated the ability of the model to fit the tag points extracted from one clinical data set. For the inverse displacement field, $D'$, and for each point, $P'$, belonging to tags in the successive frames, the Euclidean distance between the actual corresponding point $P$ of $P'$ and the predicted corresponding point obtained by $P' + D'(P')$ was computed. The mean magnitude, the maximum, and the standard deviation of the error were estimated for the healthy case. Fig. 3 pictures the mean error magnitude as a decreasing function of the spatial and temporal orders. The other statistical parameters varied in a similar fashion. The same computations were performed for the direct displacement field, $D$. Then, the mean magnitude error was generally less than 0.2 mm. With a spatial order equal to 5 and a temporal order greater than 5, the error of fit is about 0.1 mm. This is comparable to errors reported in previous studies (Denney and Prince, 1995; O'Dell, 1995). The statistics of this error term are systematically computed to give an indication of the quality of the fit.

### 4.2. Model of the moving LV

Young and Axel (1992) and O'Dell et al. (1995) have designed a 3D computer-generated model to check the accuracy of their method. We restricted this model to 2D but add a temporal variation of the model coefficients. The initial geometric model is a ring with two series of orthogonal tags described within a polar coordinate system. Let $(R, \theta)$ be the coordinates of points before motion and $(R', \theta')$, $(x', y')$ be the polar and Cartesian coordinates, respectively, during motion. The motion model is defined by the following equations:

$$\begin{cases} R' = \sqrt{\dfrac{R^2 - R_{\text{int}}^2}{\lambda(t)} g(\theta) + R'_{\text{int}}(\theta,t)^2}, \\ \theta' = \theta + \varphi(t) \cdot R + c(t), \end{cases} \tag{12}$$

$$\begin{pmatrix} x' \\ y' \end{pmatrix} = \begin{pmatrix} Tr_x(t) \\ Tr_y(t) \end{pmatrix} + \begin{pmatrix} e^{k_{\text{ell}}(t)} & 0 \\ 0 & e^{-k_{\text{ell}}(t)} \end{pmatrix} \begin{pmatrix} R' \cos\theta' \\ R' \sin\theta' \end{pmatrix}, \tag{13}$$

with

$$f(t) = \frac{1}{2}\left(1 - \cos\left(\frac{\pi t}{t_1 + N_{im}\,\Delta t}\right)\right)$$

and

$$\varphi(t) = -0.278 \times \frac{2\pi}{360} \times f(t). \tag{14}$$

The coefficients $N_{im}$ and $\Delta t$ are the number of frames in

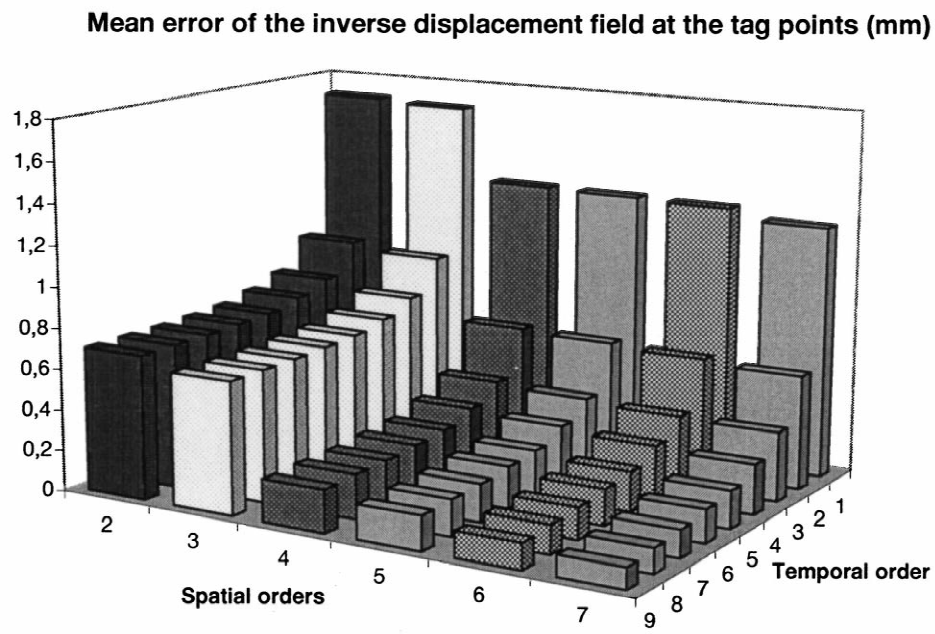


Fig. 3. Mean error (in millimeters) of the estimated inverse displacement field fitting, measured at the tag points. The spatial orders for the $x$ and $y$ directions are equal and range from 2 to 7. The temporal order varies from 1 to 7.

the temporal sequence and the time between two frames, respectively. The term $\varphi(t)\cdot R$ represents a time varying rotation which is also a function of radius, $R$. The rigid rotation is set by the time varying function $c(t) = 7.167 \times (2\pi/360) \times f(t)$. The shortening of the interior contour is described by the bivariate function

$$R'_{\text{int}}(\theta,t) = R_{\text{int}} - (R_{\text{int}} - 15)g(\theta)f(t),$$

$$\text{with } g(\theta) = 1 - 0.15\left(\cos\left(\theta + \frac{3\pi}{4}\right) + 1\right). \quad (15)$$

The wall thickening variation is defined by $\lambda(t) = 1 - 0.2f(t)$. The new Cartesian coordinates take into account the rigid translation through the time varying functions $Tr_x(t) = 0.5f(t)$ and $Tr_y(t) = f(t)$. An elliptization term is also added through the $k_{\text{ell}}$ term ($k_{\text{ell}}(t) = 0.03f(t)$). The constants of the model are defined as follows:

- the interior initial contour (endocardium), $R_{\text{int}} = 20$ mm;
- the exterior initial contour (epicardium), $R_{\text{ext}} = 30$ mm;
- the acquisition time of the first frame, $t_1 = 10$ ms;
- the frame time spacing, $\Delta t = 35$ ms.

To be close to the current acquisition conditions, we fixed the number of frames in the sequence to 7, the tag spacing to 8 mm and the tag points spacing to 2 mm. This model is able to simulate the major known components of normal LV myocardial motion.

### 4.3. Accuracy estimation based on the moving LV

A test set of 1000 material points distributed over the simulated LV myocardium, not only located on tags, was selected to evaluate the performance of the method.

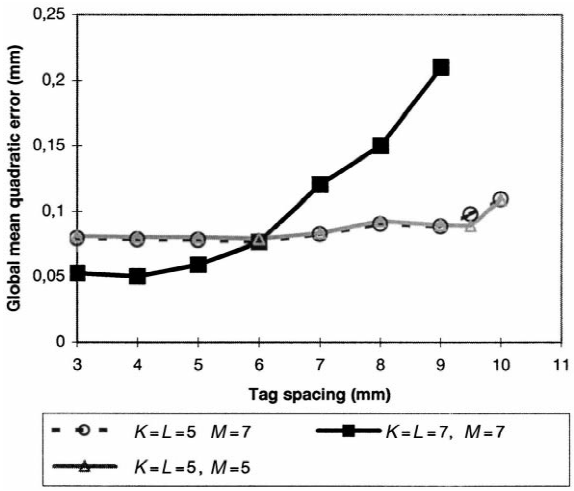


Fig. 5. Global mean quadratic error of fit as a function of the tag spacing (3–10 mm) for three combinations of spatial ($K$,$L$) and temporal ($M$) orders.

#### 4.3.1. Accuracy

The same experiment as the one conducted on tag points (see Section 4.1) was performed on the test set. Fig. 4 depicts the mean error as a function of the spatial and temporal orders of the model. The maximum error exhibits the same variations.

#### 4.3.2. Sensitivity to the tag spacing

The mean quadratic error as a function of the tag spacing (limited to 10 mm) is shown in Fig. 5 for three combinations of spatial and temporal orders.

First, it is of no use to indiscriminately increase the order of the model. Indeed, there is a relationship between

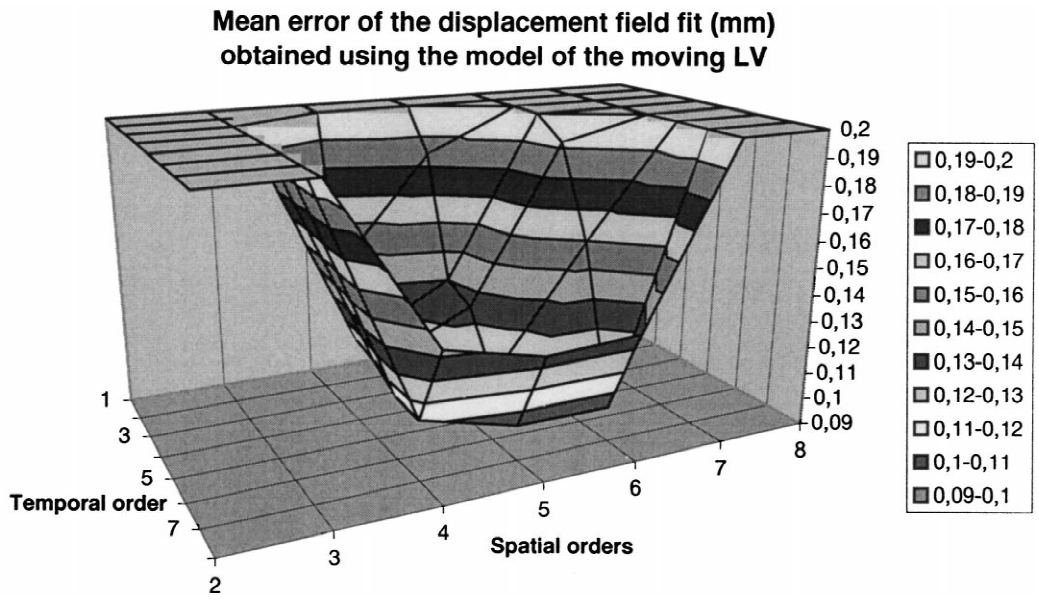


Fig. 4. Mean error of the estimated displacement field fitting measured at the test points using the LV moving model. The spatial orders are equal and range from 2 to 7. For better visualization, errors above 0.2 mm are set to this value.

the model order and both the tag spacing and the temporal resolution. For a conventional tag spacing value (8 mm), one can deduce the optimal spatial (5) and temporal (7) orders (Fig. 4). The latter is directly related to the number of image frames in the sequence (7 frames). The spatial orders are related to the tag spacing. Increasing the spatial order may affect the accuracy of the estimation by introducing spurious high order terms. An optimal coupling between tag spacing and spatial orders provides good accuracy within a reasonable computing time. Fig. 5 shows only little improvement between spatial orders 5 and 7 for a tag spacing within 3 and 6 mm, but a spatial order 5 model is faster to compute (see Section 4.4). The effect of the tag points spacing within a tag line has also been investigated. This spacing is usually 1 mm; however, our analysis using the moving heart model shows that between 1 and 3 mm the accuracy of the reconstructed field is nearly constant for a tag spacing of 8 mm when the optimal spatial and temporal orders are used.

#### *4.3.3. Sensitivity to the accuracy of the tag location*

The tags were extracted from the images by a previous semi-automatic segmentation process. We observed the dependency of the displacement estimation upon the accuracy of the tag location. A small perturbation was applied to each tag point location generated by the model. The magnitudes of the perturbations follow a Gaussian law (zero mean with a varying standard deviation) while the direction is randomly set. Fig. 6 shows the evolution of the mean quadratic error measured on four test point sets as a function of the standard deviation of the perturbation. This is computed with spatial orders set to 5 and a temporal order set to 7. The graph demonstrates the linear relationship between the quadratic error of the fit and the accuracy of the tag locations. Therefore, the accuracy of the displacement field estimation is directly related to the accuracy of the tag detection. This accuracy has not been truly investigated. Typically, the first automatic extraction step is followed by user interventions to manually correct tag locations. Atalar and McVeigh (1994) have shown that an accuracy on the order of 0.1 mm can theoretically be expected.

### *4.4. Computation time*

Fig. 7 illustrates the computing times obtained on a Silicon Graphics Indigo 2 (MIPS R4400 CPU processor) with no special optimization of the code. The computing time is approximately a quadratic function of the parameter number of the model (Space order$^2$ $\times$ Temporal order) (Fig. 7(a)). It is also linearly dependent on the number of tag points as shown in Fig. 7(b). In current practice and with the optimal orders, it takes less than 4 minutes to compute the direct spatio-temporal displacement field. Other parameters (deformation, velocities) are computed immediately.

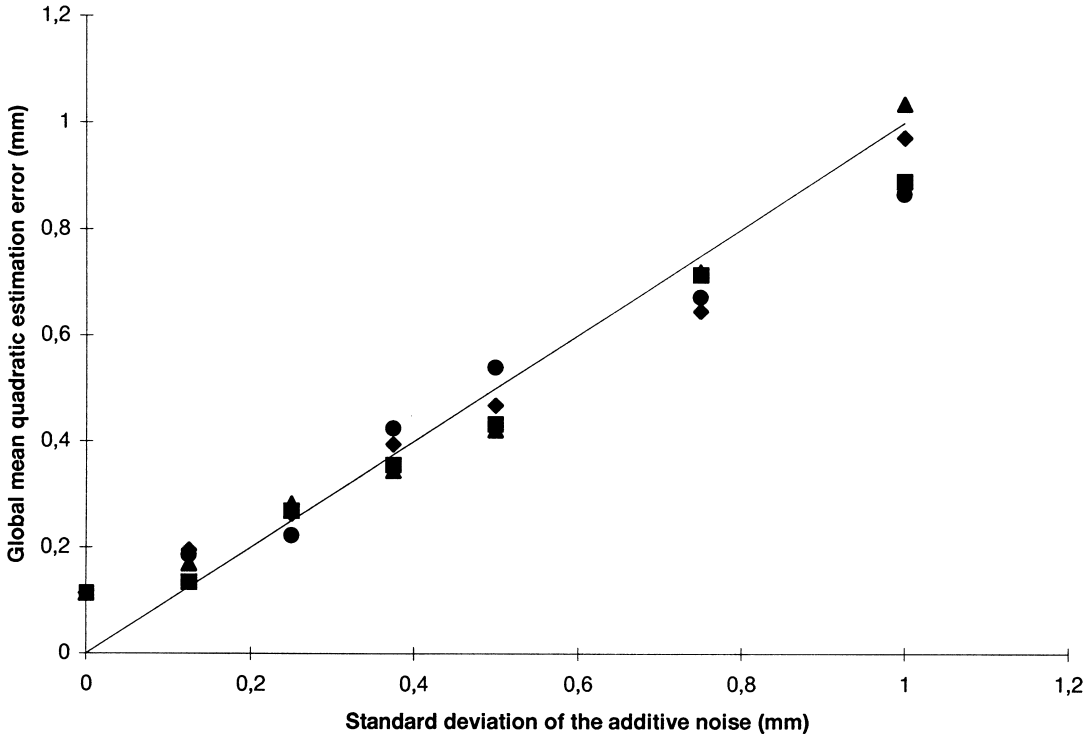


Fig. 6. Global mean quadratic error of fit as a function of the standard deviation of the noise perturbing the tag points locations. Four different sets of points have been tested.

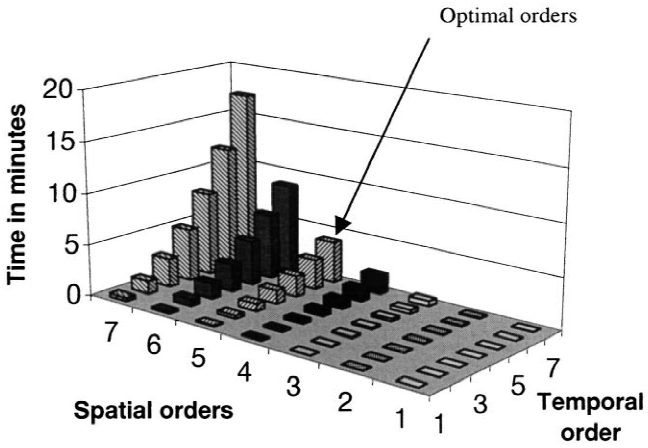


a

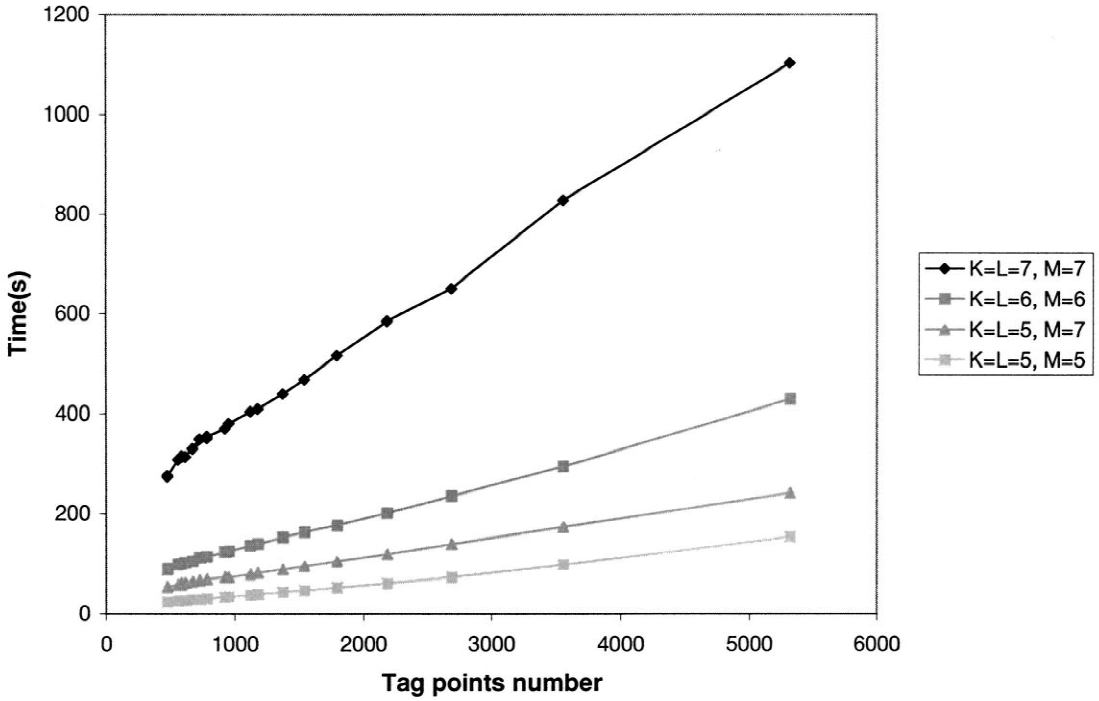


b

Fig. 7. Computing times. (a) As a function of the spatial and temporal orders; (b) as a function of the tag points number.

## 5. Results on clinical cases

Displacement and deformation fields are computed and analyzed on two clinical data sets. Fully informative visualization of vector fields is not an easy task. We used a specific visualization method developed by our group (Khouas et al., 1998). Such a method represents, in a synthetic view, the direction, orientation and magnitude of a vector field using a 2D texture model. The comparison of the results between cases was made at the maximum of the cardiac contraction, i.e., at end-systole for mid-ventricular slices. Nine images were acquired for the healthy subject and the patient at rest. Under pharmacological stress, only six images were acquired for the patient.

### *5.1. Visualization of the displacement field*

Fig. 8(a) shows the displacement field for the healthy case at end-systole. One can easily see that the displacement in the inferior, lateral and anterior regions is higher

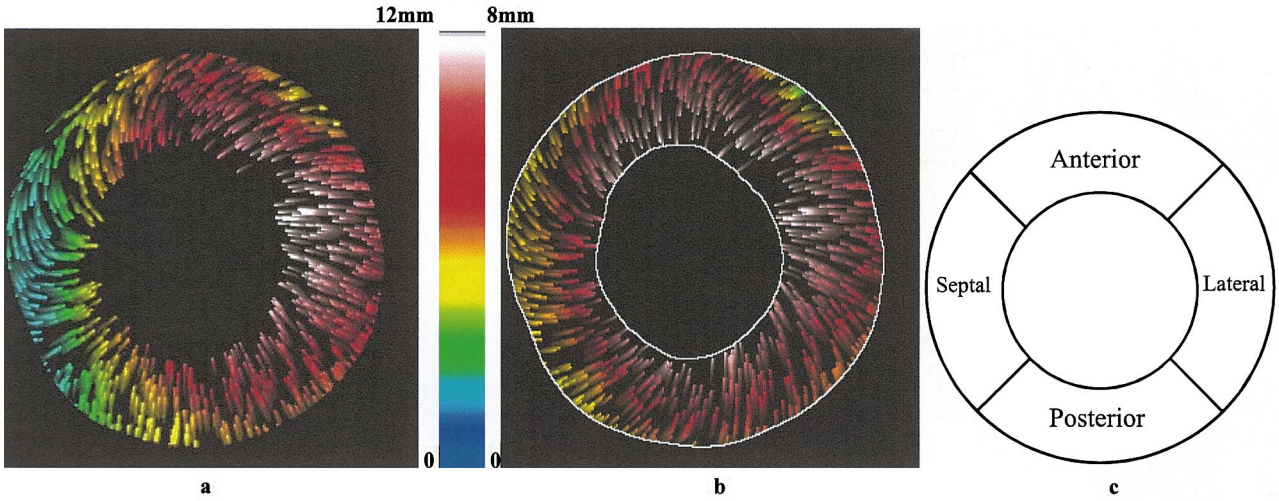


Fig. 8. Displacement field obtained at end-systole for the healthy subject. The direction of the displacement is given by the fibers while the magnitude is color-coded. The size of the region of interest which includes the myocardium is about 74×74 mm. (a) Displacement field. (b) Displacement field without the global rigid translation. Myocardial contours are displayed in white. (c) Definition of the myocardial regions.

than in the septal region, which is constrained by the right heart. The motion is mainly oriented toward the cavity's center. For the purpose of contraction analysis, it is preferable to eliminate the rigid translation that tends to complicate the interpretation. Global translation components are provided by the spatial order 0 terms of our model. This does not correspond to the true rigid translation from a continuum mechanics point of view but rather gives a mean value of the global displacement. Fig. 8(b) illustrates the displacement field once this global translation is removed. The motion is more homogeneous around the myocardium. Differences between the regions is no more significant, although the magnitude of the displacement is still slightly smaller in the septum. Note the existence of a gradient of the displacement magnitude inside the myocardial wall. The magnitude is greater when close to the endocardium.

Fig. 9 illustrates the displacement field at end-systole for the pathological case (severe postero-lateral ischemia) at rest and under pharmacological stress using the same color map as for the healthy subject. Compared to the healthy case, the magnitude of the displacement at rest is globally smaller and the orientation locally disorganized. This orientation, which is globally centripetal with the healthy subject, is clearly circumferential in the postero-lateral region (Fig. 9(a)). The pharmacological stress increases the magnitude of the displacement and re-orientates the motion toward the cavity's center except for the postero-lateral region (Fig. 9(b)). This suggests a contractile defect in this region, which was confirmed by an angiographic study. We also observe reduced wall thickness in this region. Quicktime movies were also generated and are available as Electronic Annexes (see www.elsevier.com/locate/media). They depict the evolution of the displacement field through

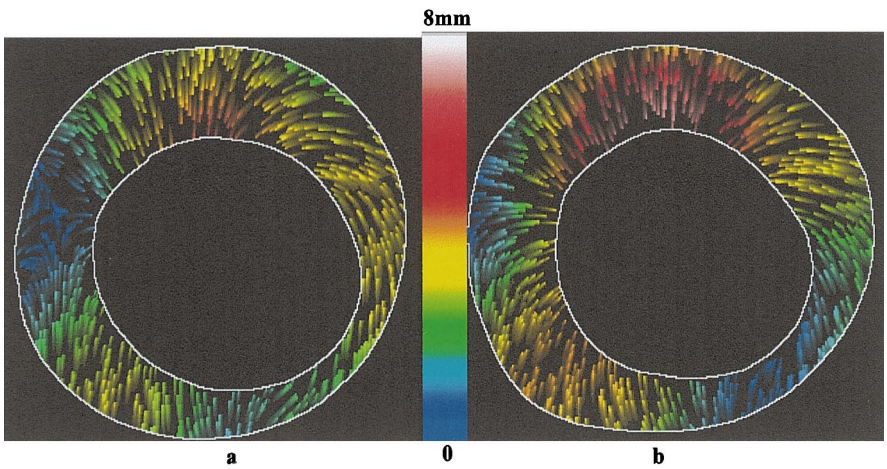


Fig. 9. Displacement field obtained at end-systole for the ischemic patient. (a) At rest; (b) under pharmacological stress (dobutamine). Myocardial contours are displayed in white.

the cardiac systole for the healthy subject and the ischemic patient. One can visualize the progressive orientation of the displacement towards the center and also the transmural gradient of the displacement magnitude for the healthy subject (End-systole corresponds to frame 6). The pathological case exhibits quite a different behavior at rest and under pharmacological stress. In that case, the end-systole is at timepoint 6 and 5, respectively.

### 5.2. Visualization of the deformation field

The deformation field is computed as a function of the coordinates after deformation using the equations below:

$$F = (I + \nabla D'(P'))^{-1}, \quad \varepsilon = \frac{1}{2}(F^{\mathrm{T}}F - I), \tag{16}$$

where $F$ is the deformation gradient tensor. The principal deformations are obtained by diagonalizing the $\varepsilon$ matrix. Fig. 10(a) represents the principal deformation field associated with the smallest eigen values for the healthy case. The principal deformation is related to the circumferential shortening of the myocardial fibers located at the middle of the LV wall which are circumferentially oriented. The orientation of the vectors is uniformly oriented along the circumferential direction and the magnitude significantly increases from the epicardium to the endocardium.

The deformation field for the pathological case at rest (Fig. 10(b)) is almost circumferentially oriented in the anteroseptal territories but the orientation is clearly toward the interior of the cavity in the posterolateral region. Moreover, the magnitude is globally smaller compared to that for the healthy subject. The result under stress (Fig. 10(c)) demonstrates an increase in magnitude over the anteroseptal region but, again, no recovery is observed in the posterolateral region.

### 5.3. Pointwise tracking

The identified model of the spatio-temporal displacement field provides a Lagrangian description of motion and, therefore, direct access to kinematic and deformation parameters of material points inside the LV myocardium. The computation of velocities, accelerations and deformations is analytical and benefits from the underlying smooth mathematical model to provide smooth temporal curves. Fig. 11(a) illustrates the variation of the two eigen values for three points belonging, respectively, to the anterior region of the healthy case and to the 'normal' anterior region of the pathological case at rest and under pharmacological stress. The two eigenvalues have almost the same evolution for the three regions although the magnitude is greater with the healthy case. Fig. 11(b) clearly shows, compared to the normal case, the perturbed behavior of these parameters in an ischemic territory. The value obtained for the abnormal region at time $t = 0$ is quite low. We still do not have a satisfactory explanation of this phenomenon. But the model, as stated, does not constrain the initial strain values.

## 6. Discussion and conclusion

The ability of the proposed spatio-temporal model to reconstruct a 2D time varying displacement field has been demonstrated. Experiments using the moving LV model have shown that a mean accuracy of 0.1 mm can be expected. With actual experiments, the accuracy primarily depends on tag location accuracy. Only the orders of the model are defined by the user. The analysis in Section 4.3 provides material to choose the optimal values for a given tagging pattern configuration (tag spacing and number of frames). The SVD decomposition algorithm introduces another parameter (Press et al., 1988) that sets the maximum rate above which a singular value is zeroed. As a consequence, equations which are corrupted by roundoff errors are ignored. For small orders, this parameter has no influence. As the orders increase, a too small or a too high value of this parameter may degrade the accuracy. After several experiments, we set this value to $10^{e}4$, which seems a good tradeoff. Another approach in order to reduce the effect of high order models is to use a regularized approach for the displacement field estimation (Bogen and Rahdert, 1996).

It is theoretically possible to consider only one point over two along each tag line to obtain the same accuracy with half the computing time. Indeed, tag tracking algorithms may incorporate some implicit smoothing so that reducing the density of points along the tags may not affect the accuracy of the motion estimation. Note that the user can control the overall accuracy of the computed displacement field by observing the statistics of the error computed on the tags.

The main characteristic of the method, as opposed to most of the previous studies (Denney and Prince, 1995; O'Dell et al., 1995; Park et al., 1996), is that it integrates the temporal behavior of the displacement field. It is, in this sense, close to the method proposed by Declerck et al. (1998a,b) in 3D, although their respective formulations are different. The principle of our method is directly applicable to 3D analysis. Considering a set of great axis images with tags parallel to the small axis image plane, one can introduce similar equations to (1)–(4) for the estimation of the displacement field along the $z$ direction. The evaluation of the accuracy with a possible different distribution of tag points should necessitate a careful evaluation. Another difference is that Declerck et al. (1998a,b) used a specific LV anatomical coordinate system and computed three intuitive deformation parameters within that system. In our system, we chose to reconstruct the displacement field based on the geometry of the tag pattern. It is always possible to express the displacement and the numerous

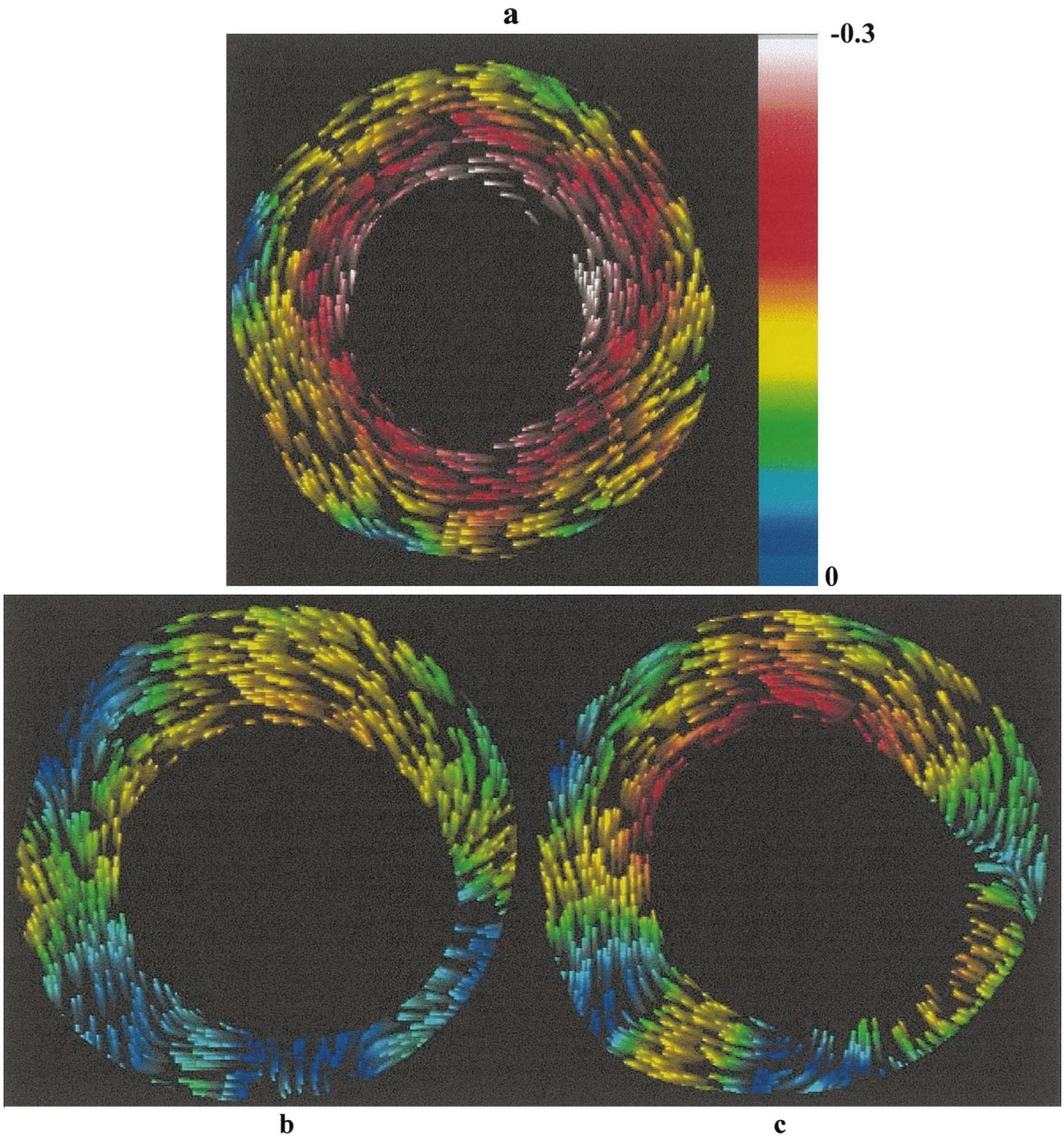


Fig. 10. Deformation field obtained at end-systole. The vectors are related to the smallest eigen value of the deformation tensor. It corresponds to the circumferential shortening for the fibers located in the middle of the myocardial wall. (a) Healthy subject. (b) Ischemic patient at rest. (c) Ischemic patient under pharmacological stress.

parameters related to deformation within a coordinate system adapted to the LV anatomy. Such a coordinate system is indeed useful since it provides a common reference system to analyze, describe and compare contractile functions. However, the definition of a system adapted to great inter-individual variations of the LV anatomy is still an open question.

Our model provides a hierarchical (coarse to fine) decomposition of the displacement field using cosine orthogonal functions. It is similar to a discrete cosine transform (DCT) on a irregular spatial domain and regular temporal domain. DCT is a very widespread tool in signal and image processing since it has very interesting properties. A statistical analysis of the model's parameters in the feature space could be performed to characterize a normal contractile function. The same approach can be used to reconstruct the displacement field inside the RV myocardium although some technical difficulties exist. The RV free wall is thin and its intersections with tag lines are quite small. It requires the adaptation of the acquisition technique (Fayad et al., 1998). Diastolic phase analysis could also be considered by triggering the image acquisi-

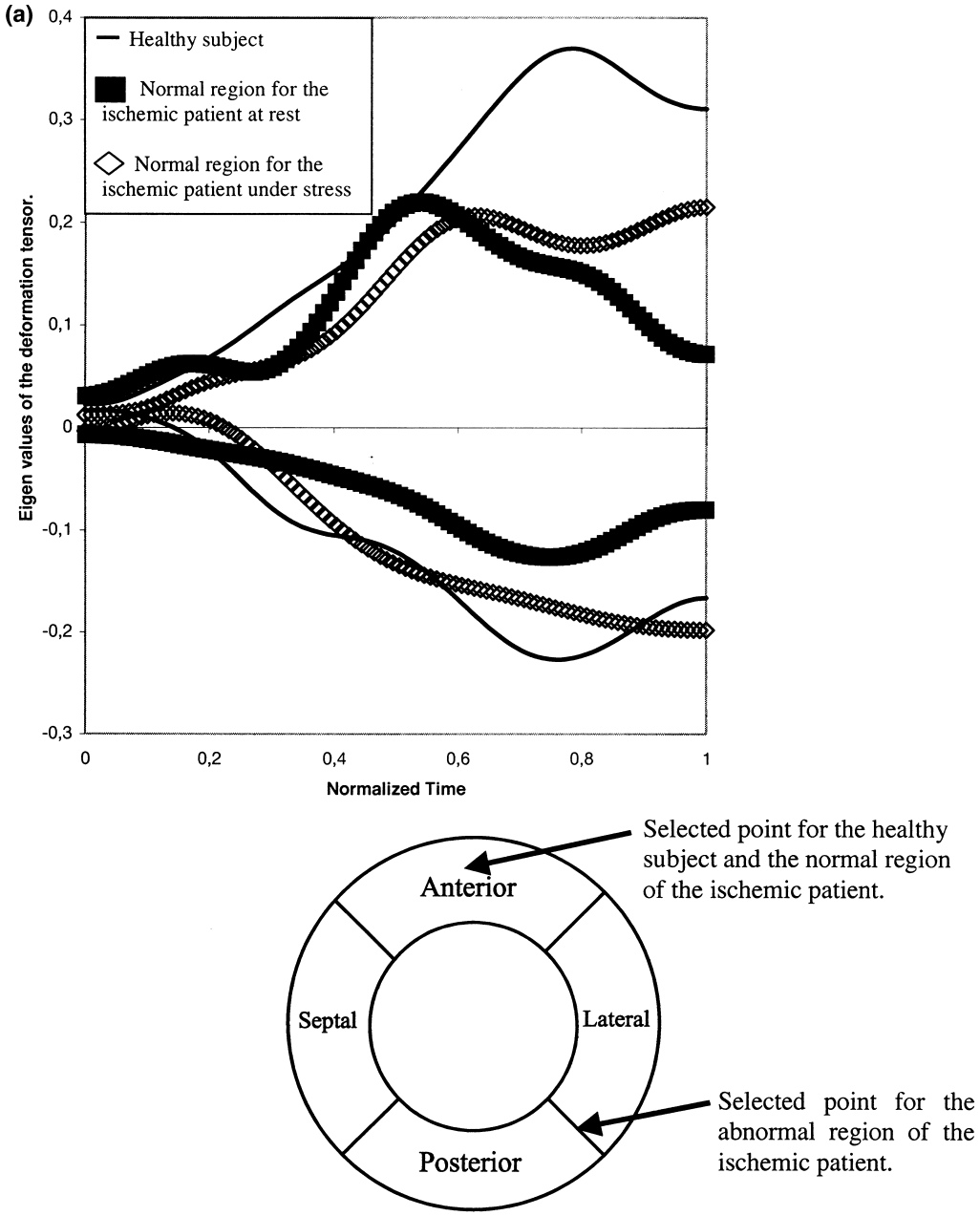


Fig. 11. Tracking the eigenvalues of myocardial points over time. (a) Within normal regions; (b) within ischemic regions as compared with the healthy subject.

tion on the end-systole. The proposed approach does not make a priori assumptions such as incompressibility. The displacement field estimation is based on the entire set of tag points and not only on the tag line intersections as with some other methods.

The proposed method, combined with a specific visualization tool, provides an innovative way to noninvasively analyze contractile function. Various spatio-temporal parameters can be accurately computed. These parameters provide a set of motion features not available before in the same context: the 2D trajectories of material/myocardial points, and the velocities or deformations over time. They are computed in 2D and time in the current implementation of the software. The accurate estimation of the true trajectories requires the extension of the method in 3D+ time. We are currently working on the generalization of the approach using long axis images. The large set of spatio-temporal data must be carefully analyzed for populations of normal subjects and ischemic patients. Therefore, we are developing specific tools to aid in the exploration of myocardial contractile function and to extract knowledge from the proposed method.

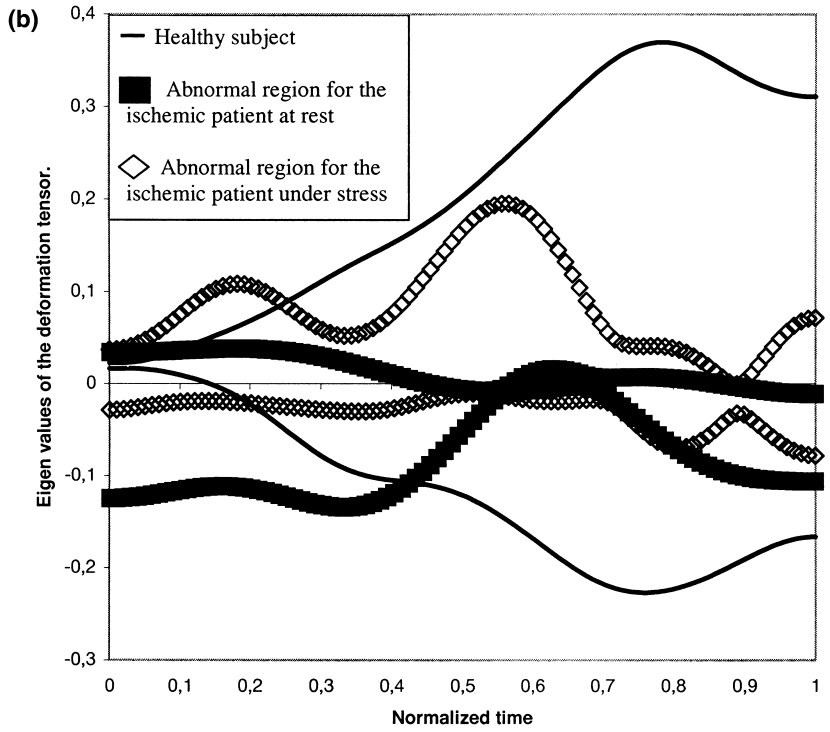


Fig. 11. (*continued*)


## Acknowledgements

The FINDTAGS analysis software was used courtesy of Dr. Elias A. Zerhouni of the Johns Hopkins University School of Medicine. This work is in the scope of the scientific topics of the GDR-PRC ISIS research group of the French National Center for Scientific Research (CNRS). It was performed in the framework of the joint Research Action 'Beating Heart' of the CNRS. This work is supported by the Région Rhône-Alpes under the grant 'Santé et HPC'. The authors are grateful to the anonymous reviewers for their careful review of the manuscript and the pertinence of their comments.


## Appendix A

We provide the mathematical details of the computation of the model's parameters for the $x$ coordinate of the inverse displacement field. Computing $\partial C_x/\partial A'_{x,i}$, $\forall i$ (see Eqs. (5) and (6)), the indices $t$, $n$, $o$ are grouped under the index $o$, and the indices $k$, $l$, $m$ under the index $k$. Let $c_o$ be the abscissa difference, we get

$$\frac{\partial C}{\partial A'_i} = 0 = \frac{\partial}{\partial A'_i}\left[\sum_o \left(\sum_k - A'_k b_{k,o} + c_o\right)^2\right] = \frac{\partial}{\partial A'_i}\left[\sum_o \left(-A'_i b_{i,o} + c_o + \sum_{k\neq i} - A'_k b_{k,o}\right)^2\right],$$

leading to

$$\frac{\partial C}{\partial A'_i} = 0 = 2A'_i \sum_o b_{i,o}^2 - 2\sum_o b_{i,o}\left(c_o - \sum_{k\neq i} A'_k b_{k,o}\right) = 2\sum_o b_{i,o}\left(-c_o + \sum_k A'_k b_{k,o}\right).$$

Expanding the terms again, we obtain for each combination of $k$, $l$, $m$

$$\begin{aligned} 0 = {} & \sum_{k'=0}^{K-1}\sum_{l'=0}^{L-1}\sum_{m'=0}^{M-1} A'_{x,k',l',m'} \sum_{t=t_o}^{t_f}\sum_{n=\min(t)}^{\max(t)}\sum_{o=1}^{O(n)} \cos\left(\frac{\pi k x'(\cdot)}{X}\right) \\ & \cdot \cos\left(\frac{\pi l y'(\cdot)}{Y}\right)\cdot\cos\left(\frac{\pi m t}{T}\right)\cdot\cos\left(\frac{\pi k' x'(\cdot)}{X}\right) \\ & \cdot \cos\left(\frac{\pi l' y'(\cdot)}{Y}\right)\cdot\cos\left(\frac{\pi m' t}{T}\right) \\ & - \sum_{t=t_o}^{t_f}\sum_{n=\min(t)}^{\max(t)}\sum_{o=1}^{O(n)} \cos\left(\frac{\pi k x'(\cdot)}{X}\right) \\ & \cdot \cos\left(\frac{\pi l y'(\cdot)}{Y}\right)\cdot\cos\left(\frac{\pi m t}{T}\right)\cdot(x(n,t_0) - x'(\cdot)) \end{aligned}$$

where $(\cdot)$ stands for $(o,n,t)$. The matrix form is given by Eq. (7) with matrices $B$ and $C$ given by

$$\begin{aligned} B_{i,j} = {} & \sum_{t=t_o}^{t_f}\sum_{n=\min(t)}^{\max(t)}\sum_{o=1}^{O(n)} \cos\left(\frac{\pi k(i) x'(\cdot)}{X}\right)\cdot\cos\left(\frac{\pi l(i) y'(\cdot)}{Y}\right) \\ & \cdot \cos\left(\frac{\pi m(i) t}{T}\right)\cdot\cos\left(\frac{\pi k'(j) x'(\cdot)}{X}\right) \\ & \cdot \cos\left(\frac{\pi l'(j) y'(\cdot)}{Y}\right)\cdot\cos\left(\frac{\pi m'(j) t}{T}\right), \end{aligned}$$

$$C_i = \sum_{t=t_0}^{t_f} \sum_{n=\min(t)}^{\max(t)} \sum_{o=1}^{O(n)} \cos\left(\frac{\pi k(i) x'(\cdot)}{X}\right) \cdot \cos\left(\frac{\pi l(i) y'(\cdot)}{Y}\right) \cdot \cos\left(\frac{\pi m(i) t}{T}\right) \cdot (x(n,t_0) - x'(\cdot)),$$

where $k(i) = \text{int}(i/LK)$, $l(i) = \text{int}((i - k(i)ML)/M)$, $m(i) = i - k(i)ML - l(i)M$.

## References


Amini, A.A., Chen, Y., Curwen, R.W., Mani, V., Sun, J., 1998. Coupled B-snake grids and constrained thin-plate splines for analysis of 2D tissue deformations from tagged MRI. IEEE Trans. Med. Imaging 17 (3), 344–356.

Atalar, E., McVeigh, E.R., 1994. Optimization of tag thickness for measuring position with magnetic resonance imaging. IEEE Trans. Med. Imaging 13 (1), 152–160.

Axel, L., Dougherty, L., 1989. Heart wall motion: improved method of spatial modulation of magnetization for MR imaging. Radiology 183, 745–750.

Bogen, D.K., Rahdert, D.A., 1996. A strain energy approach to regularization in displacement field fits of elastically deforming bodies. IEEE Trans. Pattern Analysis Machine Intelligence 18 (6), 629–635.

Buchalter, M.B., Weiss, J.L., Rogers, W.L., Zerhouni, E.A., Weisfeldt, M.L., Beyar, R., Shapiro, E.P., 1990. Noninvasive quantification of left ventricular rotational deformation in normal humans using magnetic resonance imaging myocardial tagging. Circulation 81, 1236–1244.

Clark, N.R., Reichek, N., Bergey, P., Hoffman, E.A., Brownson, D., Palmon, L., Axel, L., 1991. Circumferential myocardial shortening in the normal human left ventricle. Assessment by magnetic resonance imaging using spatial modulation of magnetization. Circulation 84, 67–74.

Declerck, J., Ayache, N., McVeigh, E.R., 1998a. Use of a 4D planispheric transformation for the tracking and the analysis of LV motion with tagged MR Images. INRIA, Sophia Antipolis, Technical Report No. RR-3535.

Declerck, J., Feldmar, J., Ayache, N., 1998b. Definition of a four dimensional continuous planispheric transformation for the tracking and the analysis of left-ventricle motion. Medical Image Analysis 2 (2), 197–213.

Denney, T.S., McVeigh, E.R., 1997. Model-free reconstruction of the three-dimensional myocardial strain from planar tagged MR Images. J. Magn. Reson. Imaging 7, 799–810.

Denney, T.S., Prince, J.L., 1995. Reconstruction of 3D left-ventricular motion from planar tagged cardiac MR images: an estimation theoretic approach. IEEE Trans. Med. Imaging 14 (4), 625–635.

Fayad, Z.A., Ferrari, V.A., Kraitchman, D.L., Young, A.A., Palevsky, H.I., Bloomgarden, D.C., Axel, L., 1998. Right ventricular regional function using MR tagging: normals versus chronic pulmonary hypertension. Magn. Reson. Med. 39, 116–123.

Guttman, M.A., Prince, J.L., McVeigh, E.R., 1994. Tag and contour detection in tagged MR images of the left ventricle. IEEE Trans. Med. Imaging 13 (1), 74–88.

Guttman, M.A., Zerhouni, E.A., McVeigh, E.R., 1997. Analysis of cardiac function from MR Images. IEEE CG&A 17 (1), 30–38.

Khouas, L., Clarysse, P., Friboulet, D., Odet, C., 1998. Fast 2D vector field visualization using a 2D texture synthesis based on an auto-regressive filter. Application to cardiac imaging. Machine Graphics Vision 7 (4), 751–764.

Maier, S.E., Fisher, S.E., McKinnon, G.C., Hess, O.M., Krayenbuehl, H.P., Boesiger, P., 1992. Evaluation of left ventricular segmental wall motion in hypertrophic cardiomyopathy with myocardial tagging. Circulation 86, 1919–1928.

Meyer, F.G., Constable, R.T., Sinusas, A.J., Duncan, J.S., 1996. Tracking myocardial deformation using phase contrast MR velocity fields: a stochastic approach. IEEE Trans. Med. Imaging 15, 1–12.

Moore, C.C., O'Dell, W.G., McVeigh, E.R., Zerhouni, E.A., 1992. Calculation of three-dimensional left ventricular strains from biplanar tagged MR images. J. Magn. Reson. Imaging 2, 165–175.

Mosher, T.J., Smith, M.B., 1994. A DANTE tagging sequence for the evaluation of translational sample motion. Magn. Reson. Med. 15, 334–339.

O'Dell, W.G., 1995. Myocardial deformation analysis in the passive dog heart using high resolution MRI tagging. PhD Thesis, Johns Hopkins University, Baltimore, 239 pp.

O'Dell, W.G., Moore, C.C., Hunter, W.C., Zerhouni, E.A., McVeigh, E.R., 1995. Three-dimensional myocardial deformations: calculation with displacement field fitting to tagged MR images. Radiology 195, 829–835.

Park, J., Metaxas, D., Axel, L., 1996. Analysis of left ventricular wall motion based on volumetric deformable models and MRI-SPAMM. Medical Image Analysis 1 (1), 53–71.

Pelc, N.J., Herfkens, R.J., Shimakawa, A., Enzmann, D.R., 1991. Phase contrast cine magnetic resonance imaging. Magn. Reson. Q. 7, 229–254.

Press, W.H., Flannery, B.P., Teukolsky, S.A., Vetterling, W.T., 1988. In: Numerical Recipes in C, The Art of Scientific Computing. Cambridge University Press, New York.

Radeva, P., Amini, A.A., Huang, J., 1997. Deformable B-solids and implicit snakes for 3D localization and tracking of SPAMM MRI data. Computer Vision Image Understanding 66 (2), 163–178.

Wedeen, V.J., 1992. Magnetic resonance imaging of myocardial kinematics. Technique to detect, localize, and quantify the strain rates of the active human myocardium. Magn. Reson. Med. 27, 52–67.

Young, A.A., 1998. Model tags: direct 3D tracking of the heart wall motion from tagged MR Images. In: Wells, W.M., Colchester, A., Delp, S. (Eds.), Medical Image Computing and Computer-Assisted Intervention-MICCAI'98. Cambridge, MA, USA, pp. 92–101.

Young, A.A., Axel, L., 1992. Three-dimensional motion and deformation of the heart wall: estimation with spatial modulation of magnetization – A model-based approach. Radiology 185, 241–247.

Young, A.A., Kraitchman, D.L., Dougherty, L., Axel, L., 1995. Tracking and finite element analysis of stripe deformation in magnetic resonance tagging. IEEE Trans. Med. Imaging 14 (3), 413–421.

Zerhouni, E.A., Parish, D.M., Rogers, W.J., Yang, A., 1988. Human heart: tagging with MR imaging – a method for noninvasive assessment of myocardial motion. Radiology 169, 59–63.

Zhu, Y., Drangova, M., Pelc, N.J., 1997. Estimation of deformation gradient and strain from cine-PC velocity data. IEEE Trans. Med. Imaging 16 (6), 840–851.

# Tracking Geometrical Descriptors on 3-D Deformable Surfaces: Application to the Left-Ventricular Surface of the Heart

Patrick Clarysse,* Denis Friboulet, and Isabelle E. Magnin, *Member, IEEE*

***Abstract*—Motion and deformation analysis of the myocardium are of utmost interest in cardiac imaging. Part of the research is devoted to the estimation of the heart function by analysis of the shape changes of the left-ventricular endocardial surface. However, most clinically used shape-based approaches are often two-dimensional (2-D) and based on the analysis of the shape at only two cardiac instants. Three-dimensional (3-D) approaches generally make restrictive hypothesis about the actual endocardium motion to be able to recover a point-to-point correspondence between two surfaces. The present work is a first step toward the automatic spatio-temporal analysis and recognition of deformable surfaces. A curvature-based and easily interpretable description of the surfaces is derived. Based on this description, shape dynamics is first globally estimated through the temporal shape spectra. Second, a regional curvature-based tracking approach is proposed assuming a smooth deformation. It combines geometrical and spatial information in order to analyze a specific endocardial region. These methods are applied both on true 3-D X-ray data and on simulated normal and abnormal left ventricles. The results are coherent and easily interpretable. Shape dynamics estimations and comparisons between deformable object sequences are now possible through these techniques. This promising framework is a suitable tool for a complete regional description of deformable surfaces.**

***Index Terms*—Curvature-based shape description, differential geometry, shape deformation analysis, 3-D cardiac image analysis.**

## I. Introduction

CERTAIN pathologies, such as *ischemia*, tend to modify the kinetics of the heart motion [68]: necrosed regions do not deform anymore while contractility decreases in ischemic less-drained regions; compensation phenomena often appear that tend to roughly preserve the global function. The reliable estimation of the heart motion through cardiac imaging is a particularly hard problem due to the difficult accessibility of the heart inside the chest and to its complex nonrigid behavior. Tracking the motion of the heart is possible on a slice-by-slice basis using quasi real-time techniques such as echography or X-ray computed tomography (CT). More recently, electrocardiogram (ECG) gated fast gradient-echo sequences allow the acquisition of temporal series of heart slices within one breath-hold in magnetic resonance imaging (MRI). Up to now, only the unique multisources X-ray scanner prototype dynamic spatial reconstructor (DSR) can reconstruct true three-dimensional (3-D) cardiac data volume series with a spatially isotropic resolution [57]. Future imaging systems will tend to provide spatial and temporal reconstructions with even better resolutions. Clinical examination results in a very rich and large amount of data that is often not easily interpretable and almost unexploited. Therefore, the development of 3-D image analysis techniques for the extraction of relevant and quantitative information about the cardiac function is of a great importance for the diagnosis and treatment of heart diseases.

In this paper, we focus on the analysis of the shape deformations of the heart wall surfaces throughout a sequence of 3-D images sampling the deformation cycle. We are more specifically interested in the tracking and analysis of the motion of the inner left-ventricular (LV) surface named *endocardium*. It is well known, since the original work of Tenant and Wigers [68], that myocardial ischemic diseases modify the kinetic of the inner part of the myocardium. Therefore, researchers proposed many different methods for noninvasively characterizing the LV *wall motion* from medical images [4], [34], [55], [63]. These methods generally start from two-dimensional (2-D) contours of the endocardium extracted from end-diastolic and end-systolic ventriculograms, partition the contours in segments and compute wall motion indexes in these segments. Without being exhaustive, let us mention the long-axis method [35], the radial methods [30], the rectangular methods [66], the area-based methods [19], and the centerline method [10]. They are based on different reference systems. These methods have several drawbacks. They made assumptions about the "idealized" geometry of the LV and strongly depend on external or internal references and coordinate systems. As a matter of fact, they are extremely sensitive to translational and rotational motion. None of them have made the consensus [34]. There is also a major approximation in these approaches: They use 2-D information to characterize an eminently 3-D-spatial and one-dimensional (1-D) temporal phenomenon.

Some researches have attempted to characterize the 3-D deformation of the endocardium throughout the cardiac cycle. Assuming the only available input data are the endocardial surfaces at successive cardiac instants, it is impossible to

Manuscript received December 14, 1994; revised January 12, 1997. This work was supported in part by the French Ministry of Education and Research (MESR/DRED) under a grant. The Associate Editor responsible for coordinating the review of this paper and recommending its publication was J. Duncan. *Asterisk indicates corresponding author.*

*P. Clarysse is with CREATIS, CNRS Research Unit (UMR 5515), INSA-502, 69621 Villeurbanne Cedex, France (e-mail: patrick.clarysse@creatis.insa-lyon.fr).

D. Friboulet and I. E. Magnin are with CREATIS, CNRS Research Unit (UMR 5515), INSA-502, 69621 Villeurbanne Cedex, France.

Publisher Item Identifier S 0278-0062(97)05639-5.

determine the exact mechanical deformation function that maps surface at cardiac instant $t$ onto surface at cardiac instant $t+1$: this is a very underconstrained problem. Therefore, it is inconceivable to be able to find the true spatio-temporal trajectory of any point of the surface given only this little information. Solutions have then been proposed which consist either in forcing a point-to-point correspondence by using geometrical and smoothing constraints [24], [31], either in introducing additional information from tagged imaging [51]–[52] in order to restrict the solution space.

Our approach does not aim at reconstructing a point-to-point correspondence and does not require additional information. We propose to *track the evolution of geometrical surface parameters* throughout the cardiac cycle. Moreover, a global description of the geometrical evolution of the endocardial surface is provided while a regional analysis of the evolution of geometrical parameters provides a more local description of the surface deformation.

### A. Related Works

Recently, much work aiming at the nonrigid motion estimation of deformable objects has been proposed. Some of them have been designed for and/or applied to the motion estimation of the beating heart. One can coarsely distinguish volumic-based methods that try to estimate the motion within the myocardium and shape-based methods [15]. In the *volumic-based methods*, a dense velocity field is computed from the observation of the spatio-temporal variation of the intensity function with optical flow methods [65], [38] or directly obtained from phase contrast cine MR imaging [53], [44]. MR tagging [3], [72] was specially designed for cardiac motion estimation. It relies on the generation and the tracking of virtual stripes deforming with the myocardium. MR tagging processing techniques result in a continuous strain field interpolated from true 3-D sparse physical correspondences [50], [71] or in parameter functions describing some intuitive global deformations [51]–[52].

*Shape-based approaches* assume that the shape deformation of the myocardial surfaces is characteristic of the pathological state of the heart. This hypothesis originates from numerous studies [4], [39]–[41], [68], [63]. The key problem with such approaches is the search for a reliable point-to-point correspondence (matching) between the surfaces. The difference between the methods relies on the way this problem is addressed, but, as said before, additional constraints are necessary to find a solution to the correspondence problem. Several researchers uses curvature cues of the surfaces and smoothing processes to guide the matching algorithm. Curvature was used by a number of authors to represent the shape of the ventricles or to derive wall stress approximations via the thickness [29], and also to define indexes related to the wall motion [39]–[41].

Yales' group uses a two-stage process [1], [24]. First, based on reliable shape cues (curvature extrema), major corresponding points between two surfaces are estimated through the minimization of a combined bending and conformal stretching energy term. Second, a dense smooth displacement field is computed. Then, the trajectories of some surface points can be compared with the tracking of surgically implanted markers [24]. The INRIA's group [17]–[18] uses a similar approach based on changes in the surface curvature, formulating an explicit mapping between two surfaces and using a finite-element resolution scheme. Mishra, Kambhamettu, and Goldgof introduce an explicit hypothesis of conformal motion to find an optimal matching [45], [31]. The physics-based framework developed by Metaxas and Terzopoulos [43] are used by Park jointly with tagging information to recover a surface model relying on parameter functions describing the radial and longitudinal contractions, the twisting and the long-axis deformation [52]. Using deformable models, it is also possible to perform a modal analysis to get the significant modes of deformation [49], [54].

### B. Starting Hypothesis

A deformable object (LV) at sample time $t$ is considered as a subset of $\Re^3$ and represented by its surface, i.e., a 2-D C2-differential manifold of $\Re^3$ that defines the shape. The subset of admissible deformations of the surface are C1-continuous mappings on the admissible shape space that prevent tears and cracks and conserve the topological properties of the surface. In addition, these deformation mappings are *nonrigid*, that is they belong to the class of complex deformations that generally do not preserve distances between points or angles between curves onto the surfaces. The term "*deformation cycle*" refers to a complete periodic cycle of deformation of an object. In the context of this paper, the surfaces are given as a 3-D connected component of voxels issued from a segmentation process, for instance. The methods presented hereafter assumes that normal and abnormal global and regional function of the LV induce different *shapes dynamics*. Thus, they are less constraining than methods based on static shapes only [4]. Moreover, surface deformations are supposed to be smooth.

### C. Generic Approach

Our shape-based approach aims at quantitatively characterizing the deformation of the LV inner surface by the evolution of a geometrical description of the surface. Global and regional curvature-based descriptions of the surface, suitable for the analysis of deformable surfaces, are proposed. Friboulet *et al.* have demonstrated the stability of computed curvatures on a sequence of 3-D CT volumic sequence of a dog's LV [28].

To compute the curvature on voxel-based surfaces, we implement a method originally proposed by Sander and Zucker [61], and we first evaluate its accuracy both from a qualitative and quantitative point of view. We use the curvature indexes proposed by Koenderinck and Van Doorn [33] to locally characterize the surface since it allows the decoupling of the shape attribute of a surface from its scale. Therefore, it takes into account one of the problems of the shape-based approaches relying on the wide variation of the people LV size. According to several studies [4], [39]–[41], abnormal regional function can be correlated to abnormal shape patterns at end systole. However, it is likely that shape evolution can more precisely reflect regional function than the shape at only one instant.

In order to characterize the evolution of the surface during a deformation cycle, we first consider the temporal evolution of a global curvature-based shape descriptor of a deformable object. To provide a more local analysis of the behavior of the surface and, since it is very unlikely to find the true point-to-point correspondence, we then propose to track the evolution of curvature indexes in selected regions or patches. The region matching problem consists in looking for the closest shape patch within a spatial neighborhood from one frame to the next. Geometrical parameters of corresponding patches can then be computed, analyzed and compared. These global and regional approaches can be seen as two complementary steps of a deformable surface recognition process. The first step is designed to recognize some global LV behaviors while the second one is to give a more local (segmental) description of the surface evolution.

We test the methods both on simulated sequences of deformable objects and on a actual LV surface of a healthy dog heart. We first illustrate the basic properties of the proposed approach on a sequence of deforming ellipsoids. We then consider some more reliable approximations of the beating LV. We simulate a dilated myocardiopathy which has a global effect on the diastolic and systolic cardiac function as well as ischemic hypokinetic and akinetic regions where the function is only locally altered.

It should be noted that the methodology we use is generic and could be applied to any deformable object accessed through its continuous or discrete surface as far as a local parameterization (normal to the surface and principal directions) at each surface point is available.

Section II describes the methods used for the surface description, the accuracy estimation and the global and regional deformation analysis. Experiments are presented in Section III both on simulated and actual X-ray data of a LV. In Section IV, we discuss the results and present some possible incoming extensions of this work.

## II. Methods

First, the main steps of the discrete curvature estimation algorithm are outlined. Section II-B indicates which surface descriptors we use, and the reasons for this choice. Section II-C shows how the accuracy of the discrete curvature values are evaluated. At last, we propose global and local techniques to analyze the temporal evolution of the curvatures in order to assess the geometrical deformation of an object. Notations and differential features are defined in Appendix A.

### A. Discrete Curvature Computation

In computer vision, curvature was first introduced in range image analysis [6]. Its property of invariance under rigid mappings makes it attractive for pattern recognition [6]–[8], [22]–[23], [32], [37], [69] and for matching [1], [31], [45]. Other interesting features are curvature extrema [46] or umbilics [62]. For an *analytic surface representation* $\mathbf{x}(u,v)$, assuming the parametric equations are not too complex, one can calculate the analytic formulae of the various differential features (Appendix A). When the surface is given as a set of discrete points in space, a discrete estimation of the curvature can be computed. Flynn and Jain decompose the approaches in analytic estimates and numerical estimates [26]. With *analytic estimation*, a continuous surface $\mathbf{x}(u,v)$ is locally fitted. Various kinds of fit are possible: orthogonal polynomials [6], linear regression with a local geometric model [59], spline-based methods [69]. Note that in some studies [60], the surface model is a graph function $\mathbf{x}(u,v) = (u,v,h(u,v))$ (Monge patch) and the surface support is the tangent plane, while in one of the methods presented in [67] the surface support is directly onto the surface itself, leading to a unique mapping of surface points in the parameter space $(u,v)$. *Numerical estimation* approximates the surface derivatives and the curvatures in a few directions. Another technique consists in obtaining a *triangularized version of the surface*. The Gaussian curvature is then concentrated at the vertices of the flat triangles and is calculated considering the angles between the edges of the triangles at each vertex [9], [13], [67]. Measures of the mean curvature $H$ can be defined on the edges of the triangles [9]. An interesting approach estimates the curvature directly from the intensity function and its partial derivatives [48], [20]. The curvature extrema and ridge lines can then be detected. However, this method needs to estimate third-order derivatives of the intensity function and is therefore sensitive to noise.

Starting with a discrete surface in a voxel form, we choose to implement a robust algorithm proposed by Sander and Zucker [61]. It starts with a local analytic approximation of a 3-D discrete surface and, in a second step, performs an iterative refinement of the local model to increase the consistency of the curvature values in a given neighborhood. We briefly review the main steps of this method.

*1) Initial Curvature Estimation:* At each point $p \in S$, the surface is approximated by an analytical quadric surface (graph of a differentiable function) given by

$$\Phi(u,v) = \left(u, v, n(u,v) = \frac{1}{2}\left(au^2 + 2buv + cv^2\right)\right). \quad (1)$$

The coefficients $a, b$, and $c$ of the local model at a point $p$ are computed taking into account the positions of the points lying in a neighborhood $\delta(p)$ of $p$ and an estimation of the normal $\vec{N}$ to the surface at $p$. The model results from the least mean square resolution, singular value decomposition (SVD) method [56], of a linear system where both position and normal information is used

$$\begin{cases} \frac{1}{2}\left(au_i^2 + 2bu_iv_i + cv_i^2\right) = n_i \\ au_i + bv_i = -N_{x_i} \\ bu_i + cv_i = -N_{y_i} \end{cases} \qquad i = 1 \cdots \mathrm{I} \quad (2)$$

with $(N_{x_i}, N_{y_i}, 1)$ the coordinates of $\vec{N}$ at point $i$ ($i = 1 \cdots \mathrm{I}, \mathrm{I}$ is the number of surface points in the neighborhood $\delta(p)$). It is easy to deduce the initial estimates of the principal curvatures and directions from the Hessian matrix of the parameterization about $p$. The principal curvatures $k_1$ and $k_2$ are given by

$$k_1 = \frac{1}{2}\left(a + c + \sqrt{(a-c)^2 + 4b^2}\right) \quad (3)$$

$$k_2 = \frac{1}{2}\left(a + c - \sqrt{(a-c)^2 + 4b^2}\right). \quad (4)$$

In the principal direction system $(\vec{M},\vec{m},\vec{N})$, the local surface model simply becomes

$$\Phi(u,v)=\left(u,v,\frac{1}{2}\left(k_1u^2+k_2v^2\right)\right). \tag{5}$$

*2) Local Model Refinement:* As the first step often produces outlying values, it is necessary to improve the initial estimates. We consider a $L$-contextual neighborhood $\vartheta_p$ of $p$ i.e., the set of all points $Q_\alpha \in \delta(p)$ such that $p$ is close enough to the local model at $Q_\alpha$. The distance of a point $p$ to a local surface model is approximated by the $z$ coordinate of $p$ relative to the local tangent plane system at $Q_\alpha$. The points $Q_\alpha$, located at a distance less than a maximum threshold $D$ from the surface model, belong to the contextual neighborhood $\vartheta_p$. Then, for each $Q_\alpha \in \vartheta_p$, we calculate what the local information in $p$ ought to be according to the local information in $Q_\alpha$. Given $k_{1_\alpha}$, $k_{2_\alpha}$, and $M_{p_\alpha}$, $N_{p_\alpha}$ for $\alpha = 1\cdots L$, a better estimate of the local information in $p$ is calculated in a least mean square sense (see [61 p. 844] for details). To evaluate the quality of the fit, three residual error terms measure the quadratic shift between the values at $p$ and at the neighboring points for the curvature values $(E^2_{k_p})$, the normal vector $(E^2_{N_p})$, and the maximum principal direction vector $(E^2_{M_p})$. The global residual error at iteration $t$ is then defined as

$$\varepsilon^t=\sum_{p\in S}\left(E^2_{k_p}+E^2_{N_p}+E^2_{M_p}\right). \tag{6}$$

The process iterates until $\varepsilon^t$ becomes sufficiently small and does not vary anymore. It was argued with empirical considerations that the algorithm converges.

### B. Surface Descriptors

Many curvature measures can be computed. Gaussian $(K)$ and mean $(H)$ curvatures are the most widely used indicators for surface labeling. The signs of the couple $(K,H)$ allow the distinction between eight elementary surface types [6]. However, this representation is not as easily interpretable and as rich as we would expect. Koenderinck and Van Doorn recently introduced two new shape descriptors based on the principal curvature system, which are the shape index $s$ and the curvedness $c$ [33]

$$s=\frac{2}{\pi}\mathrm{Arc\,tan}\frac{k_2+k_1}{k_2-k_1}=\frac{2}{\pi}\mathrm{Arc\,tan}\frac{-H}{(H^2-K)^{\frac{1}{2}}},\quad k_1\geq k_2$$

$$c=\left(\frac{k_1^2+k_2^2}{2}\right)^{\frac{1}{2}}=(2H^2-K)^{\frac{1}{2}}. \tag{7}$$

The shape index $s$ gives a continuous distribution of surface types between $-1$ and $+1$ (Fig. 1). The curvedness $c$ is inversely proportional to the size of the object. Note that $c^2$ is the potential energy of an ideal-thin-flexible plate of elastic material which is a measure of the strain energy of the deformation [1]. The couple $(s,c)$ permits an easy distinction between 2 similar points on spheres with different radii: they have the same shape index, but their curvedness is different. In other words, the shape index is invariant by homothety while the curvedness is not. Planar points have an undefined shape index.

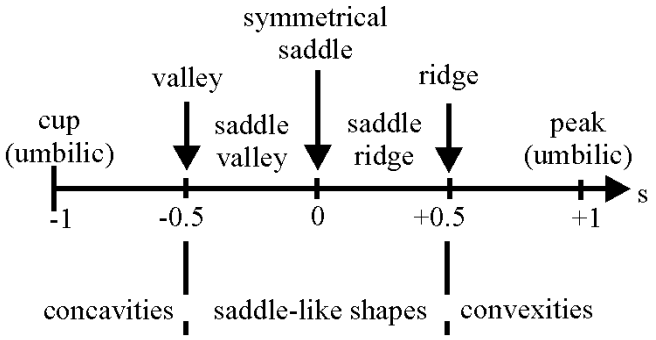


Fig. 1. Continuous distribution of the surface types according to the value of the shape index $s$ belonging to the interval $[-1,+1]$.

### C. Accuracy of the Computed Curvature

As previously mentioned, many methods have been proposed to estimate the curvature. However, the accuracy of the computed curvature is generally not directly available. In order to evaluate the reliability of the estimation, we estimate the accuracy on selected objects whose shape is similar to that encountered on the LV surface (elliptical and saddle like shapes). The principle of our accuracy estimation scheme consists in directly comparing the curvature values of a discrete voxel object with its continuous analytical model. We choose superquadric models [5] as prototype shapes. One of their advantages is that they can be mathematically expressed both by a parametric and an implicit form providing us both the continuous and discrete descriptions of object we need (Appendix B). The superellipsoid, for instance, can model a wide variety of regular shapes ranging from elliptical shapes $(\varepsilon_1=\varepsilon_2=1)$ to star-like shapes $(\varepsilon_1,\varepsilon_2\gg 2)$ through cylindrical shapes $(\varepsilon_1\leq 1,\varepsilon_2=1)$, flat beveled shapes $(\varepsilon_1$ or $\varepsilon_2=2)$ and pinched shapes $(\varepsilon_1$ or $\varepsilon_2>2)$. For the estimation of the accuracy, we use both ellipsoid and hyperboloid superquadric models.

The comparison strategy is as follows. Given the parameters of a superquadric $(a_1,a_2,a_3,\varepsilon_1,\varepsilon_2)$, we generate the discrete object $\theta_v$ using the inside–outside function following: $(x,y,z)\in\theta_v$ if $F_{\text{in-out}}(x,y,z)=(F(x,y,z))^{\varepsilon_1}\leq 1$ [64]. The discrete surface $\theta_d$ is the set of the border points of $\theta_v$ which are connected to the background. The discrete curvatures at each point of $\theta_d$ are computed with the discrete curvature estimation algorithm described in Section II-A. To compare the curvature results of the discrete surface with the curvature values of the corresponding continuous surface, we first look for the corresponding point on the equivalent continuous surface $\theta_c$ for each discrete point of $\theta_d$. This corresponding point is the nearest one in the Euclidean distance sense. The algorithm is as follows.

For each discrete point $P_d(x_d,y_d,z_d)\in\theta_d$:

1) Calculate the initial 2-D parameters $(\eta_{c_o},\omega_{c_o})$ of the continuous model from $P_d(x_d,y_d,z_d)$.
2) Calculate $(\eta_c,\omega_c)$ such that $P_c(x_d(\eta_c,\omega_c),\ y_d(\eta_c,\omega_c),\ z_d(\eta_c,\omega_c))\in\theta_c$ is the closest one to $P_d$, that is $||P_d-P_c||^2$ is minimal. The minimization process is realized by the simplex method [56].
3) Calculate the true analytical differential characteristics at $P_c$. The parametric formulation allows us to compute

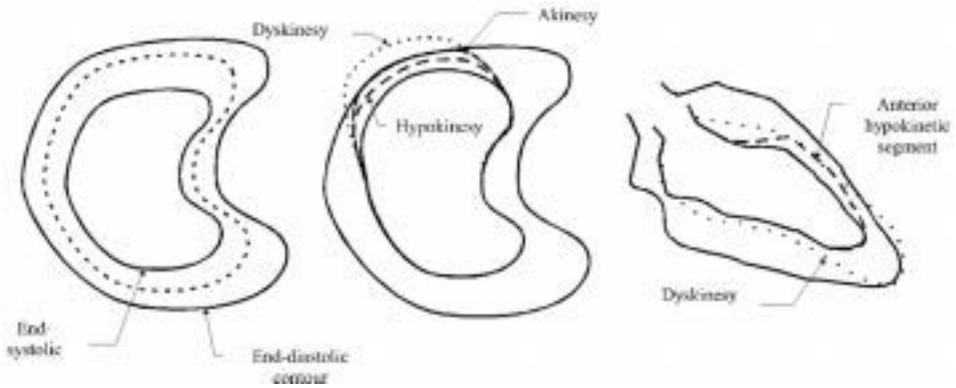


(a) (b) (c)

Fig. 2. Wall motion. (a) Normal behavior from the end-diastolic to the end-systolic contours in a short-axis view. The global shape of the contour is almost preserved during the motion. In case of dilated myocardiopathy, the magnitude of the wall motion is globally decreased (dashed line). (b) Different stages of ischemia: hypokinesia corresponds to a reduction of the wall motion magnitude along a segment (thick dashed line); akinesia is a total absence of motion in a segment (dense dashed line); a paradoxical expansion (dyskinesia) is observed when the muscle is unable to resist to the systolic stress (point line). (c) Right anterior oblique projection.

differential features of the surface. Principal curvatures are given by $k_{1,2} = H \pm \sqrt{H^2 - K}$, with $k_1 \geq k_2$. A summary of the calculations is given in Appendix B.

4) Compare the discrete and continuous values of the curvatures.

Once the correspondences are found, absolute and relative errors are easy to calculate between the points on the continuous surface and the corresponding ones on the discrete surface.

### *D. Smoothly Deformable Surfaces and Their Curvature Description*

We aim at characterizing the temporal evolution of a surface over the deformation cycle through the corresponding evolution of curvature-based descriptors of the surface. We investigated two complementary approaches to do this. The global approach depicts the evolution of the distribution of the curvature indexes (7) onto the surface. The local curvature approach uses the refined local surface model to generate a region-based correspondence from which curvature descriptors are tracked throughout the deformation cycle.

*1) Global Approach:* Looking at 2-D medial short-axis or long-axis views of a normal left ventricle, we observe that, during the contraction, the global shape of the endocardial contour remains almost the same in spite of the complex existing circumferential, longitudinal, and torsion motion [Fig. 2(a)]. On the contrary, in case of ischemia, the motion is significantly modified in and around the infarcted zone resulting in either a hypokinetic, either an akinetic or even a diskinetic myocardial segment [68], [63]. Moreover, the global shape of the endocardium exhibits a large abnormal evolution of its shape [Fig. 2(b)].

From these empirical considerations, we define a global 3-D shape index which is tracked over time. The global shape index or *shape spectrum* represents the normalized distribution of shape categories all over the surface. Starting from the index formalized by Dorai and Jain for static free form object recognition [22]–[23], we define our temporal shape index as

$$\gamma(h,t) = \frac{1}{A} \iint_S \delta_1(s(p_t) - h)\, dS \tag{8}$$

where $A = \iint_S dS$ is the total area of the surface $S$, $dS$ is a small region around $p_t$, and $\delta_1$ is the 1-D Dirac delta function. The argument $h$ ranges over the shape index domain $[-1,+1]$ and $t$ is the discrete time variable taking its value in $\{0,1,\cdots,T\}$. In fact, (8) summarizes the area of $S$ at each shape index value at time $t$.

The discrete version of (8) is derived by dividing the shape index range into $B$ bins and counting the number of points falling in each bin $k$ and normalizing it by the total number $N$ of discrete points of the surface $S$ at each time instant $t$

$$\Gamma\left(h = \frac{k}{B}, t\right) = \frac{1}{N} \sum_{i=1}^{N} \chi_k(s(p_{it})) \quad k \in \{1,2,\cdots B\}$$

with

$$\chi_k(x) = \begin{cases} 1, & \text{if } \frac{k-1}{B} \leq x < \frac{k}{B} \\ 0, & \text{otherwise.} \end{cases} \tag{9}$$

We get similar equations for the curvedness. This results in two 2-D global temporal distributions of the curvature features of the surface that can be analyzed and compared.

*2) Curvature-Based Region Tracking:* Up to now, much work in the shape-based approaches to the LV motion analysis has concerned the search for a point-to-point correspondence [1]–[2], [24], [31]. The principle of these methods basically consists in using curvature cues to constrain the correspondence [1]–[2], [24] and/or trying to fulfill a usually conformal motion constraint [1]–[2], [24], [31], [45]. The method presented in [12] decomposes the rigid and nonrigid part of the motion. The nonrigid part assumes some known correspondences. The rigid part is described by a moving object-centered coordinate system translating and rotating around the LV long axis. On the contrary, our approach does not try to recover a surface mapping and makes little assumption about the actual motion of the LV. We propose a curvature-based region tracking scheme to follow shape changes in a specific region of the endocardium. The main hypothesis in the sequel is that the shape of the LV evolves rather smoothly over time in order to be able

to associate regions between successive surfaces. Therefore, the algorithm combines geometrical information through the concept of similar-shape patch (SSP) defined below, and spatial information that will allow to associate regions. Let us define a *similar-shape patch* as a connected surface patch whose points have similar shape index. In our context, similar means that the shape index of the SSP points is within a given interval $s \pm \Delta s$. An SSP is characterized by a parameter vector whose components are mean values and standard deviations of the shape index and the curvedness over the patch, its area and its geodesic center. The goal is to track a SSP over the deformation cycle and to visualize and analyze the temporal evolution of the SSP parameters.

In order to automatically associate SSP's between successive surfaces, a simple region matching process has been designed. First, a reference point $p^t$ is designated onto the initial surface $S^t$. According to its curvatures, the point $p^t$ defines a reference SSP$^t$ within a limited neighborhood size *maxd*. The geodesic patch center of SSP$^t$, $p_c^t$, as well as the vector components of SSP$^t$ are computed. Then, $p_c^t$ is mapped onto the surface $S^{t+1}$ through a simple two-step point-to-point algorithm giving $p^{t+1}$.

The first step compensates for a rigid part of the motion. The rigid part of the motion (translation and rotation), although proved to exist, is difficult to estimate [55], [70]. Friboulet *et al*. have demonstrated that, based on a shape principal axes study [25], the great axis of the LV is well defined and can undergo a rotation up to 10° [27]. However, the orthogonal axes lying in the small-axis plane were found not significant. We effectively observed, on our LV dog sequence, that the change of the LV shape between end-systole and the beginning of the filling of the cavity results in a dramatic rotation of the principal axes in the small axis plane. Therefore, the rigid motion compensation procedure simply eliminates the translation of the LV center of gravity.

The second step estimates a nonrigid part of the motion making a locally homothetic motion assumption. The principle of the correspondence search is as follow. At instant $t$, given the local refined surface model at a point $p_c^t$ of the surface $S^t$ (after rigid motion compensation), a ray is traced normally to $S^t$ toward the surface $S^{t+1}$ (instant $t+1$). The intersection $p^{t+1}$ of the ray with the surface $S^{t+1}$ gives the corresponding point of $p_c^t$.

It is important to notice that this process, which is a point-to-point correspondence problem, is not the most crucial part of the method. It is a way to initialize the region correspondence. Other existing sophisticated point matching algorithms can perform well in this task (we have also implemented the algorithm described in [31]).

Taking into account the mean shape parameter of $p_c^t$, the SSP relative to $p^{t+1}$ is then computed as well as its associated parameter vector. The geodesic patch center $p_c^{t+1}$ is projected onto surface $S^{t+2}$. The process is repeated on the successive surfaces of the cardiac cycle.

Tracking the SSP's over time gives information on the evolution of the geometrical parameters measured in this region. This evolution can be depicted by temporal graphs to allow analysis and comparisons (Figs. 7 and 8).

## III. Experiments

Experiments are conducted both on synthesized deformable objects and on left ventricular surfaces segmented from a 3-D X-ray CT image sequence.

### A. Discrete Curvature Computation and Accuracy Estimation

The sizes $r_0, r$ of the spherical initial and refinement neighborhoods $\delta(p)$ and $\vartheta_p$ are related to the actual size of the object and to the size of the minimum surface details we want to preserve. A too wide size will eliminate surface details and increase the computational cost, while a too small size would give very rough initial estimates. The choice of $r_0$ is of importance since it defines the initial curvature values which will be homogenized in the refinement stage. We found that these sizes should ideally be set according to the underlying surface, which is a kind of "chicken and egg" problem. A high neighborhood size is more convenient to less curved regions (high curvature radius). On the contrary, a smaller neighborhood size is more suitable for high curved region (small curvature radius). For the accuracy estimation, we take initial radius value $r_0 = 3$ and $r_0 = 6$ depending on the synthetic object (see below). For the experiments on the true and simulated LV (Sections III-B and III-C), the value $r_0 = 5$ is a good compromise. The radius value $r$ is set to $r = 3 \leq r_0$ in all the experiments. Three refinement iterations were performed for all the objects. Refinement iterations improve the consistency of the curvatures and smooth their magnitude at the same time. The threshold value $D$, which determines the distance of a point $p$ to a local surface model (see Section II-A), is fixed to 1.0. This is not a critical parameter with regular smooth surfaces.

Major shape categories encountered onto the LV surface are concave and convex ellipsoidal and hyperbolic surfaces. A superellipsoid and a superhyperboloid of one piece are simulated with the algorithms described in Section II-C such that the curvature magnitudes are similar to those of the LV. The minimum and maximum values of the Gaussian curvature (given by the algorithm) onto the LV surfaces at all cardiac instants are $-0.014$ mm$^{-2}$ and 0.02 mm$^{-2}$, respectively. The synthesized objects are superquadrics for which the discrete representation is generated with the inside-outside function and the continuous representation is obtained with the algorithm described in Section II-C. There are a sphere (radius 40 voxels) and two superellipsoids ($\varepsilon_1 = \varepsilon_2 = 1$): E1, with radii 7, 10, and 35, respectively, along $x, y$, and $z$ directions with a Gaussian curvature in the range [0.0004, 0.25] and E2 with radii 30, 20, and 40 with a Gaussian curvature in the range [0.0002, 0.0044]. To check the accuracy of hyperbolic regions, two superhyperboloids of one piece are generated: H1 ($\varepsilon_1 = \varepsilon_2 = 1$) with radii 20, 20, and 35 has a Gaussian curvature in the range [$-0.001$, 0] and H2 which has the same radii, but with exponents $\varepsilon_1 = 1.2$, $\varepsilon_2 = 1$.

True and measured global mean curvatures can be computed and compared. Local absolute curvature error (AE) is calculated at each point of the surface as

$$\mathrm{AE} = |k_{\mathrm{the}} - k_{\mathrm{mes}}| \tag{10}$$

TABLE I
MEAN CURVATURE VALUES AND AE'S ON THE DIFFERENT SUPERQUADRIC OBJECTS ($k1$, $k2$: PRINCIPAL CURVATURES, $s$: SHAPE INDEX, $-1 \leq s \leq +1$, $c$: CURVEDNESS)

| Object (Mean neighborhood size in number of voxels) Radii x, y, z | Expected Mean $k_1$ mm$^{-1}$ (radius) $k_2$ mm$^{-1}$ (radius) | Measured Mean $k_1$ mm$^{-1}$ (radius) $k_2$ mm$^{-1}$ (radius) | Absolute Mean Error $k_1$ $k_2$ | Expected Mean $s$ $c$ mm$^{-1}$ | Measured Mean $s$ $c$ mm$^{-1}$ | Absolute Mean Error $s$ $c$ | Correct Classification Rate % |
|---|---|---|---|---|---|---|---|
| Sphere (100) | 0.0333 (30) | 0.0296 (33.8) | 0.0037 | 1 | 0.9268 | 0.0732 | 100 |
| 30, 30, 30 | 0.0333 (30) | 0.0370 (27) | 0.0039 | 0.0333 | 0.03365 | 0.0012 | |
| E1 (30) | 0.1412 (7.1) | 0.1118 (8.5) | 0.0284 | 0.5630 | 0.5606 | 0.0245 | 97 |
| 7, 10, 35 | 0.0158 (63.3) | 0.0135 (74) | 0.0048 | 0.1009 | 0.0850 | 0.0202 | |
| E2 (100) | 0.0469 (21.3) | 0.0473 (21.1) | 0.0032 | 0.784 | 0.7636 | 0.0263 | 100 |
| 30, 20, 40 | 0.0208 (48.1) | 0.0200 (50) | 0.0012 | 0.0365 | 0.0366 | 0.0022 | |
| H1 (30) | 0.0205 | 0.013 | 0.0090 | 0.2122 | 0.3286 | 0.13 | 100 |
| 20, 20, 35 | −0.043 | −0.0468 | 0.0044 | 0.0339 | 0.0346 | 0.0033 | |
| H2 (30) | 0.0385 | 0.0133 | 0.0255 | 0.1128 | 0.3218 | 0.21 | 96 |
| 20, 20, 35 | −0.0406 | −0.0447 | 0.0050 | 0.0422 | 0.0334 | 0.0198 | |

where $k_{\text{the}}$ is the theoretical curvature value and $k_{\text{mes}}$ is the measured value. The analysis was performed both on the principal curvatures and the proposed shape index and curvedness. An elementary classification of the surface points is performed based on the signs of the Gaussian and mean curvatures. It relies on an arbitrarily chosen null value $(1^E{-}6)$ and distributes the surface points in eight elementary surface classes.

Mean values of the principal curvatures, shape index, and curvedness are calculated over the points of the different objects. Table I summarizes the results. Results are quite satisfactory for all the shapes. Looking at the equivalent curvature radii, the value for $k_2$ with E1 should be better with a larger neighborhood size, but this should also decrease the performance for $k_1$. We globally observe that, due to discretization effects, AE's on the maximum principal curvature and the curvedness are higher with highly curved regions. High AE on the shape index is located both in high curved regions and flat regions (shape index is undefined on a plane). Surface classification is better defined with highly curved regions since there is less uncertainty on the underlying surface type. Correct classification rate is almost perfect in all the cases. The reduced correct classification rate of 96% of H2 as compared to H1 is attributable to the poor local approximation of the central part of the hyperboloid. Indeed, the increase of $\varepsilon_1$ tends to transform the thin central part of the hyperboloid into a cylinder-like shape, saddle valley points being considered as saddle cup ones by the algorithm.

In conclusion, the curvature estimation algorithm provides good and consistent estimates of the curvatures on regular and smoothed surfaces. Moreover, the algorithm does not depend on the discrete connectivity of the surface. The method is robust to noise. A dramatic improvement of the shape classification is obtained on a noisy ellipsoid (zero-mean Gaussian noise, standard deviation 0.5 applied to the surface point positions) in three refinement iterations only. On the contrary, triangulation-based methods, which give only the Gaussian curvature, are very noise sensitive as well as, in a reduced proportion, other methods like the cross patch and orthogonal walking methods presented in [67]. When sharp geometrical discontinuities exist on the surface, the algorithm has to be adapted.

### B. Synthetic Sequences

*1) Basic Examples:* In order to illustrate the method, three basic example sequences are generated. The first one is a deforming half ellipsoid whose radii (21, 27, 61) gradually decrease in the same proportion during nine instants. It will be referred as the homothetic ellipsoidal sequence. The second one is a complex ellipsoidal sequence which is composed of two steps.

a) A first deformation step from instant 1 to instant 9, generated by a decreasing exponential law $e^{-\alpha t}$ ($\alpha$ real positive) applied to the radii (each radius has a specific exponential coefficient so that the global deformation is not homothetic). The radii of the ellipsoid varies from (21, 27, 61) at time 1 to (15, 20, 47) at time 9.

b) A second deformation, given by a variation of the radii following the $1-e^{-\alpha t}$ ($\alpha$ real positive) form, from time 10 to time 13 prolonged by an isovolumic phase (instants 14–18).

The third sequence is a deforming half-ellipsoidal sequence where concavities progressively appear from time 1 to time 9 and disappear from time 10 to time 18. This model, presented in [52] as a model parameter function, is generated with the following parametric equations:

$$s(\theta,\varphi) = \begin{pmatrix} r_1(1-\gamma_1\cos(n_1\theta)\cos\theta\cos\varphi) \\ r_2(1-\gamma_2\cos(n_2\theta)\cos\theta\sin\varphi) \\ r_3(1-\gamma_3\cos(n_3\theta)\sin\theta) \end{pmatrix} \tag{11}$$

where $r_1 = r_2 = 30$, $r_3 = 70$, $\gamma_1 = \gamma_2 = 0.3$, $\gamma_3 = 0$, $n_1 = n_2 = 3$, $0 \leq \theta \leq \frac{\pi}{2}$, $-\pi \leq \varphi \leq \pi$.

*2) Simulated Harmonic LV:*

*a) Normal LV:* A synthetic normal LV sequence is obtained by fitting a spherical harmonic surface to the four-dimensional (4-D) data set presented in the following Section III-C. The fit is expressed by the linear least square minimization of an error term based on the square difference of the polar radii of a spherical harmonic model given by (12) and

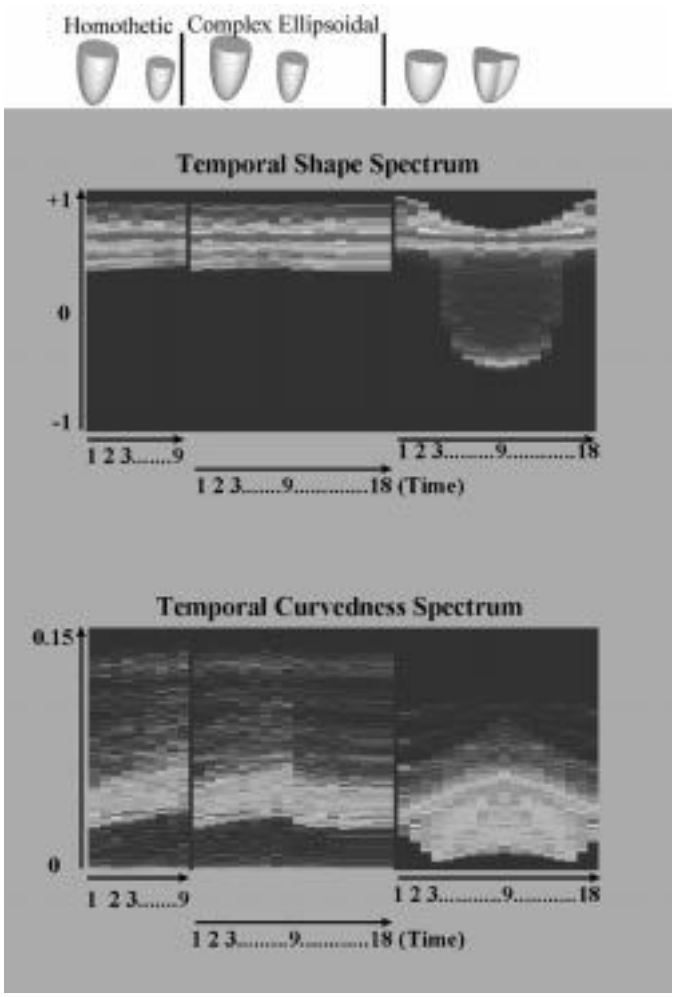


(a) (b) (c)

Fig. 3. Global shape descriptors on the ellipsoidal sequences. Top: shape spectrum. Bottom: curvedness spectrum. (a) Homothetic ellipsoidal sequence on nine instants. (b) Complex ellipsoidal sequence on 18 instants. (c) Complex sequence with concavities on 18 instants. For the sake of comparison, maximum frequency is fixed to 5% of the total number of surface points for the shape images and 2% for the curvedness images. Color scale ranges from blue (0%) to red (5 and 2%, respectively).

the 4-D surface data, as proposed in [42]

$$r(\theta,\varphi,t)=\sum_{l=0}^{L}\sum_{m=0}^{l}\sum_{k=0}^{K}\Bigg[A_{lk}^{m}P_l^m(\cos\theta)\cos(m\varphi)\cos\left(\frac{2\pi k}{\tau}t\right)+B_{lk}^{m}P_l^m(\cos\theta)\sin(m\varphi)\cos\left(\frac{2\pi k}{\tau}t\right)+C_{lk}^{m}P_l^m(\cos\theta)\cos(m\varphi)\sin\left(\frac{2\pi k}{\tau}t\right)+D_{lk}^{m}P_l^m(\cos\theta)\sin(m\varphi)\sin\left(\frac{2\pi k}{\tau}t\right)\Bigg] \tag{12}$$

where $L$ is the degree, $K$ the wave number and $\tau$ the period of the nonrigid motion. We take $L=5$ and $K=2$ to obtain a reasonably good approximation of the true temporal LV surface with 252 harmonic components [Fig. 6(a)].

*b) Pathological LV:* A dilated myocardiopathy is simulated with the same model. In practice, this pathology results in a reduced diastolic and systolic function. We simulate it by taking a reduced temporal order $K=1$.

An ischemic LV is also simulated. To do this, we locally create an ischemic zone at a given location onto the surfaces of the normal LV. The ischemic zone is composed of a patch (small portion of a surface) of the reference diastolic surface which is copied and pasted onto the other surfaces. Two new data sets are generated, one with the patch kept fixed to simulate an akinetic ischemic behavior and the other where the patch is authorized to move in order to simulate a hypokinetic ischemic LV. The same fit as before is performed on these new pathological data sets. Fig. 6(b) shows the resultant surface with the akinetic ischemic zone located in the anterior region related to the left anterior coronary territory.

### C. Actual Data of the LV

The real data is a sequence of 18 3-D X-ray CT images of a dog's heart (from the dynamic spatial reconstructor [57]) segmented to extract the opacified LV (excluding the pilars). Each data volume is a 3-D array with dimensions $98\times100\times110$ voxels. Each voxel has an isotropic resolution of 0.9 mm. The segmentation is a semi-interactive process which consists of the following:

1) estimating the gradient in the image with a 3-D Canny-Deriche operator [11];
2) calculating the local extrema of the gradient with a hysteresis technique [47];
3) extending the connected component from a user supplied point belonging to the surface;
4) applying 3-D morphological filters to close and smooth the surface, leading to a 26-connected discrete trace. The three components of the gradient at the detected surface points provide the initial estimate of the normal to the surface needed in the curvature computation algorithm.

## IV. Results and Discussion

### A. Global Descriptors

Global shape descriptors of the ellipsoidal sequences are depicted in Fig. 3. The first part of each image corresponds to the homothetic ellipsoidal sequence. Horizontal dimension relates to the nine time instants of the sequence, vertical dimension relates to the shape index scale ($-1$, $+1$) and to the curvedness scale (0, 0.15) with, respectively, 200 and 400 equidistant classes (see Section II-D). As expected, the shape index distributions of the homothetic sequence is quasi-constant over the deformation [Fig. 3(a) top]. Changes in the shape of the complex ellipsoidal sequence are not significantly visible on the global shape images because of the relatively narrow shape interval of variation. It is possible to reduce the shape interval, as far as the number of points is significant, in order to more accurately describe the shape content. As expected, curvedness distribution of the homothetic ellipsoidal sequence is linearly increasing over time [Fig. 3(a) bottom]. On the contrary, the evolution of the curvedness distribution for the complex ellipsoidal sequence [Fig. 3(b) bottom] is not linear during the contraction (times 1–9) and expansion

phases (times 10–18). The sharp well-visible rupture in the shape profiles (times 9–10) corresponds to the rapid change in the curvedness magnitudes at the beginning of the expansion. There is no more variation during the isovolumic phase (times 14–18). Fig. 3(c) shows the continuous behavior of the global descriptors when concavities progressively arise. Shape content becomes richer, part of the initial ellipsoidal shape spreading into saddle-like and concave shapes, while the curvedness globally increases. These selected examples show that the proposed global descriptors provide a realistic interpretation of the overall shape dynamics.

Fig. 4 depicts the global descriptors corresponding to the actual and the simulated heart sequences. The five image portions are relative to the actual LV surface, Fig. 4(a); the simulated normal LV surface, Fig. 4(b); the simulated dilated LV, Fig. 4(c); the hypokinetic, Fig. 4(d); akinetic LV, Fig. 4(e). The LV shape is mostly elliptical as the distribution concentrates in the upper quarter of the shape index scale. The shape distribution shift of the simulated LV is attributable to the more ellipsoid-like rounded approximation of the harmonic surfaces as we can clearly see on the 3-D views Fig. 6. Although one observes the more blurred shape distribution of the dilated LV and also some slight evolutions in the ischemic cases, the global shape distributions are not clearly distinct. In effect, it was directly observed on the cine-renderings of the 3-D views of the shape index distribution onto the LV normal surface [see four samples Fig. 5(a)] that the shape indexes (or the LV shape) do not vary significantly during the cardiac cycle. Therefore, shape regions are mostly preserved during the deformation in the normal LV. Clear variations are however observed with the curvedness distributions. The peak of the normal harmonic LV, Fig. 4(b, bottom), corresponding to the end-systole (time $\sim$9), is reduced with the ischemic LV, Fig. 4(d), (e) and cut with the dilated LV, Fig. 4(c).

Global changes in the shape deformation imply global shape changes observable by this curvature-based technique. Curvedness distributions are significantly altered by pathologies even if they are local. Reduction of the global function with the dilated myocardium do not modify the shape index distributions. This suggests that this kind of pathology essentially affects the magnitude of the motion. Although some clear differences are observable with ischemic LV, a more local analysis is required.

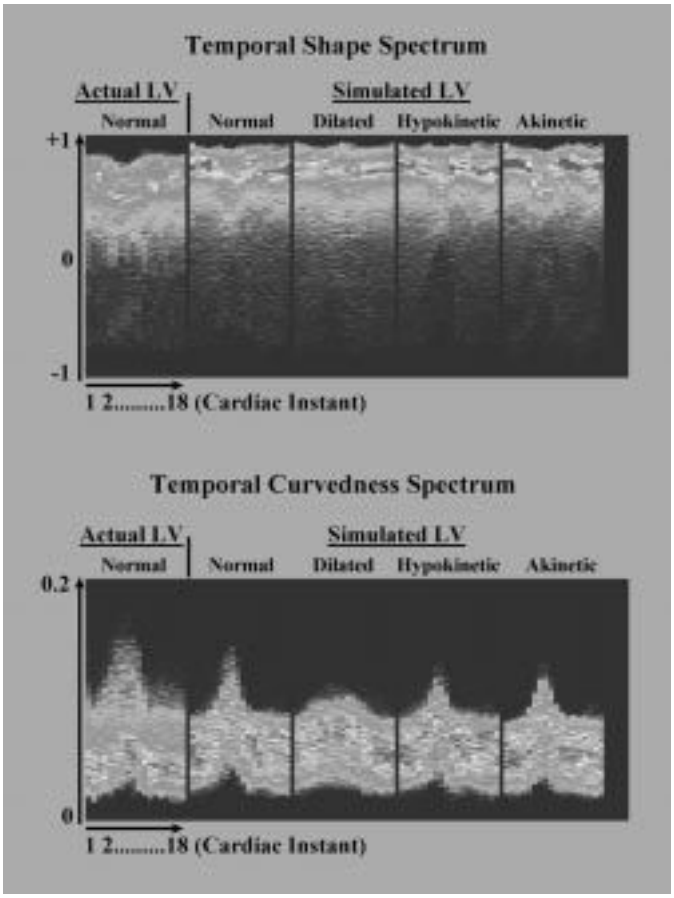


(a) (b) (c) (d) (e)

Fig. 4. Global descriptors on the actual LV data and on the simulated harmonic surfaces. Top: shape spectra. Bottom: curvedness spectra. (a) Actual LV data. (b) Spherical harmonic surface fitted to the actual LV data ($L = 5, K = 2$). (c) Spherical harmonic surface fitted to the actual LV data with $L = 5$, $K = 1$ which simulates a global decreasing of the contractile function (dilated myocardiopathy). (d) Spherical harmonic surface fitted to the modified LV data ($L = 5, K = 2$). An antero-septal hypokinetic segment is simulated by keeping a patch nearly constant but still moving along with the surface. (e) Akinetic simulated sequence where the ischemic patch nearly does not move anymore. For the sake of comparison, maximum frequency is fixed to 3% of the total number of surface points for the shape images and 1.2% for the curvedness images. Color scale ranges from blue (0%) to red (3 and 1.2%, respectively).

### *B. Curvature-Based Region Tracking*

As said before, the LV shape is quasi-stable over the cardiac cycle [Fig. 5(a)]. On the opposite, the curvedness varies largely as seen on the four free wall views in Fig. 5(b). Working on the simulated normal and ischemic LV's, three points are designated onto the surfaces as reference points. Point P1 is placed at the apex, point P2 in the anterior wall, and point P3 in the cup at the pilar anchor. These points define reference regions that are temporally tracked over the cardiac cycle. Mean curvature parameters associated to these regions are graphically represented as functions of time. In the ischemic case, the zone defined by P2 belongs to the ischemic region as shown in Fig. 6(a) and (b). The parameters of the SSP tracking algorithm are *maxd*, the maximum radius of the SSP, and $\Delta s$ the shape index interval. The maximum radius *maxd* defines the maximum dimension of the surface patch where the SSP is looked for. The curvature interval $\Delta s$ controls the spread of the SSP. They are set to 10 and 0.2, respectively for the three tracked regions.

The tracking of the apex region (P1) is very good. There is no significant differences between the temporal curves of the normal and abnormal LV at the apex [Fig. 7(a) and (b), and Fig. 8(a)]. Temporal mean shape index is nearly constant indicating the stability of the ellipsoidal shape of the apex over time [Fig. 7(a) and (b)]. For the curvedness, the well-defined systolic peak (time 8) is followed by a smaller one (time 16) corresponding to a second contraction of the apex during the diastole that is effectively observed [Fig. 8(a)].

The anterior zone P2 is initially saddle-like shaped. The shape relative to P2 with the normal LV is constant during the cardiac cycle [Fig. 7(a)]. With the akinetic LV, however, P2 becomes slightly ellipsoidal during systole as it corresponds to the ischemic less-contractile region [Fig. 7(b)].

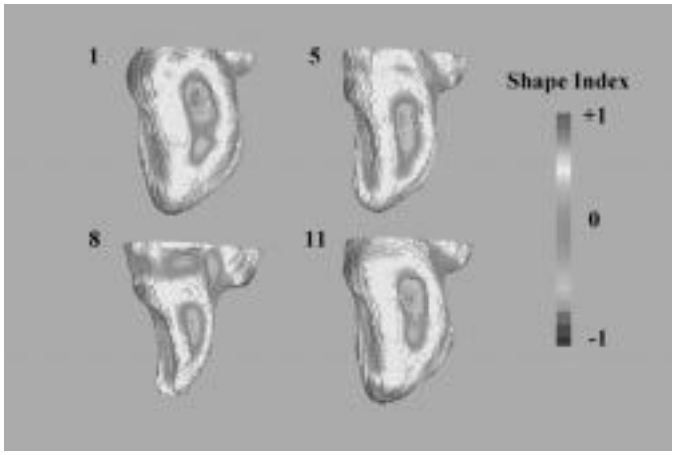


(a)

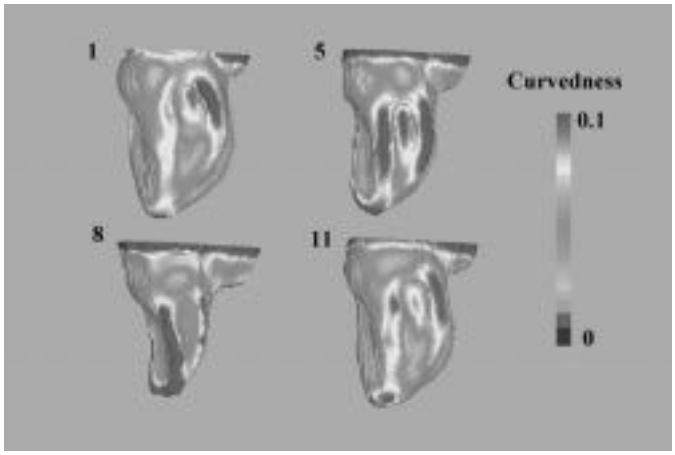


(b)

Fig. 5. (a) 3-D free wall views of the distribution of the shape index over the LV surfaces (3-D X-ray data) at four cardiac instants. It reveals the main shape attributes present on the LV: convex and concave elliptical shapes and saddle-like shapes. The shape is quasistable over the cardiac cycle (time 1 corresponds to end-diastole, time 8 to the end-systole). (b) Distribution of the curvedness at the same four instants.

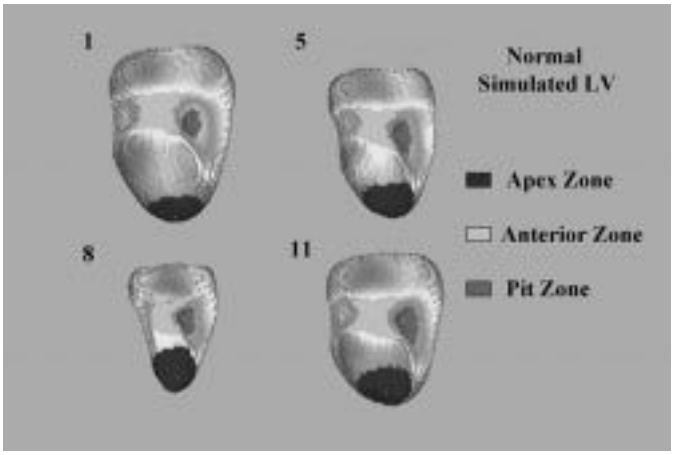


(a)

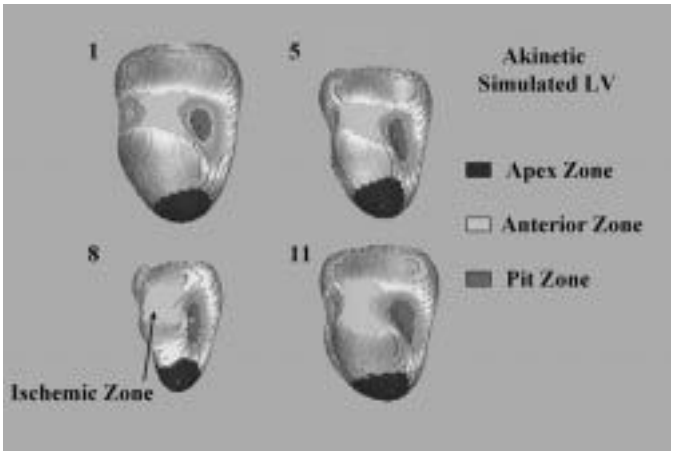


(b)

Fig. 6. (a) Anterior views of the normal harmonic LV at four cardiac instants. Three SSP's are tracked over the cardiac cycle and are identified by different colors: dark blue for the apex zone (P1), cyan for the anterior zone (P2), and red for the pit zone (P3). Time 1 corresponds to end-diastole, time 8 to the end-systole. (b) Anterior views of the akinetic harmonic LV with the tracking of the corresponding SSP's at four cardiac instants.

Mean curvedness is not significantly different between normal and abnormal LV's [Fig. 8(b)].

Results on the mean curvedness of the pit zone P3 shows a clear difference between the normal and abnormal cases [Fig. 8(c)]. The ischemic region tends to push away the neighboring regions such as P3.

We observed that the open trajectories of the geodesic centers of the SSP's are close to a loop both with the normal and abnormal left ventricles, although it is not ensured by the algorithm.

The tracking of the SSP over the cardiac cycle is satisfactory with the presented harmonic LV sequences as demonstrated by the smooth continuous graphical evolution of the mean curvature parameters of the SSP. These evolution can be intuitively interpreted in terms of deformation. If the deformations are larger however, the trace can be lost. The basic tracking algorithm can be sophisticated by taking into account other parameters of the SSP such as the area, the normals to the surface, the shape and curvedness spectra over the SSP or higher-order moments of the curvatures. The tracking should be undoubtedly more robust if it could include a neighborhood information of the SSP. Therefore, we intend to partition the entire LV surface in SSP's and track this representation as a whole.

## V. Conclusion

This paper presents a shape-based approach to the motion analysis of the LV endocardial surface. Since no information is available about the true physical deformation of the surface and since there is no explicit point-to-point correspondence, we propose to track geometrical descriptors of the surface over time. First, a curvature description of the surface is derived which basically relies on two curvature indexes that decouples the shape attribute (shape index) and the magnitude of the curvature (curvedness). Second, the shape dynamics is analyzed through a global and a regional curvature tracking approaches. The global approach shows the overall changes of the shape through the temporal shape spectra. This new representation is proved to give significant differences between normal and abnormal simulated left ventricles, especially when the pathology globally affects the function. In order to more locally analyze the LV deformation, a regional curvature tracking approach is proposed. The difficulty consists in following

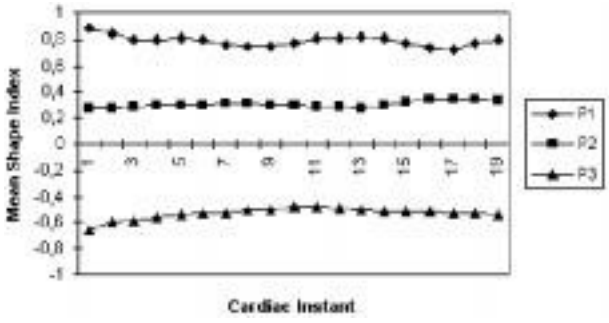


(a)

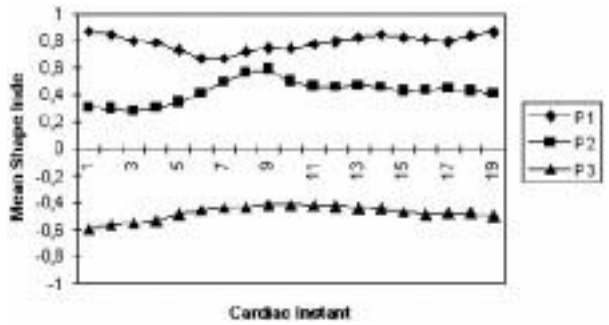


(b)

Fig. 7. Graphs of the evolution of the mean shape index over time for the three SSP's. (a) Normal simulated LV. (b) Akinetic simulated LV.

the anatomical identical regions. Therefore, the algorithm combines both geometrical information (the curvatures) and spatial information (data proximity). It relies on the definition of a SSP. The algorithms are applied to simulated normal and ischemic left ventricles. The results of the temporal tracking of the SSP are coherent and very promising since it is possible to intuitively and accurately interpret the deformation. This work is a first step toward the automatic spatio-temporal analysis of deformable surfaces and more specifically of the myocardial surfaces. Based on this framework, the next step will concern the development of a complete dynamic surface description in order to analyze the entire deformable surface at once and to be able to compare them. Adaptation and application of the methods to clinical data sets is also our primary concern.

## Appendix A
## Notations

Let $\mathbf{x}(u,v)$ be a regular parameterization of a surface $S$. The following notations are used.

| | |
|---|---|
| $N(p)=\frac{x_u \Lambda x_v}{\lvert x_u \Lambda x_v \rvert}$ | Unit normal vector at point $p \in S$. |
| $T_p(S)$ | Tangent plane at $p \in S$. |
| $x_u,\ x_v$ | First partial derivatives of $x(u,v)$. |
| $x_{uu}, x_{uv}, x_{vv}$ | Second partial derivatives of $x(u,v)$. |
| $E=\langle x_u, x_u\rangle$<br>$F=\langle x_u, x_u\rangle$<br>$G=\langle x_u, x_u\rangle$ | Coefficients of the first fundamental form of $S$ at $p$. |
| $e=\langle N, x_{uu}\rangle$<br>$f=\langle N, x_{uv}\rangle$<br>$g=\langle N, x_{vv}\rangle$ | Coefficients of the second fundamental form. |

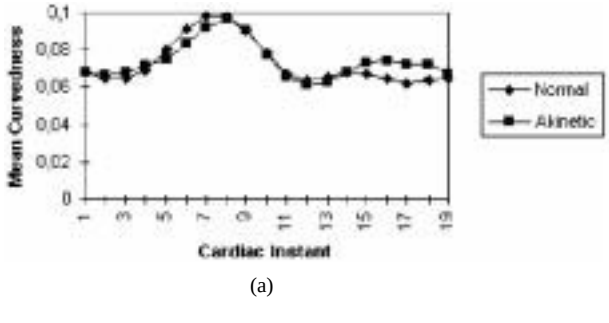


(a)

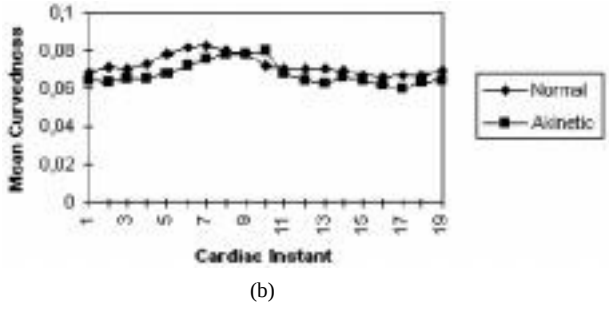


(b)

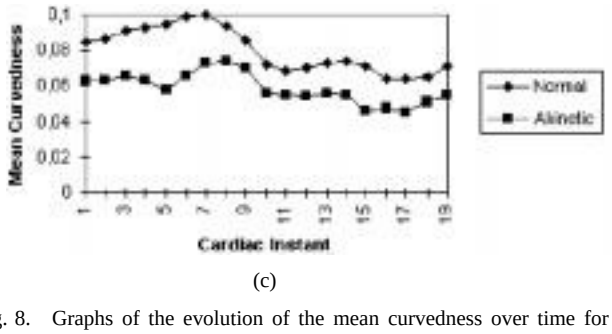


(c)

Fig. 8. Graphs of the evolution of the mean curvedness over time for the three SSP's. (a) Apex zone (P1). (b) Anterior zone (P2). (c) Pit zone (P3).

| | |
|---|---|
| $(k_1, k_2)$ | *Principal curvatures* at $p$ $(k_1 \geq k_2)$ |
| $K$ | $= k_1 k_2 = -\det \begin{pmatrix} e & f \\ f & g \end{pmatrix} \begin{pmatrix} E & F \\ F & G \end{pmatrix}^{-1}$ Gaussian curvature. (13) |
| $H$ | $= \frac{k_1 + k_2}{2} = \frac{1}{2} \frac{eG - 2fF + gE}{EG - F^2}$ mean curvature. (14) |
| $\Lambda$ | Cross product. |
| $\langle\rangle$ | Scalar product. |

(See [21] for an extended treatise on differential geometry and [2] for a summary of the main definitions.)

## Appendix B
## Differential Characteristics of the Superquadrics

The implicit equation of the superellipsoid is [5]

$$F(x,y,z) = \left( \left( \frac{x}{a_1} \right)^{\frac{2}{\varepsilon_2}} + \left( \frac{y}{a_2} \right)^{\frac{2}{\varepsilon_2}} \right)^{\frac{\varepsilon_2}{\varepsilon_1}} + \left( \frac{z}{a_3} \right)^{\frac{2}{\varepsilon_1}} = 1 \tag{15}$$

where $a_1$, $a_2$, $a_3$, $\varepsilon_1$, and $\varepsilon_2$ take real values.

The corresponding parametric equation is

$$x(\eta,\omega)=\begin{bmatrix} a_1\ \text{sign}\ (C_\omega)|C_\eta|^{\varepsilon_1}|C_\omega|^{\varepsilon_2} \\ a_2\ \text{sign}\ (S_\omega)|C_\eta|^{\varepsilon_1}|S_\omega|^{\varepsilon_2} \\ a_3\ \text{sign}\ (S_\eta)|S_\eta|^{\varepsilon_1} \end{bmatrix} \quad -\frac{\pi}{2}\le\eta\le\frac{\pi}{2},\ -\pi\le\omega\le\pi \tag{16}$$

where $C_l=\cos(l)$, $S_l=\sin(l)$. Then, we have $(\eta,\omega\in[0,\frac{\pi}{2}])$

$$x_\eta=\begin{pmatrix} -a_1\varepsilon_1 S_\eta C_\eta^{\varepsilon_1-1}C_\omega^{\varepsilon_2} \\ -a_2\varepsilon_1 S_\eta C_\eta^{\varepsilon_1-1}S_\omega^{\varepsilon_2} \\ a_3\varepsilon_1 C_\eta S_\eta^{\varepsilon_1-1} \end{pmatrix}$$

$$x_\omega=\begin{pmatrix} -a_1\varepsilon_2 C_\eta^{\varepsilon_1}S_\omega C_\omega^{\varepsilon_2-1} \\ a_2\varepsilon_2 C_\eta^{\varepsilon_1}C_\omega S_\omega^{\varepsilon_2-1} \\ 0 \end{pmatrix}$$

$$N(\eta,\omega)=\begin{bmatrix} \frac{1}{a_1}C_\eta^{2-\varepsilon_1}C_\omega^{2-\varepsilon_2} \\ \frac{1}{a_2}C_\eta^{2-\varepsilon_1}S_\omega^{2-\varepsilon_2} \\ \frac{1}{a_3}S_\eta^{2-\varepsilon_1} \end{bmatrix}=x_\eta\Lambda x_\omega.$$

The coefficients of the first fundamental form are then

$$E=\langle x_u,x_u\rangle,\quad F=\langle x_u,x_v\rangle,\quad G=\langle x_v,x_v\rangle$$

$$x_{\eta\eta}=\begin{pmatrix} -a_1\varepsilon_1 C_\omega^{\varepsilon_2}\left(C_\eta^{\varepsilon_1}-(\varepsilon_1-1)S_\eta^2 C_\eta^{\varepsilon_1-2}\right) \\ -a_2\varepsilon_1 S_\omega^{\varepsilon_2}\left(C_\eta^{\varepsilon_1}-(\varepsilon_1-1)S_\eta^2 C_\eta^{\varepsilon_1-2}\right) \\ -a_3\varepsilon_1\left(S_\eta^{\varepsilon_1}-(\varepsilon_1-1)C_\eta^2 S_\eta^{\varepsilon_1-2}\right) \end{pmatrix}$$

$$x_{\omega\omega}=\begin{pmatrix} -a_1\varepsilon_2 C_\eta^{\varepsilon_1}\left(C_\omega^{\varepsilon_2}-(\varepsilon_2-1)S_\omega^2 C_\omega^{\varepsilon_2-2}\right) \\ -a_2\varepsilon_2 C_\eta^{\varepsilon_1}\left(S_\omega^{\varepsilon_2}-(\varepsilon_2-1)C_\omega^2 S_\omega^{\varepsilon_2-2}\right) \\ 0 \end{pmatrix}$$

$$x_{\eta\omega}=\begin{pmatrix} a_1\varepsilon_1\varepsilon_2 S_\eta C_\eta^{\varepsilon_1-1}S_\omega C_\omega^{\varepsilon_2-1} \\ -a_2\varepsilon_1\varepsilon_2 S_\eta C_\eta^{\varepsilon_1-1}C_\omega S_\omega^{\varepsilon_2-1} \\ 0 \end{pmatrix}.$$

The coefficients of the second fundamental form are

$$e=\langle N,x_{uu}\rangle,\quad f=\langle N,x_{uv}\rangle,\quad g=\langle N,x_{vv}\rangle.$$

The coefficients $(a_{ij})$ of the differential of the Gauss map $dN_p$ are

$$a_{11}=\frac{1}{D}(Ff-Ge),\quad a_{12}=\frac{1}{D}(Fg-Gf)$$
$$a_{21}=\frac{1}{D}(Fe-Ef),\quad a_{22}=\frac{1}{D}(Ff-Eg)$$

with

$$D=EG-F^2.$$

The determinant of $dN_p$ is the Gaussian curvature $K$, the mean curvature $H$ is the negative of half of the trace of $dN_p$.

Similar calculations can be done for the superhyperboloid of one piece with the corresponding implicit and parametric equations given in [5].

## ACKNOWLEDGMENT

The authors wish to thank E. L. Rittman and R. A. Robb of the Mayo Foundation for providing them with the DSR data. They also wish to thank J.-M. Morvan (Department of Mathematics, Claude Bernard University, Lyon, France) and P. Croisille for valuable discussions and comments. This work is part of the GDR ISIS research group of the French National Center for Scientific Research (CNRS).

## REFERENCES

[1] A. A. Amini, R. L. Owen, P. Anandan, and J. S. Duncan, "Non-rigid motion models for tracking the left-ventricular wall," in *Lecture Notes in Computer Science: Information Processing in Medical Images.* New York: Springer-Verlag, 1991, pp. 343–356.

[2] A. A. Amini and J. S. Duncan, "Differential geometry for characterizing 3-D shape change," *SPIE Mathematical Methods in Medical Imaging*, vol. 1768, pp. 170–181, 1992.

[3] L. Axel and L. Dougherty, "MR Imaging of motion with spatial modulation of magnetization," *Radiol.*, no. 171, pp. 41–45, 1989.

[4] H. Azhari, I. Gath, R. Beyar, M. L. Marcus, and S. Sideman, "Discrimination between healthy and diseased hearts by spectral decomposition of their left ventricular three-dimensional geometry," *IEEE Trans. Med. Imag.*, vol. 10, no. 2, pp. 207–215, June 1991.

[5] A. H. Barr, "Superquadrics and angle-preserving transformations," *IEEE Comput. Graphics Applicat. Mag.*, pp. 11–23, Jan. 1981.

[6] P. J. Besl and R. C. Jain, "Invariant surface characteristics for 3-D object recognition in range images," *CVGIP: Image Understanding*, no. 33, pp. 33–80, 1986.

[7] P. J. Besl, *Surfaces in Range Image Understanding.* Berlin: Springer-Verlag, 1988.

[8] ———, "Geometric signal processing," in *Analysis and Interpretation of Range Images*, R. C. Jain and A. K. Jain, Eds. New York: Springer-Verlag, 1990, ch. 3, pp. 141–205.

[9] E. Boix, "Approximation linéaire des surfaces de $\Re^3$ et applications," Ph.D. mathematical thesis, Polytechnic School, Paris, Apr. 1995.

[10] E. L. Bolson, D. Kliman, F. Sheehan, and H. T. Dodge, "Left ventricular segmental wall motion—A new method using local direction information," *Comput. Cardiol.*, pp. 245–248, 1980.

[11] J. Canny, "A computational approach to edge detection," *IEEE Trans. Pattern Anal., Machine Intell.*, vol. 8, no. 6, pp. 679–698, Nov. 1986.

[12] C. W. Chen, T. S. Huang, and M. Arrott, "Modeling, analysis, and visualization of left ventricle shape and motion by hierarchical decomposition," *IEEE Trans. Pattern Anal. Machine Intell.*, vol. 16, no. 4, pp. 342–356, 1994.

[13] X. Chen and F. Schmitt, "Intrinsic surface properties from surface triangulation," *Rapport Telecom Paris*, no. 92 D 004, Mar. 1992.

[14] P. Clarysse, O. Jaouen, I. E. Magnin, and J. M. Morvan, "3-D representation and deformation analysis of the heart walls from X-rays and MR Images," in *Proc. Computers in Cardiology*, Sept. 25–28, 1994, pp. 657–660.

[15] P. Clarysse, "Current and future trends in cardiac image processing," presented at *2nd IEEE-EMBS Int. Summer School on Biomedical Imaging*, Berder Island, Brittany, France, June 22–July 1, 1996.

[16] L. Coghlan, H. R. Singleton, L. J. Dell'Italia, C. E. Linderholm, and G. M. Pohost, "Measurement of three dimensional normal vectors, principal curvatures, and wall thickness of the heart using cine-mri," in *Proc. SPIE Medical Imaging*, 1995, vol. 2433, pp. 292–302.

[17] I. Cohen, N. Ayache, and P. Sulger, "Tracking points on deformable objects using curvature information," in *Proc. 2nd Euro. Conf. Computer Vision*, May 8–23, 1992, pp. 458–466.

[18] I. Cohen, L. D. Cohen, and N. Ayache, "Using deformable surfaces to segment 3-D images and infer differential structures," *CVGIP: Image Understanding*, vol. 56, no. 2, pp. 242–263, 1992.

[19] G. T. Daughters, E. L. Alderman, and N. B. Ingels, "A rational approach to the clinical detection of wall motion abnormalities," in *Proc. Int. Symp. Ventricular Wall Motion*, Lausanne, Switzerland, 1982, pp. 74–82.

[20] M. H. Davis, A. Khotanzad, D. P. Flamig, and S. E. Harms, "Curvature measurement of 3-D objects: Evaluation and comparison of three methods," in *Proc. Int. Conf. Image Processing*, Washington, D.C., Oct. 23–26, 1995, vol. II, pp. 627–630.

[21] M. P. Do Carmo, *Differential Geometry of Curves and Surfaces*. Englewood Cliffs, NJ: Prentice-Hall, 1976.

[22] C. Dorai and A. K. Jain, "Shape spectra based view grouping for free-form objects," in *Proc. Int. Conf. Image Processing*, Washington, D.C., Oct. 23–26, 1995, vol. III, pp. 340–343.

[23] C. Dorai and A. K. Jain, "COSMOS—A representation scheme for 3-D free-form surfaces," Dept. Comput. Sci., Michigan State Univ., East Lansing, Tech. Rep. CPS-95-1, Jan. 1995.

[24] J. S. Duncan, P. Shi, A. Amini, R. T. Constable, L. Staib, D. Dione, Q. X. Shi, E. Heller, M. Singer, A. Chakraborty, G. Robinson, J. Gore, and A. Sinusas, "Toward reliable, noninvasive measurement of myocardial function from 4-D images," *SPIE Med. Imag.*, vol. 2168, pp. 149–161, 1994.

[25] T. L. Faber and E. M. Stokely, "Orientation of 3-D structures in medical images," *IEEE Trans. Pattern Anal. Machine Intell.*, vol. 10, no. 5, pp. 626–633, Sept. 1988.

[26] P. J. Flynn and A. K. Jain, "On reliable curvature estimation," in *Proc. IEEE Conf. Computer Vision and Pattern Recognition*, June 1989, pp. 110–116.
[27] D. Friboulet, I. E. Magnin, and D. Revel, "Assessment of a model for overall left ventricular three-dimensional motion from MRI data," *The Int. J. Cardiac Imag.*, vol. 8, pp. 175–190, 1992.
[28] D. Friboulet, I. E. Magnin, A. Pommert, and M. Amiel, "3-D curvature features of the left ventricle from CT volumic images," *SPIE Image, Signal Processing*, vol. 1768, pp. 19–24, July 1992.
[29] G. M. Hutchins, B. H. Bulkley, G. W. Moore, M. A. Piaso, and F. T. Lohr, "Shape of the human cardiac ventricles," *Amer. J. Cardiol.*, vol. 41, pp. 646–654, Apr. 1978.
[30] N. B. Ingels, C. W. Mead, G. T. Daughters, E. B. Stinson, and E. L. Alderman, "A new method for assessment of left ventricular segmental wall motion," *Comput. Cardiol.*, pp. 57–78, 1978.
[31] C. Kambhamettu and D. B. Goldgof, "Curvature-based approach to point correspondence recovery in conformal nonrigid motion," *CVGIP: Image Understanding*, vol. 60, no. 1, pp. 26–43, 1994.
[32] S. B. Kang and K. Ikeuchi, "The complex EGI: A new representation for 3-D pose determination," *IEEE Trans. Pattern Anal. Machine Intell.*, vol. 15, no. 7, pp. 707–721, July 1993.
[33] J. J. Koenderinck and A. J. Van Doorn, "Surface shape and curvature scales," *Image Vision Computing*, vol. 10, no. 8, pp. 557–565, Oct. 1992.
[34] W. G. Kussmaul, J. P. Kleaveland, G. R. Zeevi, and J. W. Hirshfeld, "Accuracy of subjective and computer-assisted assessment of angiographic left ventricular regional wall motion," *Catheterization Cardiovasc. Diag.*, vol. 20, pp. 153–164, 1990.
[35] R. F. Leighton, S. M. Wilt, and R. P. Lewis, "Detection of hypokinesis by a quantitative analysis of left ventricular cineangiograms," *Circ.*, vol. 50, pp. 121–127, 1974.
[36] J. Lessick, S. Sideman, H. Azhari, E. Shapiro, J. L. Weiss, and R. Beyar, "Evaluation of regional load in acute ischemia by three-dimensional curvatures analysis of the left ventricle," *Ann. Biomed. Eng.*, vol. 21, pp. 147–161, 1993.
[37] P. Liang and C. H. Taubes, "Orientation-based differential geometric representations for computer vision applications," *IEEE Trans. Pattern Anal. Machine Intell.*, vol. 16, no. 3, pp. 249–258, Mar. 1994.
[38] J.-M. Gorce, D. Friboulet, and I. E. Magnin, "Estimation of three-dimensional cardiac velocity fields: Assessment of a differential method and application to 3-D CT data," *Med. Image Anal.*, vol. 1, no. 3, pp. 245–261, 1997.
[39] G. B. J. Mancini, M. T. LeFree, and R. A. Vogel, "Curvature analysis of normal ventriculograms: Fundamental framework for the assessment of shape changes in man," *Comput. Cardiol.*, p. 141, 1985.
[40] G. B. J. Mancini, S. F. DeBoe, E. Anselmo, S. B. Simon, M. T. LeFree, and R. A. Vogel, "Quantitative regional curvature analysis: An application of shape determination for the assessment of segmental left ventricular function in man," *Amer. Heart J.*, vol. 113, no. 2, pp. 326–334, 1987.
[41] G. B. J. Mancini, S. F. DeBoe, M. J. McGillem, and E. R. Bates, "Quantitative regional curvature analysis: A prospective evaluation of ventricular shape and wall motion measurements," *Amer. Heart J.*, vol. 116, No. 6, pp. 1616–1621, 1988.
[42] A. Matheny and D. Goldgof, "The use of three- and four-dimensional surface harmonics for rigid and nonrigid shape recovery and representation," *IEEE Trans. Pattern Anal. Machine Intell.*, vol. 7, no. 10, pp. 967–981, Oct. 1995.
[43] D. Metaxas and D. Terzopoulos, "Shape and nonrigid motion estimation through physics-based synthesis," *IEEE Trans. Pattern Anal. Machine Intell.*, vol. 15, no. 6, pp. 580–591, June 1993.
[44] F. G. Meyer, R. T. Constable, A. J. Sinusas, and J. S. Duncan, "Tracking myocardial deformation using phase contrast MR velocity fields: A stochastic approach," *IEEE Trans. Med. Imag.*, vol. 15, no. 4, pp. 1–12, Aug. 1996.
[45] S. K. Mishra, D. B. Goldgof, T. S. Huang, and C. Kambhamettu, "Curvature-based nonrigid motion analysis from 3-D point correspondences," *Int. J. Imag. Syst. Technol.*, vol. 4, pp. 214–225, 1993.
[46] O. Monga, N. Ayache, and P. T. Sander, "From voxel to curvature," INRIA, Rapport de Recherche 1356, Dec. 1990.
[47] O. Monga and R. Deriche, "3-D edge detection using recursive filtering: Application to scanner images," *Comput. Vision, Graphics, Image Understanding*, vol. 53, no. 1, pp. 76–87, Jan. 1991.
[48] O. Monga and S. Benayoun, "Using partial derivatives of 3-D images to extract typical surface features," INRIA, Rapport de Recherche 1599, Feb. 1992.
[49] C. Wastar and N. Ayache, "Frequency-based nonrigid motion analysis: Application to four-dimensional medical images, *IEEE Trans. Pattern Anal. Machine Intell.*, vol. 18, no. 11, pp. 1067–1079, Nov. 1996.
[50] W. G. O'Dell, C. C. Moore, W. C. Hunter, E. A. Zerhouni, and E. R. McVeigh, "Three-dimensional myocardial deformations: Calculation with displacement field fitting to tagged MR Images," *Radiol.*, no. 195, pp. 829–835, 1995.
[51] J. Park, D. Metaxas, and L. Axel, "Analysis of left-ventricular wall motion based on volumetric deformable models and MRI-SPAMM," *Med. Image Anal. J.*, vol. 1, no. 1, pp. 1–19, 1996.
[52] J. Park, D. Metaxas, A. A. Young, and L. Axel, "Deformable models with parameter functions for cardiac motion analysis from tagged MRI data," *IEEE Trans. Med. Imag.*, vol. 15, no. 3, pp. 278–289, June 1996.
[53] N. J. Pelc, R. J. Herfkens, A. Shimakaya, and D. Enzmann, "Phase contrast cine magnetic resonance imaging," *Magn. Reson. Quat.*, vol. 7, no. 4, pp. 229–254, 1991.
[54] A. Pentland and B. Horowitz, "Recovery of nonrigid motion and structure," *IEEE Trans. Pattern Anal. Machine Intell.*, vol. 13, pp. 730–742, July 1991.
[55] M. J. Potel, S. A. McKay, J. M. Rubin, A. M. Aisen, and R. E. Sayre, "Three-dimesional left ventricular wall motion in man. Coordinate systems for representing wall movement direction," *Invest. Radiol.*, vol. 19, pp. 499–509, 1984.
[56] W. H. Press, B. P. Flannery, S. A. Teukolsky, and W. T. Vetterling, *Numerical Recipes in C. The Art of Scientific Computing*. 2nd ed. New York: Cambridge Univ. Press, 1992.
[57] E. L. Ritman, R. A. Robb, and L. D. Harris, *Imaging Physiological Functions: Experience with the Dynamic Spatial Reconstructor*. New York: Praeger, 1985.
[58] M. S. Sacks, C. J. Chuong, G. H. Templeton, and R. Peshock, "*In vivo* 3-D reconstruction and geometric characterization of the right ventricular free wall," *Ann. Biomed. Eng.*, vol. 21, pp. 262–275, 1993.
[59] P. T. Sander and S. W. Zucker, "Stable surface estimation," in *Proc. 8th Int. Conf. Pattern Recognition*, Oct. 1986, pp. 1165–1167.
[60] ———, "Tracing surfaces for surfacing traces," in *Proc. First Int. Conf. Computer Vision*, June 1987, pp. 241–249.
[61] ———, "Inferring surface trace and differential structure from 3-D images," *IEEE Trans. Pattern Anal. Machine Intell.*, vol. 12, no. 9, pp. 833–854, Sept. 1990.
[62] ———, "Singularities of principal direction fields from 3-D images," *IEEE Trans. Pattern Anal. Machine Intell.*, vol. 14, no. 3, pp. 309–317, 1992.
[63] U. Sigwart and P. H. Heintzen, Eds., *Proc. Int. Symp. Ventricular Wall Motion*, 1984, 327 pp.
[64] R. Solina and R. Bajcsy, "Recovery of parametric models from range images: The case for superquadrics with global deformations," *IEEE Trans. Pattern Anal. Machine Intell.*, vol. 12, no. 2, pp. 131–147, Feb. 1990.
[65] S. Song and R. Leahy, "Computation of 3-D velocity fields from 3-D cine CT images," *IEEE Trans. Med. Imag.*, vol. 10, pp. 295–306, Sept. 1991.
[66] D. K. Stewart, H. T. Dodge, and M. Frimer, "Quantitative analysis of regional myocardial performance in coronary artery desease," *Cardio-Vascular Imag. Image Processing, Theory and Practice*, vol. 72, pp. 217–224, 1975.
[67] E. M. Stokely and S. Y. Wu, "Surface parametrization and curvature measurements of arbitrary 3-D objects: Five practical methods," *IEEE Trans. Pattern Anal. Machine Intell.*, vol. 14, no. 8, pp. 833–840, Aug. 1992.
[68] R. Tennant and C. J. Wiggers, "The effect of coronary occlusion on myocardial contraction," *Amer. J. Physiol.*, vol. 112, pp. 351–361, 1935.
[69] B. Vemuri, A. Mitiche, and J. Aggarwal, "Curvature-based representation of objects from range data," *Image Vision Computing*, vol. 4, no. 2, pp. 107–114, May 1986.
[70] K. R. Walley, M. Crover, G. L. Raff, W. Benge, B. Hanaford, and S. A. Glantz, "Left ventricular dynamic geometry in the infarct and open chest dog," *Circ. Res.*, vol. 50, pp. 573–589, 1982.
[71] A. A. Young, D. L. Kraitchman, L. Dougherty, and L. Axel, "Tracking and finite element analysis of stripe deformation in Magnetic Resonance Tagging," *IEEE Trans. Med. Imag.*, vol. 14, no. 3, pp. 413–421, 1995.
[72] E. A. Zerhouni, D. M. Parish, W. J. Rogers, A. Yang, and E. P. Shapiro, "Human heart: Tagging with MR imaging—A method for noninvasive assessment of myocardial motion," *Radiol.*, vol. 169, pp. 59–63, 1988.